Hydraulic Tomography and Trichloroethene Dissolution in a Fractured Dolostone: Small Scale Laboratory Experiments

by

Rubaiat Sharmeen

A thesis
presented to the University of Waterloo
in fulfillment of the
thesis requirement for the degree of
Master of Science
in
Earth Sciences

Waterloo, Ontario, Canada, 2011

AUTHOR'S DECLARATION

I hereby declare that I am the sole author of this thesis. This is a true copy of the thesis, including any required final revisions, as accepted by my examiners.

I understand that my thesis may be made electronically available to the public.

Rubaiat Sharmeen

Abstract

In fractured geologic media, flow and contaminant transport are predominantly controlled by the fractures, their distribution and connectivity. The accurate characterization of fractured geologic medium, imaging of fracture patterns and their connectivity have been a challenge for decades. Given the complexities of fractured networks in the subsurface and Dense Non Aqueous Phase Liquid (DNAPL) contamination, in this thesis, transient hydraulic tomography (THT), a recently developed tool for characterizing aquifer heterogeneity is evaluated under laboratory conditions to delineate discrete fractures. Laboratory experiments and modeling studies are also conducted to understand TCE plume behavior.

A dolomite rock sample, which is 91.5 cm in length, 60.5 cm in height and 5 cm thick, was fractured in the laboratory to perform the experiments. After the fractured block was enclosed in a flow cell, flow-through and pumping tests were conducted to characterize the fractured rock block. The data from the pumping tests were then analyzed using the SSLE code developed by *Zhu and Yeh* [2005] and transient hydraulic tomography (THT) was conducted to image the fracture pattern and their connectivity through the delineation of K and S_s distributions (the tomograms). Synthetic pumping tests, identical in configuration to the laboratory ones were also conducted using HydroGeoSphere (HGS) [*Therrien et al*, 2009] in a synthetic replica of the fractured block to compare the observed and simulated drawdowns. Then synthetic THT analysis was performed utilizing the synthetic pumping test data to compare the tomograms obtained from the THT analysis of synthetic and laboratory pumping tests.

Results suggest that the THT analysis of multiple laboratory pumping tests captured the fracture pattern and their connectivity quite well and they became more vivid with the additional pumping tests. The estimated high hydraulic conductivity (K) and low specific storage (S_s) zones clearly show the fractures and their connectivity. The pattern of K and S_s tomograms obtained from the analyses of synthetic and laboratory pumping tests were similar. Estimated K and S_s values for the fractures and the matrix may not exactly replicate the actual K and S_s values for the fractured rock, but the model also provides uncertainty estimates associated with the resulting K and S_s tomograms.

In this study, two cases of transient hydraulic tomography (THT) analysis of the laboratory pumping tests were performed by changing the location of 2nd and 3rd pumping tests among the three to examine if there is any significant impact of these pumped location on the pattern of resulting

hydraulic conductivity (K) and specific storage (S_s). The initial pumping test was the same for two cases. Results show that the patterns of estimated K and S_s tomograms obtained from these two cases are similar, although the pumped locations (2^{nd} and 3^{rd} tests among the three) utilized for the inversion were different for two cases suggesting that the location of these later pumping tests does not significantly impact the estimates for this fractured rock block. However, the initial test should be selected carefully as that seems to set the pattern of the tomograms.

The estimated K and S_s tomograms were validated by predicting five independent pumping tests conducted in the fractured rock block. These five pumping tests were not included during the construction of the K and S_s tomograms. For most of the independent pumping tests, good correspondence between the simulated and observed drawdown was achieved.

The study indicates that, it is possible to delineate discrete fractures, their pattern and connectivity by carefully applying of THT analysis of multiple pumping tests based on the inverse code SSLE [*Zhu and Yeh,* 2005]. In addition, hydraulic tomography seems to be a cost effective tool for characterizing fractured rock since it does not require the detailed information on fracture geometry parameters such as aperture, trace length, orientation, spatial distribution, and connectivity, which are difficult to quantify. These parameters are usually unavailable between boreholes. Therefore, THT appears to be a promising approach in delineating fractures and their connectivity in subsurface. However, it is still at the early stage as the study was conducted in the laboratory under controlled conditions. Small scale field experiments need to be conducted to validate THT as a tool for the characterization of hydraulic parameters of fractured rocks.

Upon completion of the hydraulic characterization, several conservative tracer tests were conducted using bromide (Br^-) as a conservative tracer to aid in the design of TCE dissolution experiment. Once the tracer experiments were completed, a known volume of pure phase TCE was injected at a known location in the flow cell to create a well-defined source zone. A constant hydraulic gradient was maintained by fixing the hydraulic heads at the two head tanks to induce steady groundwater flow through the flow cell. Water samples were obtained at a down gradient monitoring port for 3 months to obtain a long-term breakthrough curve of TCE in the aqueous phase. The purpose of this experiment was to study TCE dissolution behaviour in the fractured rock sample. Then HydroGeoSphere (HGS) was used to model the aqueous phase TCE transport using two separate approaches: 1) the Discrete Fracture Network modeling approach and 2) the stochastic continuum approach, to investigate whether they can capture the dissolution behavior.

Both approaches were able to capture the pattern of the breakthrough curve in the fractured rock. The discrete fracture approach captured the observed TCE plume and the dissolution behavior quite well. On the other hand, the stochastic continuum approach, in which the fractured rock block was treated as porous medium having a heterogeneous *K* field obtained from THT analysis, also appeared to be promising in capturing the aqueous phase transport of TCE. Despite some early time deviation, the simulated breakthrough curve captured the overall observed concentration profile. However, the stochastic continuum approach seems to be more cost effective as it does not require detailed information about fracture aperture and their spatial distribution which are difficult if not impossible to obtain between boreholes. Note that, the studies were conducted based on a laboratory experiment conducted in a controlled environment. The experimental block was well characterized and the geometry of the experimental block as well as the flow through the system was well understood from the hydraulic and tracer experiments. Thus small scale field experiment is required to support this conclusion.

Acknowledgements

This research project was supported by the Strategic Environmental Research & Development Program (SERDP) and the University of Waterloo.

I would like to thank all of my committee members, Dr. Edward Sudicky, Dr. Jim Yeh, Dr. Young-Jin Park and Dr. Steven J. Berg for their constructive feedback and advice over last two years and reviewing my thesis. I greatly appreciate Dr. Park's help and guidance to complete some part of this research project. This work would not have been possible without the help and guidance of Dr. Berg. I am really appreciative of his willingness to share his expertise, experience and knowledge. Our discussions have always been useful to solve problems and pointing me in new directions. I especially thank my thesis supervisor Dr. Walter A. Illman who has mentored me throughout this research and provided me with the opportunity to gain invaluable learning experience. I extremely appreciate his guidance and advice during the course of my Masters.

Thanks also go out to Paul Johnson, Wayne Noble and Rob McLaren for their technical assistances. Many part of this research work required their expertise and experience and it would not have gone so smoothly without their efforts.

I would also like to thank my fellow graduate student Fatemeh Vakili, who has been a great support over last two years.

Finally, I would like to thank my parents and brother for their care and support, and especially my husband, without whose love and support I would have never been able to complete my Masters.

.

Dedication

To my parents

Table of Contents

List of Figures

List of Tables

Chapter 1
Introduction

1.1 Problem Statement

Flow and transport through fractured geologic media have been an ever present challenge for hydrogeologists. Fractures are very common in subsurface geologic formations, and typically are the major conduits for groundwater flow and solute transport in a fractured media. The spatial distribution of these fractures, their connectivity and fracture hydraulic properties thus determine the extent of groundwater flow and contamination. Therefore, delineation of these fractures and their connectivity, and understanding the transports processes through them are critical in predicting flow and transport behavior through the fractured geologic media as well as to prevent and remediate groundwater contamination.

1.2 Review of Fractured Rock Characterization Approaches

Subsurface flow and transport are controlled by the hydraulic properties of the medium (i.e. porosity, hydraulic conductivity (K), specific storage (S_s) and their spatial variability, which are critical to estimate for any geologic media. In a fractured geologic medium, the high contrast of these hydraulic properties between the fractures and the matrix along with their spatial variability make it even more challenging to characterize the medium accurately.

The difficulties to characterize a fractured geologic medium have led to the development of different mathematical models based on different conceptualizations of fractured rock, For example, the equivalent porous media concept [e.g., *Bear*, 1972] assumes that in a large enough volume of the fractured formation, fracture density is sufficiently high so that the representative elementary volume (REV) of the fractured media behaves mathematically like a porous medium.

A fractured geologic medium consists of two distinct voids or pore spaces consisting of matrix pore spaces (primary pores) and fractures of variable sizes (secondary pores). Fractures (secondary pores) can be characterized as open conduits, but typically consist only a small percentage of the total volume of the medium. On the other hand, matrix pores (primary pores) are small, consist a larger portion of the total volume of the media in comparison to the fractures, but have a smaller lateral continuity [*Duguid and Lee*, 1977]. The effect of the different characteristics of these two types of pore spaces and the slow mass transfer process between the fracture and the matrix has led to the creation of dual porosity/mass transfer model [e.g., *Bibby*, 1981; *Moench*, 1984; *Zimmerman et al.*,

1993; *McKenna et al.*, 2001]. The dual porosity model assumes that a fractured medium contains two interacting overlapping continua: primary porosity or the matrix continuum that stores the bulk of the fluid and the high permeability, secondary porosity or the fracture continuum that stores as well as conducts fluid. On the other hand, in a dual permeability model [e.g., *Duguid and Lee*, 1977; *Gerke and Vangenuchten*, 1993a; b; *Illman and Hughson*, 2005] both the fracture and matrix continua conduct and store water. The dual permeability model considers matrix and fracture flow separately and assumes mass exchange between these two heterogeneous continua through a fracture-matrix interaction parameter. These models overcome the problem related to the slow mixing process between the fracture and the matrix, but they are only appropriate when a large volume of fractured media is considered, where fracture density is significantly high. Thus, flow and transport behavior predicted by these models are averaged over a large volume of fractured media, which may not be adequate when finer details to the fractured geologic medium including information on discrete fractures are required. For example, the prediction of rapid ground water flow and transport through the fracture network may necessitate the need for explicit accounting of discrete features. This need has therefore led to the development of discrete fracture network models [e.g., *Long et al.*, 1982; *Schwartz et al.*, 1983; *Smith and Schwartz*, 1984; *Dershowitz and Einstein*, 1988; *Dverstorp and Andersson*, 1989; *Cacas et al.*, 1990a;b; *Dverstorp et al.*, 1992; *Slough et al.*, 1999; *Benke and Painter*, 2003; *Darcel et al.*, 2003;*Park et al.*, 2001a; b; 2003; *Cvetkovic et al.*, 2004; *Painter and Cvetkovic*, 2005; *Wellman and Poeter*, 2005]. Some of the discrete fracture network (DFN) models determine the fracture aperture using the well known "cubic law" [*Romm*, 1966] and assign an "effective hydraulic aperture" to each fracture, which is proportional to the cubic root of the flow rate through the corresponding fracture. However, the idea of DFN is not only to image the large or dominant fractures but also thousands of fractures having different size and shape. The discrete fracture network models are almost always built by surveying the fractures and their geometry at a given site. It relies on the accurate measurements of the fracture size, shape, aperture and their spatial distribution. Thus it requires hydraulic and tracer tests performed at a very high spatial resolution and use of specialized geophysical tools to collect detailed deterministic and/or statistical information of the geometry of fractured zone and the spatial distribution of fracture apertures. *Neuman* [1987, 2005] discussed difficulties and limitations associated with discrete fracture approach in detail, thus a stochastic continuum concept [e.g., *Tsang et al.*, 1996; *Di Federico and Neuman*, 1998a; b; Di *Federico et al.*, 1999; *Vesselinov et al*., 2001a, 2001b; *Hyun et al.*, 2002; *Ando et al*., 2003; *Illman and Hughson*, 2005] may be utilized to model flow and transport in fractured geologic media. The

stochastic continuum concept emphasizes more on the hydraulic test results performed on a suitable scale than the fracture geometric data [*Neuman*, 2005]. It represents fractured rock as equivalent homogeneous porous medium with ground water flow governed by Darcy's law and treats the fractures and their properties as the spatially correlated random fields [*Selroos et al.*, 2002].

Over the past few decades, different techniques have been established to characterize fractured media. For example, *Hsieh et al.* [1985] conducted cross-hole hydraulic tests at the Oracle site in Arizona consisting of fractured granite and obtained the anisotropy of hydraulic conductivity (K) and specific storage (S_s) by treating the fractured rock as a uniform, anisotropic medium. *Neuman and Depner* [1988] applied the stochastic continuum approach to fractured rock. They measured hydraulic conductivity at small and large scales by packer tests and cross-hole tests respectively at the fractured granitic rocks near Oracle, Arizona and estimated anisotropic covariance function of log hydraulic conductivities at the site.

Numerous single-hole pneumatic injection tests in unsaturated fractured tuffs at the Apache Leap Research Site (ALRS) in central Arizona, USA, conducted by *Guzman et al*. [1996] were interpreted by *Illman* and *Neuman* [2000] and *Illman* [2005] using type curve methods. *Vesselinov* and *Neuman* [2001] analyzed selected single-hole pneumatic injection tests at the ALRS using a numerical inverse model by treating the medium to be medium. Moreover, *Illman* and *Neuman* [2001] interpreted one of many cross-hole pneumatic injection tests at the same site, while steady-state analysis [*Illman and Neuman*, 2003] and asymptotic approach [*Illman and Tartakovsky*, 2005a; b] were utilized to interpret the rest of the tests to infer the bulk pneumatic properties and fracture connectivity of the unsaturated fractured tuffs. *Illman* and *Tartakovsky* [2006] modified the asymptotic solution developed by *Illman and Tartakovsky* [2005a; b] to interpret three dimensional cross-hole hydraulic tests in fractured granite at the Grimsel site in Switzerland.

Vesselinov et al. [2001a, 2001b] interpreted the cross-hole pneumatic injection tests [*Illman*, 1999] in the unsaturated fractured tuffs using a numerical inverse model. They analyzed the data in two ways: (1) considering the pressure responses at one borehole monitoring interval at a time treating the fractured rock spatially uniform and (2) considering the pressure responses at borehole monitoring intervals from multiple tests simultaneously and thus introduced pneumatic tomography to delineate subsurface heterogeneity in both permeability and porosity.

Le Borgne et al. [2006] and *Williams and Paillet* [2002] used cross-borehole flow meter pulse tests to characterize subsurface connections between discrete fractures. In this method, hydraulic stress is

applied to a borehole through short period of pumping and the propagation of the pulse through the flow system is monitored using a flow meter during stressed period.

In an effort to improve the characterization approaches of fractured rock, *Day-Lewis et al.* [2000] combined geostatistical simulation and non-linear regression with hydraulic head data to infer fracture hydraulic connectivity. Their approach relied on simulated annealing and hydraulic connection data to identify fracture zone geometry. In a different study at the US Geological Survey Fractured Rock Hydrology Research Site near Mirror Lake, Grafton County, New Hampshire, USA, *Day-Lewis et al.* [2003] identified preferential flow paths in fractured rock using time-lapse difference-attenuation radar tomography. *Day-Lewis et al.* [2006] analyzed the tracer and cross-hole radar difference-attenuation data from the same site and constructed a suite of ground water flow and transport models based on geophysical data. They combined time-lapse geophysical data with conventional hydrologic characterization and found that the combination improved the fractured rock characterization.

Few of these hydrologic and geophysical approaches made significant advances in identifying fracture connectivity in space, although the characterization approaches are still under considerable debate [e.g., *Illman*, 2004, 2006; *Knudby and Carrera*, 2005; *Knudby and Carrera*, 2006]. Recent advances in characterizing subsurface heterogeneity using hydraulic tomography (HT) and pneumatic tomography (PT) [e.g., *Gottlieb and Dietrich*, 1995; *Butler et al.*, 1999; *Vasco et al.*, 2000; *Yeh and Liu*, 2000; *Vesselinov et al.*, 2001a; b; *Bohling et al.*, 2002; 2007; *Liu et al.*, 2002; 2007; *Brauchler et al.*, 2003; *McDermott et al.*, 2003; *Zhu and Yeh*, 2005; 2006; *Illman et al.*, 2007; 2008; 2009; *Li et al.*, 2007; 2008; *Hao et al.*, 2008; *Castagna et al*, 2011; *Liu and Kitanidis*, 2011] may lead to a promising solution of this ever challenging problem of mapping fracture pattern, their hydraulic parameters and their connectivity in a fractured geometric media.

1.3 Hydraulic Tomography

During a hydraulic tomography (HT) survey, water is sequentially extracted from or injected into different areas of an aquifer and the corresponding pressure responses are monitored at other intervals to obtain drawdown or buildup data set. *Yeh and Liu* [2000] developed a geostatistical inverse algorithm called sequential successive linear estimator (SSLE) to analyze HT data. SSLE is an iterative geostatistical inverse method that analyzes available head data from sequential pumping test to estimate distribution of hydraulic parameters. In the laboratory *Liu et al.* [2002] and *Illman et al.*

[2007, 2008 and 2010] demonstrated the effectiveness of steady state hydraulic tomography (SSHT) using SSLE to estimate the heterogeneity in hydraulic conductivity (K). *Zhu and Yeh* [2005; 2006] extended SSLE to analyze transient hydraulic tomography (THT) data. THT uses the transient records from sequential pumping tests conducted at the different vertical intervals of the aquifer to estimate the aquifer heterogeneity not only in hydraulic conductivity (K) but also specific storage (S_s). *Liu et al.* [2007] demonstrated encouraging results from the laboratory sandbox experiment for THT. They not only identified the K and S_s distribution in the laboratory sandbox using THT but also successfully reproduced the observed drawdown as a function of time of an independent aquifer test using estimated K and S_s field. *Straface et al.* [2007] estimated transmissivity and storativity fields, consistent with the site geology by applying THT to a well field at Montalto Uffugo Scalo, Italy.

Berg and Illman [2011] showed promising results in characterizing a highly heterogeneous glaciofluvial aquifer – aquitard system by performing transient hydraulic tomography (THT) using the SSLE at the North Campus Research Site, located at the University of Waterloo, Waterloo, Ontario. They conducted 9 pumping tests in the field in a 3D network of pumping and monitoring wells and performed THT in 3D by inverting each individual test as well as sequentially interpreting 4 pumping tests with SSLE to estimate hydraulic conductivity (K) and specific storage (S_s) distributions as well as their uncertainties. Inversion of individual pumping tests was able to capture the main aquifer zone, however the details were lacking in comparison to the THT analysis of 4 pumping tests. They validated the resulting K and S_s distributions from both individual and multiple tests visually by comparing them to stratigraphy and permeameter K estimates. They also simulated these 9 pumping tests using estimated K and S_s tomograms and compared the simulated drawdown to the observed records. The study showed that it is possible to map the K and S_s distributions of a highly heterogeneous porous medium and their uncertainties by analyzing individual as well as multiple pumping tests by means of THT code of *Zhu and Yeh* [2005]. However, inversion of multiple pumping tests improves not only the estimate K and S_s field but also their ability to predict independent pumping tests.

1.4 Studies of Hydraulic Tomography in Fractured Rock

In a fractured medium, fractures usually have higher hydraulic conductivity (K) and lower specific storage (S_s) values than the rock matrix. Thus, while pumping tests are conducted, pressure propagates rapidly through connected fractures unlike the rock matrix, thereby delineating high hydraulic conductivity and low specific storage distributions of the fractured media. *Hao et al*. [2008]

recently applied HT data analysis algorithm SSLE to a synthetically generated fractured media to investigate the feasibility of HT to detect fracture zones and their connectivity. The hypothetical fractured rock aquifer was a 2D vertical square domain which was 40 m by 40 m in dimension. Constant head boundaries of 100 m were assigned around the domain. The domain consisted of 1m by 1 m elements and they created orthogonal fracture zone sets consisting of five vertical and two horizontal facture zones embedded in a rock matrix. They satisfactorily imaged the high hydraulic conductivity zones from the observation data collected from multiple pumping tests, which reflected the fracture pattern and its connectivity in the synthetic fractured aquifers although estimated values of K and S_s fields were smoother than the true fields. They found that, fracture pattern and connectivity became more vivid and the estimated hydraulic properties approached true values as the number of wells and monitoring ports increased.

Illman et al. [2009] interpreted two cross-hole pumping tests at the Mizunami Underground Research Laboratory (MIU) construction site in central Japan and analyzed them using the THT code of *Zhu and Yeh* [2005] to map the three-dimensional distribution of K and S_s, their connectivity, as well as their uncertainty. They were able to identify two fast flow pathways or conductive fault zones at the site, although they used only two cross-hole pumping tests for inversion purposes. Moreover, the pumping tests were not conducted in a controlled environment. They assessed the soundness of the estimated fracture K and S_s tomograms using three different approaches: (1) by comparing the calibrated and observed drawdown records as well as predicted the drawdown responses at the monitoring intervals that were not used in the construction of the K and S_s tomograms; (2) by comparing the estimated K and S_s tomograms to previously known fault locations, and (3) by utilizing coseismic groundwater pressure changes recorded during several large earthquakes as a means to evaluate the K and S_s tomograms. The K and S_s tomograms estimated by *Illman et al.* [2009] were encouraging. The THT analysis produced connective pathways of high K and low S_s zones but due to the availability of only 2 cross-hole tests for the analysis, the K and S_s tomograms did not provide details to the faults at the site. In addition, there were no additional pumping tests available to validate the K and S_s tomograms. The results obtained from the study conducted by *Illman et al.* [2009] was the motivation to conduct a laboratory fractured rock block experiment in which THT can be evaluated in a controlled setting.

1.5 DNAPL Dissolution Studies

Contamination of groundwater by dense non-aqueous phase liquids (DNAPL) is very common. These organic liquids usually have high density, low viscosity and relatively low solubility. Because of these characteristics, once spilled on the ground, these liquids rapidly migrate downward. Once in the subsurface, DNAPLs become a potential long term source of groundwater contamination due to the low groundwater velocity as well as their low solubility [*Pankow and Cherry*, 1996]. Mass transfer between the non-aqueous to aqueous phase is an important process for DNAPLs commonly found in contaminated groundwater. This mass transfer process determines the concentration of the chlorinated solvents in groundwater, which often exceeds drinking water standards, although the mass transfer is believed to be a slow process. Therefore, during the last few decades, numerous studies have been conducted to understand the DNAPL dissolution process.

Several laboratory column or sandbox experiments were conducted over the last two decades to understand the process and significant progress has been made in developing correlations to describe the mass transfer between the non-aqueous phase to aqueous phase in a relatively homogeneous porous medium [*Miller et al.*, 1990; *Powers et al.*, 1992, 1994a, b; *Geller and Hunt*, 1993; *Imhoff*, 1994a, b, 2002; *Nambi and Powers*, 2000; *Saba and Illangasekare*, 2000].

When a dense non-aqueous phase liquid is spilled, it infiltrates into the ground leaving behind droplets trapped in the pore spaces and pools on top of the impermeable layer. The trapped droplets in pore spaces constitute DNAPLs at residual saturation. These trapped residual DNAPL remains immobile under typical hydraulic gradients [*Pankow and Cherry*, 1996]. Several active remediation techniques have been developed for removal of DNAPLs in the source zone [*Mackay and Cherry, 1989; Pankow and Cherry, 1996; Rao et al.*, 1997; *Dekker and Abriola*, 2000 b; *Rathfelder et al.*, 2001; *Saenton et al.*, 2002; *Brooks et al.*, 2002; 2004; *McGuire et al.*, 2006; *Page et al.*, 2007 etc.]. However, most of the efforts have failed to remove the source completely. Moreover, the high expense for complete cleanup makes it an impractical choice in most cases. The failure and expense of complete cleanup has led to an increased interest in partial source-zone remediation followed by passive or natural remediation that does not require expensive maintenance other than monitoring. Several studies [*Jawitz et al.*, 2003., 2005; *Lemke et al.*, 2004b; *Soga et al.*, 2004; *Fure et al.*, 2006; *Park and Parker*, 2005; *McGuire et al.*, 2006; *Page et al.*, 2007 etc] were conducted to assess the utility of this approach. However, one of the important factors in designing remediation system is the time length required to dissolve the source, which is determined by the dissolution rate of DNAPL

mass. Thus a sound understanding of the fundamental processes that control the dissolution of DNAPL is needed.

The dissolution of DNAPL source may be either equilibrium controlled or kinetic. The dissolution process (either equilibrium or kinetic) determines the time required to dissolve the source and the concentration in the dissolved plume [*Borden and Piwoni*, 1992]. *Unger et al.* [1998] suggested that different DNAPL mass transfer models can have significant impacts on source depletion rates through an extensive numerical analysis in synthetic heterogeneous aquifers under natural-gradient conditions. From the multi-realization analysis based on the compositional, multiphase flow model, CompFlow [*Unger*, 1995; *Unger et al.*,1996;1998], they found the type of the dissolution model (equilibrium versus kinetic) to have more influence on source-zone depletion or mean dissolution time than the parameters controlling multiphase flow or degree of heterogeneity in the aquifer's permeability. However, the synthetic aquifer used for the simulations were based on the Borden aquifer which is known to be low in heterogeneity in terms of hydraulic conductivity.

Maji and Sudicky [2008] presented a comparison of the various alternative DNAPL-aqueous-phase mass transfer models developed through laboratory column experiments for the prediction of DNAPL source-zone depletion time. They incorporated various dissolution models into the compositional, multiphase flow model, CompFlow [*Unger*, 1995; *Unger et al.*,1996,1998)] and predicted the time required for the complete depletion of a DNAPL source due to natural dissolution in order to investigate the influence of mass transfer characteristics in DNAPL source depletion and contaminant flux reduction. The hydrogeologic setting used for the simulations was representative of a heterogeneous fluvial aquifer in Southwest Germany, which was comprehensively characterized in three dimensions for hydrogeological parameters. The hydraulic conductivity heterogeneity at this site is considerably higher than at the Borden site. They found the type of the dissolution model, the parameters controlling dissolution rate and the aquifer heterogeneity to have equal influence on the DNAPL source depletion and dissolved flux reduction. Therefore they suggest that it is equally important to characterize the heterogeneity of the aquifer hydraulic conductivity and have knowledge of the dissolution kinetics prior to the design of a remediation methodology.

Fried et al. [1979]; *Abriola and Pinder* [1985a, b]; *Hunt et al.* [1988a, b]; *Anderson et al.* [1992a, b], *Johnson and Pankow* [1992], *Geller and Hunt* [1993] etc. studied the dissolution of residual DNAPL located above and below the water table. These studies suggested that long contact times between the DNAPL and groundwater result in a dissolved concentration near or at equilibrium, at

least around the source zone. Numerical studies [e.g., *Abriola and Pinder*, 1985a, b; *Pinder and Abriola*, 1986, *Corapcioglu and Baehr*, 1987; *Unger et al*., 1995 etc] utilized the local equilibrium assumption (LEA) to explain the mass transfer between the non-aqueous and the aqueous phases. The local equilibrium assumption (LEA) implies that the dissolved concentration of contaminant in the groundwater at the source corresponds to its solubility in water.

Frind et al. [1999] simulated the dissolution of the Borden emplaced- DNAPL source field experiment and they found that the dissolution at the Borden emplaced source occurred mostly at or close to equilibrium except at late-time. They attribute the late time tailing to the decreasing mole fraction rather than the mass transfer kinetics. However, the hydraulic conductivity at Borden is relatively homogeneous. They suggested the mass transfer to be an equilibrium process at the homogeneous medium, while the situation may be different for a heterogeneous medium.

Several laboratory studies conducted in relatively heterogeneous sand [e.g., *Mayer and Miller*, 1996; *Powers et al*., 1998; *Nambi and Powers*, 2000 etc] suggest that the heterogeneity of the medium has a significant impact on the dissolution behavior. Laboratory experiments conducted by *Schwille* [1988] and *Lamarche* [1991] suggest equilibrium mass transfer takes place at early time while non-equilibrium mass transfer occurs at the tailing stage. *Powers et al*. [1991] investigated the circumstances under which mass transfer process would not follow the equilibrium behavior. They identified several factors that accelerate non-equilibrium mass transfer such as small areal extent spills, high Darcy velocities, large size of NAPL blobs and low residual NAPL saturations. *Powers et al*. [1992] correlated the mass transfer rate to the Reynolds number, the median grain size, and a porous medium uniformity index based on a laboratory column experiment. *Powers et al*. [1994a] developed a phenomenological model where they described the NAPL blobs by spheres of different radii and proposed a general correlation for transient dissolution rates in terms of porous media properties, the Reynolds number and NAPL properties. Similar to *Schwille* [1988] and *Lamarche* [1991], *Powers et al*. [1994b] also suggested an equilibrium mass transfer takes place at early time and kinetic mass transfer at later time. *Imhoff et al*. [1994a] developed a new experimental technique using gamma attenuation to determine the mass transfer rate coefficient and showed mass transfer rate coefficient to be a function of Darcy flux and DNAPL volumetric content. *Imhoff et al*. [1994a, b] graphically compared the mass transfer rates expressed in terms of Sherwood number as a function of the Reynolds number obtained from several different investigations [*Miller et al.,* 1990; *Parker et al.,* 1991; *Geller and Hunt*, 1993; *Powers et al.,* 1992]. *Imhoff et al.* [1996] investigated dissolution

fingering, an important kinetic dissolution process on the basis of an experimental observation and *Imhoff and Miller* [1996] modeled the dissolution fingering phenomenon. Trapped NAPL ganglia within the pore space reduce the permeability of the medium to aqueous phase flow. *Imhoff and Miller* [1996] suggest that when fluid flow is imposed on such a system, the aqueous phase may interact with dissolution-induced permeability changes and lead to fingered patterns, known as dissolution fingering. Other Laboratory investigations and modeling studies [*Hunt et al.*, 1988a; b; *Conrad et al.*, 1992; *Malone et al.*, 1993; *Wilkins et al.*, 1995; *Imhoff et al.*, 1998; *Saba and Illangasekare*, 2000; *Nambi and Powers*, 2003; *Phelan et al.*, 2004 etc] also found evidence of non-equilibrium effects in mass transfer processes and treated the mass transfer as a non-equilibrium process.

Field data, however, frequently indicates contaminant concentrations in groundwater below their corresponding equilibrium values [*Mackay et al*., 1985; *Feenstra*, 1986; *Feenstra and Cherry*, 1988], also supporting kinetic dissolution behavior. This lower concentration or kinetic dissolution behavior may result from dilution by clean water, trapped DNAPL droplets at the dead end pores or residual zones at low permeability areas that get dissolved later than the DNAPLs in high permeability areas [*Frind et al.* 1999].

In a fractured geologic medium, the DNAPLs preferentially migrate along the fractures under the influence of gravitational, viscous and capillary forces. DNAPL in the hydraulically active fractures acts as a persistent source of aqueous phase contamination, until all of the mass disappears through dissolution. On the other hand, some DNAPL mass gets trapped in the dead end fractures which may cause the pooling of DNAPL. A portion of the DNAPL mass also diffuses to the rock matrix having very low permeability [*Mackay and Cherry, 1989; Parker et al.*, 1991]. In the 1970s and 1980s, the urgent need to safely dispose radioactive waste in fractured geologic media led to several studies [e.g., *Neretnieks*, 1980; *Schwartz et al.*, 1983; *Keller et al.*, 1986 etc] to understand the flow and transport through fracture rock. Fracture–matrix interaction has been the focus of the researchers for decades [e.g., *Neretnieks*, 1980; *Neretnieks et al.*, 1982; *Maloszewski and Zuber*, 1993; *Liu et al.*, 2004a; *Wu et al.*, 2010] and matrix diffusion has been gradually considered as one of the most important mechanisms controlling the contaminant transport processes in fractured geologic media. The matrix diffusion process in a fractured porous media is considered as the transient attenuation mechanism that retards the aqueous phase contaminant migration along the fractures [*Neretnieks*, 1980; *Therrien and Sudicky*, 1996; *VanderKwaak and Sudicky*, 1996]. In absence of attenuation

process such as sorption, matrix diffusion, biological or chemical transformation, advective contaminant migration in dissolved phase can result into rapid contamination along the fractures. The DNAPL mass diffused into the matrix reenters the adjacent fractures once the DNAPL in the fractures are completely dissolved and gets flushed in aqueous phase with flowing water [*Neretnieks*, 1980; *Therrien and Sudicky*, 1996; *VanderKwaak and Sudicky*, 1996; *Slough et al.*, 1999].

Over the past few decades, several studies [e.g., *Tang et al.*, 1981; *Rasmuson et al.*, 1982; *Sudicky and Frind*, 1982; *Pruess and Narasimhan*, 1985; *Berkowitz*, 2002; *Liu et al.*, 2003, 2004a; *Hu et al.*, 2004; *Reimus and Callahan*, 2007 etc.] have been conducted to understand and model transport phenomena in fractured porous media.

VanderKwaak and Sudicky [1996] developed a transient two dimensional groundwater flow and contaminant transport model to study DNAPL dissolution in discrete fracture networks. The model accounted for matrix diffusion, equilibrium sorption and nonlinear relative transmissivity and was based on local equilibrium partitioning of contaminant dissolution. They found that the time required for dissolution depends on the flow and transport properties of fractures and matrix as well as the fracture connectivity.

Dickson and Thomson [2003] predicted the fate of DNAPLs in a fractured rock system through laboratory dissolution experiments conducted in two dolomitic limestone having variable aperture fractures using 1,1,1-trichloroethane and Trichloroethene. They showed three distinct and characteristic stages of effluent concentration profile, which are initial pseudosteady stage, transient stage, and tailing stage. They also developed an empirical model describing the initial pseudosteady and transient stages of dissolution, using the experimental data. The developed empirical model relates the Sherwood number (*Sh*) to various dimensionless numbers such as the Reynolds (Re) number, tracer aperture ratio and the normalized aperture saturation obtained from the dissolution experiments. The Sherwood number is a ratio that represents the mass transfer rate to the diffusion rate and is the product of the lumped mass transfer coefficient and a characteristic length squared divided by the free water diffusion coefficient. Reynolds number is also a dimensionless number calculated from the characteristic length, density, kinematic viscosity and dynamic viscosity of the fluid. As the empirical model was developed using experimental data, it is valid under certain range of Reynolds number (Re).They note that their model is sensitive to a morphology index, which represents the ratio of DNAPL-water interfacial area to DNAPL volume. They utilized the empirical

model to predict effluent concentration data from two separate and independent dissolution experiments.

A more recent laboratory experiment conducted by *Schaefer et al.* [2009] investigated DNAPL architecture and dissolution in a discretely fractured sandstone using Tetrachloroethene (PCE). They found effluent DNAPL concentrations to approach equilibrium condition as the flow velocity through the fracture decreases, indicating that PCE dissolution into the mobile water is mass-transfer-controlled. From lumped mass transfer coefficient estimated using the same approach as *Dickson and Thomson* [2003], they suggest that the DNAPL dissolution rate in fractures is a relatively slow process compared to that in sand. They attribute this slow dissolution rate to the heterogeneity, DNAPL distribution and decreased efficiency of mixing and mass transfer in fractures relative to unconsolidated media. At the end, they described DNAPL dissolution by a Reynolds number correlation that incorporates DNAPL architecture in terms of friction loss aperture and DNAPL-water interfacial area.

Most of the dissolution studies in fractured rock consider empirical relationships based on Sherwood and Reynolds numbers. Certainly a large number of studies show that one can use such relationships. However, this may be due to the fact that there have been no methods to accurately characterize the heterogeneity of the fractured porous medium and DNAPL distribution.

Here, a TCE dissolution experiment was performed in a hydraulically well characterized fractured dolomite in the laboratory in order to investigate the DNAPL dissolution behavior in a controlled environment and predict DNAPL dissolution through a different approach. I first try to image the heterogeneity patterns of hydraulic conductivity of the fractured rock with hydraulic tomography and then use an equilibrium dissolution model HydroGeoSphere (HGS) [*Therrien* et al., 2009] to simulate the TCE breakthrough curve. The purpose of this portion of the study is to investigate if DNAPL dissolution behavior can be predicted with an equilibrium dissolution model when the heterogeneity distribution and the location of the DNAPL are known.

1.6 Objectives of the Study

The main objectives of this study are:

- to investigate the utility of transient hydraulic tomography (THT) along with the inverse algorithm SSLE developed by *Zhu and Yeh* [2005] to image the K and S_s heterogeneity

pattern of fractured geologic media and their uncertainties. This includes the delineation of the pattern of discrete fractures and their connectivity;

- to investigate the transport behavior of aqueous phase Trichloroethylene (TCE) undergoing dissolution from a source zone in discrete fractures and;
- to investigate whether the transport behavior of the aqueous phase of TCE in a fractured rock block can be captured through numerical modeling with HydroGeoSphere (HGS) by treating dissolution as an equilibrium process using:
    1) a Discrete Fracture Network Approach – where a discretely fractured domain is used for the simulation and the fractures are assigned an aperture thickness; and
    2) a Stochastic Continuum Approach – where the domain is treated as a porous medium with the hydraulic conductivity (K) field obtained from THT analysis.

1.7 Thesis Content

Given the complexities of fractured networks in subsurface and Dense Non Aqueous Phase Liquid (DNAPL) contamination, laboratory experiments were designed with an intention to demonstrate hydraulic tomography as a tool to delineate discrete fractures and understand TCE plume behavior.

A dolomite rock sample, which is about 91.5 cm in length, 60.5 cm in height and 5 cm thick, was fractured in the laboratory to perform the flow and transport experiments. After the fractured block was enclosed into a flow cell, flow-through and pumping tests were conducted to characterize the fractured rock block. The data from the pumping tests were then included in the SSLE code developed by *Zhu and Yeh* [2005] and transient hydraulic tomography (THT) was conducted to delineate the K and S_s distributions (or tomograms from now on) and their uncertainty estimates. Imaging of the K and S_s tomograms, if they are conducted at a high enough resolution can result in the imaging of the fracture pattern and their connectivity.

Upon completion of the hydraulic characterization, several conservative tracer tests were conducted using bromide (Br^-) as a conservative tracer to aid in the design of TCE dissolution experiment. Once the tracer experiments were completed, a known volume of pure phase TCE was injected at a known location in the flow cell to create a well-defined source zone. A constant hydraulic gradient was maintained by fixing the hydraulic heads at the two head tanks to induce steady groundwater flow through the flow cell. Water samples were obtained at a down gradient monitoring port for 3 months

to obtain a long-term breakthrough curve of TCE in the aqueous phase. The purpose of this experiment was to study TCE dissolution behaviour in the fractured rock sample. Then HydroGeoSphere (HGS) was used to model the aqueous phase TCE transport using two distinct approaches – 1) the Discrete Fracture Network modeling approach and 2) the stochastic continuum approach, to investigate whether they can capture the transport behavior.

This thesis is organized into 10 chapters. The hydraulic tests and the transient hydraulic tomography (THT) studies are described first, which are presented in Chapter 2 through Chapter 5. Then the tracer tests, TCE dissolution experiment and the dissolution modeling approaches are explained, which are presented in Chapter 7 through Chapter 9. The main conclusions of THT and TCE dissolution studies conducted in the fractured rock sample are summarized in Chapter 10.

Chapter 2
Rock Sample and Experimental Set-up

2.1 Description of the Rock Sample

A dolostone rock sample was obtained for the laboratory experiments from a rock supplier for home landscaping called Stone Landscapes, Waterloo, Ontario. According to Stone Landscapes, the rock specimen is from Wiarton, Ontario and from a geological formation called Guelph Formation. The Guelph Formation is a carbonate ramp sequence and mainly composed of tan to dark brown, microcrystalline to fine crystalline, pervasive and massive dolomites [*Zheng and Coniglio,* 1998].

The dolomite rock sample (Figure 2.1) was approximately 91.5 cm in length, 60.5 cm in height and 5 cm thick (36 in x 24in x 2in). The rock sample was bent holding with C-clamps placing a triangular bar underneath, in order to induce tension fractures. Figure 2.2 is a photograph of the rock specimen after it was fractured in the laboratory. Dimensions of the rock block and the fractures are shown in Figure 2.3.

Figure 2.1: Photograph of the Dolostone Rock Sample

Figure 2.2: Photograph of the Dolomite Rock Sample Fractured in the Laboratory

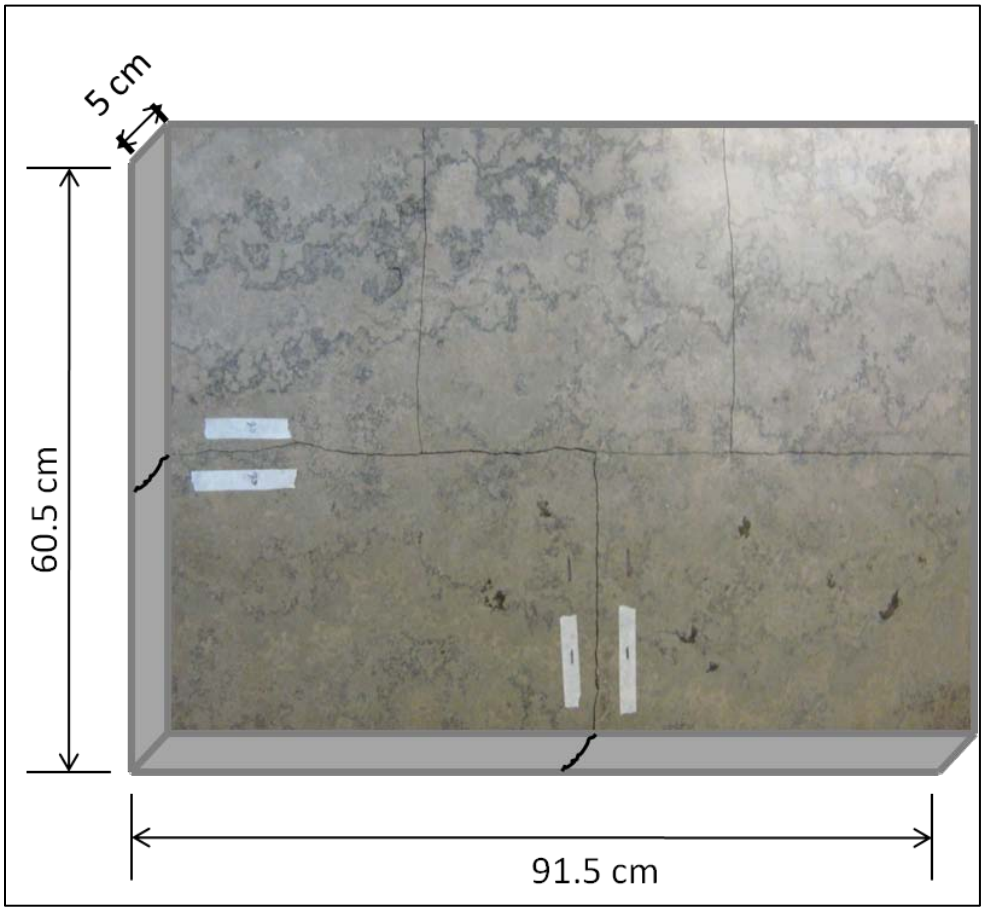

Figure 2.3: Dimensions of the Fractured block

2.2 Preparation of the Flow Cell

The fractured rock was enclosed in a flow cell (Figure 2.6) to perform hydraulic tests. Titanium putty (Devcon, Danvers, MA, USA) was used to attach the brass fittings that were used as ports to the front surface of the rock and to seal the edge of the fractures (Figure 2.4) leaving the left and right end of the fractured rock open. Then resin (Environmental Technology, Inc., CA, USA) which is usually used for surface finishing was carefully poured to cover the front, back, top and bottom surface of the rock (Figure 2.5) to prevent any evaporation, leakage and to make the surfaces smooth. After the resin dried and hardened, water was injected to the left most port (Figure 2.5) which came out to the other side and vice versa which ensured that the horizontal fracture did not become sealed. The same procedure was repeated for the vertical fractures to ensure that they were not sealed.

Figure 2.4: Photograph of the Sealed Fractures and the Ports

Figure 2.5: Photograph of the Fractured Rock Block Covered with Resin

The sealed fractured block was then placed into the flow cell leaving sufficient room (~6 in) for water reservoirs at the left and right ends. The flow cell was constructed of stainless steel and plexiglass was used as a front plate. The dimensions of the flow cell are 122 cm in length, 65 cm in height and 6.5 cm thick (48 in x 26 in x 2.5 in). Silicon was used to seal between the box and the rock block.

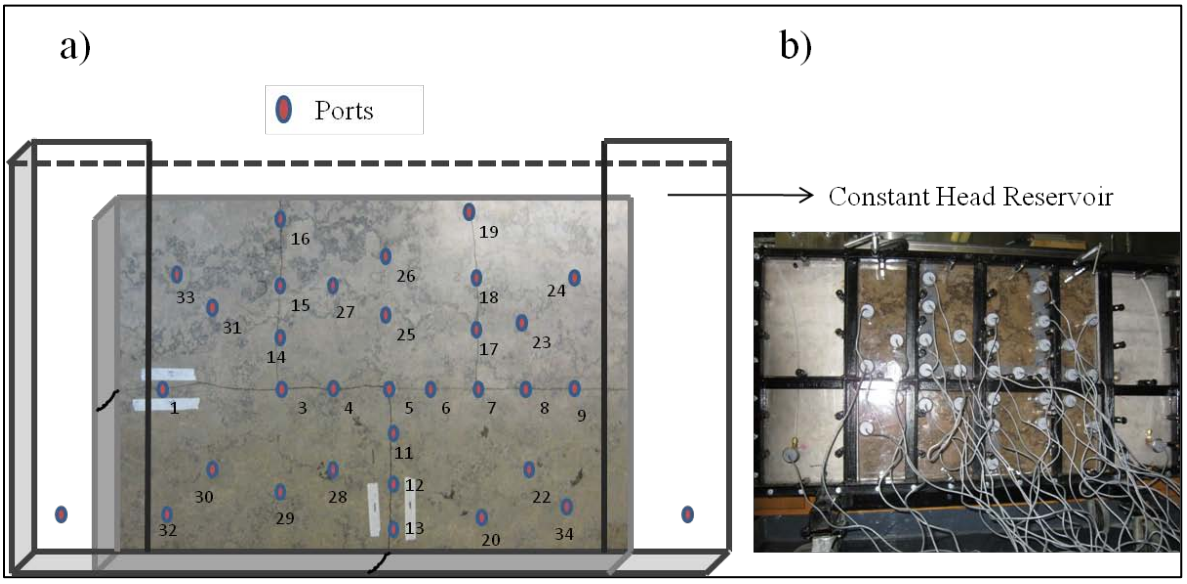

Figure 2.6: a) Schematic Diagram of the Flow cell and b) Photograph of the Tank Holding the Fractured Block

The fractured block had constant head reservoirs at the left and right boundaries and "no-flow" conditions at the remaining outer boundaries. The left and right edge of the rock was open to the constant head reservoirs allowing water flow through the fracture.

2.3 Pressure Transducers and Data Collection

The flow cell was equipped with 29 ports that could be used to monitor water pressure or to pump water from it. Red ovals in the schematic diagram (Figure 2.6a) show their locations. Designs of the ports are shown in Figure 2.7. The port locations were designed to mimic borehole placement in the field. That is, the ports were placed along vertical and slanted lines resembling boreholes as shown in Figure 2.7 Each port was connected to a 0-1 PSIG pressure transducer (model 209, Alpha Controls & Instrumentation, Markham, ON, Canada)) to record pressure head at different locations of the fractured domain during the hydraulic tests. Seventeen pressure transducers were placed on fractures, ten were installed on the matrix and two were utilized to record pressure head in the constant head reservoirs. Ports placed on fractures were also utilized for water extraction during the pumping tests.

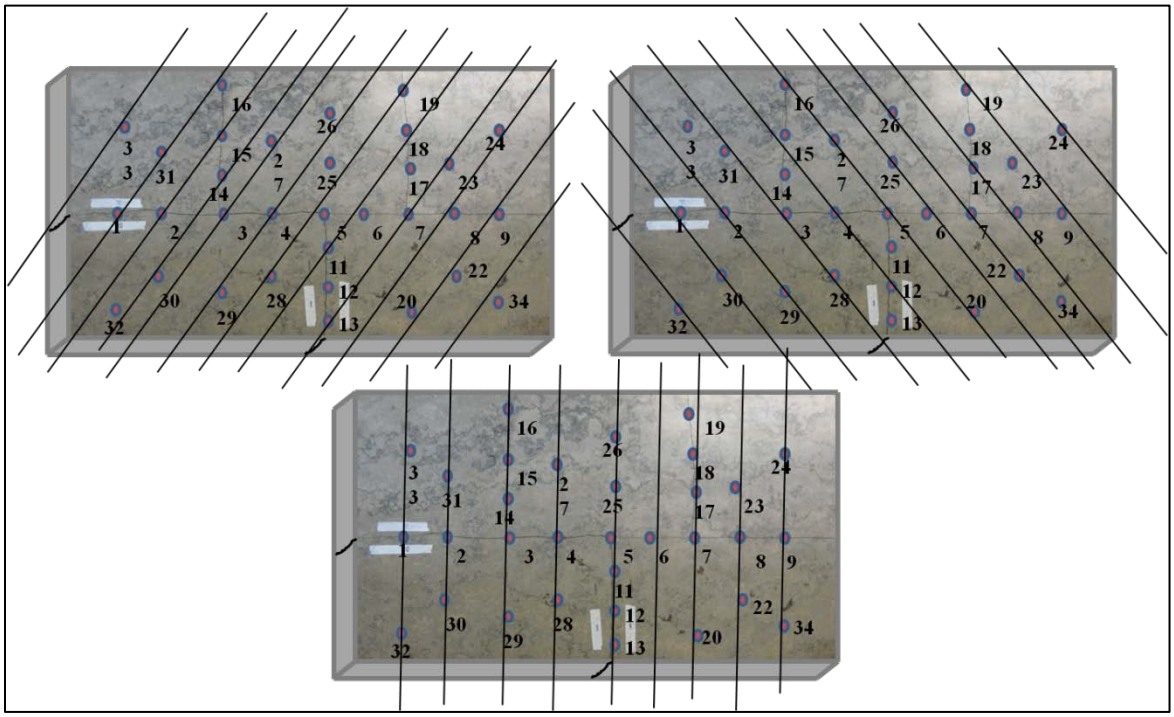

Figure 2.7: Design of Ports

2.4 Experimental Set-up for the Hydraulic Tests

2.4.1 Flow-Through Tests

After the fractured block was enclosed in a flow cell, four flow-through tests were conducted following the work of *Illman et al*. [2007, 2010] to estimate effective hydraulic conductivity of the fractured block. Flow-through tests were conducted by fixing the hydraulic gradient across the rock sample and measuring the water outflow rate at the effluent dripping point using a graduated cylinder. Hydraulic gradient across the rock block was fixed by setting drip points at the end reservoirs at different heights. A peristaltic pump (MasterFlex, Model 7550-30, Cole-Parmer, Montreal, QC, Canada) was used to supply water continuously into the influent reservoir and the drip point maintained constant head. Figure 2.8 is a schematic diagram of the experimental set-up for the flow-through tests.

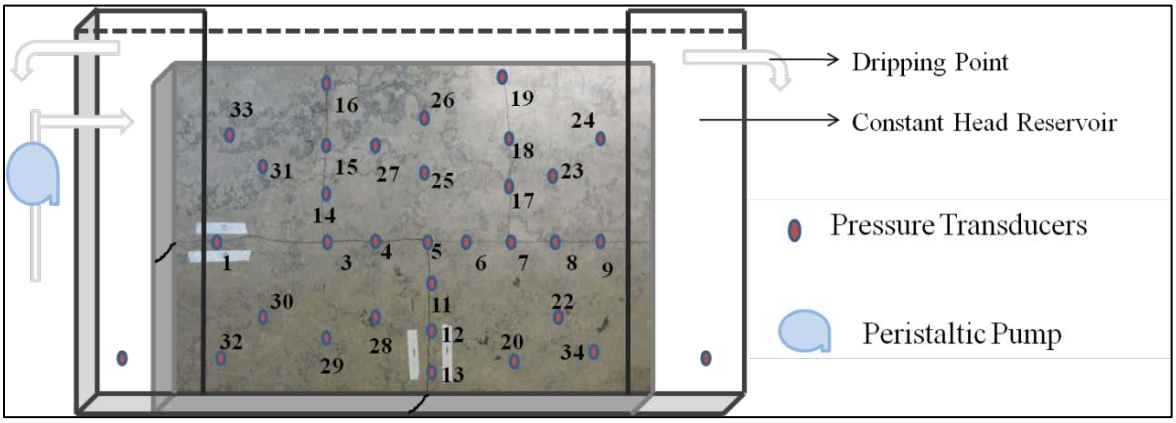

Figure 2.8: Experimental Set-up of the Flow-through Tests

2.4.2 Pumping Tests

Upon completion of the flow-through tests, 17 pumping tests were conducted at each of the fracture ports. A peristaltic pump was used to extract water from the pumping port and a pulse dampener was used in between the pump and the pumped port to reduce the noise resulting from oscillations of the peristaltic pumps.

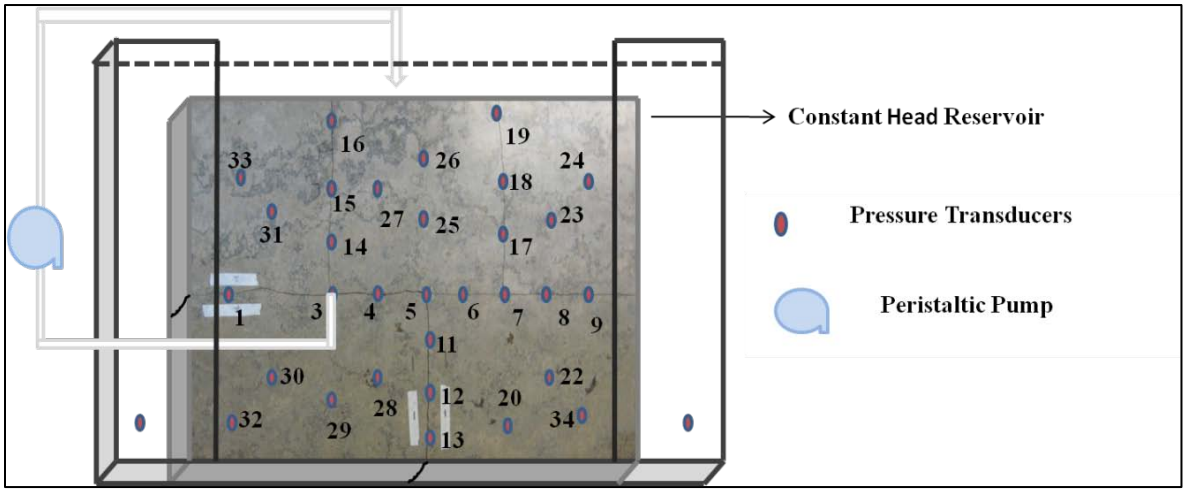

Figure 2.9: Experimental Set-up of the Pumping Tests

Figure 2.9 shows the experimental set-up for the pumping tests. Twenty-seven pressure transducers (0-1 PSIG model 209, Alpha Controls & Instrumentation, Markham, ON, Canada) recorded pressure responses at different heights of the fractured domain and two of them recorded pressure head in the constant head reservoirs during each test. Both reservoirs were fixed at the same level and the

constant head was maintained throughout the test by putting back the extracted water to the top of the tank, from where it went to the both reservoirs. Pumping tests were conducted at each of the 17 fracture ports to collect as much information as possible.

Chapter 3
Hydraulic Tests

3.1 Flow-Through Tests and Estimated Hydraulic Properties

Four flow-through tests were conducted to estimate an effective hydraulic conductivity of the experimental block and to estimate the hydraulic aperture. Flow rate was measured in both directions (left to right and right to left) by fixing the hydraulic gradient across the fractured block and for two different hydraulic gradients in each direction. Table 3-1 provides a summary of the flow-through tests and Table 3-2 summarizes the estimated hydraulic properties from the flow-through tests.

Table 3-1: Summary of the Flow-Through Tests

Test	Direction of Flow	Hydraulic Gradient	Flow Rate (mL/s)
Test 1	Left to Right	0.05	0.28
Test 2	Left to Right	0.13	0.50
Test 3	Right to Left	0.06	0.27
Test 4	Right to Left	0.13	0.51

From the flow-through tests, the hydraulic aperture of the horizontal fracture was estimated using the Cubic Law, given by equation *(1)* [*Romm*, 1966] –

$$e_h = \left(\frac{12\mu QL}{\rho g W \Delta H}\right)^{1/3} \qquad [1]$$

where, e_h is hydraulic aperture (L), μ ($ML^{-1}T^{-1}$) is the fluid viscosity at room temperature (20°C), Q (L^3T^{-1}) is the discharge or flow rate through fracture, L (L) is the fracture length in the direction of flow, W (L) is the fracture width perpendicular to the direction of flow, ρ (ML^{-3}) is the fluid density at room temperature, g (LT^{-2}) is the acceleration due to gravity, and ΔH (L) is the hydraulic head loss across the fracture plane.

The estimated values of hydraulic aperture of the horizontal fracture from four different flow-through tests varied from 0.047 cm to 0.05 cm, which are listed in Table 3-2.

Reynolds number (*Re*) was calculated for the estimated hydraulic aperture to check if the flow was laminar. Reynolds number (*Re*) is given by equation (*2*) [*Bear,* 1972] -

$$Re = \frac{Vd\rho}{\mu} \qquad [2]$$

where, *Re* is the Reynolds number, *V* (LT^{-1}) is the Darcy velocity, d (L) is the characteristics length (fracture aperture in this case), ρ (ML^{-3}) and μ ($ML^{-1}T^{-1}$) are the density and viscosity of water respectively at room temperature. Reynolds number (*Re*) for the different hydraulic apertures estimated from different flow through tests are listed in Table 3-2.

The flow is considered to be laminar and linear when the Reynolds number (*Re*) is in between 1 to 10 and the Darcy's law is applicable to the flow condition [*Bear,* 1972]. From Table 3-2 it can be seen that *Re* was comparatively larger for the larger hydraulic gradient (Test 2 and 4) as the velocity increases with increasing hydraulic gradient and vice versa. However, Reynolds number (*Re*) estimated from each flow-through test ranged from 4.7 to 8.88 (within the range of 1-10) which imply that the flow through the fracture was laminar and linear, where Darcy's law is applicable.

From the flow-through tests, the effective hydraulic conductivity (K_{eff}) of the fractured block was estimated using Darcy's Law, given by equation *(3)* -

$$Q = -KA\frac{dh}{dl} \qquad [3]$$

where, *Q* (L^3T^{-1}) is the discharge or flow rate through the system, *K* (LT^{-1}) is effective hydraulic conductivity (K_{eff}) of the aquifer; *A* (L^2) is bulk cross-sectional area and $\frac{dh}{dl}$ is the hydraulic gradient across the system. Estimated effective hydraulic conductivity (K_{eff}) from four different flow-through tests are listed in Table 3-2, which varied from 1.30×10^{-2} cm/s to 1.70×10^{-2} cm/s.

Table 3-2: Estimated Hydraulic Properties from Flow-Through Tests

Test	Hydraulic Aperture (cm)	Reynolds No (*Re*)	Effective *K* (cm/s)
Test 1	0.05	4.87	1.70×10^{-2}
Test 2	0.047	8.70	1.30×10^{-2}
Test 3	0.048	4.70	1.50×10^{-2}
Test 4	0.047	8.88	1.30×10^{-2}

3.2 Pumping Tests Description

Pumping tests were conducted at each of the ports completed on a fracture using a peristaltic pump. The left and right end of the domain was set as constant head boundaries and the rest of the outer boundaries of the fractured rock were treated to be no-flow. The duration of each pumping test ranged from 3 to 10 minutes. During each test, pressures were recorded at 30 to 31 ports (described in section 2.3) located along the fractures, matrix and constant head reservoirs, while pumping took place at one port located on a fracture. Similar to *Illman et al*. [2007, 2011], pressure transducers were calibrated prior to each pumping test for three different reservoir heads. To develop a static, initial condition, head data were recorded at each pressure transducer for several minutes before starting each pumping test. Then each pumping test was run until steady-state conditions which were visually confirmed by observing the stabilization of all head measurements on the data logger connected to a computer. During all of the pumping tests recorded hydraulic heads in ports completed on fractures reached steady-state within 2 to 3 seconds after the water extraction was started and no drawdown was observed at any of the matrix ports, which was expected due to the very high contrast between the hydraulic conductivity of the fracture and matrix.

Table 3-3: Summary of the Pumping Tests

Pumped Port	Pumping Rate (mL/s)	Duration (min)	Maximum Observed Drawdown (cm)	Port of Maximum Drawdown
Port 1	4	10	8	Port 3
Port 3	2.5	10	10	Port 15
Port 4	2.5	10	10.4	Port 3
Port 5	4	10	17.3	Port 11
Port 6	2.5	10	10	Port 11
Port 7	2.5	5	7.8	Port 19
Port 8	4	10	9.5	Port 7
Port 9	4	10	5.9	Port 8
Port 11	4	10	17	Port 13
Port 12	4	10	19.7	Port 13
Port 13	4	10	18.7	Port 12
Port 14	2.5	10	16.2	Port 15
Port 15	1.7	10	14.9	Port 16
Port 16	1	10	11.7	Port 15
Port 17	2.5	3	29.7	Port 18
Port 18	1.7	10	21.3	Port 17
Port 19	1	10	18.4	Port 18

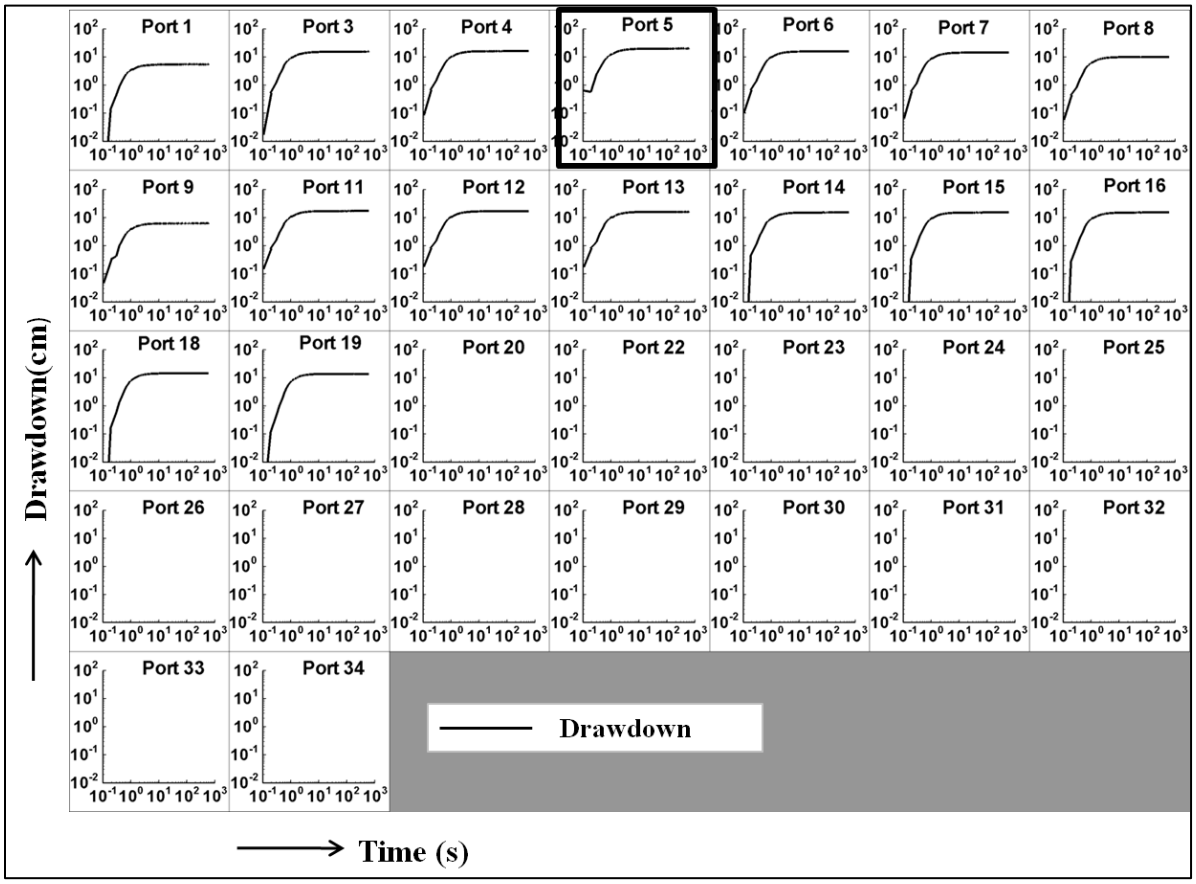

Figure 3.1: Observed drawdown at fracture and matrix ports during a pumping test at port 5. The pumped port is indicated by the black rectangular box.

Table 3-3 summarizes all the pumping tests. Figure 3.1 shows the drawdown responses recorded at the fracture and matrix ports during the pumping test at port 5. Drawdown at the pumping port has been highlighted with black rectangular box in Figure 3.1. In this case the pumping rate is 4 mL/s. Pumping and observation ports are indicated on Figure 2.9. Similar plots for the remaining 16 pumping tests are provided in Appendix A .

3.3 Pumping Tests Simulated Using HydroGeoSphere

The groundwater flow and solute transport code, HydroGeoSphere (HGS) was used to simulate the pumping tests in a synthetic replica of the fractured block to compare the observed and simulated drawdown.

The domain used for the forward simulation was 91.5 cm in length by 60.5 cm in height and 5 cm thick (one element thick) and was composed of variably-sized rectangular elements. The element size varied from 0.05 cm by 0.01 cm to 1.375 cm by 1.375 cm. The finer elements were located along the fracture and the coarser elements were located near the boundary. The boundary conditions were constant head (63.5 cm) for left and right boundaries and no flow for the remaining outer boundaries. Figure 3.2a shows domain used for simulating the pumping tests and Figure 3.2b shows the fracture faces. The darker areas in Figure 3.2a indicate the highly refined areas of the model domain.

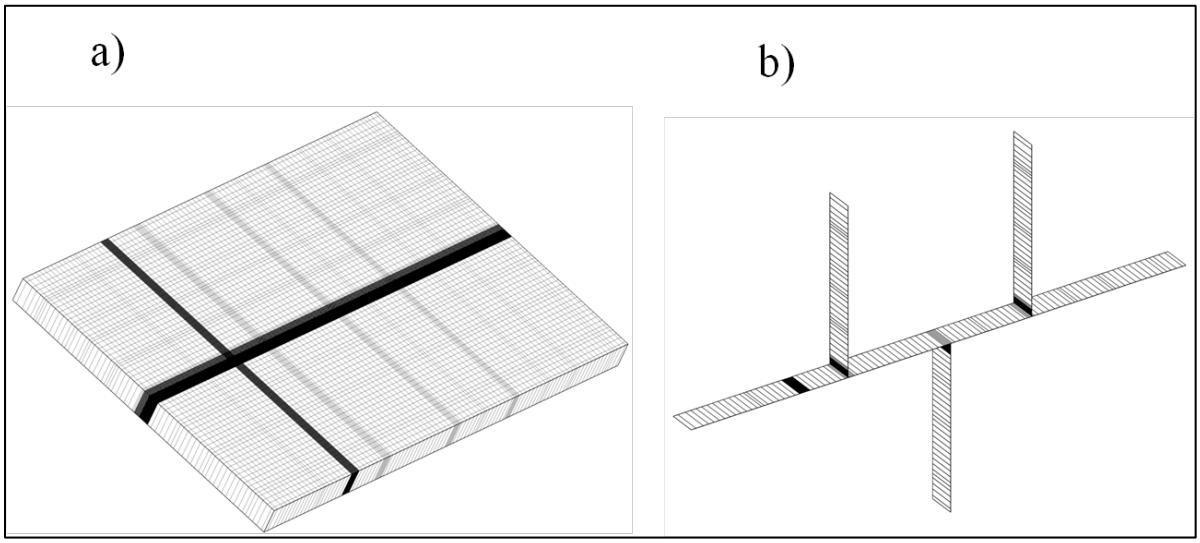

Figure 3.2: a) Mesh Used for Forward Pumping Tests and b) Fracture Faces.

An aperture thickness, obtained from the flow-through tests were assigned to the fractures and very low hydraulic conductivity (K = 1.00×10^{-7} cm/s) was assigned to the matrix to simulate the pumping tests. HGS calculated the fracture hydraulic conductivity (K_f) from the aperture thickness using equation *(4)* [*Therrien et al.*, 2009].

$$K_f = \frac{\rho g {W_f}^2}{12\mu} \qquad [4]$$

where, K_f [LT^{-1}] is the fracture hydraulic conductivity, W_f (L) is the fracture aperture; ρ (ML^{-3}) and μ (ML^{-1}T^{-1}) are the density and viscosity of water, respectively.

Matrix hydraulic conductivity (K_m) and specific storage (S_s) values (Given in Table 3-4) for both fractures and matrix were obtained from the literature [i.e, *De Marsily*, 1986; *Domenico and Schwartz*, 1997; *Schwartz and Zhang*, 2003 etc.]. I started with the literature values and simulated the

pumping test at port 5 (indicated in Figure 2.9). The parameters were then adjusted for this test through trial-and-error until a good match was obtained between the observed and simulated drawdown curves. The manual calibration resulted in higher specific storage values (for both fractures and matrix) than the literature values to match early time observed drawdown. Table 3-4 summarizes the calibrated parameters. These parameters were then utilized to simulate 8 more pumping tests having flow rates identical to the laboratory tests, using HGS in the discretely fractured domain to compare the observed and simulated drawdown. Pumped ports and the corresponding pumping rates are listed in Table 3-5. Pumping and observation ports are indicated in Figure 2.9.

Table 3-4: Parameters Used to Simulate the Pumping Tests using HGS (Calibrated for the test at port 5)

Parameter		Source
Aperture (cm)	0.049	Flow-through Tests (0.047 cm – 0.05 cm)
Fracture Hydraulic Conductivity, K_f (cm/s)	17.46	Calculated by HGS
Matrix Hydraulic Conductivity, K_m (cm/s)	1.00×10^{-7}	*De Marsily*, 1986; *Domenico and Schwartz*, 1997; *Schwartz and Zhang*, 2003 etc (1.00×10^{-7} cm/s to 1.00×10^{-4} cm/s)
Fracture Specific Storage, S_{sf} (cm^{-1})	8.00×10^{-4}	*Singhal and Gupta*, 2010 1.00×10^{-9} cm^{-1} to 1.00×10^{-6} cm^{-1}
Matrix Specific Storage, S_{sm} (cm^{-1})	3.0×10^{-3}	*Singhal and Gupta*, 2010 (1.00×10^{-9} cm^{-1} to 1.00×10^{-6} cm^{-1})

Table 3-5: Pumping number and Rates for the synthetic pumping tests simulated using HGS.

Pumped Port	Pumping Rate (mL/s)
Port 3	2.5
Port 5	4
Port 7	2.5
Port 12	4
Port 13	4
Port 15	1.7
Port 16	1
Port 18	1.7
Port 19	1

Observed and simulated drawdown curves at the pumping and the monitoring ports during the pumping test at port 5 that was calibrated to adjust the parameters; are shown in Figure 3.3. The solid line represents observed drawdown and the dashed line represents simulated drawdown. Drawdown at the pumping port has been highlighted with black rectangular box in Figure 3.3. Similar plots for the remaining 8 pumping tests that were simulated using the parameters obtained from the calibration of the test at port 5 are provided in Appendix B.

Examination of Figure 3.3 (and additional figures in Appendix B) reveals that, for all of the pumping tests, a good match between the observed and simulated drawdown was obtained for the steady state portion of the drawdown curves at the fracture observation ports. However, simulated early time drawdown deviated from the observed quite a bit, especially at the ports closer to the pumping port. The early-time drawdown is controlled by the specific storage (S_s), while the late time drawdown is dominated by the hydraulic conductivity (K) of the aquifer. Thus, the early time deviation may be due to the fact that, during all of the pumping tests fracture ports reached steady state within 2 to 3 seconds after the water extraction was started and for the synthetic case, it was difficult to reproduce the early-time drawdown within such a short period of time. Storage at the pulse damper during the pumping tests in the laboratory could also be responsible for this early time

deviation. Similar to the observed cases, there was no drawdown at the matrix ports for the simulated cases due to the very low matrix hydraulic conductivity.

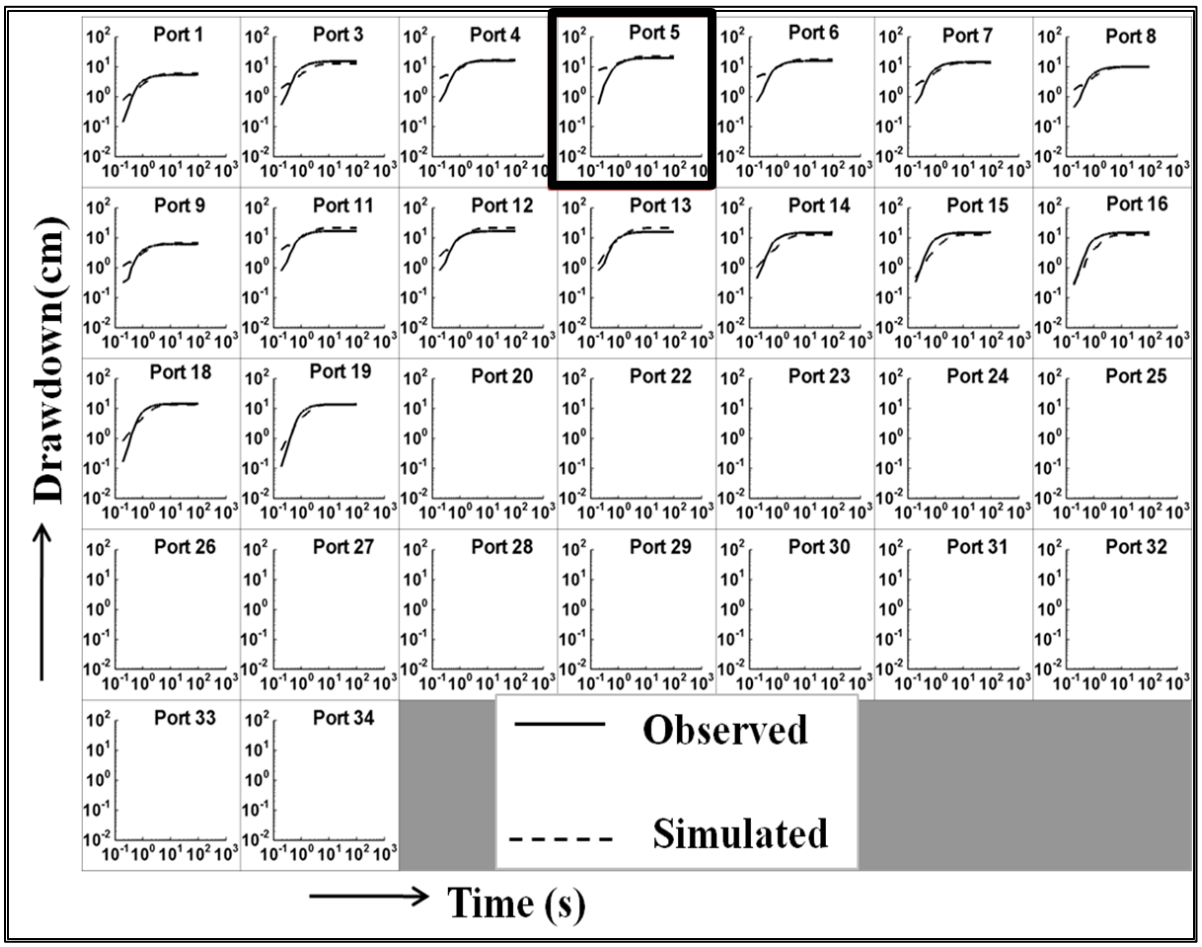

Figure 3.3: Observed and Simulated Drawdown during Pumping Test at Port 5. The solid line represents observed drawdown and the dashed line represents simulated drawdown. The pumped port is indicated by the black rectangular box.

Chapter 4
Transient Hydraulic Tomography

One of the main objectives of this study was to investigate the utility of transient hydraulic tomography (THT) based on the inverse algorithm SSLE developed by *Zhu and Yeh* [2005] to image the K and S_s tomograms as well as their uncertainties and to examine whether the delineation of discrete fractures and their connectivity are possible or not. To achieve this objective, transient hydraulic tomography (THT) was conducted in the fractured rock by inverting both synthetic and laboratory data.

Steady-state hydraulic tomography (SSHT) uses one data point per drawdown curve (Figure 4.1a) and estimates hydraulic conductivity (K), while THT uses several data points per drawdown curve (Figure 4.1b) from multiple pumping tests to estimate hydraulic conductivity (K) and specific storage (S_s) of the aquifer. Thus, THT incorporates significantly more information of the aquifer from each pumping test. This is the reason why THT was chosen to delineate discrete fractures.

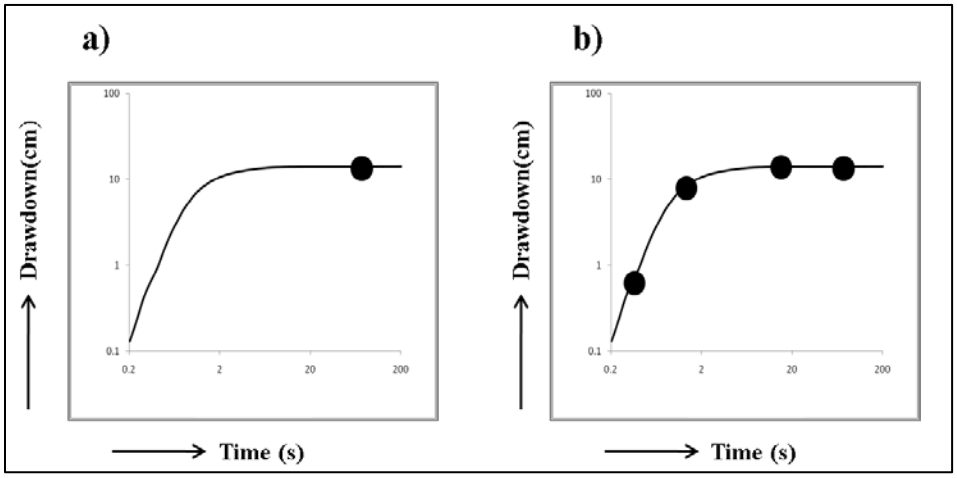

Figure 4.1: a) Head Data Required for SSHT and b) Head Data Required for THT

4.1 Inverse Model

The theory behind SSLE is briefly presented here after *Zhu and Yeh* [2005]. They describe fully saturated, three-dimensional, transient groundwater flow in a heterogeneous, porous media by equation (5):

$$\nabla \cdot [K(x)\nabla H] + Q(x_p) = S_s(x)\frac{\partial H}{\partial t} \quad [5]$$

where, H is total head [L], $\boldsymbol{x}$ is the spatial coordinate x = {x1,x2,x3} [L], $Q(\boldsymbol{x}_p)$ is the pumping rate [1/T] at location $\mathbf{x_p}$, $K(\mathbf{x})$ is the hydraulic conductivity [LT^{-1}], and S_s ($\mathbf{x}$) is specific storage [L^{-1}], and boundary and initial conditions are given by equation (*6*) and (*7*) respectively:

$$H|_{\Gamma 1} = H_1,\ [(\mathbf{x})\nabla H]\cdot\mathbf{n}|_{\Gamma 2} = q \quad [6]$$

$$H|_{t=0} = H_0 \quad [7]$$

where, H_1 is prescribed total head at the Dirichlet boundary (Γ_1), q is the specified flux [LT^{-1}] at the Neumann boundary Γ_2, $\mathbf{n}$ is a unit vector normal to the union of Γ_1 and Γ_2 and H_0 is the initial total head.

SSLE is an extension of the SLE (successive linear estimator) approach [i.e., *Yeh et al.*, 1996; *Yeh and Zhang*, 1996; *Zhang and Yeh*, 1997; *Hughson and Yeh*, 2000 etc.]. The SLE approach is similar to cokriging [*Yeh et al.*, 1995a] that seeks mean parameter fields conditioned on available point data as well as geologic and hydrologic structures (i.e., spatial covariance functions of parameters and hydraulic heads, and their cross-covariance functions). Unlike cokriging, SLE updates both conditional means and covariances of the estimates using a linear estimator based on differences between observed and simulated hydraulic heads successively to consider the nonlinear relation between information and parameters [*Zhu and Yeh* 2005]. This allows the non-linear relation between head and K to be handled more effectively, thus allowing systems with higher $\sigma^2_{\ln K}$ to be handled.

Instead of including data sets simultaneously, the SSLE approach relies on the SLE concept to sequentially include data sets from each pumping test and updates covariances and cross covariances in the estimation process. As hydraulic tomography (HT) experiments generate large amounts of data, classical inverse parameter estimate approaches may experience significant computational burden, numerical instabilities [*Yeh*, 1986; *Hughson and Yeh*, 2000] and even non-uniqueness. To process the large amount of data efficiently and characterize aquifer heterogeneity, *Zhu and Yeh* [2005] developed the geostatistical inverse algorithm SSLE that includes observation data from individual pumping tests sequentially, instead of analyzing all of them simultaneously. The sequential method reduces the computational load and avoids solving huge systems of equations and therefore reduces numerical difficulties.

SSLE treats the natural logs of hydraulic parameter fields as spatial stochastic processes to address the issue of non-uniqueness. It assumes that $lnK = \overline{K} + f$ and $lnS_s = \overline{S} + s$ where $\overline{K}$ and $\overline{S}$ are mean values, and f and s are perturbations. Transient hydraulic head is represented by $H = \overline{H}$ + h, where $\overline{H}$ is the mean and h is the perturbation. Therefore, SSLE requires the mean parameter distributions, conditioned on the observations of the pumping tests. Any available 'hard' data (direct hydraulic parameter estimates from slug tests, permeameter tests, grain size analysis, etc.) can also be incorporated in SSLE to condition the estimates [*Yeh and Liu*, 2000; *Zhu and Yeh*, 2005].

Substituting the stochastic variables into the groundwater flow equation (5) and taking the conditional expectation and conditioning with some observations (hydraulic head and parameter estimates) the mean flow equation becomes:

$$\nabla\cdot [\overline{K}_{\text{con}}(\text{x})\, \nabla\overline{H}_{\text{con}}] + (x_p) = \bar{S}_{\text{con}}(x_p)\frac{\delta\bar{H}_{con}}{\delta t} \qquad [8]$$

where, $\overline{K}_{\text{con}}$, $\overline{H}_{\text{con}}$ and $\bar{S}_{\text{con}}$ are conditional effective hydraulic conductivity, hydraulic head, and specific storage respectively [*Zhu and Yeh*, 2005].

The following paragraph is quoted from Zhu and Yeh [2005] to precisely describe the estimation process. “The estimation procedure starts with a weighted linear combination of direct measurements of the parameters and transient head data at different locations to obtain the first estimate of the parameters. The weights are calculated based on statistical moments (namely, means and covariances) of parameters, the covariances of heads in space and time, the cross covariance between heads and parameters. The first estimate is then used in the mean flow equation (8) to calculate the heads at observation locations and sampling times (i.e., forward simulation). Differences between the observed and simulated heads are determined subsequently. A weighted linear combination of these differences is then used to improve the previous estimates."

Once SSLE meets the convergence criteria (number of iterations or if the change in the estimated parameters is below a previously set value) for a specific pumping test, it starts analyzing the data set from the next pumping test and the procedure continues until all of the pumping tests have been analyzed. SSLE updates the estimates of hydraulic parameters (K and S_s) after each iteration is completed and the following iteration starts with these updated values of parameters (K and S_s). This process continues until the model has gone through the last iteration of the last test. As SSLE includes pumping tests sequentially, final inversion results many not be consistent with the 1st data set. To address this issue, *Zhu and Yeh* [2005] introduced a looped iteration scheme that reanalyzes the data

set from earlier tests after the analysis of each test is completed and the process continues throughout the inversion.

4.2 Inverse Model Set-up

THT analysis of synthetic data (synthetic THT from now on) was performed, before performing transient hydraulic tomography (THT) analysis utilizing laboratory data (real THT from now on). Synthetic THT was conducted inverting three of the nine synthetic pumping tests conducted by HGS, described in section 3.3). Upon completion of the synthetic THT, two cases of the real THT were performed by inverting two different sets of pumping tests conducted in the fractured dolostone enclosed in a flow cell (Figure 2.9), described in section 3.2. Each of the two real THT cases was conducted inverting three laboratory pumping tests.

All stochastic inversions of individual pumping tests were performed using 30 to 32 processors for the synthetic case and 8 to16 processors for the real case on a PC-cluster (consisting of 1 master and 12 slaves each with Intel Q6600 Quad Core CPUs running at 2.4 GHz with 16 GB of RAM per slave) at the University of Waterloo. The operating system managing the cluster was CentOS 5.3 based on a 64-bit system.

4.2.1 Model Domain used for Synthetic and Real THT Analysis

This section describes the model domain that was used for the synthetic as well as the real THT analysis. A 91.5 cm by 60.5 cm and 5 cm (one element) thick domain was used for the inversion of both synthetic and laboratory data and the domain was composed of variably-sized rectangular elements. The domain was discretized into 14140 nodes and 6900 elements. The element size varied from 0.5 cm by 0.5 cm to 1.75 cm by 1.75 cm. The finer elements are located along the ports to match the port location and the element center and the coarser elements are located near the boundary. The boundary conditions were constant head for left and right boundaries and no flow for the remaining outer boundaries. The hydraulic head for both the left and right boundary of the model domain was 63.5 cm which was identical to the actual experiment. Figure 4.2 shows the computational grid used for the both synthetic and real THT analysis.

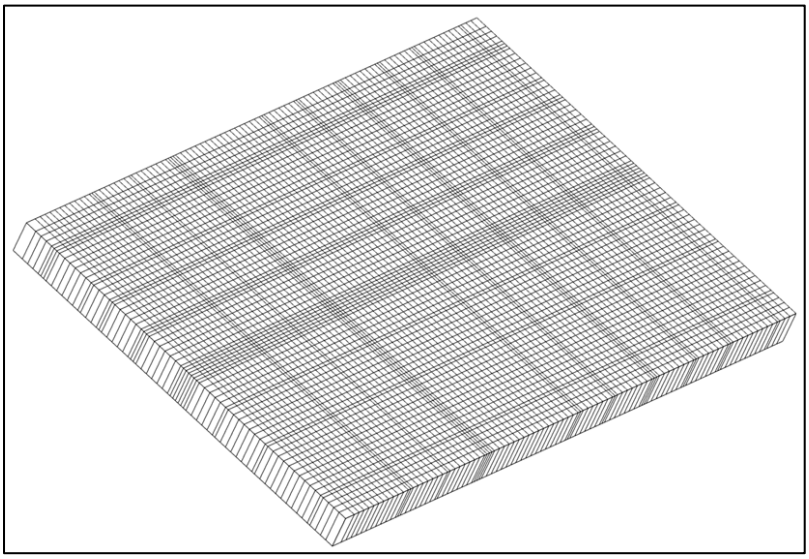

Figure 4.2: Computational grid Used for THT analysis.

4.2.2 Model Input for both the Synthetic and the Real THT Analysis

This section describes the model (SSLE) inputs for both the synthetic and the real THT analyses. SSLE inputs include mean K and S_s values for the model domain, estimates or guesses of variances and the correlation scales for both parameters, volumetric discharge (Q) from each pumping test and observed pressure head data at various selected times per drawdown curve from each pumping tests. Here, the model was not conditioned with additional data, although point (small-scale) measurements of K and S_s can also be input to the model to condition the estimates.

One can estimate the mean values or initial homogeneous field of K and S_s in a number of ways. For example, literature values of effective hydraulic conductivity (K_{eff}) and specific storage ($S_{s\,eff}$) that are considered reasonable for the aquifer can be used as initial model input. An alternative could be estimating a geometric mean of the small-scale measurements (i.e., core, slug, and single-hole data), if small-scale data are available. The initial homogeneous K and S_s field can also be populated by the equivalent hydraulic conductivity and specific storage estimates obtained by analyzing the pumping test data sets treating the medium to be homogeneous.

Here, the latter option was chosen and the initial homogeneous K and S_s were estimated by coupling PEST [*Doherty*, 2005] with forward SSLE [*Zhu and Yeh* 2005] and matching the drawdown responses at the pumping port. The homogeneous K and S_s for the fractured rock were estimated by matching the pumping port drawdown for 3 individual laboratory pumping tests conducted at Ports 3,

5 and 7 (port are indicated in Figure 2.9). The model domain and the boundary conditions used for the parameter estimation purpose was the same as the one described in section 4.2.1. Estimates of homogeneous K and S_s along with the corresponding confidence intervals are presented in Table 4-1.

Table 4-1: Parameters Estimated by PEST

Pumped Port	Port 3	Port 5	Port 7
Estimated K (cm/s)	2.80×10^{-2}	1.40×10^{-2}	3.00×10^{-2}
Max K (cm/s)	3.90×10^{-2}	1.70×10^{-2}	4.00×10^{-2}
Min K (cm/s)	2.10×10^{-2}	1.10×10^{-2}	2.00×10^{-2}
Estimated S_s (/cm)	1.30×10^{-3}	2.00×10^{-2}	4.00×10^{-3}
Max S_s (/cm)	7.50×10^{-3}	4.00×10^{-2}	2.00×10^{-3}
Min S_s (/cm)	2.30×10^{-3}	1.00×10^{-2}	9.00×10^{-3}

From Table 4-1 it is seen that the estimates of homogeneous K and S_s from all 3 cases were close to one another. Therefore arithmetic mean of the estimated homogeneous K and S_s (K= 1.4×10^{-2} cm/s and S_s = 5.0×10^{-3} cm^{-1}) were incorporated into SSLE for the inversion of the synthetic as well as the laboratory data. The model starts the inversion (for both synthetic and real THT) with these homogeneous estimates of K and S_s and updates them at the end of each iteration and the following iteration starts with these updated values of K and S_s. This process continues until the model goes through the last iteration of the last test.

SSLE also requires the estimates of the hydrogeologic structure (correlation length and the variances of the K and S_s) for inversion. One can assume correlation length and the variances or conduct a geostatistical analysis of small scale data to estimate the variance and the correlation length. Here, a correlation length of 1 cm and a variance of 5 were used for the THT analyses (for both synthetic and real cases), which were determined through trial and error. It is a well-known fact that it is difficult to estimate the variance and the correlation scale accurately and thus the estimation always involves some uncertainty. Here, a unit correlation length (1cm) was used for the THT analyses, as larger correlation implies homogeneous field of hydraulic properties. However, a previous numerical study conducted by *Yeh and Liu* [2000] has shown that the variance and the

uncertainty in the correlation scales have negligible effects on the estimated K field based on hydraulic tomography (HT), because HT utilizes a large number of head measurements, which already hold information of the detailed site-specific heterogeneity [*Zhu and Yeh*, 2005, 2006; *Liu et al*., 2007].

As mentioned earlier, the synthetic THT analysis was performed by inverting three synthetic pumping tests sequentially, which include the tests at the ports 5, 7 and 3. Pumped ports are indicated in Figure 4.3a and the pumping rate and the test order are listed in Table 4-2. The pumping tests utilized in the construction of synthetic THT were identical to the ones used in real THT case 1 described in the following paragraph.

Here, two cases of real transient hydraulic tomography (THT) analysis were performed changing the locations of 2nd and 3rd pumping tests among the three, to compare the estimated hydraulic conductivity (K) and specific storage (S_s) field and evaluated if the estimated K and S_s pattern changes by changing these later pumping locations. However, the 1st test included to the inverse model was the same for both cases. Real THT case 1 includes 3 pumping tests; tests at ports 5, 7 and 3 which are identical to one used to perform synthetic THT. Pumped ports are indicated in Figure 4.3a. In real THT case 2, tests at ports 5, 16 and 19 were inverted sequentially to estimate the K and S_s tomograms for the fractured dolostone. Pumped ports are indicated in Figure 4.3b. The pumping tests analyzed to perform each of the two real THT cases, their order and pumping rates are summarized in Table 4-2.

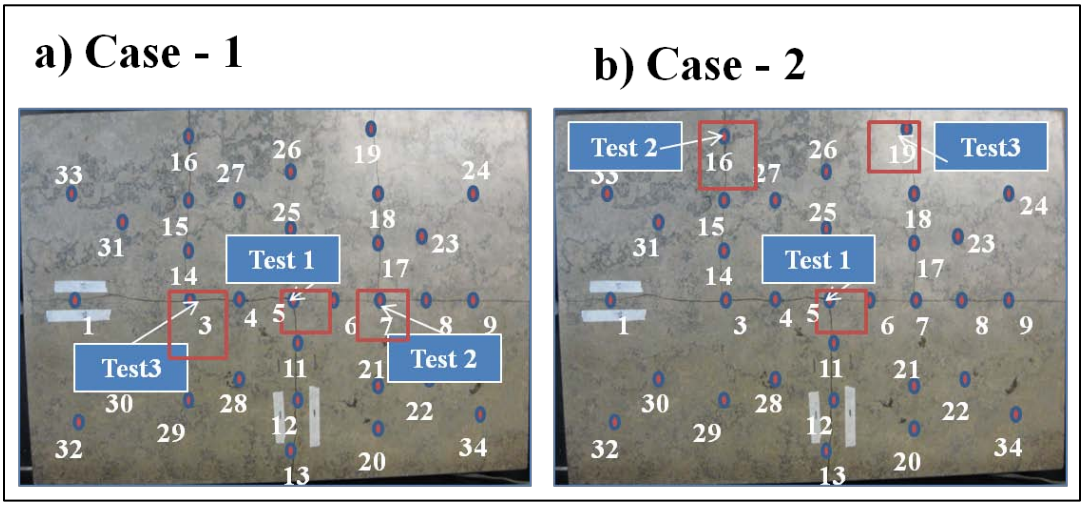

Figure 4.3: a) Pumping Tests Included in Synthetic THT as well as Real THT Case 1 and b) Pumping Tests Included in Real THT Case 2.

Table 4-2: Summary of Pumping Tests Analyzed for the Synthetic and Real THT Cases

THT Cases	Test Order	Pumping Test Location	Extraction Rate (mL/s)
Synthetic THT	Test 1	Port 5	4
	Test 2	Port 7	2.5
	Test 3	Port 3	2.5
Real THT Case 1	Test 1	Port 5	4
	Test 2	Port 7	2.5
	Test 3	Port 3	2.5
Real THT Case 2	Test 1	Port 5	4
	Test 2	Port 16	1
	Test 3	Port 19	1

The locations for the pumping tests were selected for their ability to stress the entire fractured block. For example, for all the THT cases pumping test at port 5 (Figure 4.3) was included first for inversion followed by two other tests with lower pumping rates. The reason behind it was that, pumping test at port 5 (Figure 4.3) stressed all the fractures more or less as it is located approximately at the middle of the fractured block and it had the highest flow rate, thus had the highest signal to noise ratio. *Illman et al.* [2008] showed that including the data with the highest signal-to-noise ratio first into inverse SSLE appeared to improve the results. After the test at port 5, in real THT case 1, pumping tests at port 7 and port 3 and in case 2, tests at port 16 and port 19 were included in the inverse model. Results not included here showed that the change in the order of the second and third pumping tests did not change the pattern of the resulting K and S_s tomograms significantly.

For the synthetic as well as two real THT cases, 4 data points (at 0.5s, 1s, 3s and 20s) were extracted from each observation port (both fracture and matrix observation ports) to represent the entire drawdown curve and the transient behavior in detail. The total number of observed data points used from each pumping test ranged from 116 to 120. In total, 356 drawdown records from 3 different pumping tests were utilized to perform synthetic as well as each of the 2 real THT cases.

Figure 4.4 shows the extracted data points per drawdown curve at the fracture observation ports from the synthetic pumping test at port 5 for the synthetic THT analysis, while Figure 4.5 shows the same from the laboratory pumping test at port 5 for each of the two real THT analysis. In Figure 4.4 Figure 4.5 the solid line represents the drawdown curve at each fracture port and the circles represent the data points used for inversion. Similar plots showing the data points extracted from the fracture observation ports from rest of the pumping tests utilized for the construction of the synthetic and the real THT cases are included in Appendix C.

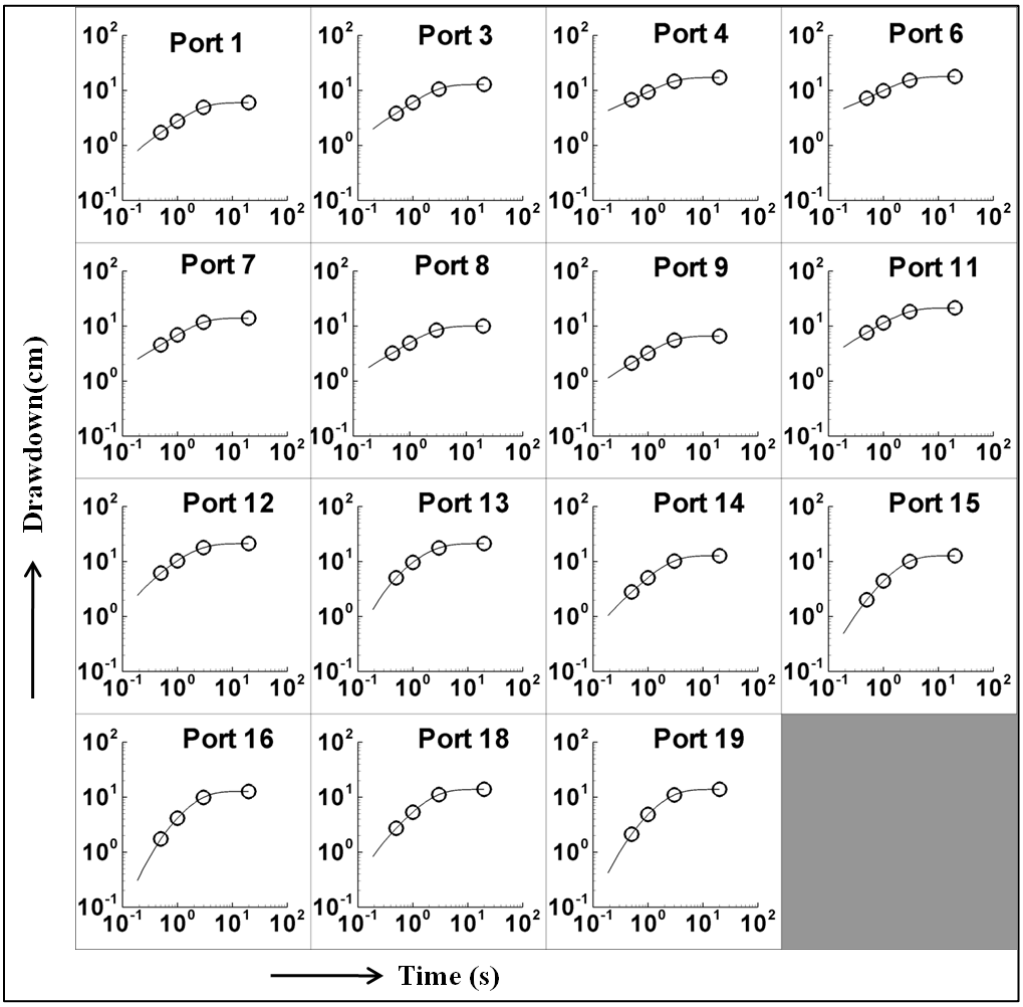

Figure 4.4: Selected Data Points at the Fracture Observation Ports from pumping test at port 5 for Synthetic THT analysis. The solid line represents the drawdown curve at each fracture port and the circles represent the data points used for inversion.

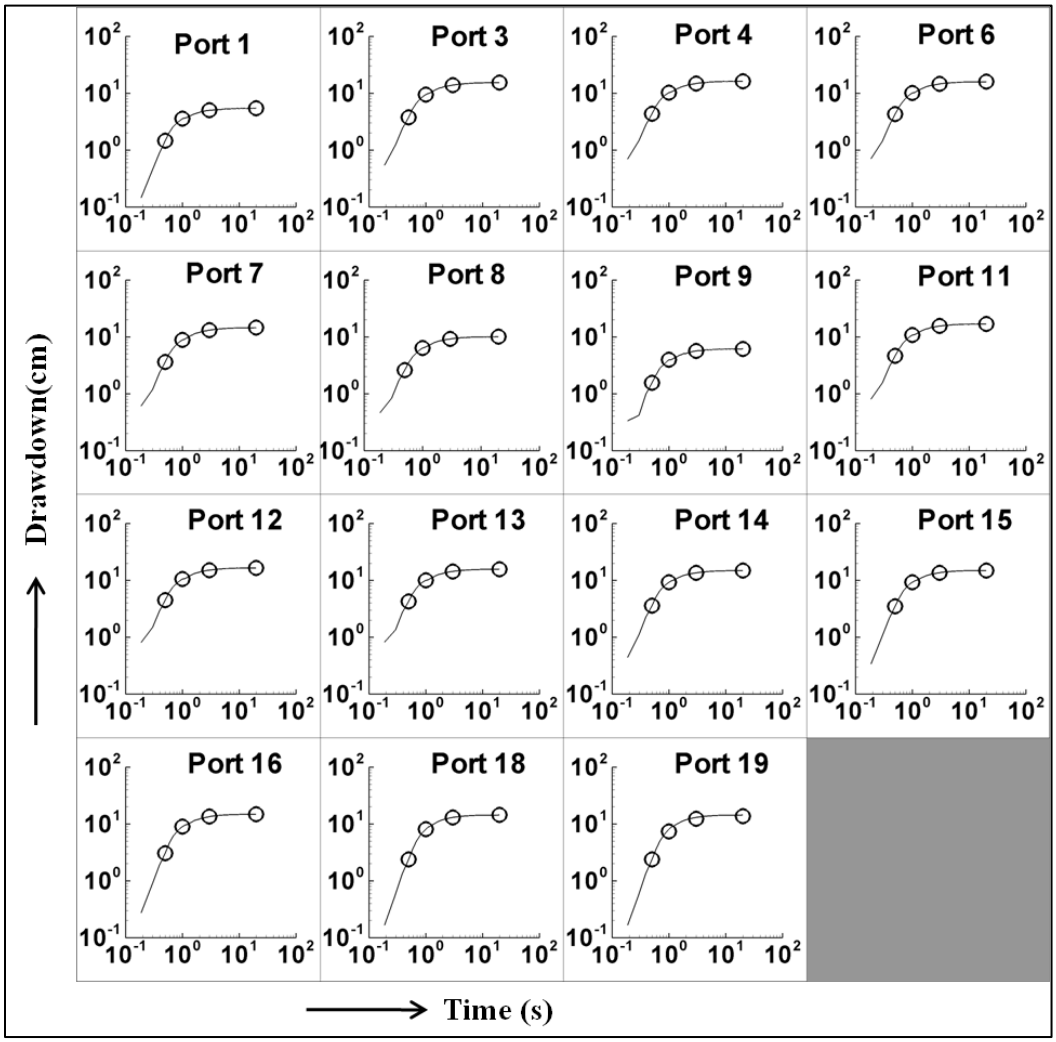

Figure 4.5: Selected Data Points at the Fracture Observation Ports from pumping test at port 5 for Real THT cases 1 and 2. The solid line represents the drawdown curve at each fracture port and the circles represent the data points used for inversion.

Matrix observation ports are not included in Figure 4.4 and Figure 4.5, as none of the matrix ports responded during the synthetic or laboratory pumping tests. Zero drawdown was input to the inverse model for each matrix observation port for both synthetic and real THT cases.

Chapter 5
Transient Hydraulic Tomography Results

5.1 *K* and S_s Tomograms Obtained from Synthetic THT

Figure 5.1 represents the *K* – Tomogram and Figure 5.2 represents the S_s – Tomogram obtained from the inversion of synthetic pumping tests. Figure 5.1a; b; c and Figure 5.2a; b; c represent the *K* and S_s – tomograms after including 1 test, 2 tests and 3 tests respectively. Figure 5.1d and Figure 5.2d show the variance estimates associated with the estimated *K* and S_s – Tomograms, respectively, for the inverse modeling of 3 tests. Red ovals indicate pumped locations used in synthetic THT, while observation intervals are indicated by the black ovals.

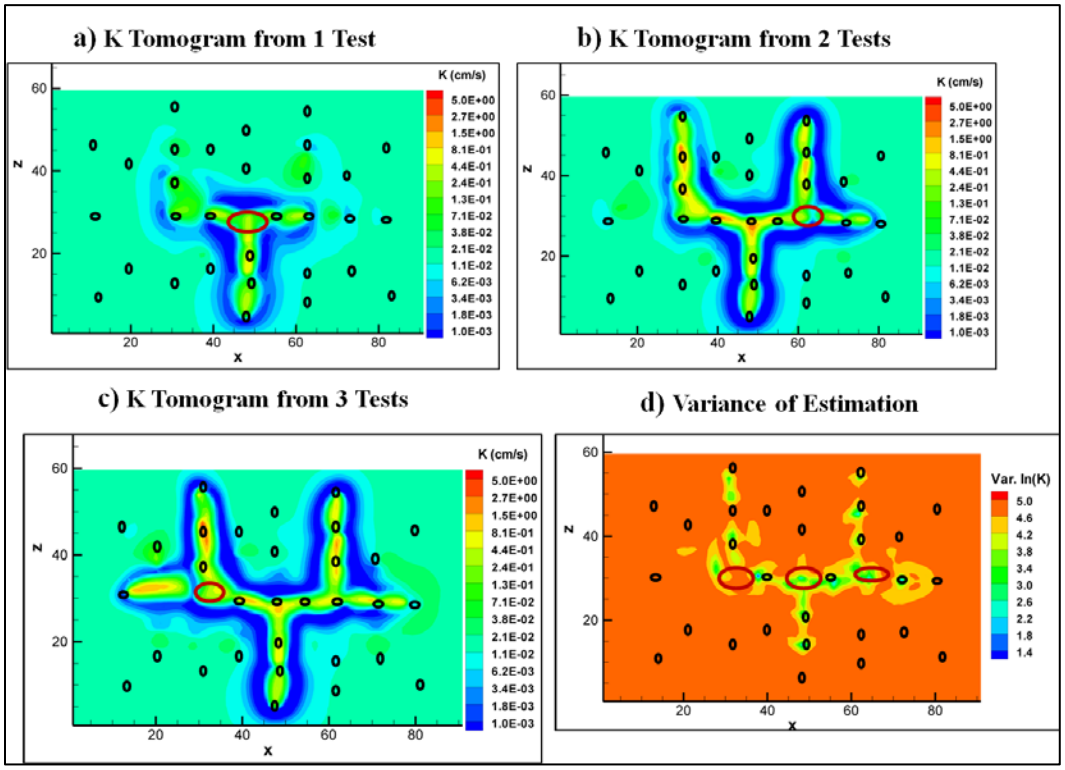

Figure 5.1: *K* - Tomograms (cm/s) obtained from synthetic THT analysis: a) *K* - Tomogram after 1 Test; b) *K* – Tomogram after 2 Tests; c) *K* – Tomogram after 3 Tests and d) Variance associated with the Estimated *K*- Tomogram (Figure 5.1c). Pumped locations are indicated by the red ovals, while observation intervals are indicated by the black ovals. The image in each figure represents the x-z plane through the middle of the domain thickness.

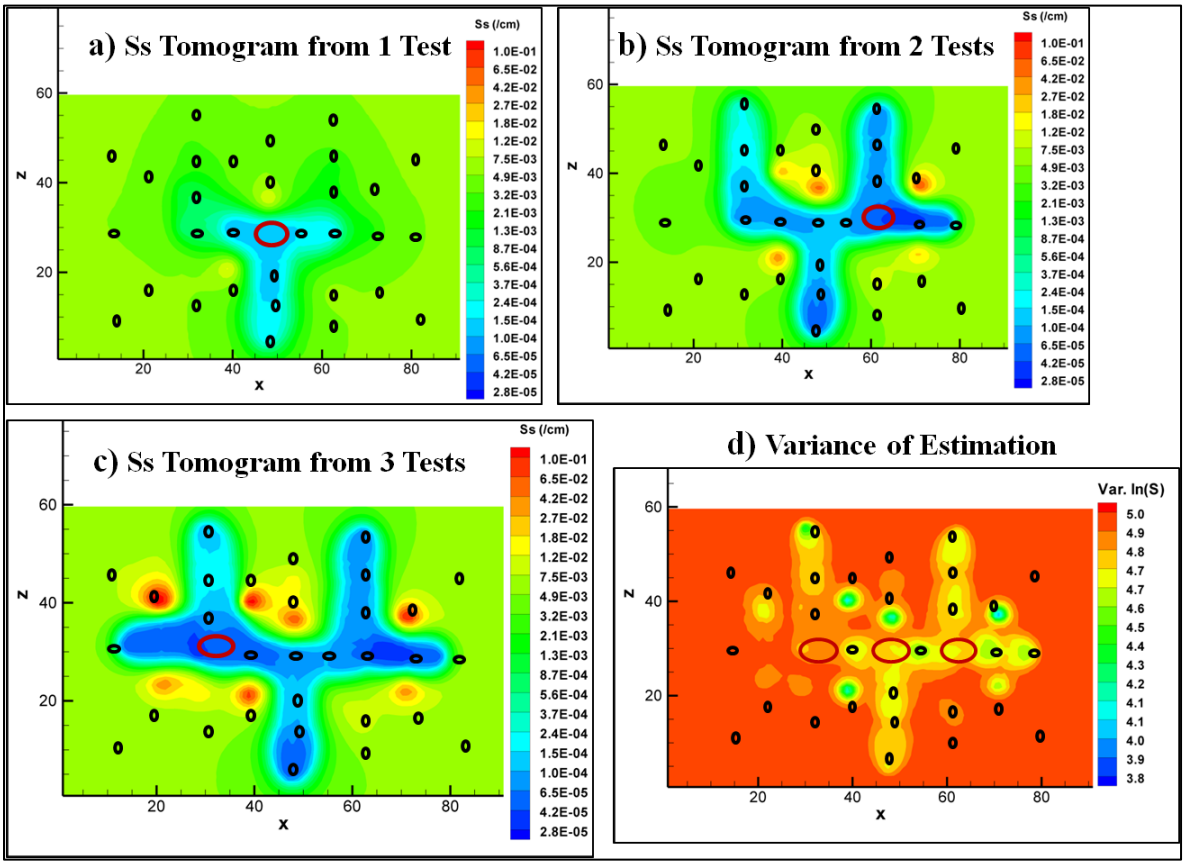

Figure 5.2: S_s - Tomograms (cm^{-1}) obtained from the synthetic THT analysis: a) S_s - Tomogram after 1 Test; b) S_s – Tomogram after 2 Tests; c) S_s – Tomogram after 3 Tests and d) Variance associated with the Estimated S_s – Tomogram (Figure 5.2c). Pumped locations are indicated by the red ovals, while observation intervals are indicated by the black ovals. The image in each figure represents the x-z plane through the middle of the domain thickness.

The high K – zone in Figure 5.1a; b and c and low S_s – zone in Figure 5.2a; b and c clearly show the fracture pattern and their connectivity, indicating that the synthetic THT analysis captured the fracture pattern quite well. The high K (Figure 5.1a, b and c) and low S_s (Figure 5.2a, b and c) zones do not continue to the edge of the rock, which may be due to the boundary effect.

The purpose of conducting synthetic THT analysis was to examine how good THT is in imaging the fractured rock when there is no experimental noise in the data set. Later a comparison of the K and S_s tomograms obtained from the inversion of synthetic pumping tests to those obtained from real THT case 1 is represented, as the pumping tests utilized for real THT case 1 were identical to the synthetic case.

5.2 *K* and S_s Tomograms Obtained from Real THT Cases

Figure 5.3 shows the *K* – Tomogram and Figure 5.4 shows the S_s – Tomogram obtained from the inversion of 3 pumping tests (Case 1). Figure 5.3a; b; c and Figure 5.4a; b; c represent the *K* – tomogram and S_s – tomogram after1 test, 2 tests and 3 tests respectively. Figure 5.3d and Figure 5.4d shows the variance associated with the Estimated *K* and S_s – Tomogram (in Figure 5.3c) respectively. Red ovals indicate pumped locations used in case 1, while observation intervals are indicated by the black ovals.

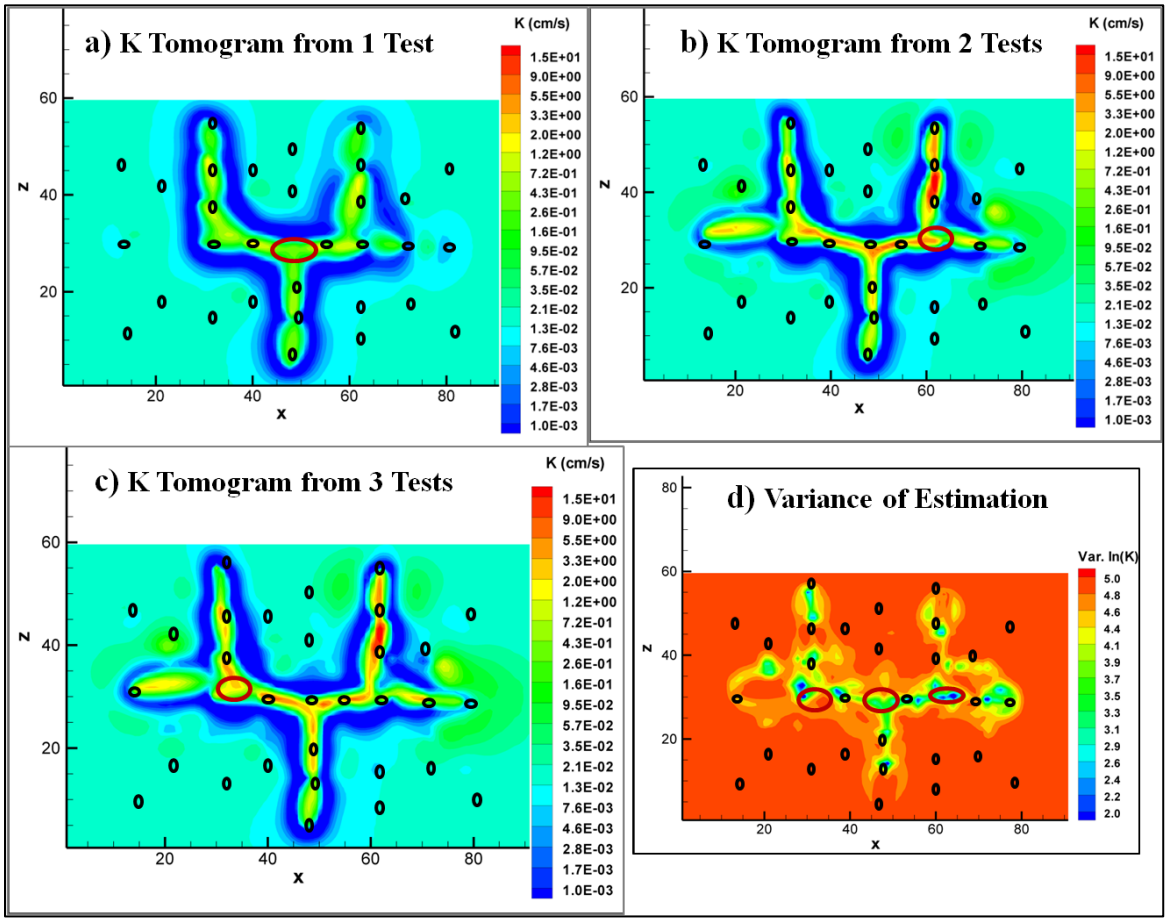

Figure 5.3: *K* - Tomograms (cm/s) obtained from the inversion of three pumping tests in Case 1: a) *K* - Tomogram after 1 Test; b) *K* – Tomogram after 2 Tests; c) *K* – Tomogram after 3 Tests and d) Variance associated with the Estimated *K*- Tomogram in Case 1 (Figure 5.3c). Pumped locations are indicated by the red ovals, while observation intervals are indicated by the black ovals. The image in each figure represents the x-z plane through the middle of the domain thickness.

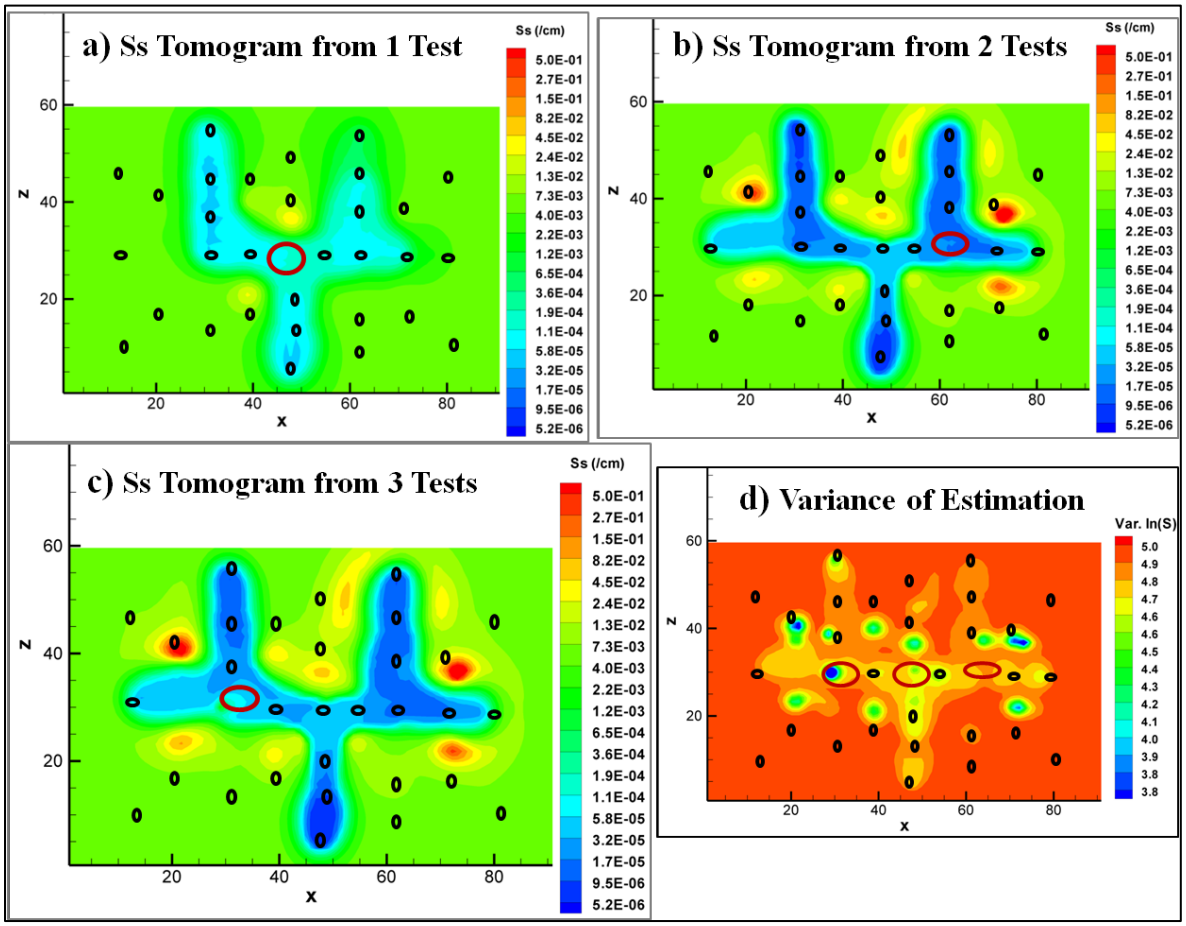

Figure 5.4: S_s - Tomograms (cm^{-1}) obtained from the inversion of three pumping tests in Case 1: a) S_s - Tomogram after 1 Test; b) S_s – Tomogram after 2 Tests; c) S_s – Tomogram after 3 Tests and d) Variance associated with the Estimated S_s – Tomogram in Case 1 (Figure 5.4c). Pumped locations are indicated by the red ovals, while observation intervals are indicated by the black ovals. The image in each figure represents the x-z plane through the middle of the domain thickness.

From the K - tomograms (Figure 5.3a; b and c) and S_s - tomograms (Figure 5.4a; b and c) obtained from 3 tests in real THT case 1, it is evident that transient hydraulic tomography (THT) captured the fracture pattern quite well and they become more vivid with addition of each test. The high K – zone in Figure 5.3a; b and c and low S_s – zone in Figure 5.4a; b and c clearly show the fractures and their connectivity, although the high K (Figure 5.3a, b and c) and low S_s (Figure 5.4a, b and c) zone do not continue to the edge of the rock, which could be due to the boundary effect. Similar pattern of K and S_s were obtained from synthetic THT analysis.

Similar K and S_s tomograms were obtained from the inversion of 3 pumping tests in real THT case 2. Figure 5.5a; b; c and Figure 5.6a; b; c represent the K – and S_s – tomograms after one, two and three tests respectively. Figure 5.5d and Figure 5.6d show the variance associated with the Estimated K and S_s - Tomograms (in Figure 5.5c and Figure 5.6c) respectively. Red ovals indicate pumped locations used in real THT case 2, while observation intervals are indicated by the black ovals.

Examination of Figure 5.3, Figure 5.4, Figure 5.5 and Figure 5.6 revealed that the pattern of estimated K and S_s tomograms and the variance associated with the estimates remained similar in these two cases of THT analysis, although the pumped locations utilized for the inversion were different for two cases.

Estimated K and S_s values for the fractures and the matrix may not exactly replicate actual values. Estimated matrix hydraulic conductivity (K) and specific storage (S_s) values seem to be higher than the literature values (listed in Table 3-4). One of the reasons behind it could be that SSLE is a porous media code and for a porous media code it is difficult to handle the high contrast between the fracture and matrix hydraulic conductivity (K) and specific storage (S_s) values. Moreover, all the inversions were conducted for 20 seconds (as all the fracture observation port reached steady-state within 2 to 3 seconds and no drawdown was observed in the matrix ports) and it is almost impossible to estimate matrix hydraulic conductivity (K) and specific storage (S_s) within this short period of time as no flow takes place in the matrix during this time period. It is a well known fact that, estimating hydraulic conductivity (K) and specific storage (S_s) of a fractured rock has been a challenge for decades and the estimation often involves uncertainty. The advantage of SSLE is that, it gives the variance associated with estimates. The variance maps associated with estimated K- tomograms (Figure 5.3d, Figure 5.5d) and S_s – tomograms (Figure 5.4d, Figure 5.6d) indicate that the matrix estimates have a high degree of uncertainty, reflecting the observation of no drawdowns at these ports. However, the goal of this study was to image fracture pattern and their connectivity using THT analysis based on inverse algorithm SSLE, which has been clearly achieved.

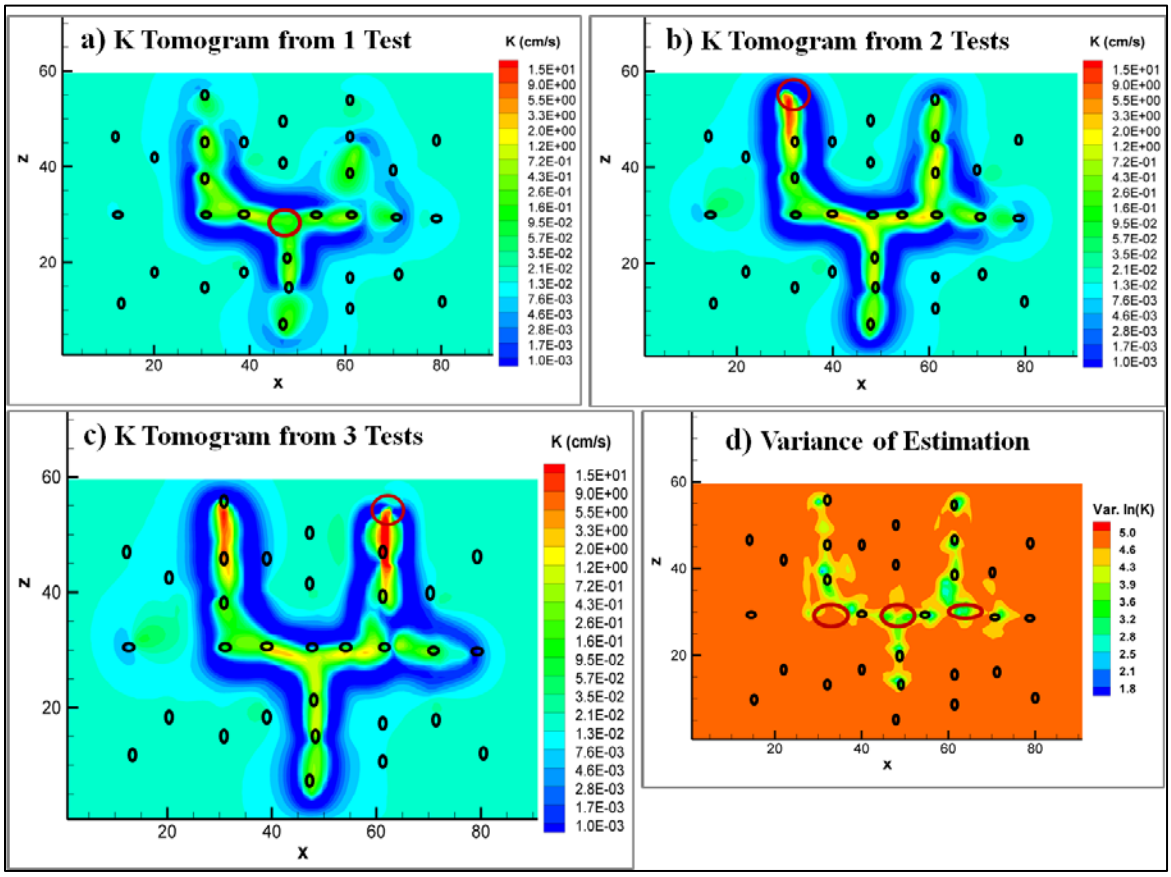

Figure 5.5: *K* - Tomograms (cm/s) obtained from the inversion of three pumping tests in Case 2: a) *K* - Tomogram after 1 Test; b) *K* – Tomogram after 2 Tests; c) *K* – Tomogram after 3 Tests and d) Variance associated with the Estimated *K*- Tomogram in Case 2 (Figure 5.5c). Pumped locations are indicated by the red ovals, while observation intervals are indicated by the black ovals. The image in each figure represents the x-z plane through the middle of the domain thickness.

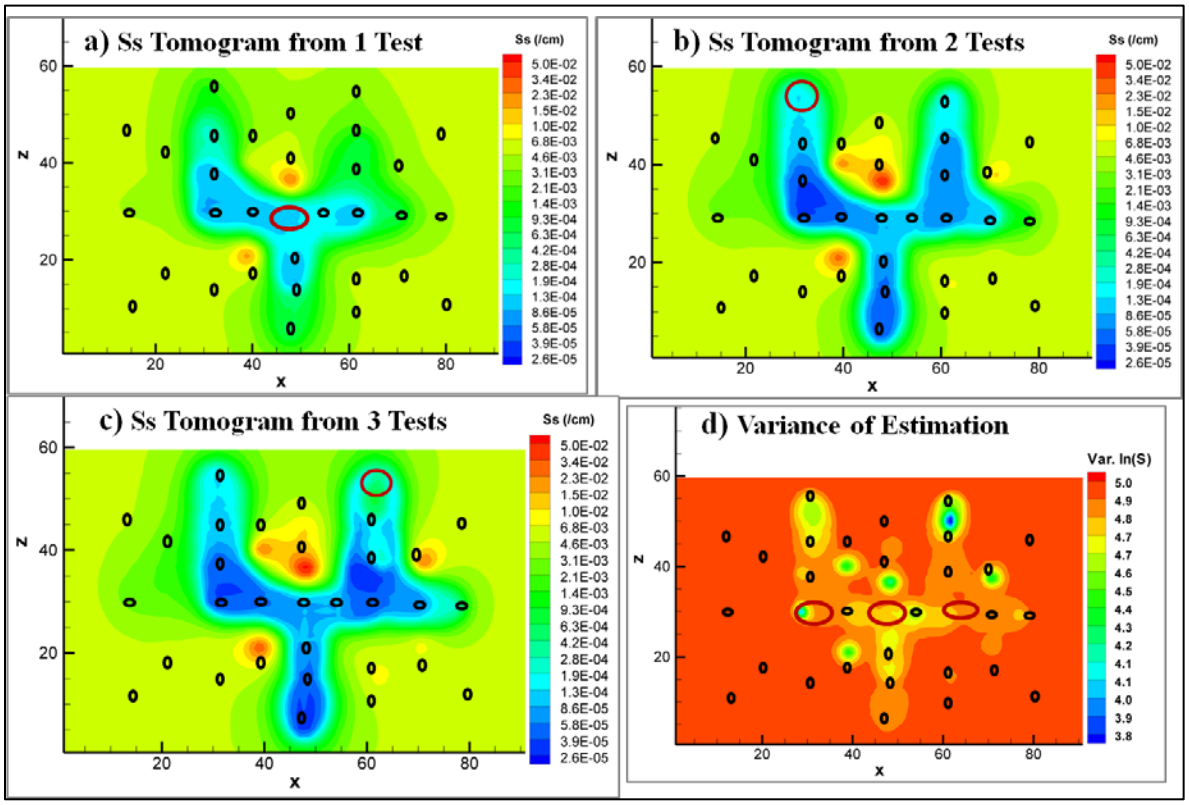

Figure 5.6: S_s - Tomograms (cm^{-1}) obtained from the inversion of three pumping tests in Case 2: a) S_s - Tomogram after 1 Test; b) S_s – Tomogram after 2 Tests; c) S_s – Tomogram after 3 Tests and d) Variance associated with the Estimated S_s – Tomogram in Case 2 (Figure 5.6c). Pumped locations are indicated by the red ovals, while observation intervals are indicated by the black ovals. The image in each figure represents the x-z plane through the middle of the domain thickness.

Chapter 6
Discussion and Findings from THT

In this chapter, the K and S_s tomograms obtained from the inversion of synthetic pumping tests to those obtained from real THT case 1 are compared first and then the performance of THT analyses of the laboratory data (THT case 1 and THT case 2) are assessed.

6.1 Comparison of K and S_s tomograms obtained from synthetic THT to those obtained from the inversion of laboratory data

Here K and S_s tomograms generated by synthetic THT are compared to those generated by the real THT case 1 to examine how the estimates from the inversion of noise free data match the estimates from the inversion of laboratory data that contains experimental noise.

Visual assessment reveals that the patterns of estimated K and S_s tomograms generated by the synthetic THT (Figure 5.1 and Figure 5.2) and the ones generated from the inversion of laboratory data (real THT case 1) (Figure 5.3 and Figure 5.4) are quite similar.

Figure 6.1a and b represents the scatter plots of K and S_s values, respectively, obtained from the synthetic THT analysis to those obtained from the THT analysis of laboratory data (real THT case 1). The solid line represents the 1:1 line. From Figure 6.1a and b, it can be seen that the data points cluster around the 1:1 with some bias indicating a good match between these two sets of tomograms.

Two criteria, the average absolute error norm *(L1)* and the mean squared error norm *(L2)* were used to quantitatively evaluate the soundness-of-fit between the two sets of tomograms. Both *L1* and *L2* norms were calculated so that the average absolute error and mean squared error can be compared. The *L1* and *L2* norms are computed using the equations *(9)* and *(10)* respectively -

$$L1 = \frac{1}{n}\sum_{i=1}^{n}|\chi_i - \widehat{\chi_i}| \qquad [9]$$

$$L2 = \frac{1}{n}\sum_{i=1}^{n}(\chi_i - \widehat{\chi_i})^2 \qquad [10]$$

where, χ_i and $\widehat{\chi_i}$ represent the estimates from the two sets of data, n is the total number of data points and i indicates the data number. To compute the *L1* and *L2* norms, K and S_s values for each element of the model domain estimated by synthetic THT and real THT case 1 were evaluated. Corresponding

L1 and *L2* norms for the *K* and S_s estimates are included on each scatter plot. The smaller the *L1* and *L2* norms, the more consistent are the two data sets.

The visual assessment, scatter plots (Figure 6.1) and *L1* and *L2* norms presented on each scatter plot (Figure 6.1) indicate a good fit between these two sets of tomograms (*K* and S_s tomograms obtained from the synthetic THT analysis to those obtained from the THT analysis of laboratory data case 1) suggesting that the noise in the experimental data was too small to significantly impact the estimates.

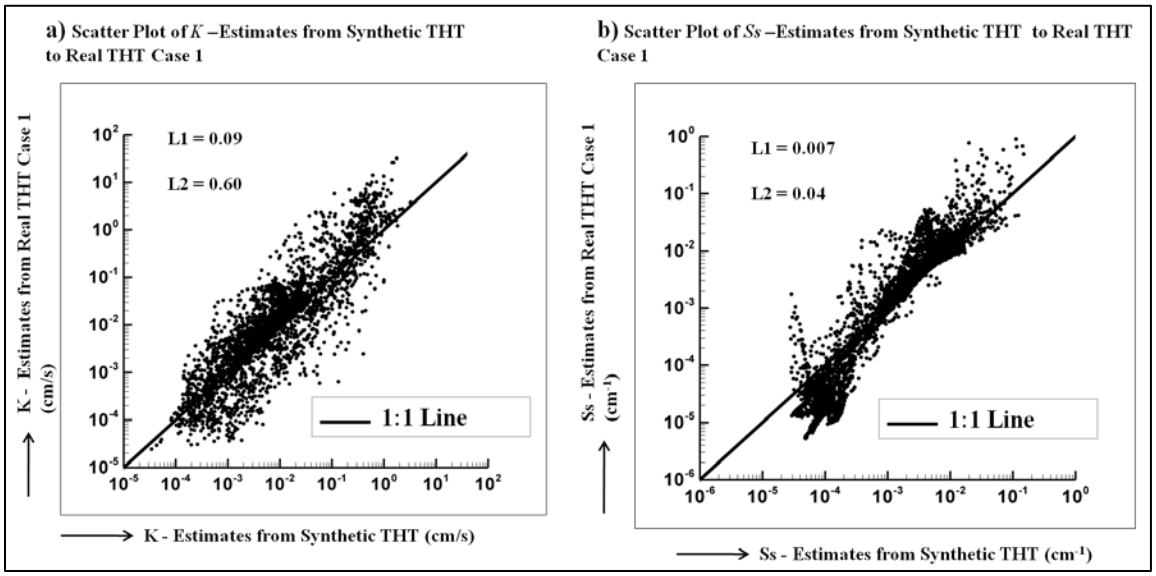

Figure 6.1: Scatter plots of (a) *K* and (b) S_s values from Synthetic THT to THT analysis of laboratory data (THT case1). The solid line represents the 1:1 line.

6.2 Performance assessment of THT analysis of Laboratory data in imaging fractured rock

Here, the performance of the THT analysis of laboratory data (real THT case 1 and real THT case 2) is assessed by - 1) visual assessment of estimated *K* and S_s patterns generated by 2 real THT cases; 2) comparison of *K* and S_s estimates obtained from two real THT cases; 3) comparison of estimated *K* values obtained from the THT analysis of laboratory pumping tests to those obtained from the flow through tests; 4) simulating the pumping tests that were used for the construction of THT cases using the estimated *K* and S_s tomograms and comparing the simulated drawdowns to the observed (i.e., calibration); and 5) simulating 5 independent pumping tests that were not included in inversion using the estimated *K* and S_s tomograms and comparing the simulated drawdowns to the observed (i.e.,

prediction). For both the calibrations and predictions the simulated and observed drawdown from each pumping test are quantitatively compared by estimating corresponding R^2 values, mean absolute error (*L1*) and the mean square error (*L2*) norms along with qualitative assessment to evaluate how well fractured block is captured by THT analysis based on the inverse algorithm SSLE.

6.2.1 Visual Assessment

The estimated K and S_s pattern generated by 2 THT cases are visually compared with the photograph of the fractured dolostone (Figure 2.2) to evaluate how well the fracture pattern is captured by THT analysis based on the SSLE code. The visual comparison of snapshot of the fractured dolostone (Figure 2.2) and estimated K and S_s tomograms (Figure 5.3; Figure 5.4; Figure 5.5 and Figure 5.6) reveal that the transient hydraulic tomography (THT) analysis of the laboratory pumping tests captured the fracture pattern and their connectivity quite well. The high K – zone in Figure 5.3a; b; c (case 1) and Figure 5.5a; b; c (case 2) and low S_s – zone in Figure 5.4a; b; c (case 1) and Figure 5.6a; b; c (case 2) clearly show the fractures and their connectivity, although the high K and low S_s zone do not continue to the edge of the rock, which may be due to the boundary effect, as pointed out earlier.

6.2.2 Comparison of K and S_s Estimates from two real THT Cases

Here the K and S_s tomograms generated by real THT case 1 are compared to the ones generated by real THT case 2 to evaluate if there is any significant impact of the location of pumped port on the estimates. Visual assessment reveals that the patterns of estimated K and S_s tomograms in case 1 (Figure 5.3 and Figure 5.4) and case 2 (Figure 5.5 and Figure 5.6) are similar, although the locations of 2^{nd} and 3^{rd} pumping tests utilized for the inversion were different for these two cases.

Figure 6.2a and b represent the scatter plots of K and S_s values, respectively, from real THT Case 1 to Case 2. The solid line represents the 1:1 line. From Figure 6.2a and b it can be seen that the data points cluster around the 1:1 line with some bias indicating a good fit between the K and S_s estimates from Case 1 and Case 2.

Two criteria, the average absolute error norm *(L1)* and the mean squared error norm *(L2)* were used to quantitatively evaluate the goodness-of-fit between the two sets of tomograms. Corresponding *L1* and *L2* norms for the *K* and *Ss* estimates are included on each scatter plot

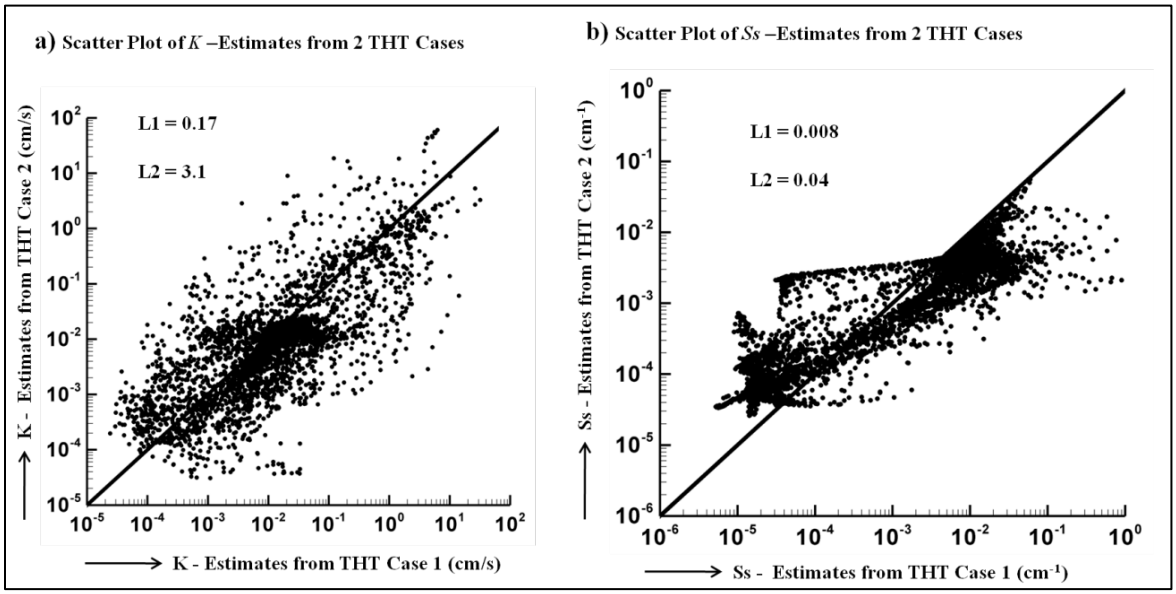

Figure 6.2: Scatter plots of (a) K and (b) Ss values from Case 1 to Case 2. The solid line represents the 1:1 line.

These results indicate that the changing the location of the 2nd and 3rd pumping tests do not significantly impact the estimates from hydraulic tomography in this fractured rock block. A similar observation was noted by *Illman et al*. (2009). However, the first pumping test (1st data set) included to the inverse model must be selected carefully, as the choice of the first pumping test seems to set that pattern of the estimates in this case. Here the pumping test at port 5 (Figure 4.3) was inverted 1st during all the THT cases. As described in section 4.2.2, pumping test at port 5 (Figure 4.3) had the highest flow rate and stressed all the fractures more or less as it is located approximately at the middle of the fractured block. *Illman et al.* [2008] also showed a similar finding. They found that including the data with the highest signal-to-noise ratio first into the HT code improve the results. The main reason behind it could be that SSLE updates the tomogram after each iteration and uses a weighted linear combination of the differences between the simulated and observed pressure heads to improve the estimates. Therefore, the K and S_s distribution estimated in the beginning of inversion process significantly impact the estimated tomograms.

6.2.3 Comparison of estimated *K* values obtained from real THT cases with the ones obtained from the flow through tests

To quantitatively compare the K estimates from real THT cases with the effective hydraulic conductivity (K_{eff}) obtained from flow-through tests, the geometric mean of K estimates obtained from

each of the two real THT cases was calculated. The comparison is presented in Table 6-1, which reveals that the geometric mean of THT *K* estimates and effective hydraulic conductivity values obtained from the flow-through tests are similar.

Table 6-1: Comparison of THT *K* Estimates with the Effective *K* obtained from Flow-through Tests

	Flow-Through Test 1	Flow-Through Test 2	Flow-Through Test 3	Flow-Through Test 4
Estimated Effective K_{eff} (Flow-through Test) (cm/s)	1.70×10^{-2}	1.30×10^{-2}	1.50×10^{-2}	1.30×10^{-2}
Geometric Mean of Estimated *K* (real THT Case 1) (cm/s)	1.30×10^{-2}			
Geometric Mean of Estimated *K* (real THT Case 2) (cm/s)	1.00×10^{-2}			

6.2.4 THT Calibration

The *K* and S_s tomograms estimated from the two THT cases were used to reproduce the three pumping tests (tests at ports 5, 7 and 3 in real THT case 1 and tests at 5, 16 and 19 in case 2), that were used for their creation. Forward simulations were performed using SSLE [*Zhu and Yeh* 2005] and the model domain used for the simulation was same as the one used for inversion, which is described in section 4.2.1.

Comparisons of observed and calibrated drawdown curves in real THT case 1 are presented in Figure 6.3; Figure 6.4; and Figure 6.5. Figure 6.3 represents the observed and simulated drawdown curves at the monitoring ports during the pumping test at port 5. The solid line represents observed drawdown curve while the dashed line represents calibrated drawdown curve. Drawdown data that were input into the THT algorithm are also included in this plot as the black circles. Similar comparisons of observed and simulated drawdown curves at the monitoring ports during the pumping tests at ports 7 and 3 for case 1 are provided in Figure 6.4 and Figure 6.5 respectively.

Good matches between the observed and calibrated drawdown curves at the monitoring intervals were obtained during all three pumping tests in real THT case 1. However, the observed and

simulated drawdowns during the tests at ports 7 and 3 seemed to match better in comparison to the ones during the test at port 5, which was the 1st test included in the inversion. As no looping was conducted during the inversion, estimates from the later tests (pumping tests at ports 7 and 3) became dominant, leading to a better match between the observed and simulated drawdown during the tests at ports 7 and 3. However, for the calibrated pumping tests, there was no drawdown at the matrix ports, which was consistent with the observed cases.

Similar plots comparing the observed and calibrated drawdown curves in real THT case-2 presented in Appendix D also showed good matches between the observed and simulated drawdown curves at the monitoring intervals during the calibrated pumping tests. Thus overall, simulated drawdown responses using K and S_s tomograms estimated by THT captured the observed drawdown behaviors in the monitoring ports quite well, indicating that THT did a good job in capturing the fracture pattern and their connectivity.

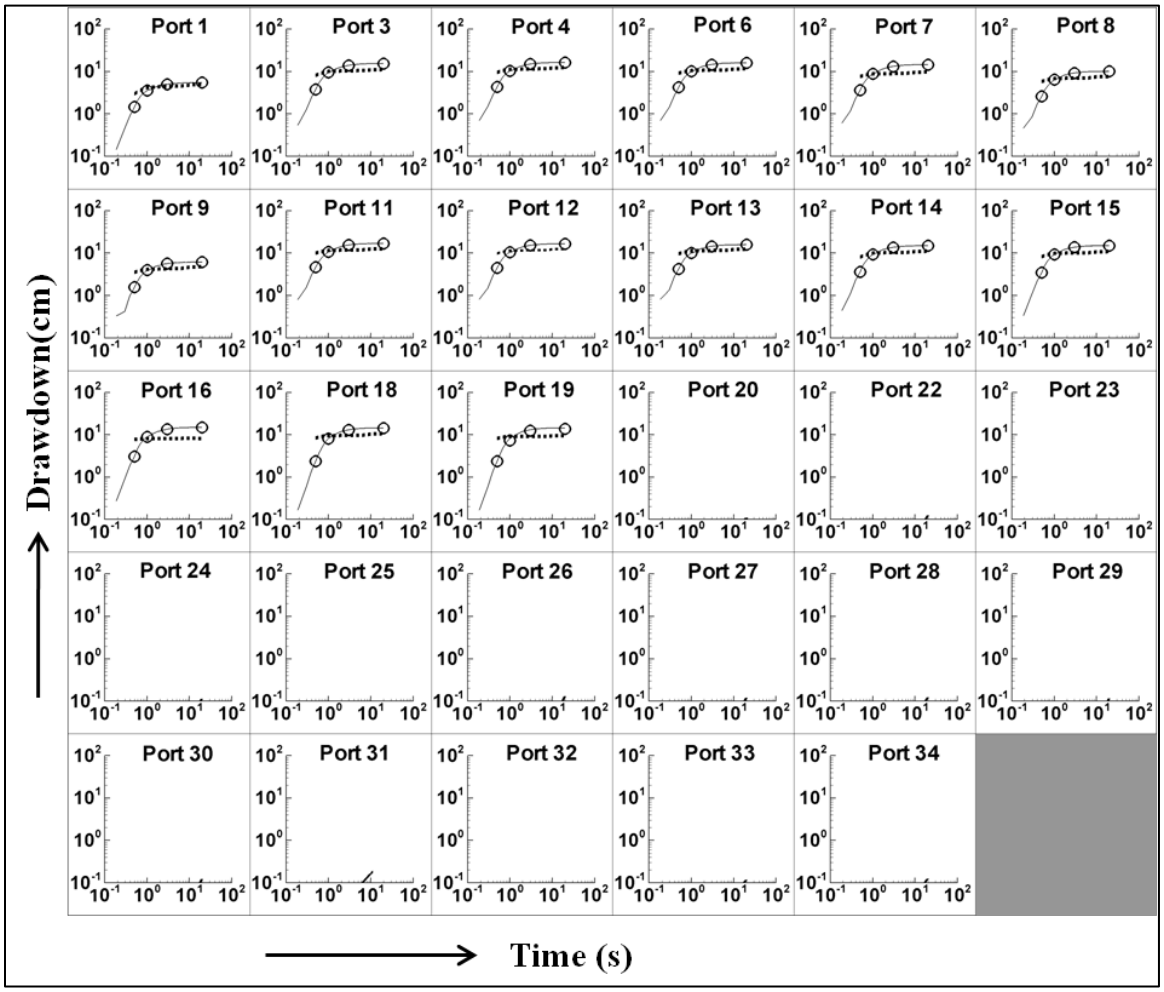

Figure 6.3: Observed and Calibrated Drawdown (cm) versus Time (s) at the monitoring ports during the Pumping Test at Port 5 in real THT Case 1. The solid line represents observed drawdown curve while the dashed line represents calibrated drawdown curve. The black circles indicate the match points.

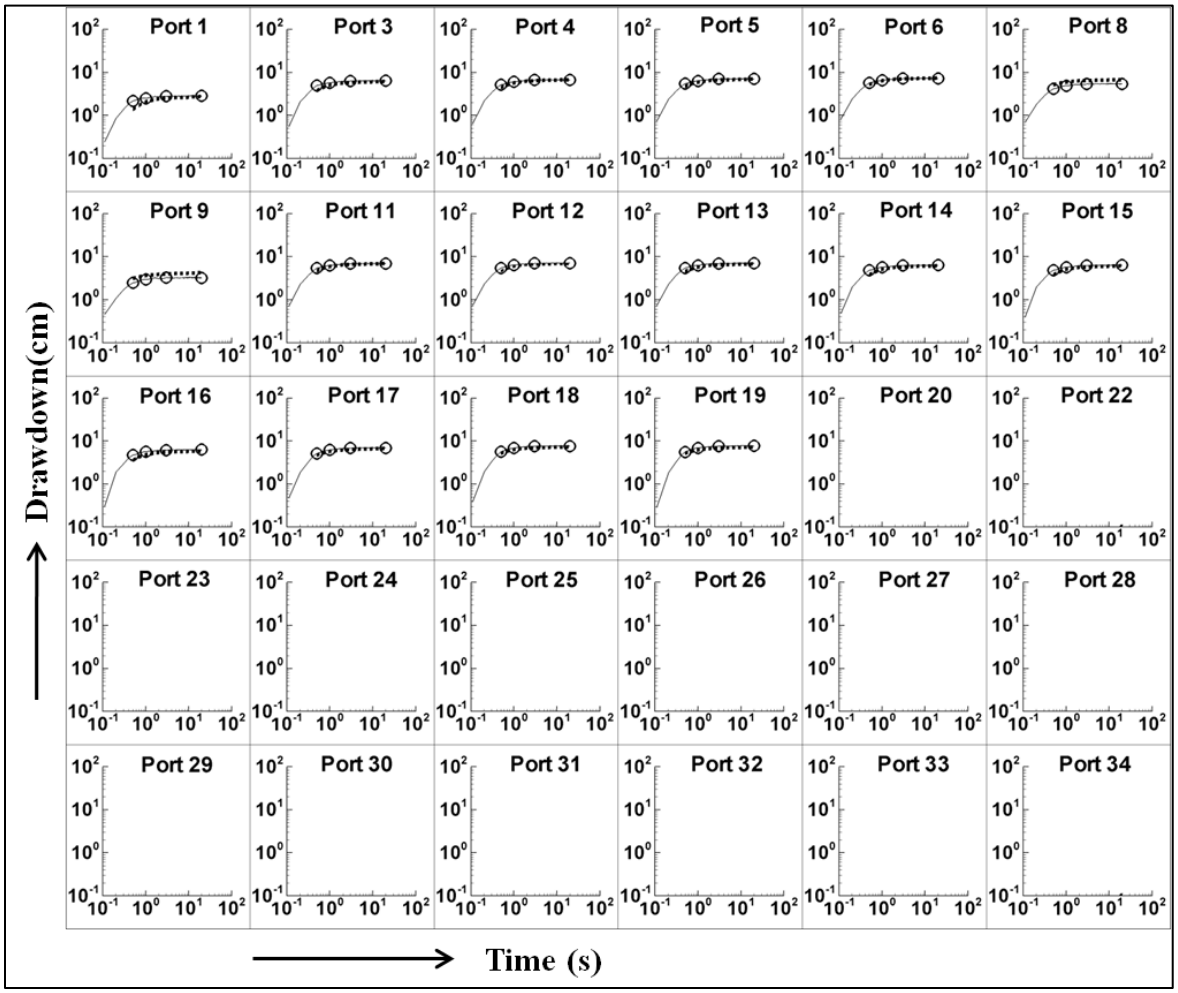

Figure 6.4: Observed and Calibrated Drawdown (cm) versus Time (s) at the monitoring ports during the Pumping Test at Port 7 in real THT Case 1. The solid line represents observed drawdown curve while the dashed line represents calibrated drawdown curve. The black circles indicate the match points.

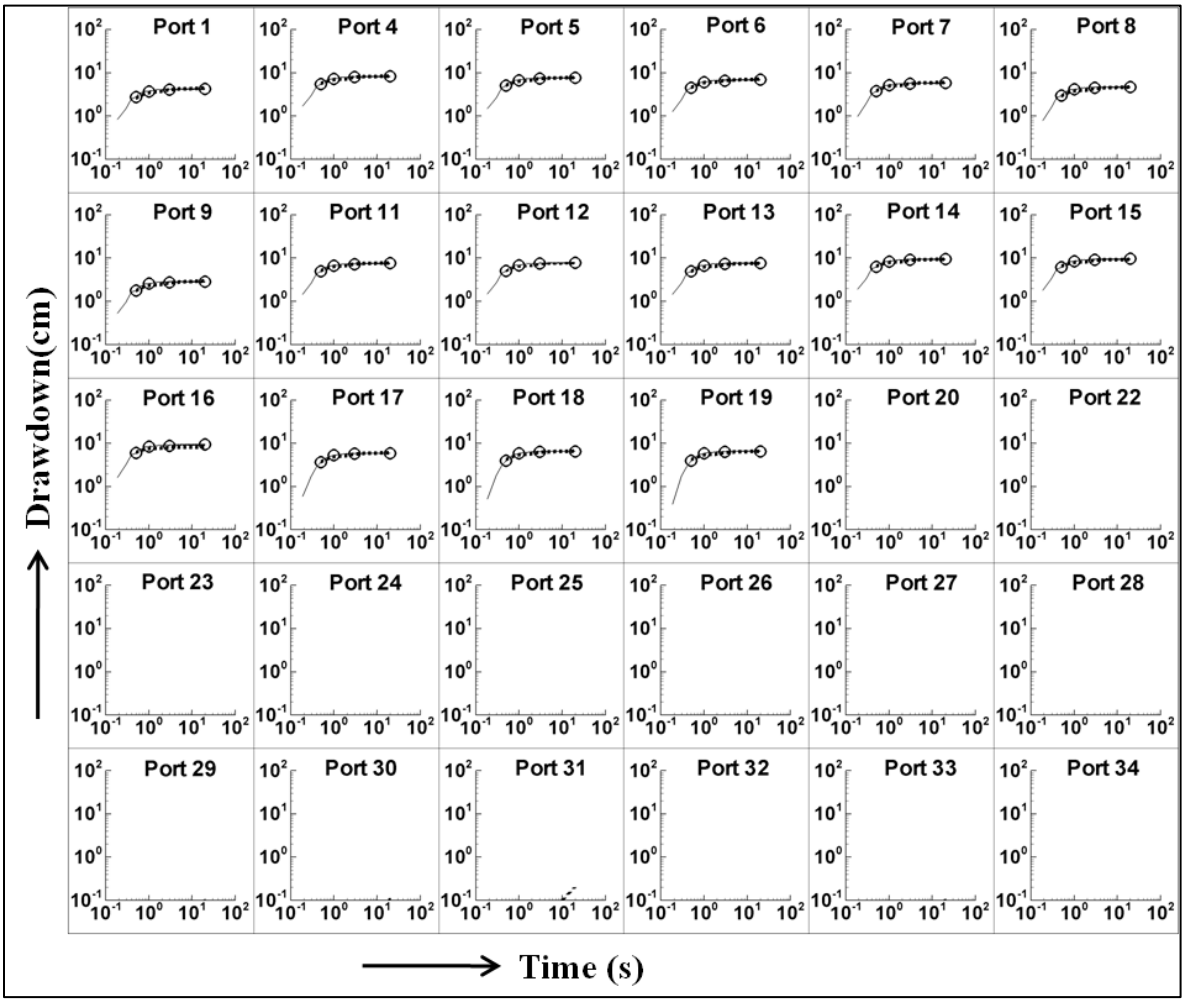

Figure 6.5: Observed and Calibrated Drawdown (cm) versus Time (s) at the monitoring ports during the Pumping Test at Port 3 in real THT Case 1. The solid line represents observed drawdown curve while the dashed line represents calibrated drawdown curve. The black circles indicate the match points.

Figure 6.6 represents the scatter plots of observed versus simulated drawdowns from the 3 pumping tests that were utilized for the construction of real THT case 1. The pumped port is mentioned in bold letters on each plot. The solid line is a 1:1 line indicating a perfect match. The dashed line is a best fit line, and the parameters describing this line, coefficient of determination (R^2) as well as *L2* norm for the corresponding tests are included on each plot.

R^2 values indicate the quality of match between the simulated and observed drawdowns. Two data sets are considered to have a high correlation when the R^2 value is close to 1 and the data set clusters

around the 1:1 line. The slope and the intercept of the linear model fit are the indication of bias. Similar calibration scatter plots for THT case 2 can be found in Appendix D.

From Figure 6.6, it can be seen that for the test at port 5 the points cluster around the 1:1 with some bias and the linear model fit indicates that the simulated drawdowns underestimate the observed. For the 2nd (test at port 7) and 3rd (test at port 3) pumping tests, the estimated drawdown was found to improve significantly. Improvement can be seen clearly from the plots as the data points cluster around the 1:1 line and the linear model fit almost overlaps the 1:1 line for the tests at port 7 and 3. Corresponding R^2 values also indicate a good correlation between observed and calibrated drawdowns. The larger the R^2 values, the more closely the estimates agree. The matches observed for the calibration scatter plots for real THT case 2 provided in Appendix D are similar to those for real THT case 1. However, in case 2 is the pumping tests at port 16 (2nd test) and port 19 (3rd test) had poorer match than the 2nd and 3rd pumping tests in real THT case 1.

To further quantitatively compare the simulated and observed drawdown values, the mean absolute error (*L1*) and the mean square error (*L2*) norms were calculated using equations *(9)* and *(10)* respectively, for the pumping tests used for the construction of two real THT cases. To compute the *L1* and *L2* norms, observed and simulated drawdown were evaluated at each monitoring port. The *L1* and *L2* norms and corresponding R^2 values for the pumping tests utilized for real THT case 1 and case 2 are presented in Table 6-2 and Table 6-3 respectively. The smaller the *L1* and *L2* norms and larger R^2 values are the more consistent are the estimates. In Table 6-2 and Table 6-3, the *L1* and *L2* norms appear to be the largest for the pumping test that was inverted 1st, and found to improve significantly with the addition of each test, which is consistent with the R^2 values, indicating a better match between the observed and simulated drawdown for the later pumping tests (tests at port 7 and 3). This is attributed to the fact that no looping was conducted during the inversion and therefore the estimates from the later tests (pumping tests at ports 7 and 3) became more dominant, leading to a better match between the observed and simulated drawdowns during the tests at ports 7 and 3.

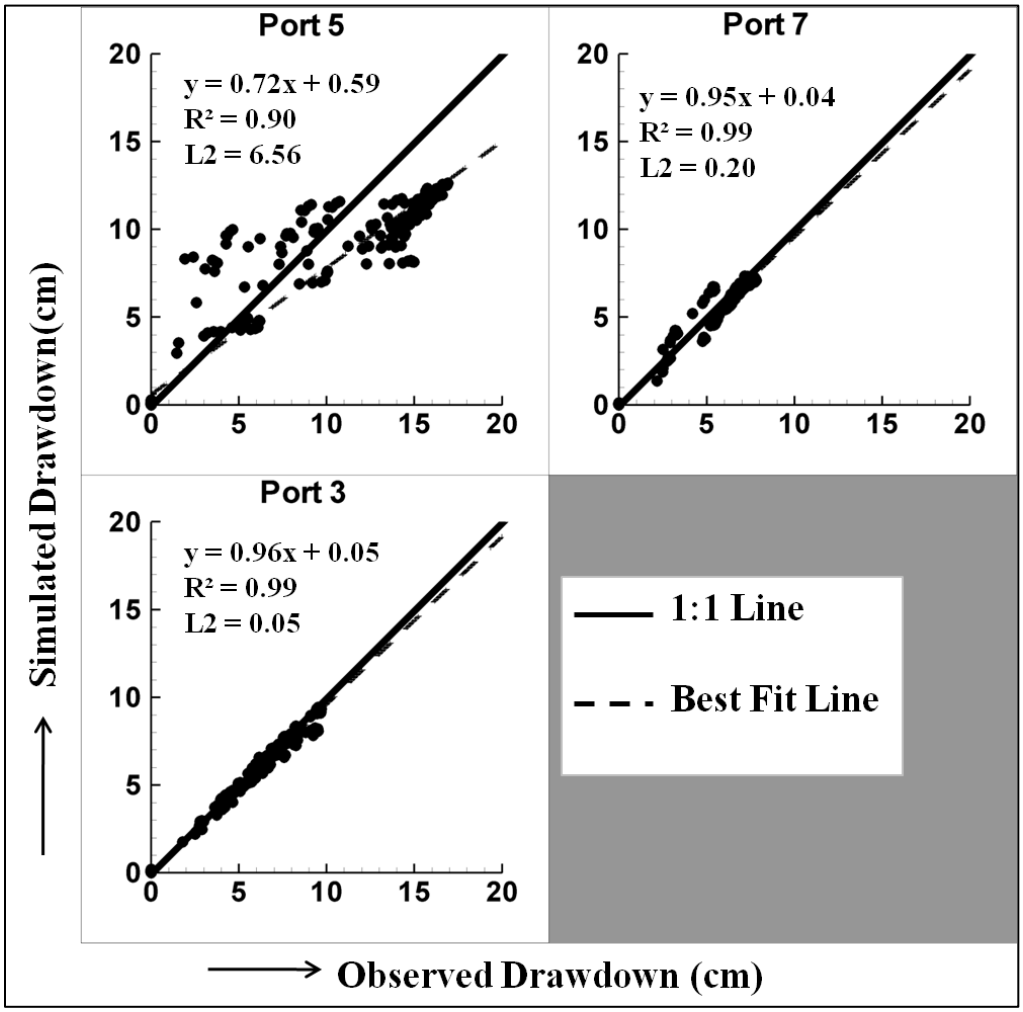

Figure 6.6: Calibration Scatter plots for real THT Cases 1. The pumped port is shown in bold letters on each plot. The solid line is a 1:1 line indicating a perfect match. The dashed line is a best fit line, and the parameters describing this line as well as *L2* norm for the corresponding tests are on each plot.

Table 6-2: *L1, L2* norms and R^2 values of observed versus simulated drawdown from pumping Tests at Ports 5, 7 and 3 (Case 1)

Pumped Port	L1	L2	R^2
Port 5	1.60	6.56	0.90
Port 7	0.29	0.20	0.99
Port3	0.12	0.05	0.99

Table 6-3: *L1, L2* norms and R^2 values of observed versus simulated drawdown from pumping Tests at Ports 5, 16 and 19 (Case 2)

Pumped Port	L1	L2	R^2
Port 5	1.62	6.58	0.86
Port 16	0.34	0.29	0.92
Port 19	0.31	0.72	0.94

6.2.5 Prediction of Pumping Tests Using Estimated *K* and S_s Tomograms from real THT cases

The K and S_s tomograms estimated for the two real THT cases were used to predict 5 pumping tests (tests at ports 4, 6, 12, 15 and 18), that were not used in the construction of the tomograms, also referred to as independent pumping tests. Forward simulations were performed using SSLE [*Zhu and Yeh* 2005] and the model domain was same as the one used for the inversion, which is described in section 4.2.1.

Comparisons of observed and predicted drawdown curves in real THT case 1 are presented in Figure 6.7 (test at port 4); Figure 6.8 (test at port 6); Figure 6.9 (test at port 12); Figure 6.10 (test at port 15) and Figure 6.11 (test at port 18). The solid line represents observed drawdown curve while the dashed line represents the drawdown predicted by the THT tomograms. Similar plots comparing the observed and predicted drawdown curves for the 5 pumping tests for case-2 are included in Appendix D.

Examination of Figure 6.7; Figure 6.8; Figure 6.9; Figure 6.10 and Figure 6.11 reveals that, during the independent tests, the simulated drawdown matched the observed for most of the monitoring intervals, but there are some exceptions for ports near the pumped port due to excessive noise resulting from pumping. However, the simulated and observed drawdowns seem to match better at later time. At early time, some of the matches are poor and some are of intermediate to fair quality. The drawdown is controlled by the specific storage (S_s) at early time and hydraulic conductivity (K) at late time. As discussed earlier, estimated tomograms do not exactly replicate the actual values for the fractured rock, which led to these deviations between observed and predicted drawdowns. However, there was no drawdown (real THT case 1) or a very small drawdown (real THT case 2) at the matrix ports for the simulated cases, which was consistent with the observed matrix drawdown.

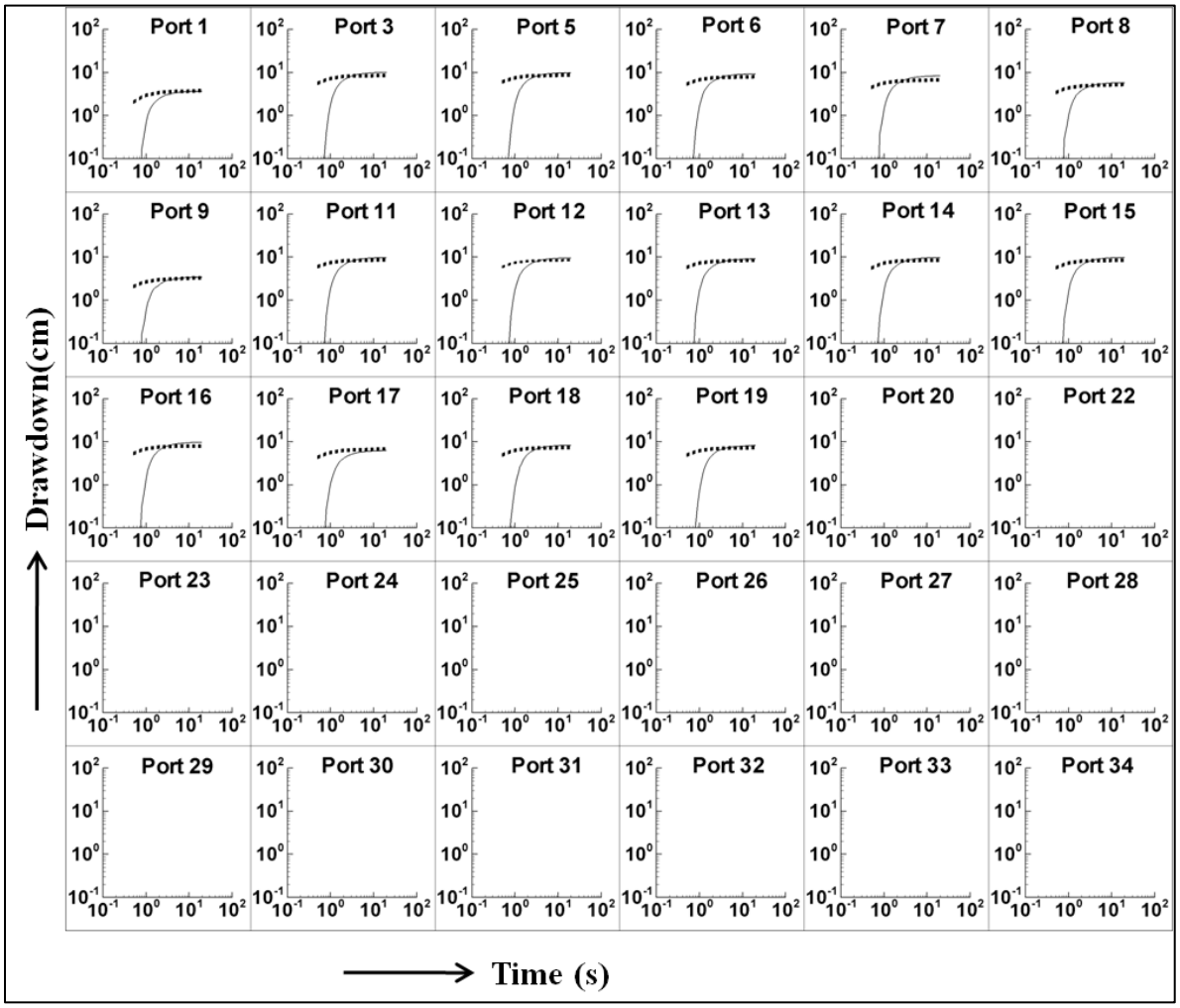

Figure 6.7: Observed and Predicted Drawdown (cm) versus Time (s) at the monitoring ports during the Pumping Test at Port 4 in Case 1. The solid line represents observed drawdown curve while the dashed line represents predicted drawdown curve.

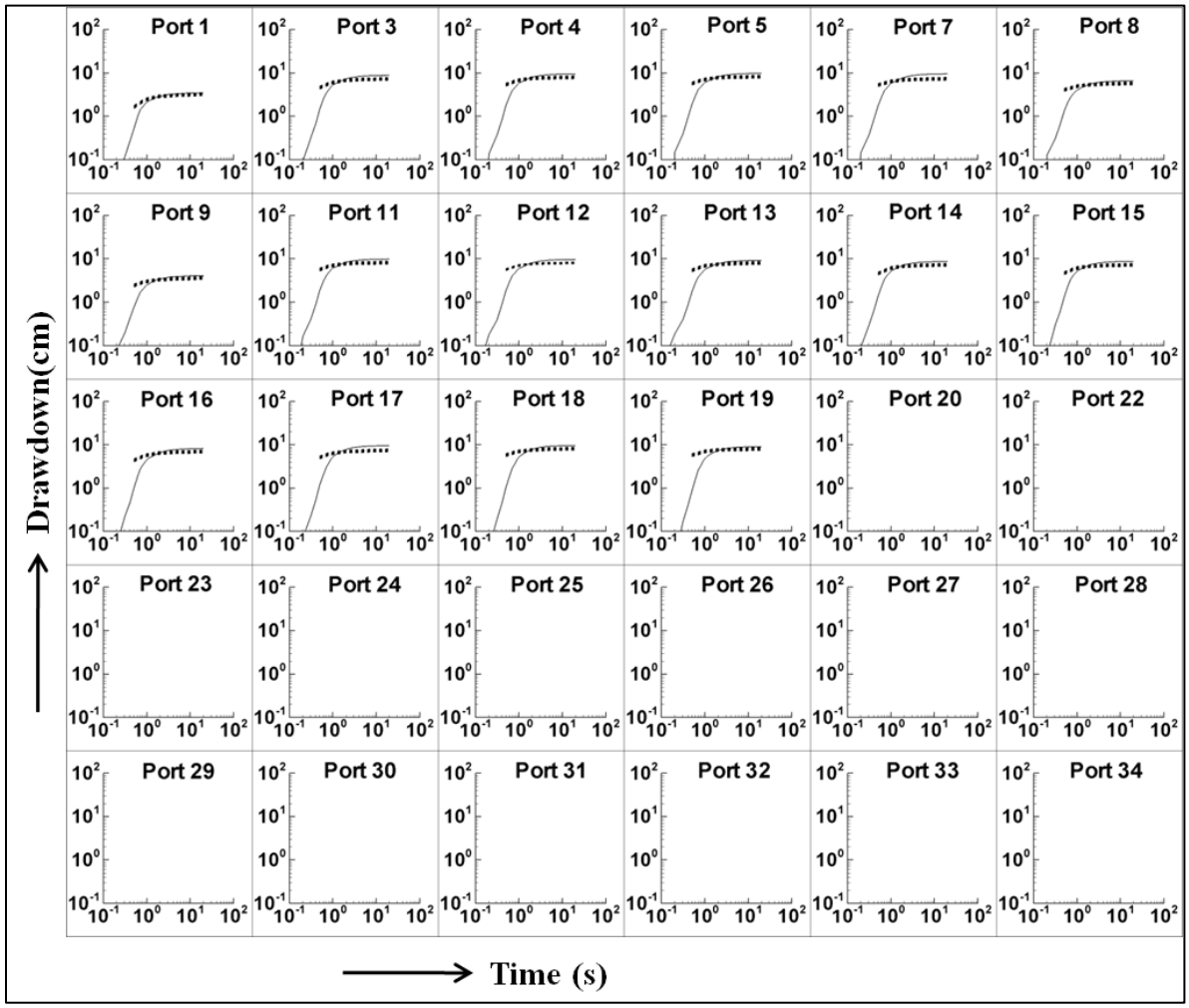

Figure 6.8: Observed and Predicted Drawdown (cm) versus Time (s) at the monitoring ports during the Pumping Test at Port 6 in Case 1. The solid line represents observed drawdown curve while the dashed line represents predicted drawdown curve.

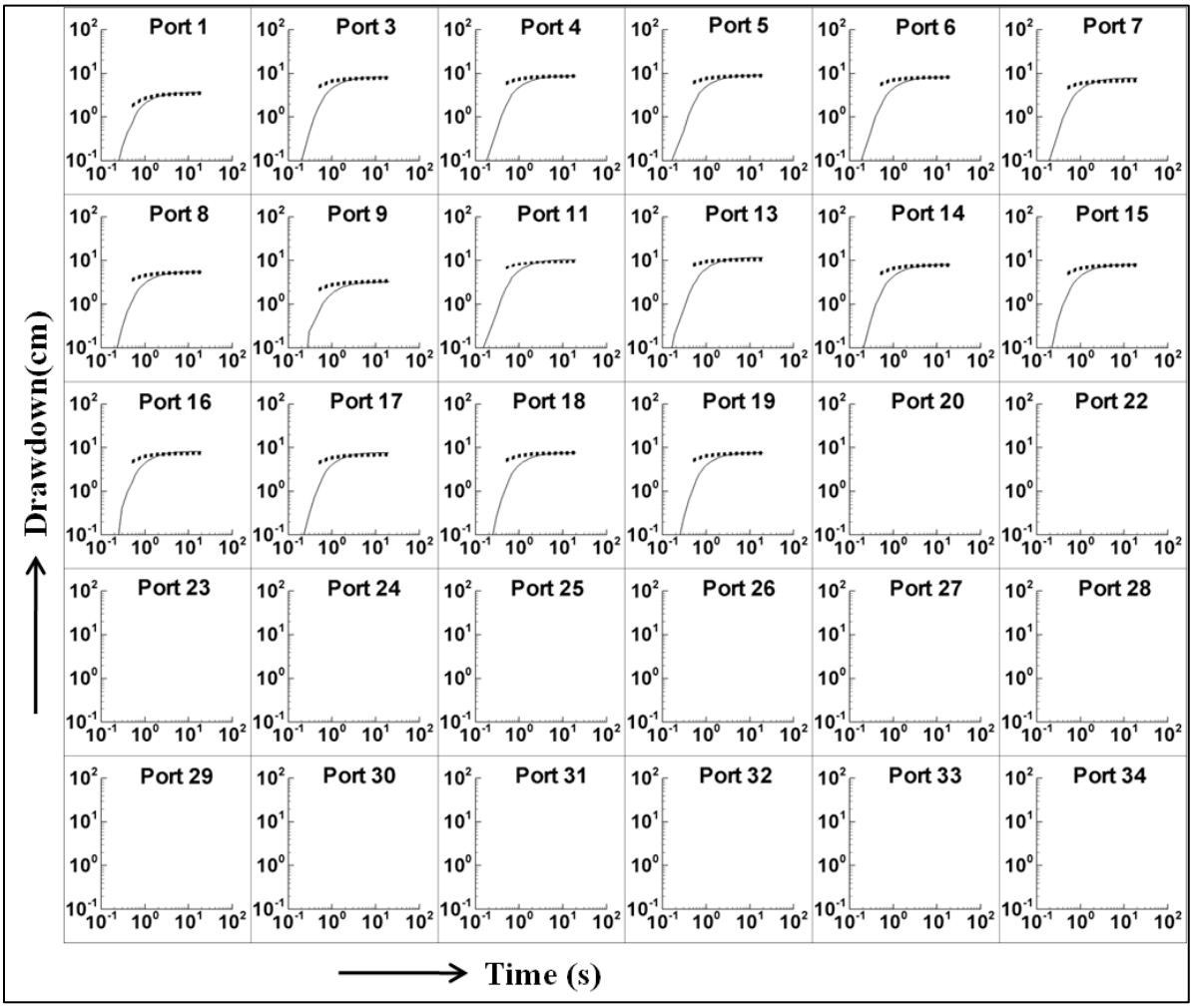

Figure 6.9: Observed and Predicted Drawdown (cm) versus Time (s) at the monitoring ports during the Pumping Test at Port 12 in Case 1. The solid line represents observed drawdown curve while the dashed line represents predicted drawdown curve.

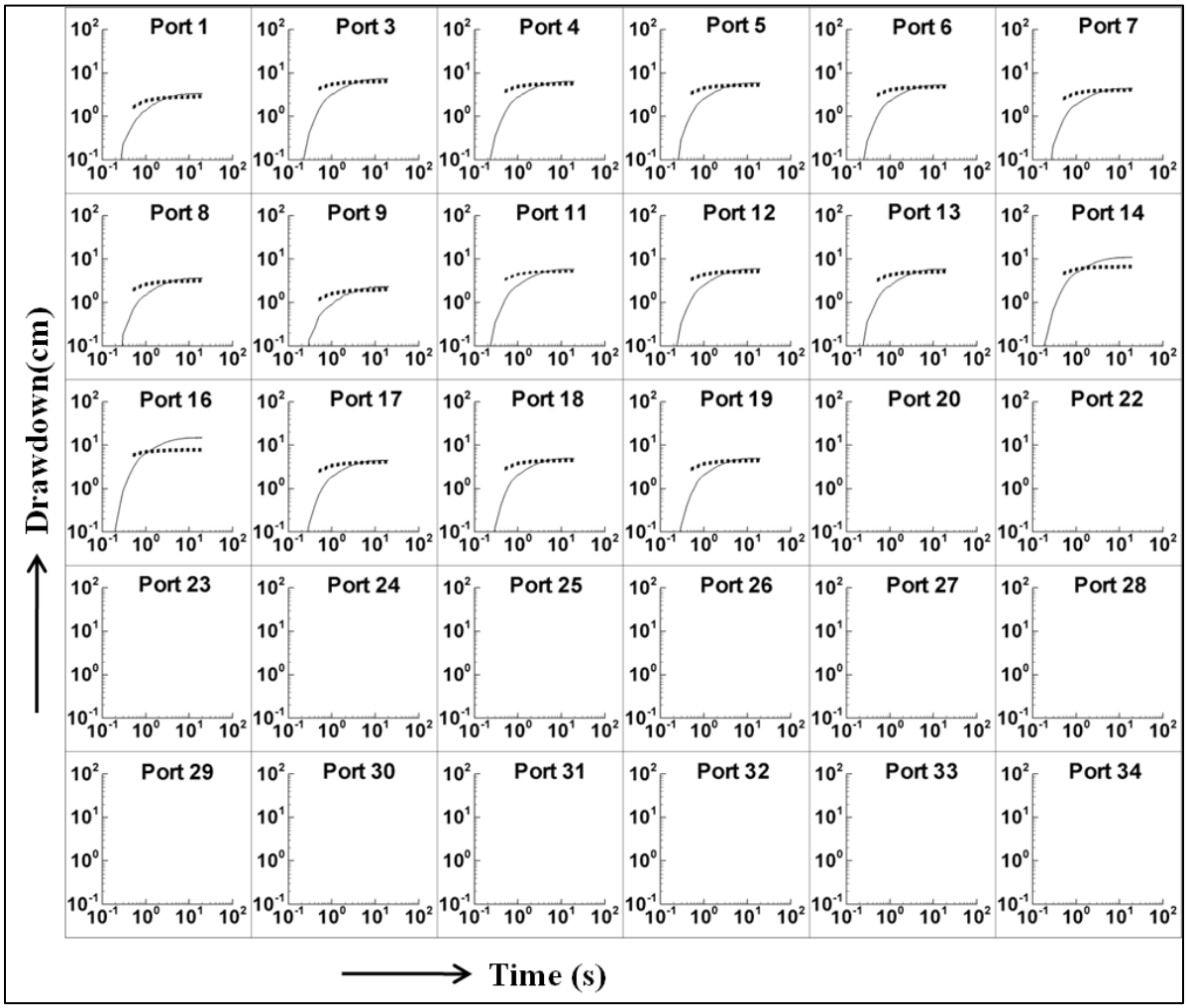

Figure 6.10: Observed and Predicted Drawdown (cm) versus Time (s) at the monitoring ports during the Pumping Test at Port 15 in Case 1. The solid line represents observed drawdown curve while the dashed line represents predicted drawdown curve.

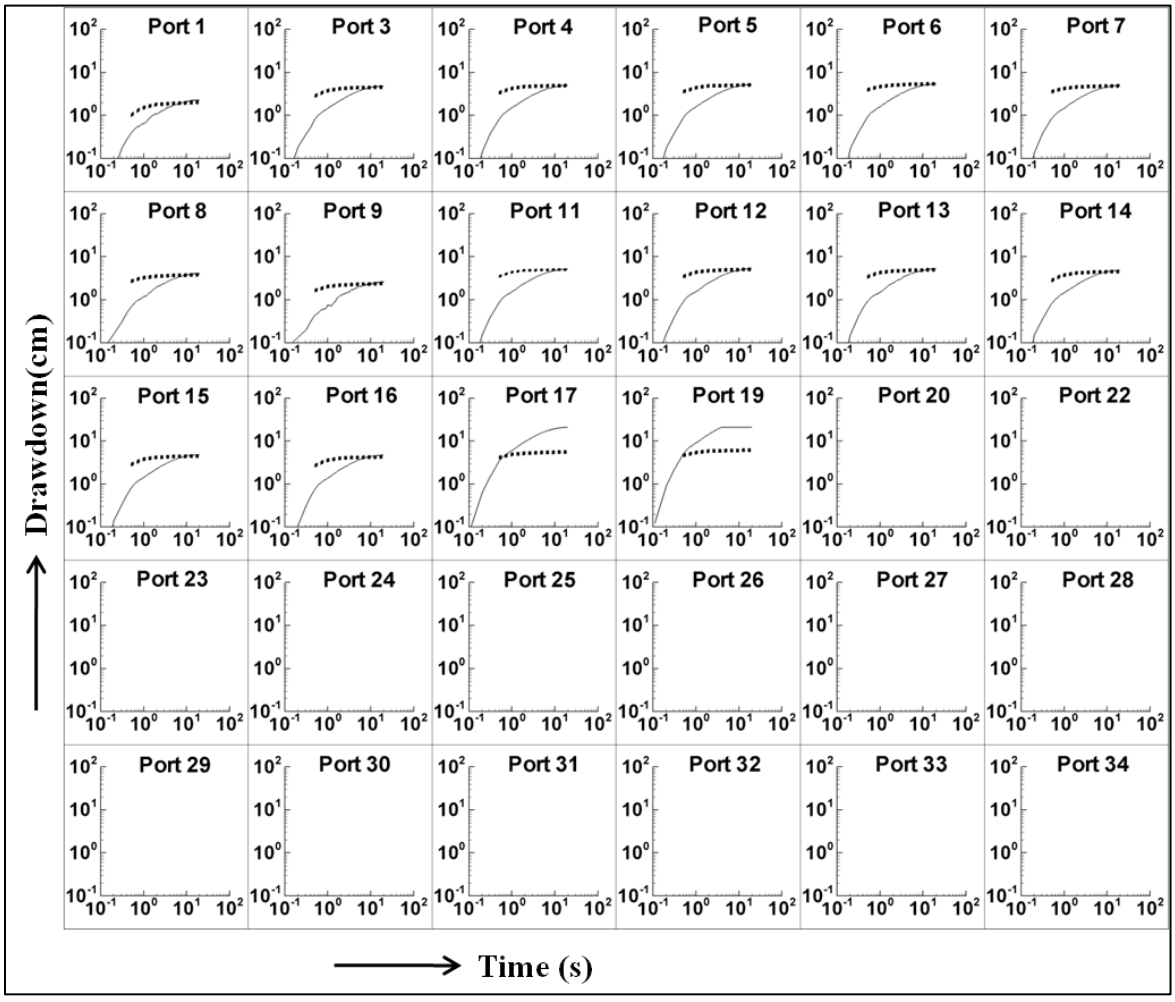

Figure 6.11: Observed and Predicted Drawdown (cm) versus Time (s) at the monitoring ports during the Pumping Test at Port 18 in Case 1. The solid line represents observed drawdown curve while the dashed line represents predicted drawdown curve.

Figure 6.12 shows the scatter plots of observed versus simulated drawdowns for the 5 independent pumping tests for real THT case 1. The pumped port is shown in bold letters on each plot. The solid line is the 1:1 line indicating a perfect match. The dashed line is a best fit line, and the parameters describing this line, coefficient of determination (R^2) as well as *L2* norm for the corresponding tests are included on each plot. Similar scatter plots for the independent pumping tests for real THT case 2 can be found in Appendix D.

From Figure 6.12, it can be seen that for most tests the data points cluster around the 1:1 line with some bias indicated by the slope of the linear model fit. The only exception is the pumping test at port

18, suggesting comparatively poor estimates for the pumping test at that port. The scatter plots for the independent tests in real THT case 2 provided in Appendix D also show similar matches between the observed and simulated drawdowns. Corresponding R^2 values also indicate a good correlation between observed and predicted drawdowns. The larger the R^2 values, the more closely the estimates agree.

To further quantitatively compare the simulated and observed drawdown values, the mean absolute error (*L1*) and the mean square error (*L2*) norms were calculated for each of the 5 predicted pumping tests using the same procedure described in section 6.1. To compute the *L1* and *L2* norms the observed and simulated drawdowns were evaluated at each monitoring port. The *L1* and *L2* norms as well as R^2 values for the predicted pumping tests in real THT case 1 and case 2 are presented in Table 6-4 and Table 6-5 respectively. The smaller the *L1* and *L2* norms and the larger the R^2 values, the better the matches between the observed and simulated drawdown.

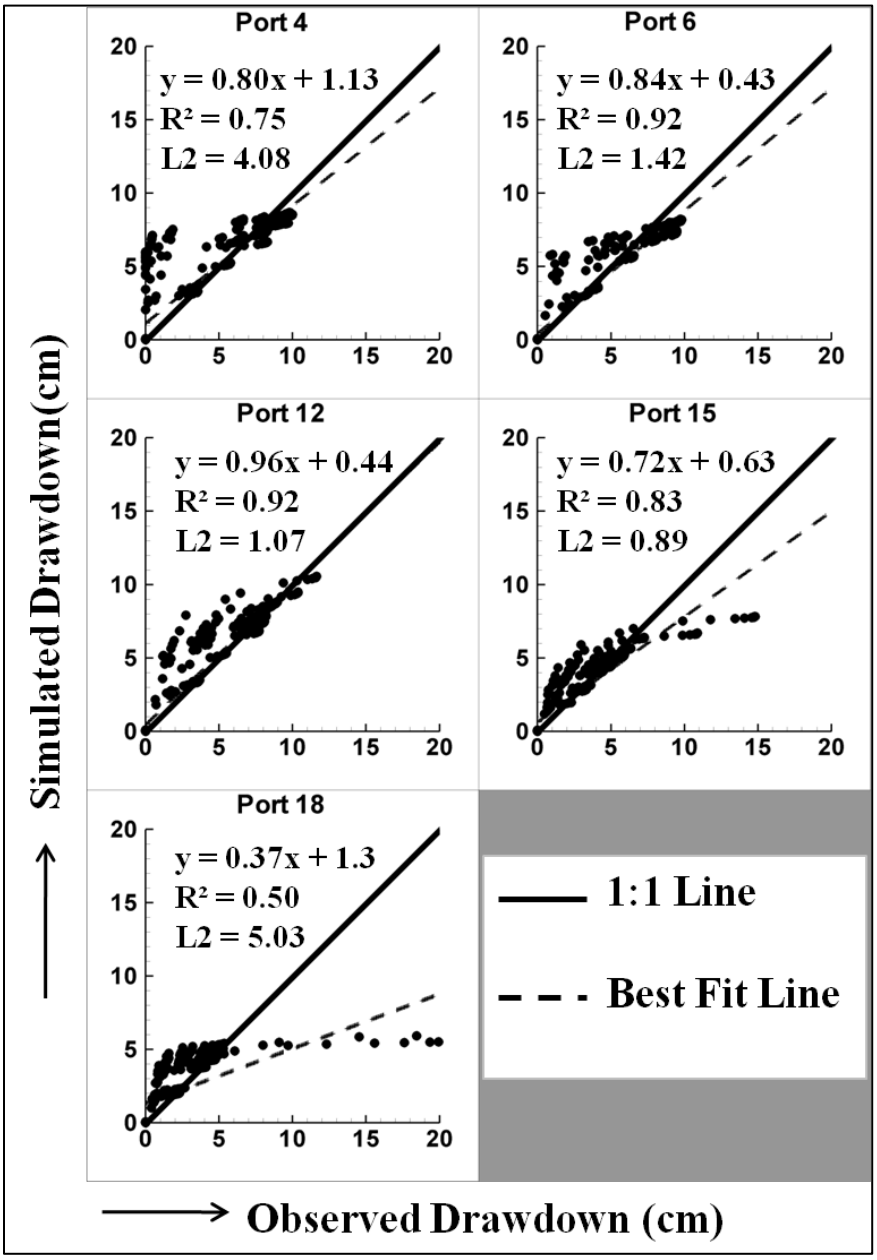

Figure 6.12: Validation Scatter plots for real THT Cases 1. The pumped port is shown in bold letters on each plot. The solid line is a 1:1 line indicating a perfect match. The dashed line is a best fit line, and the parameters describing this line as well as *L2* norm for the corresponding tests are on each plot.

Table 6-4: *L1*, *L2* norms and R^2 values of observed versus simulated drawdown from pumping Tests at Ports 4, 6, 12, 15 and 18 (Case 1)

Pumped Port	L1	L2	R^2
Port 4	1.04	4.08	0.75
Port 6	0.75	1.42	0.92
Port 12	0.48	1.07	0.92
Port 15	0.50	0.89	0.83
Port 18	0.82	5.03	0.50

Table 6-5: *L1*, *L2* norms and R^2 values of observed versus simulated drawdown from pumping Tests at Ports 4, 6, 12, 15 and 18 (Case 2)

Pumped Port	L1	L2	R^2
Port 4	1.45	5.21	0.85
Port 6	1.28	4.20	0.88
Port 12	1.32	4.82	0.89
Port 15	0.59	1.05	0.88
Port 18	0.97	2.74	0.93

SSLE being a porous media code, it is difficult to handle the high contrast between the fracture and matrix hydraulic conductivity (K) and specific storage (S_s) values for the model. Therefore, the estimated K and S_s values for the fractures and the matrix may not exactly replicate actual values, which led to the deviation in the drawdown responses at the monitoring intervals during some of the pumping tests. But for most cases, simulated drawdown responses captured the observed drawdown behaviors in the monitoring ports quite well, indicating that THT analysis of the laboratory data did a good job in capturing the geometry of the fractured block, which is encouraging. Based on this study it can be said that hydraulic tomography appears to be a promising tool to delineate fracture pattern and their connectivity, which has been a challenge for hydrogeologists for decades. The advantage of

HT is that, it does not require the accurate measurements of the fracture size, shape, aperture, detailed deterministic or statistical information of the geometry of fractured zone and the spatial distribution of fracture apertures; the information typically not available between boreholes. Rather, THT relies on pumping test data, which are relatively easy to collect and comparatively less expensive. Thus, THT holds a significant potential as a fractured rock characterization tool.

Illman et al. [2007] discusses the non-uniqueness of estimated *K*-tomograms, as there could be an infinite number of solutions to the steady-state inverse problem for a heterogeneous *K* field, even when all of the forcing functions are fully specified. Similarly non-uniqueness of computed heterogeneous *K* and S_s field could also be an issue for the transient inverse problem. But this is not the case here. *Yeh et al.* [1996]; *Yeh and Liu,* [2000]; *Liu et al.* [2002] and *Yeh and Simunek* [2002] argue that when data are available at all estimated locations, the inverse problem becomes well-posed and ultimately lead to a unique solution. Moreover, *Yeh et al.* [2011] suggest that the problem of non-unique solution arises from a lack of information required to make the problems well defined. They also suggest the necessary conditions for a inverse model of groundwater flow to be well defined, which are presented here after *Yeh et al.* [2011] –"*full specifications of 1) flux boundaries and source/sink, and 2) heads everywhere in the domain at least at three times (one of which is t=0) and head change everywhere over the times must be nonzero for transient flow*". They examined through numerical experiments that when the necessary conditions are fulfilled, the inverse problem results to a unique solution. Here THT analysis of multiple pumping tests was conducted, thus making more data available for analysis than typical pumping test. The method is robust. Here it is visually confirmed that the *K* and S_s tomograms obtained from the inverse problem are consistent with the fracture patterns of the experimental block (Figure 2.2). In addition, estimated tomograms were validated through the prediction of independent pumping tests, which should provide more confidence in the solution of the inverse problem.

6.3 Conclusions and Findings from THT Analysis

This study leads to the following major findings and conclusions regarding the THT analysis of multiple pumping tests based on the inverse algorithm SSLE conducted in a fractured rock block in the laboratory.

It is possible to delineate discrete fractures, their pattern and connectivity by carefully applying THT analysis of multiple pumping tests along with the inverse code SSLE developed by *Zhu and Yeh*

[2005]. From the estimated K and S_s - tomograms obtained from THT analysis of laboratory and synthetic data, it is evident that THT captured the fracture pattern quite well and they became more distinct with addition of each test. Estimated K and S_s values for the fractures and the matrix may not exactly replicate the actual values but the model also provides uncertainty estimates associated with the resulting K and S_s tomograms, which are given in the corresponding variance maps. However, the purpose of the study was to capture the fracture pattern (the pattern of K and S_s tomograms) using THT, which has been achieved here. The high hydraulic conductivity (K) and low specific storage (S_s) zone clearly show the fractures and their connectivity, although the high K and Low S_s zone do not continue to the edge of the rock, may be due to the boundary effect.

Here two cases of transient hydraulic tomography (THT) analysis were performed using the laboratory pumping tests changing the location of 2nd and 3rd pumping tests to examine if there is any significant impact of these later pumping tests locations on the pattern of resulting hydraulic conductivity (K) and specific storage (S_s). Results show that the patterns of estimated K and S_s tomograms in real THT case 1 and case 2 are similar, although the pumped locations (2nd and 3rd test) utilized for the inversion were different for two cases. It indicates that, changing the location of 2nd and 3rd pumping tests does not have significantly impact on the estimates. However, the initial pumping test must be selected carefully as that seems to set the pattern of the estimated tomograms.

K and S_s tomograms generated by the real THT cases were used to simulate the pumping tests that were used for the construction of THT. These results revealed that the simulated drawdown responses captured the observed drawdown behavior quite well for most of the cases. 5 independent pumping tests (that were not included during the inversion) were also simulated using estimated K and S_s tomograms generated by each of the two real THT cases to evaluate to what extent they can predict independent pumping tests. For most cases, the predicted drawdown responses from the independent pumping tests captured the observed behavior at later time, while at early time predicted drawdown deviates from the observed for some tests. All the inverse simulations were run for 20 seconds and the matrix ports had no drawdown (in real THT case 1) or a very small drawdown (in real THT case 2) for all the calibrated and predicted cases, which was consistent with the observed data. SSLE being a porous media code, it is difficult for the model to handle the high contrast between the fracture and matrix hydraulic conductivity (K) and specific storage (S_s) values. Thus, estimated K and S_s values may not exactly replicate the actual values for the fractured rock, which leads to the little deviation in the simulated drawdown responses at the monitoring intervals. But overall, simulated drawdown

responses captured the observed behaviors both at the fracture and matrix ports quite well, indicating that the K and S_s tomograms estimated using THT successfully captured fracture pattern and their connectivity.

It can be concluded that the results from this study are encouraging in that the pattern of K and S_s tomograms generated by THT analysis based on the inverse algorithm SSLE, are consistent with the fracture pattern. THT appears to be a promising approach in delineating fractures and their connectivity in the subsurface. However, it is still at the early stage as the study was conducted based on the laboratory experiments in a controlled environment. Thus small scale field experiments need to be done to validate THT as a tool to characterize fractured rock.

Chapter 7
Tracer Tests

Upon completion of the hydraulic tests, two tracer tests were conducted using bromide (Br^-) as conservative tracer to aid in the design of Trichloroethene (TCE) dissolution experiment. The tracer tests and the results obtained from the tests are described in this chapter.

7.1 Description

The preparation of the flow cell has been described in section 2.2. Tracer tests were conducted by fixing the hydraulic gradient across the rock sample. The hydraulic gradient was fixed by setting drip points at the end reservoirs at different heights. A peristaltic pump was used to supply water continuously into the influent reservoir and the drip point was maintaining constant head in the influent and effluent reservoirs. Figure 7.1 represents the schematic diagram of the experimental set-up for the tracer experiments, where injection and all the sampling ports are indicated. Figure 7.2a shows the photograph of the flow cell and in Figure 7.2b injection and sampling ports on the horizontal fracture are indicated on the photograph with rectangular white box.

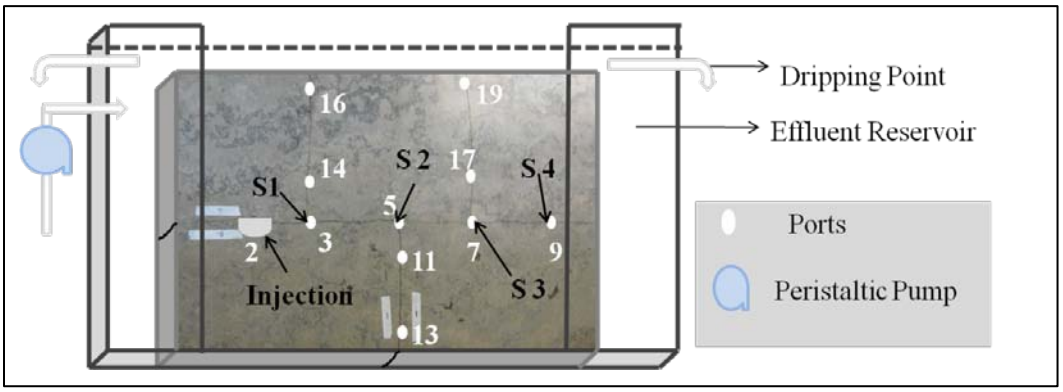

Figure 7.1: Schematic Diagram of the Experimental Set-up for the Tracer Experiments. The white ovals indicate the sampling ports. S1, S2, S3 and S4 are the four sampling ports.

Before injecting the tracer a steady flow field was established by fixing the hydraulic gradient across the rock sample and the flow rate was measured at the effluent dripping point. Once the flow field became stable, 100 mg/L bromide (Br^-) solution was injected into a hole below the flow path marked as "injection" (port 2) in Figure 7.1. The hole was made and filled with sand prior to the enclosure of the fractured block into the flow cell. Before the hole was filled with sand, the porosity

and hydraulic conductivity of the sand were measured in the laboratory, which were approximately 0.1 cm/s and 0.4 – 0.5 respectively. A brass fitting was placed on the rock to cover the hole using titanium putty (Devcon, Danvers, MA, USA). To hold the sand in place, a stainless steel mesh was placed underneath the brass fitting. The injection and sampling ports were equipped with Swagelok fittings (brass Swagelok tube fitting bored-through male connector, 1/16 in. Tube OD x 1/8 in. Male NPT) in order to hold the stainless steel needle used for injection or sample collection and a one-way luer stopcock to prevent any fluid loss while injecting or sampling. The bromide (Br^-) solution was injected into the sand filled hole (marked as port 2 in Figure 7.1) using a peristaltic pump connected to the needle at a known rate by opening the stopcock. After a certain time, the injection was stopped and the stopcock was closed. Each sampling port was also equipped with a Swagelok fitting to hold the needle used to collect the sample and a one-way luer stopcock to prevent any fluid loss while sampling. Deionised (DI) water used for all the tracer experiments.

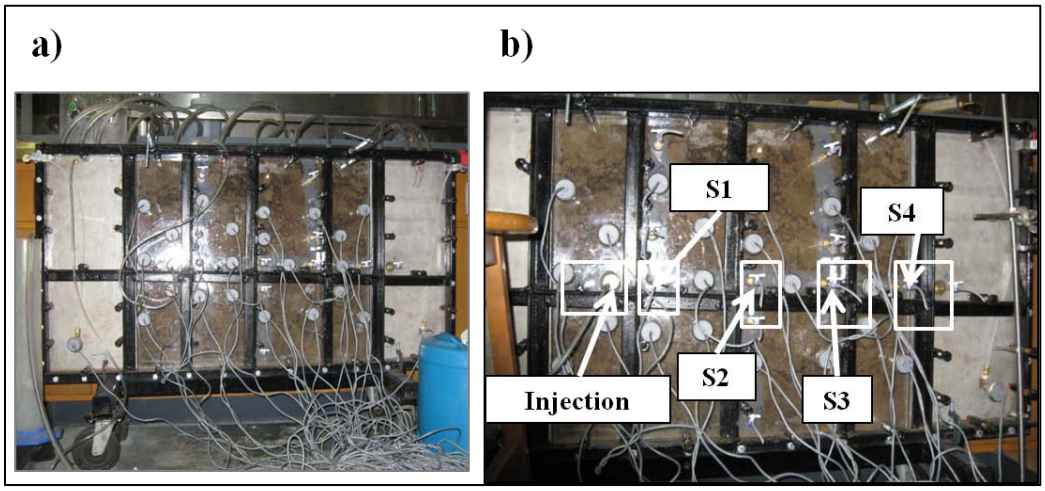

Figure 7.2: a) Photograph of the Experimental block and b) Injection and sampling ports. Injection and sampling ports are indicated in the flow cell with white rectangular box. S1, S2, S3 and S4 are the four sampling ports.

During each tracer test, the ambient flow rate was approximately 2.7 mL/min. After the flow field was established, a tracer solution with bromide (Br^-) at a concentration of 100 mg/L was injected into port 2 (Figure 7.1) at a rate of 15 mL/min during the 1st test and 14 mL/min during the 2nd tests for 60 seconds. The down gradient monitoring ports 3, 5, 7, 9 indicated in Figure 7.1 were sampled periodically. During sampling each cycle, port 3 was sampled first, as it was the closest to the source (injection port) and then port 5, 7 and 9 (Figure 7.1) were sampled respectively. The duration of the

experiment was approximately 23 minutes and 36 minutes for the 1st and 2nd tracer experiments, respectively. Each of the 4 sampling ports was sampled 10 times during the 1st test, while each of them was sampled 15 times during the 2nd test. In total 40 and 60 samples were collected during the 1st and 2nd tracer experiment respectively.

Samples were collected using 1.5mL vials, which were filled to the top to avoid volatilization and mass loss in the head space. Water samples taken during each tracer test were chilled in a refrigerator at 4°C until they were analyzed. A dionex ICS-2000 Ion Chromatograph (IC) equipped with an Ion-Eluent Generator and conductivity detector was used to determine the bromide concentrations. The procedure of analysis can be found in Appendix E.

7.2 Results and Discussion

Similar results were obtained from both tracer experiments. Bromide breakthrough curves at the monitoring ports 3, 5, 7 and 9 (indicated in Figure 7.1) from tracer experiment 1 and 2 are presented in Figure 7.3 and Figure 7.4 respectively. The solid black line parallel to the vertical axis in Figure 7.3 and Figure 7.4 shows the time when injection was stopped. The pattern of the break through curve at a specific monitoring port obtained from each test was identical. Vertical fracture ports 11, 13, 14, 16, 17, 19 (indicated in Figure 7.1) were also sampled once at the end of each experiment and no bromide was detected.

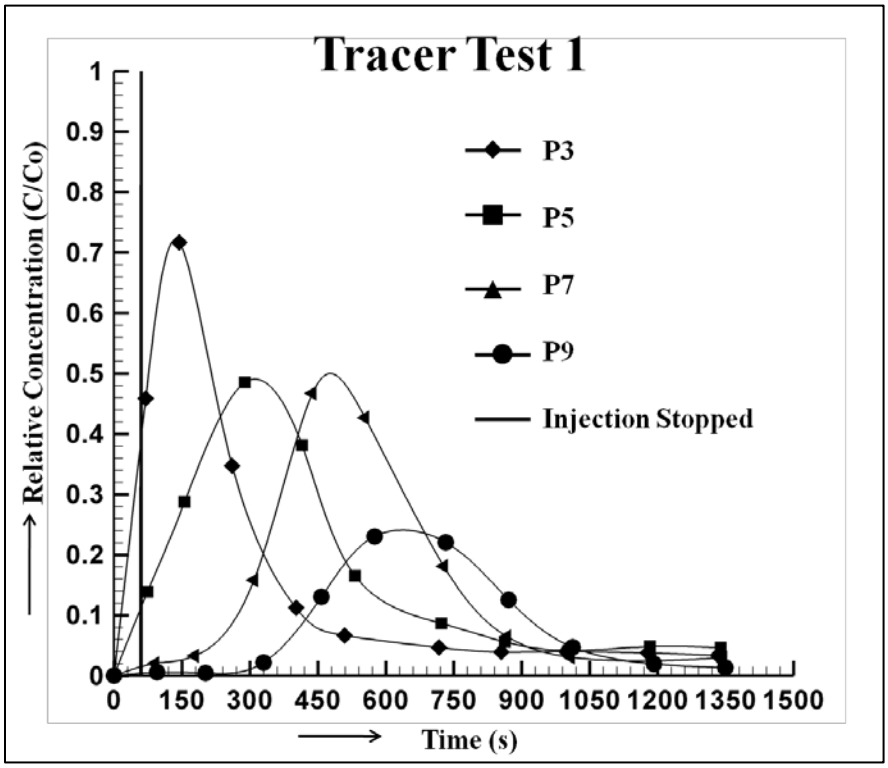

Figure 7.3: Bromide Break-though Curves at the Monitoring Port during Tracer Test 1. The black vertical line indicates the injection stop time.

Examination of Figure 7.3 and Figure 7.4 shows that the bromide concentration reached its peak at all of the monitoring ports within a few second of injection. In both tracer experiments, the volume of injected solution was larger than the hole, used for injection. Therefore, the bromide mass reached flow path (horizontal fracture) as soon as it was injected, leading to the peak concentration at the monitoring ports within a few seconds of injection. This was the reason why the highest bromide concentration was found at port 3 (closest to the source) during the 1st sample. The peak arrival time at ports 5, 7 and 9 (indicated in Figure 7.1) increased as the distance from the source increased. A quick calculation revealed that the peak arrival time at the monitoring ports roughly matched the flow velocity.

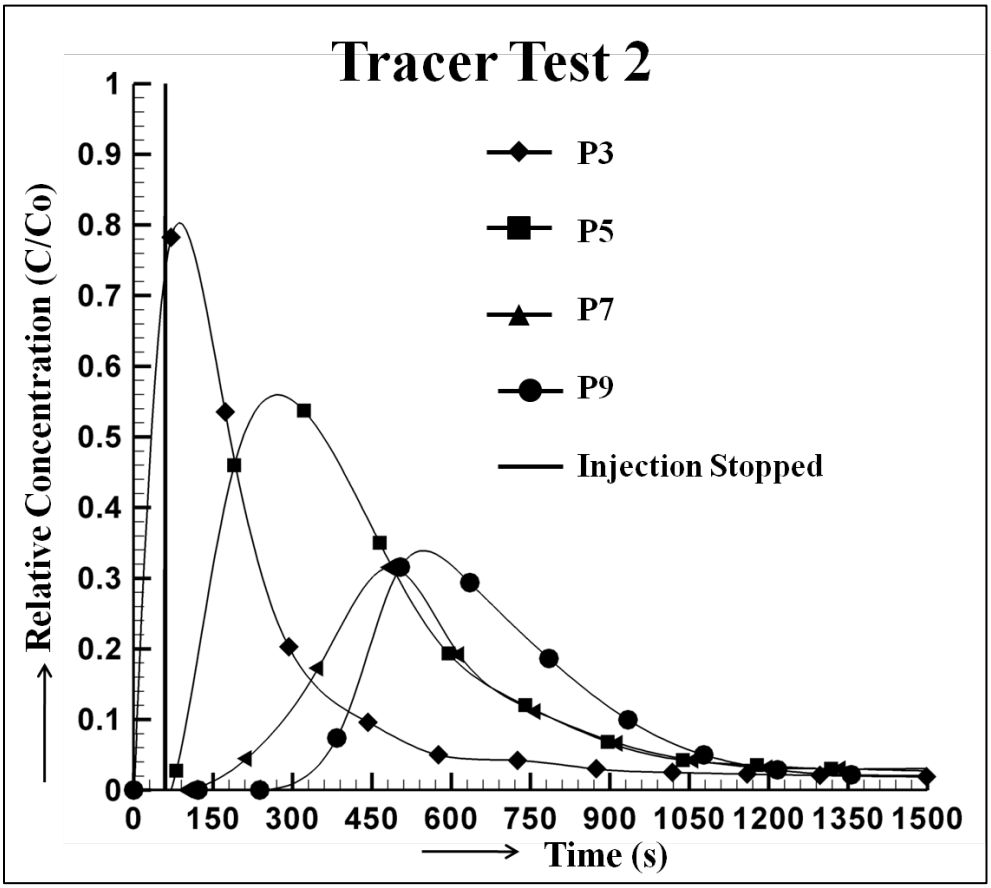

Figure 7.4: Bromide Break-though Curves at the Monitoring Port during Tracer Test 2. The black vertical line indicates the injection stop time.

Similarly, from Figure 7.3 and Figure 7.4 it can be found that the peak concentration was the highest for port 3, decreased gradually for ports 5, 7 and 9. Thus, the breakthrough curve became broader along the flow path. During each test, the highest peak concentration was found at the monitoring port (port 3) that was sampled 1st in each cycle. The peak concentration went down gradually along the flow path, as the sampling port move further from the source.

Table 7-1: Injected Mass and the Mass Crossing Sampling Ports during Tracer Test 1

Injected Mass		Mass Crossing Sampling Ports	
Port	Mass (mg)	Port	Mass (mg)
2	1.5	3 5 7 9	0.9 0.98 0.87 0.5

Table 7-2: Injected Mass and the Mass Crossing Sampling Ports during Tracer Test 2

Injected Mass		**Mass Crossing Sampling Ports**	
Port	**Mass (mg)**	**Port**	**Mass (mg)**
2	1.4	3 5 7 9	0.95 1.2 0.71 0.72

The mass crossing each sampling port during each tracer experiment was estimated from the bromide breakthrough curves using trapezoidal rule. Table 7-1 and Table 7-2 summarize the injected mass as well as the mass crossing the sampling ports during tracer experiment 1 and 2 respectively.

From Table 7-1and Table 7-2, it is evident that there is a significant difference in the injected mass and the mass crossing the sampling ports. During both tests, mass crossing port 5 is the closest to the injected. Although highest peak was found at port 3, mass crossing port 3 was less than the one that past port 5. Port 3, being the closest to the injection port, I assume, I missed the peak at port 3 where the bromide concentration reached its peak as soon as it was injected. The difference between injected mass and the mass that passed the sampling port became larger for port 7 and 9, as the sampling port moves further from the source. This difference is attributed to the bromide mass lost in samples collected at the ports closer to the source.

From the experience of the tracer experiments I decided to inject a TCE volume less than the pore volume of the sand that was used to fill the source hole, so that it does not overflow the hole and reach the flow path (horizontal fracture) as soon as it is injected, allowing me to capture entire breakthrough curve. Regarding sampling, I decided to sample only one down gradient monitoring port (port 9) during the trichloroethene (TCE) dissolution experiment instead of sampling 4 ports to prevent the mass loss. Port 9 was chosen to collect samples because it was the closet to the effluent reservoir.

Chapter 8
TCE Dissolution Experiment

After completing the tracer experiments, a known volume of Trichloroethene (TCE) was injected into a small reservoir to create a well characterized source zone. A constant flow field was established to conduct TCE dissolution experiment. In this chapter, the TCE dissolution experiment and the results obtained from the experiment are discussed.

8.1 Experimental Set-up and Description

The experimental set-up for the TCE dissolution experiment was same as the one used for the tracer experiments, described in section 7.1. Figure 8.1 represents the schematic diagram of the experimental set-up for the TCE dissolution experiment, where the injection and sampling ports are indicated as “Injection” and “Sample” respectively. Figure 8.2a is a photograph of the flow cell and in Figure 8.2b, the injection and sampling ports are indicated on the photograph with rectangular white box. All parts of the experimental system that would be in contact with water in the tank were constructed or sealed with inert materials. For example, the influent and effluent reservoirs were made of stainless steel. As mentioned in section 2.2, titanium putty (Devcon, Danvers, MA, USA) was used to attach the brass fittings (that were used as ports) to the front surface of the rock and sealed around it as well as to seal along the length of the fractures. Similar to the tracer tests, injection and sampling ports were equipped with Swagelok fittings to hold the stainless steel needle used for injection or sample collection and a one-way luer stopcock to prevent any fluid loss while injecting or sampling. Deionised (DI) water was used for the TCE dissolution experiment.

Before injecting TCE into the fractured rock, a steady flow field was established by fixing the hydraulic gradient across the rock sample and the flow rate was measured at the effluent drip point using graduated cylinder. Hydraulic head of the left and right reservoirs were approximately 60cm and 59 cm respectively, although they varied quite a bit. Once the flow field was stable, 2.25mL (3.3 gm) of pure phase (99%) TCE (Sigma Aldrich, St. Louis, MO, USA) was injected in a small reservoir using a syringe into the flow cell to create a source zone. The source zone was created by injecting the TCE into the sand filled hole below the flow path marked as “Injection” in Figure 8.1. The volume of injected TCE was selected based on the porosity of the sand (F-35 Bag sand, US Silica, Frederick, MD, USA) that was used to fill the hole. The sand porosity was measured at the laboratory

which was 40% to 50%. I decided to inject 2.25 mL TCE assuming the pore volume to be 35%, so that it does not overflow the reservoir. It is assumed that injected TCE occupies the bottom part of the reservoir. The source hole, where the TCE was injected has been described in section 7.1.

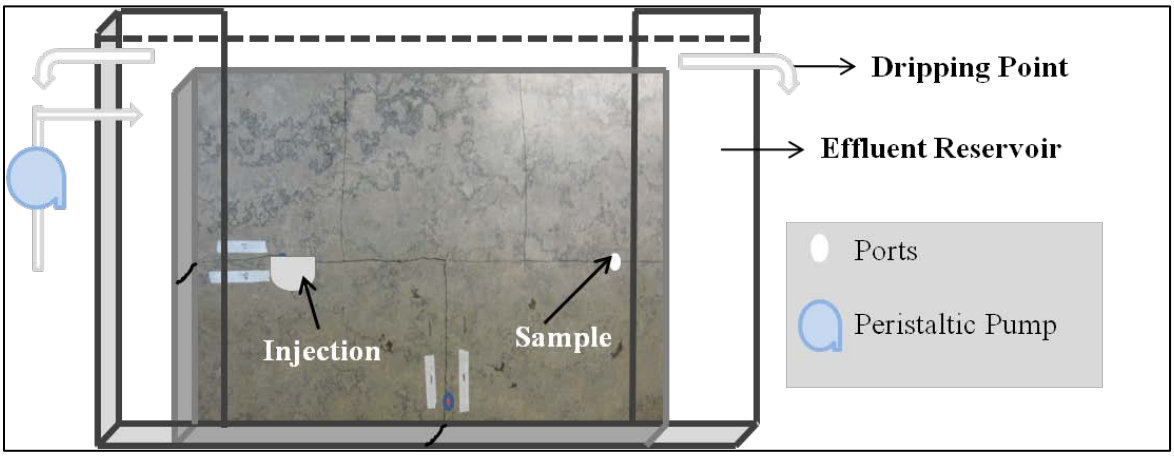

Figure 8.1: Schematic Diagram of the experimental set-up for the TCE dissolution experiment. The white oval indicates the sampling port.

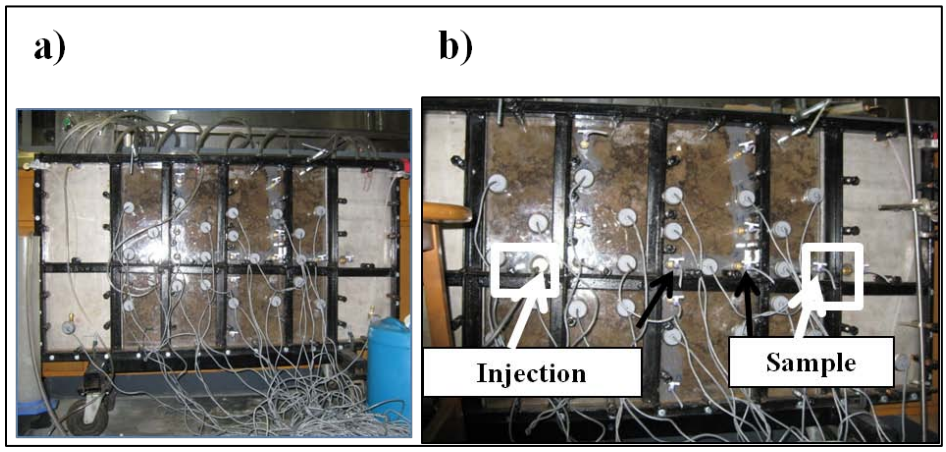

Figure 8.2: a) Photograph of the experimental block and b) Injection and sampling ports. Injection and sampling ports are indicated in the flow cell with white rectangular box.

After the injection, the down gradient monitoring port indicated as "Sample" in Figure 8.1 was sampled periodically using a needle for 86 days to monitor the TCE breakthrough curve. In total, 175 samples were withdrawn during the first 86 days referred to as the"1st part" of the TCE dissolution experiment. To monitor the TCE breakthrough in the fractured rock sample, only one down gradient monitoring port was sampled to reduce the mass loss that was discussed at the end of section 7.2. The

rate of flow through the fracture was also measured periodically at the effluent dripping point throughout the experiment.

To conduct the 2nd part of the dissolution experiment, after 86 days of injection, flow through the fractured domain was shut off over a period of three weeks to let TCE diffuse into the flow path. After this period of flow shutoff, water flow through the fractured rock block was resumed and sampling continued for another two weeks to observe the anticipated rebound in concentration at the monitoring port.

Samples were collected in 2mL vials and they were filled to the top to avoid volatilization and mass loss in the head space. Each water sample withdrawn during the dissolution experiment was chilled in a refrigerator at 4°C until they were analyzed. TCE concentrations were determined using a Hewlett Packard 5890 Series II gas chromatograph (GC) equipped with a Ni63 ECD detector. The procedure of analysis is included in Appendix E.

8.2 Results and Discussion

Figure 8.3 shows the TCE breakthrough curve over 86 days which is also plotted along with the flow rate through the fractured rock block. In Figure 8.3, the left axis shows the TCE concentration and the right axis shows the flow rate. The solid black circles represent the TCE concentration, while the black rectangles represent the flow rate over time.

Examination of Figure 8.3 reveals that the flow rate was mostly stable throughout the experiment, with an exception at early time. The measured flow rate at the effluent drip point varied in between 2 mL/min to 3 mL/min except at very early time. At very early time flow rate went down to 1mL/min to 1.2mL/min due top very frequent sampling. Very frequent sampling (every 15 minutes) following the injection of TCE was likely responsible for this early time fluctuation of flow rate, as it became stable when the sampling was slowed down.

From the TCE concentration profile in Figure 8.3 it can be seen that at the monitoring port, TCE concentration reached its peak after 20 to 25 hours of injection which was about 67 ppm and declined gradually to 1ppm after 12 days and 0.1 ppm after 86 days of injection.

TCE mass removed through dissolution was estimated from the TCE concentration profile using trapezoidal rule which revealed that only 21% of the injected mass was recovered in 86 days. Therefore, TCE concentration at the monitoring port reached its tailing stage instead of staying at the peak, although the source was not depleted completely. One potential explanation may be the

physical diffusive phenomenon due to the development of a concentration gradient over time between the source zone and the flow path. As the injected TCE was sitting at the bottom of the sand filled hole below the flow path, a layer of dissolved TCE developed in between the source zone and the flow path within a few hours of injection. Thus, after a few hours of injection, TCE had to diffuse from the source zone to the flow path through this dissolved layer, which was the anticipated phenomenon behind the TCE concentration going down gradually at the monitoring port before the complete depletion of the source zone. To investigate this, flow through the fractured domain had been shut off for three weeks and the 2nd part of the dissolution experiment (TCE rebound) was conducted.

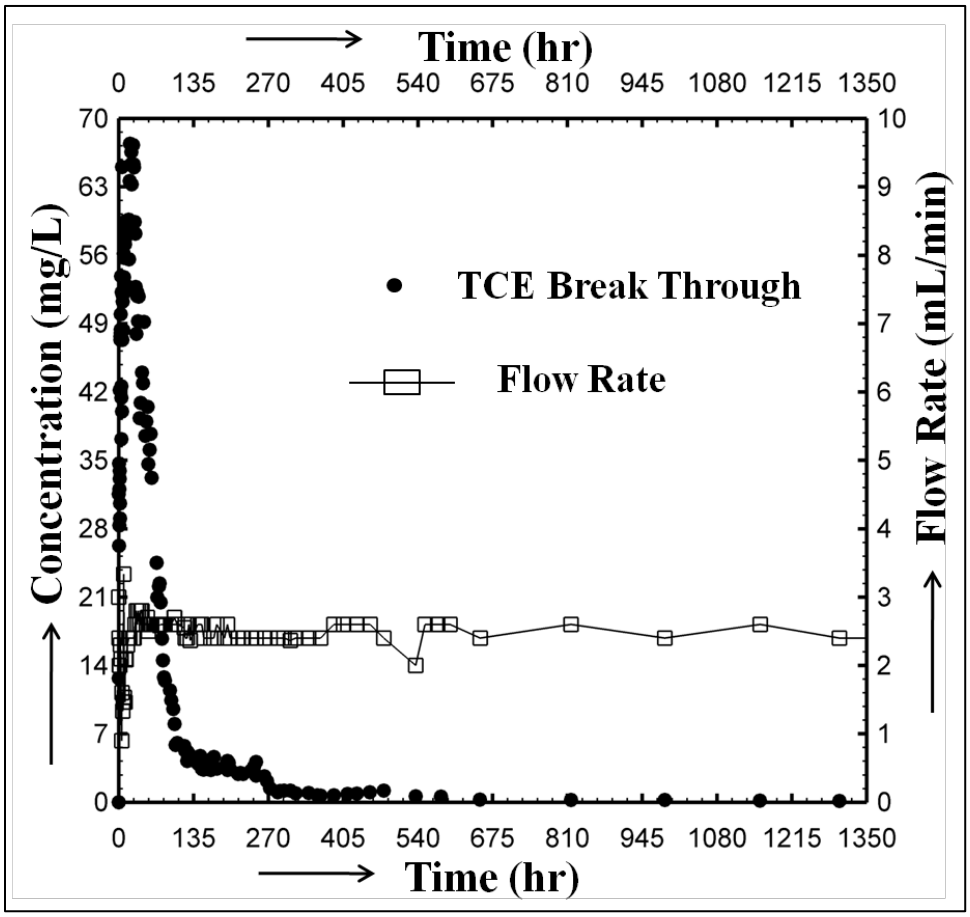

Figure 8.3: TCE Breakthrough Curve from the 1st part of Dissolution Experiment and Flow Rate over Time. Solid black circles represent the TCE concentration while the black rectangles represent the flow rate over time.

During the 2nd part of the dissolution experiment, the flow through the fractured domain was turned off to investigate whether an increase in TCE concentration due to TCE diffusion through the dissolved layer to the flow path is observed or not. The flow was resumed after three weeks and the down gradient monitoring port was being sampled again for another two weeks to examine if there is any rebound in TCE concentration at the monitoring port.

Figure 8.4a represents the TCE concentration profile over 121 days (1st and 2nd part of the dissolution experiment) and a portion of the breakthrough curve, indicated by a rectangular box in Figure 8.4a has been expanded in Figure 8.4b for ease of visualization. Similar to Figure 8.3, in Figure 8.4a and b, the left axis shows the TCE concentration and the right axis shows the flow rate. The solid black circles represent the TCE concentration, while the black rectangles represent the flow rate over time.

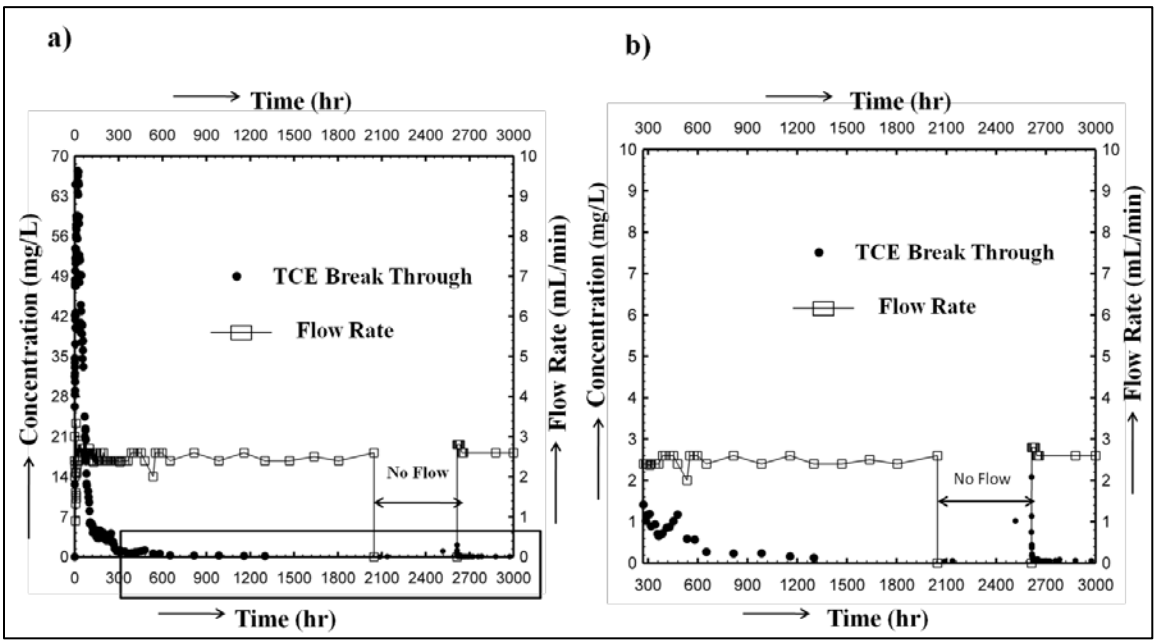

Figure 8.4: a) TCE Concentration Over 121 Days and b) Rebound in TCE Concentration. Solid black circles represent the TCE concentration while the black rectangles represent the flow rate over time.

Examination of Figure 8.4a and b reveal that, a slight rebound was observed in TCE concentration. TCE concentration increased to 2 ppm from 0.1 ppm and started to decrease again within a few minutes of starting the flow. In 121 days, the total dissolved mass was estimated to be 21.2 % of the injected mass.

To examine whether the rest of the mass diffused into the matrix, TCE concentration that could be diffused into the matrix in 121 days (to different distances from the fracture) was calculated using 1-D diffusion equation given by equation (*11*) –

$$C_i\,(x,t) = C_0 erfc[\frac{x}{2\sqrt{tD_d}}] \qquad [11]$$

where, *Ci* is the TCE concentration at a distance *x* from the fracture at time *t*, *Co* is the initial concentration and *erfc*[*y*] is the complementary error function. In equation (*11*), D_d is the effective diffusion coefficient given by $D_d = D_0\tau$, where, D_0 is the free solution diffusion coefficient and τ is tortuosity. The free solution diffusion coefficient (D_0) and tortuosity (τ) values used for the calculation were 1.0×10^{-5} cm^2/s [*i.e.*, *Perry*, 1984; *Pankow and Cherry*, 1996] and 0.1 respectively.

Estimated diffusive TCE front is shown in Figure 8.5 and the calculated concentration at corresponding distances are listed in Table 8-1. From Figure 8.5 and Table 8-1 it is evident that TCE penetrated about 0.1 cm (1 mm) into the rock matrix. Penetrated TCE mass into the rock matrix (both side of the horizontal fracture) was then estimated by multiplying the average concentration (arithmetic mean of all 9 concentrations given in Table 8-1) by the penetration volume. Penetration volume and estimated penetrated TCE mass into the rock matrix are also presented in Table 8-1. From Table 8-1, it is evident that approximately 0.02 gm of TCE could be penetrated into the rock matrix, which is only 0.61% of total injected mass. Therefore, the rest of the TCE mass is probably still present at the bottom of the hole.

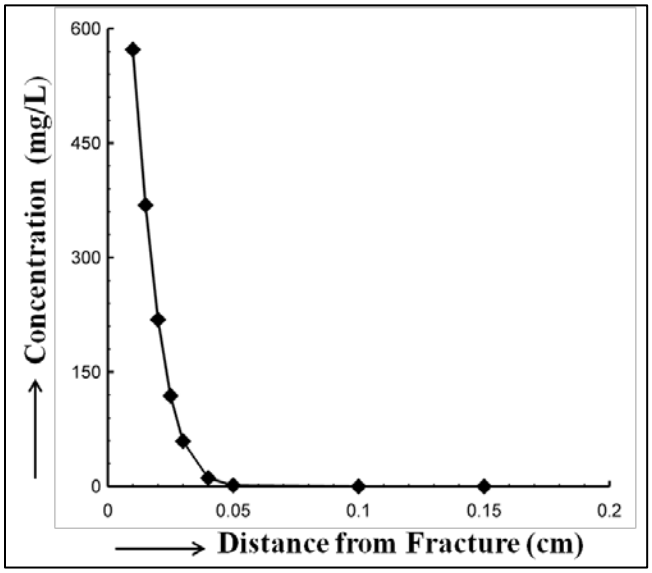

Figure 8.5: The Profile of Estimated Diffusing TCE Front into the Rock Matrix

Table 8-1: Estimated TCE concentration and Diffused Mass in the Rock Matrix

Distance From Fracture (cm)	Concentration (mg/L)	Average Concentration (mg/L)	Volume (cm^3)	Mass (gm)
0.01	5.72E+02	1.50E+02	68.63	0.02
0.015	3.68E+02			
0.02	2.18E+02			
0.025	1.19E+02			
0.03	5.92E+01			
0.04	1.11E+01			
0.05	1.44E+00			
0.1	1.42E-07			
0.15	0.00E+00			

The dissolution experiment in the laboratory helped to understand the TCE dissolution behavior in a fractured rock environment. Upon completion of the laboratory experiment, the transport of aqueous phase TCE originating from the source zone was modeled using: 1) assumed hydraulic properties of the fractured block based on the discrete fracture network modeling concept and, 2) the estimated K distribution obtained from the THT analysis of cross-hole pumping tests. This modeling effort is described in the next chapter.

Chapter 9
Numerical Modeling of Aqueous Phase TCE Transport

Upon completion of the laboratory TCE dissolution experiment, Hydrogeosphere (HGS) was used to simulate the 1st portion (0 – 86 days) of the aqueous phase TCE breakthrough curve. The aqueous phase TCE was simulated using two approaches: 1) discrete fracture network modeling approach and 2) stochastic continuum approach. The goal of theses modeling study was to capture the pattern breakthrough curve as well as to compare the results from these two approaches.

9.1 Discrete Fracture Network Modeling Approach

In the discrete fracture network modeling approach, a discretely fractured domain, with known geometry of fractures of the laboratory fractured block was used for the simulation. A uniform aperture thickness estimated from the flow-through tests was assigned to all fractures and a very low hydraulic conductivity (K) was assigned to the matrix.

9.1.1 Model Set-up

A model domain, 91.5 cm in length, 60.5 cm in height and 1 cm thick (one element thick) was used for the dissolution modeling using the discrete fracture network modeling approach. The model domain was the same as the one used for simulating the pumping tests using HGS, described in section 3.3, with the only exception that the thickness of the model domain is different. The model domain used for simulating TCE dissolution was of unit thickness and composed of variably-sized rectangular elements. The element size varied from 0.05 cm by 0.01 cm to 1.375 cm by 1.375 cm. The finer elements are located along the fracture and the coarser elements are located near the boundary.

Figure 9.1a) shows the mesh used for simulating the aqueous phase TCE transport, where the location of the source is indicated with a black circle and Figure 9.1b) shows the fracture faces. The model domain was very finely discretized around the source zone indicated in Figure 9.1a, to account for the steep concentration gradient, expected to develop from the source zone into the flow path. The darker areas in Figure 9.1 indicate the highly refined areas of the model domain.

The flow boundary conditions were constant head for left and right boundaries and no flow for the remaining outer boundaries. Equilibrium dissolution from the immobile phase was simulated for the

source zone. For equilibrium dissolution, aqueous phase concentration is same as the contaminant solubility. The boundary condition assigned at the source zone assumes that an immobile liquid phase dissolves into water until all dissolvable material is exhausted. In this transport boundary condition, each chosen nodes is assigned a first-type concentration value which is equal to the mass of dissolvable material per unit volume of porous medium and the concentration is maintained until all the material associated with a node is dissolved [*Therrien et al*., 2009]. Equation (*6*) describes the transport boundary condition.

$$\int_0^{T_0} \int_{Vn_i} -\nabla[qC - D\nabla C]\, dV_{ni} dt = Mo_{ini} \qquad [6]$$

$$C = Co, \text{ when } 0 \leq t < To$$

where, *To* is the dissolution time, Vn_i is the volume associated with node n_i, Mo_{ini} initial mass stored at node n_i, q is the Darcy flux, *C* is the concentration, *Co* is the aqueous phase solubility, and *D* is the dispersivity.

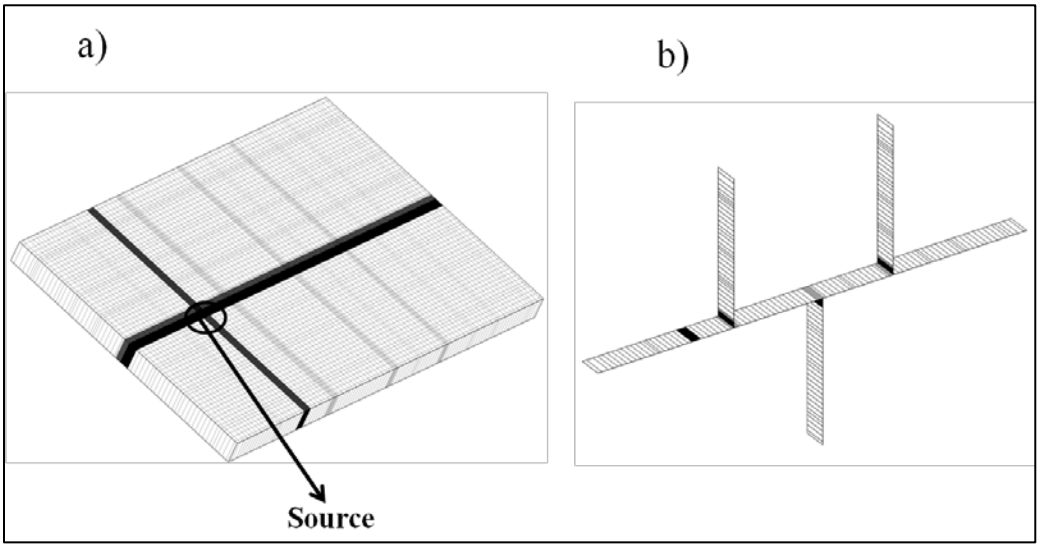

Figure 9.1: a) Mesh Used for TCE Dissolution Modeling using Discrete Fracture approach and b) Fracture Faces.

9.1.2 Model Input

A uniform aperture value, obtained from flow-through tests was assigned to the fractures and a very low hydraulic conductivity (1.0×10^{-7} cm/s) was assigned to the matrix to simulate aqueous phase TCE

transport. As described in section 3.3, HGS calculates the fracture hydraulic conductivity (K_f) from the aperture thickness. The matrix hydraulic conductivity (K_m) used for the transport modeling was determined through manual calibration of pumping test at port 5, simulated using HGS to match the simulated drawdown with the observed, described in section 3.3. The experimental rock is representative of Guelph formation. Therefore, a porosity value representative of the Guelph formation obtained from *Zheng* [1999] was used as matrix porosity. According to *Zheng* [1999], the bulk porosity of Guelph dolomite can range from 0.1% to 14.4%. Here the matrix porosity was chosen to be 0.1% as the experimental rock seems to be quite tight.

To simplify the transport modeling, a model domain having a unit thickness was used for the simulation, by scaling down the thickness by a factor of 5. Before conducting transport simulations, the flow through the fractured domain was simulated by fixing the hydraulic gradient across the model domain to match the experimental flow velocity. As the domain thickness was scaled down by a factor of 5, the fluid flux through the domain, volume of the source zone and the injected mass were also reduced by the same factor.

The source zone was assigned the hydraulic conductivity of sand that was measured in the laboratory using the falling head method. The porosity of the sand was also measured in the laboratory which was used as the source zone porosity for dissolution modeling. TCE solubility to water at room temperature (20°C) was obtained from literature [e.g., *Russel et al*., 1992; *Pankow and Cherry*, 1996]. Initially I started with the literature value (1.0×10^{-5} cm^2/s) [i.e., *Perry*, 1984; *Pankow and Cherry*, 1996 etc.] for the free solution diffusion coefficient of TCE, but the manual calibration resulted in a higher value (3.1×10^{-3} cm^2/s) than the literature value to match the break-through curve. Other transport parameters used for dissolution modeling such as tortuosity and dispersivity were also determined through trial and error. The simulation was conducted several times by varying each of these parameters manually until a good match between the observed and simulated break-through curves was obtained. Among the transport parameters, dispersivity was found to affect the pattern of the breakthrough curve most. Table 9-1 summarizes the flow and transport parameters used to obtain the simulated breakthrough curve presented here.

Table 9-1: Flow and Transport Parameters Used for TCE Dissolution Modeling in Discrete Fracture Approach

Parameters Used			Source
Fracture	Aperture (cm)	0.049	Flow-through tests
	Fracture Hydraulic Conductivity, K_f (cm/s)	17.5	Calculated by HGS
	Longitudinal Dispersivity (cm)	1.96	
	Transverse Dispersivity (cm)	0.176	
Matrix	Matrix Hydraulic Conductivity, K_m (cm/s)	1.0×10^{-7}	*De Marsily*, 1986; *Domenico and Schwatrz*, 1997; *Schwartz and Zhang*, 2003 etc. (1.0×10^{-7} cm/s to1.0×10^{-4} cm/s)
	Matrix Porosity	0.1%	*Zheng*, 1999 (0.1% – 14.4%)
	Source Hydraulic Conductivity, K_s (cm/s)	0.1	Hydraulic conductivity of sand (used to fill the source hole) measured in the laboratory.
Source	Source Porosity	50%	Porosity of sand (used to fill the source hole) measured in the laboratory.
	Tortuosity	0.65	
	Free Solution Diffusion Coefficient (cm^2/s)	3.1×10^{-3}	*Perry*, 1984; *Pankow and Cherry*, 1996. (1.0×10^{-5} cm^2/s)
TCE	Solubility (mg/L)	1000	*Russel et al*., 1992; *Pankow and Cherry*, 1996. (1000 mg/L – 1100 mg/L)

9.2 Stochastic Continuum Modeling Approach

In the stochastic continuum modeling approach, the model domain was treated as a porous medium and the hydraulic conductivity (*K*) field obtained from Transient Hydraulic Tomography (THT) was utilized for simulating aqueous phase TCE transport using HGS.

9.2.1 Model Set up

A model domain, 91.5 cm in length, 60.5 cm in height and 5 cm thick (one element thick) was used for the transport modeling using the stochastic continuum approach. The model domain was same as the one used for transient hydraulic tomography (THT) analysis using SSLE, described in section 4.2.1. The model domain was composed of variably-sized rectangular elements and it was discretized into 14140 nodes and 6900 elements. The element size varied from 0.5 cm by 0.5 cm to 1.75 cm by 1.75 cm. The finer elements are located along the ports to match the port location and the element center and the coarser elements are located near the boundary.

Figure 9.2 shows the mesh used for simulating TCE dissolution using the stochastic continuum approach, where the location of the source is indicated with a black circle. Here the model domain used for the simulation was same as the one used for inversion, as the *K*-tomogram obtained from the THT analysis was used for dissolution modeling. Therefore, in this case, the model domain was not finely discretized around the source zone like the discrete fracture approach, described in section 9.1.1, although it would have been useful to deal with the concentration gradient, expected to develop from the source zone into the high *K* zone.

The flow boundary conditions were constant head for left and right boundaries and no flow for the remaining outer boundaries. The transport boundary condition, assigned to the source zone was same as the one described in section 9.1.1.

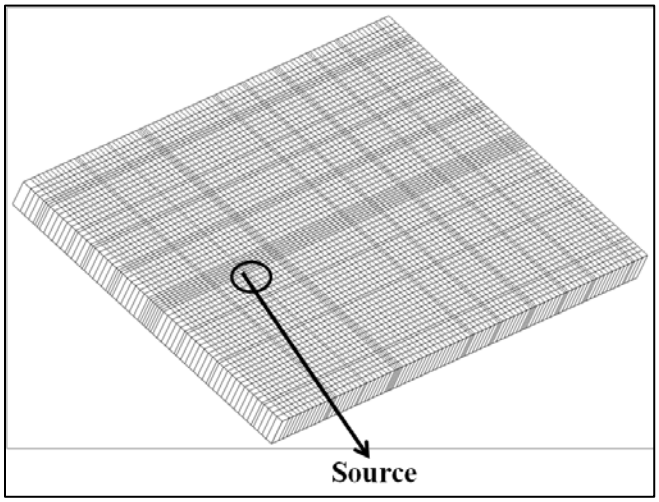

Figure 9.2: Mesh Used for TCE Dissolution Modeling using Stochastic Continuum Approach

9.2.2 Model Input

In this case, to simulate the transport of aqueous phase TCE, each element of the model domain was assigned a hydraulic conductivity (*K*) obtained from the THT analysis (case 1), described in section 5.2. All the elements in the model domain were also assigned a bulk porosity value. (The experimental rock is representative of Guelph formation. Therefore, a porosity value representative of the Guelph formation obtained from *Zheng* [1999] was used for the model domain. According to *Zheng* [1999], the bulk porosity of Guelph dolomite can range from 0.1% to 14.4%. Here the bulk porosity was chosen to be 1%. Before conducting transport simulations, the flow through the porous medium was simulated by fixing the hydraulic gradient across the model domain to match the experimental flow velocity.

Similar to the discrete fracture approach, here TCE solubility to water at room temperature (20°C) was obtained from literature [e.g., *Russel et al*., 1992; *Pankow and Cherry*, 1996 etc.]. Initially I started with the literature value [i.e., *Perry*, 1984; *Pankow and Cherry*, 1996 etc.] for the free solution diffusion coefficient of TCE, but the manual calibration resulted in values (1×10^{-7} cm^2/s in case 1 and 1×10^{-6} cm^2/s in case 2) little lower than the literature value to match the break-through curve. Other transport parameters used for dissolution modeling such as tortuosity and dispersivity were also determined through trial and error. The simulation was conducted several times by varying each of these parameters manually until a good match between the observed and simulated break-through curves was obtained. Among the transport parameters, dispersivity was found to affect the pattern of

the breakthrough curve most. Two best cases simulated using different transport parameters are presented here. Table 9-2 and Table 9-3 summarize the flow and transport parameters utilized to simulate TCE dissolution in case 1 and case 2 respectively using stochastic continuum approach.

Table 9-2: Flow and Transport Parameters Used for TCE Dissolution Modeling in Stochastic Continuum Approach (Case 1)

Parameters Used			Source
Porous Medium	Hydraulic Conductivity, *K* (cm/s)	*K*-Tomogram Obtained from THT analysis (Case 1)	THT analysis of laboratory pumping Tests (Case 1)
	Longitudinal Dispersivity (cm)	91	
	Transverse Dispersivity (cm)	5.76	
	Vertical Transverse Dispersivity (cm)	6.76	
	Porosity	1%	*Zheng*, 1999 (0.1% – 14.4%)
	Tortuosity	0.65	
TCE	Free Solution Diffusion Coefficient (cm^2/s)	1.00×10^{-7}	*Perry*, 1984; *Pankow and Cherry*, 1996. (1.0×10^{-5} cm^2/s)
	Solubility (mg/L)	1000	*Russel et al*., 1992 (US EPA Ground Water Issue, 1992); *Pankow and Cherry*, 1996; (1000 mg/L – 1100 mg/L)

Table 9-3: Flow and Transport Parameters Used for TCE Dissolution Modeling in Stochastic Continuum Approach (Case 2)

Parameters Used			Source
Porous Medium	Hydraulic Conductivity, *K* (cm/s)	*K*-Tomogram Obtained from THT analysis (Case 1)	THT analysis of laboratory pumping Tests (Case 1)
	Longitudinal Dispersivity (cm)	91	
	Transverse Dispersivity (cm)	6.76	
	Vertical Transverse Dispersivity (cm)	6.76	
	Porosity	1%	*Zheng*, 1999 (0.1% – 14.4%)
	Tortuosity	0.65	
TCE	Free Solution Diffusion Coefficient (cm^2/s)	1.0×10^{-6}	*Perry*, 1984; *Pankow and Cherry*, 1996. ($1.0E\times10^{-5} cm^2/s$)
	Solubility (mg/L)	1100	*Russel et al*., 1992 (US EPA Ground Water Issue, 1992); *Pankow and Cherry*, 1996; (1000 mg/L – 1100 mg/L)

9.3 Results and Discussion

9.3.1 Discrete Fracture Network Modeling Approach

Comparison of the observed and simulated TCE concentration profiles (simulated using the discrete fracture network modeling approach) is presented in Figure 9.3a. In Figure 9.3b, the selected portion of the breakthrough curve, indicated with the black rectangular box (in Figure 9.3a), has been expanded to examine how the simulated concentration matched the observed data at early time. The solid black circles represent the observed TCE concentration from the laboratory experiment, while the diamonds represent the simulated concentration using the discrete fracture network modeling approach.

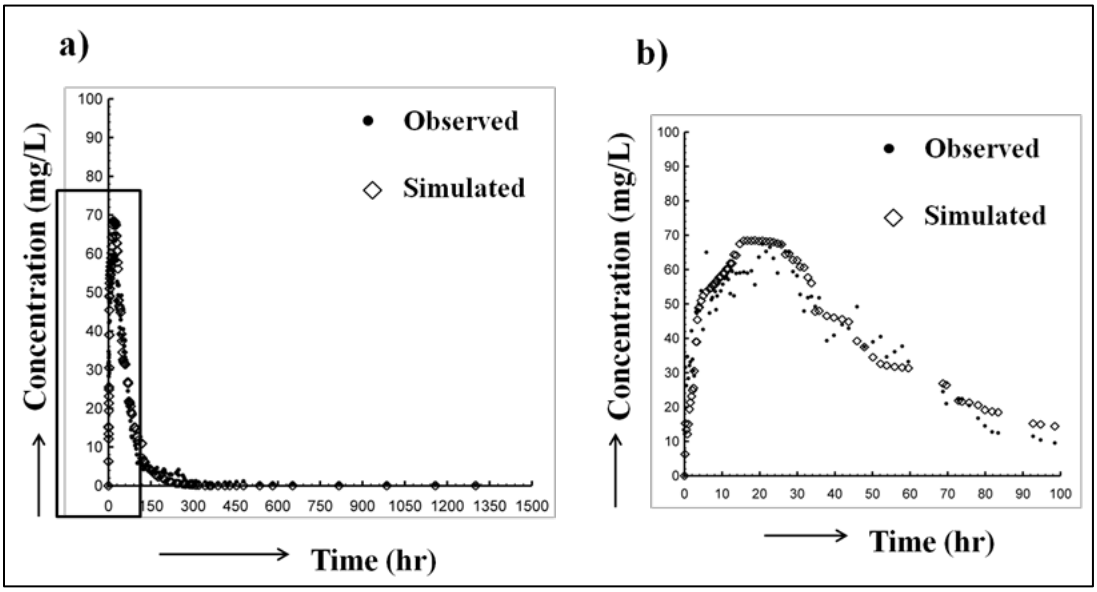

Figure 9.3: a) Observed and Simulated Breakthrough Curves (using discrete fracture network modeling approach) and b) Observed and Simulated Breakthrough Curves at Early Time. The solid black circles represent the observed TCE concentration in the laboratory experiment while the diamonds represent the simulated concentration.

From Figure 9.3, it can be seen that a good match was obtained between the observed and simulated breakthrough curves using the discrete fracture network modeling approach indicating that this approach can capture the TCE breakthrough curve quite well.

The time stepping is probably responsible for the steps or plateaus in simulated concentration in Figure 9.3b. The convergence criteria of the model was set in a way that, if the change in estimated

concentration was below the convergence criteria (a previously set threshold), a previously set time-step multiplier came into effect leading to a larger time-step. This process continued until the change in estimated concentration was below the convergence criteria. Once the change in estimated concentration was above the previously set threshold, the time step was cut down by the same factor leading to a smaller time-step. This back and forth adjustment of time-step was probably responsible for the steps or plateaus in simulated concentration in Figure 9.3b.

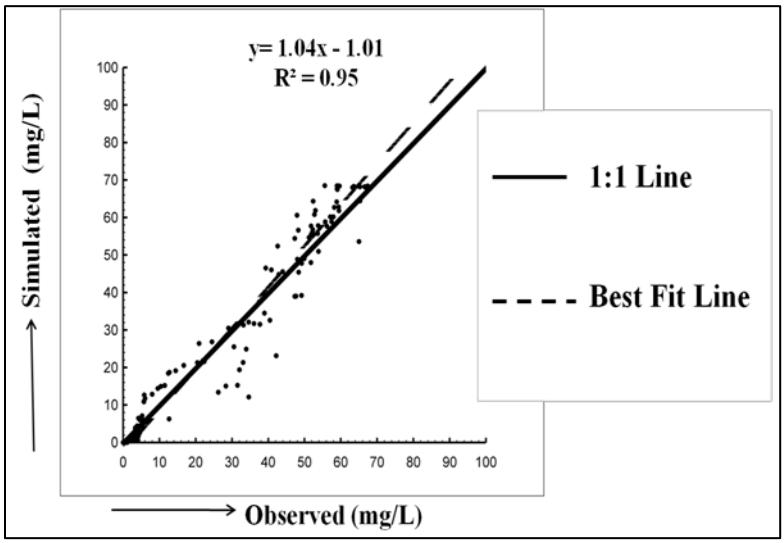

Figure 9.4: Scatter Plot of Observed and Simulated TCE Concentration (using the discrete fracture network modeling approach). The solid line is a 1:1 line indicating a perfect match. The dashed line is a best fit line, and the parameters describing this line are on the plot.

Figure 9.4 is a scatter plot comparing simulated and observed TCE concentration at the sampling port. The solid line is a 1:1 line indicating a perfect match. The dashed line is a best fit line, and the parameters describing this line are included on the plot. The scatter plot is presented as an assessment of how well the simulated breakthrough curve was able to capture the observed. The R^2 value indicates the Correlation between the simulated and observed values. The correspondence between the simulated versus the observed concentration values can be considered to be good when the data set clusters around the 1:1 line and the R^2 value is close to 1. The slope and the intercept of the linear model fit are the indication of bias. From Figure 9.4, it is seen that the data points cluster around the 1:1 line indicating a good match between the observed and simulated breakthrough curve. The R^2 value was also very close to 1 (0.95) indicating that simulated concentration profile captured the observed pattern quite well.

As mentioned in section 9.1.2, the simulation was conducted several times changing some of the parameters such as dispersivity and free solution diffusion coefficient until a good match between the observed and simulated breakthrough curves was obtained and the simulated breakthrough curve shown here is the one that best matched the observed. The set of parameters used to produce the simulated breakthrough curve are listed in Table 9-1 and section 9.1.2 describes how the parameters were selected. Note that, a similar match can be obtained using a different combination of transport parameters such as dispersivity and free solution diffusion coefficient, which suggest non-uniqueness of the parameters.

The purpose of modeling the TCE breakthrough curve using the discrete fracture network modeling approach was to investigate whether the TCE breakthrough curve can be captured in a fractured rock environment when the fracture geometry, fracture aperture and the flow through the system are well known. In this case, the geometry of the fractured rock, fracture aperture and the flow through the system were well characterized through the hydraulic and tracer tests conducted ahead of the dissolution experiment. The fracture geometry of the numerical model closely resembles the fracture patterns in the rock block in the laboratory. Also, the mesh was very finely refined around the source zone to deal with concentration gradient expected to develop over time from the source zone into the flow path, discussed in section 8.2. Finally, result shows that it is possible to capture the pattern of TCE dissolution in a fractured rock environment using discrete fracture network modeling approach.

9.3.2 Stochastic Continuum Modeling approach

In this case, the hydraulic conductivity (K) field obtained from "Real THT analysis Case 1" was used and the model domain was treated as a porous medium to simulate the transport of aqueous phase TCE. As mentioned in section 9.2.2, the simulation was conducted several times by varying the parameters until a good match between the observed and simulated breakthrough curves was attained and the two best cases are presented here.

A comparison of observed and simulated TCE concentration profiles (stochastic continuum modeling approach) for case 1 is presented in Figure 9.5a. In Figure 9.5b a selected portion of the breakthrough curve indicated with the black rectangular box (in Figure 9.5a) has been expanded to examine how the simulated concentration matched the observed at early time. A similar comparison of observed and simulated breakthrough curves for case 2 is presented in Figure 9.7a and Figure 9.7b. The solid black circles represent the observed TCE concentration from the laboratory experiment,

while the diamonds represent the simulated concentration using the stochastic continuum modeling approach.

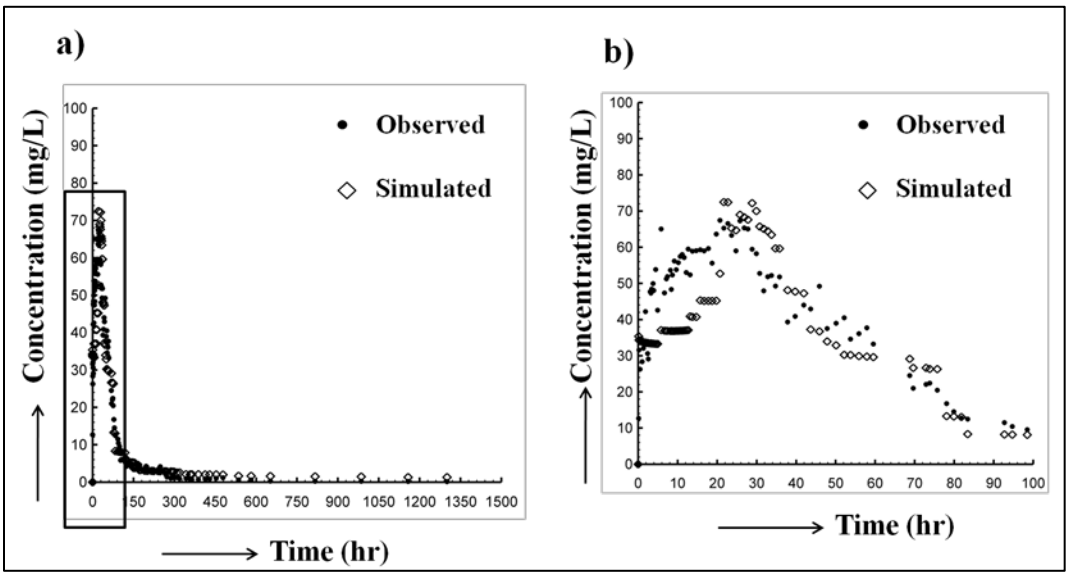

Figure 9.5: a) Observed and Simulated Breakthrough Curves in Case 1 (using the stochastic continuum modeling approach) and b) Observed and Simulated Breakthrough Curves at Early Time. The solid black circles represent the observed TCE concentration in the laboratory experiment while the diamonds represent the simulated concentration.

Examination of Figure 9.5 reveals that the match between the observed and simulated concentration profiles in case 1 is fair except at early time (0 – 20 hours). At early time, the simulated concentration was lower than the observed in case 1 (Figure 9.5b). On the other hand, from Figure 9.7 it can be seen that at early time, simulated concentrations matched the observed quite well for case 2. But in case 2 (Figure 9.7b) the simulated peak concentration was much higher than observed and the peak arrived earlier in the simulated case than the observed. In case 2 (Figure 9.7a), the simulated TCE concentration was found to be a little higher than the observed at the tailing stage too, which was expected as the peak concentration was much higher than the observed in this case.

There could be couple of reasons behind the deviation of the simulated TCE breakthrough curve from one observed one, which are -

- In the stochastic continuum modeling approach, the mesh was not finely discretized around the source zone what was done for the discrete fracture network modeling approach to deal

with the concentration gradient expected to developed overtime from the source zone into the high *K* zone, discussed in section 8.2.

- The estimated hydraulic conductivity (*K*) field from the THT analysis used to simulate the aqueous phase TCE transport might play a role behind this deviation. As discussed in section 5.2 estimated hydraulic conductivity (*K*) values may not exactly replicate actual *K* values for the fractured block.
- At early time of the dissolution experiment in the laboratory, flow through the fractured rock (Figure 8.3) fluctuated quite a bit due to very frequent sampling, which was discussed in section 8.2, while in the synthetic case the flow rate was stable throughout the duration of the simulation. Therefore, the flow rate for the synthetic case did not exactly match the observed at early time, which may have caused the discrepancy between the observed and simulated concentration.

However, the overall the pattern of the TCE breakthrough curve was captured using the stochastic continuum modeling approach for both cases 1 and 2. However, it was difficult to match both the peak arrival time and the peak concentration simultaneously.

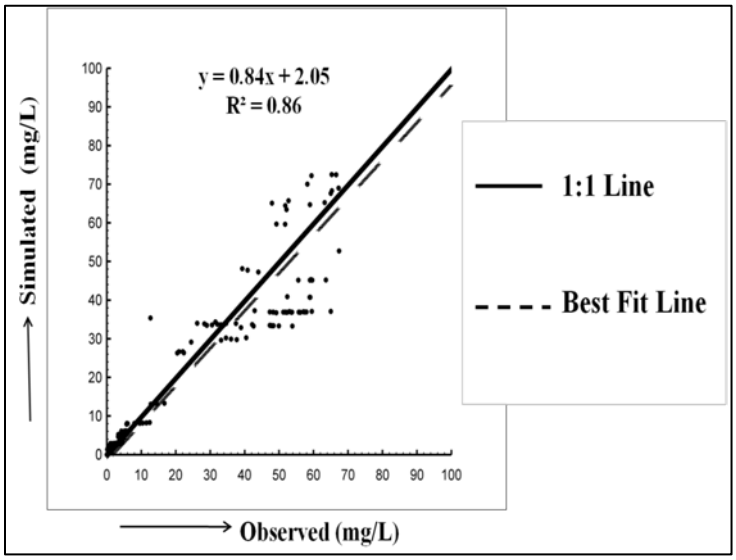

Figure 9.6: Scatter Plot of Observed and Simulated TCE Concentration in Case 1 (using the stochastic continuum modeling approach). The solid line is a 1:1 line indicating a perfect match. The dashed line is a best fit line, and the parameters describing this line are on the plot.

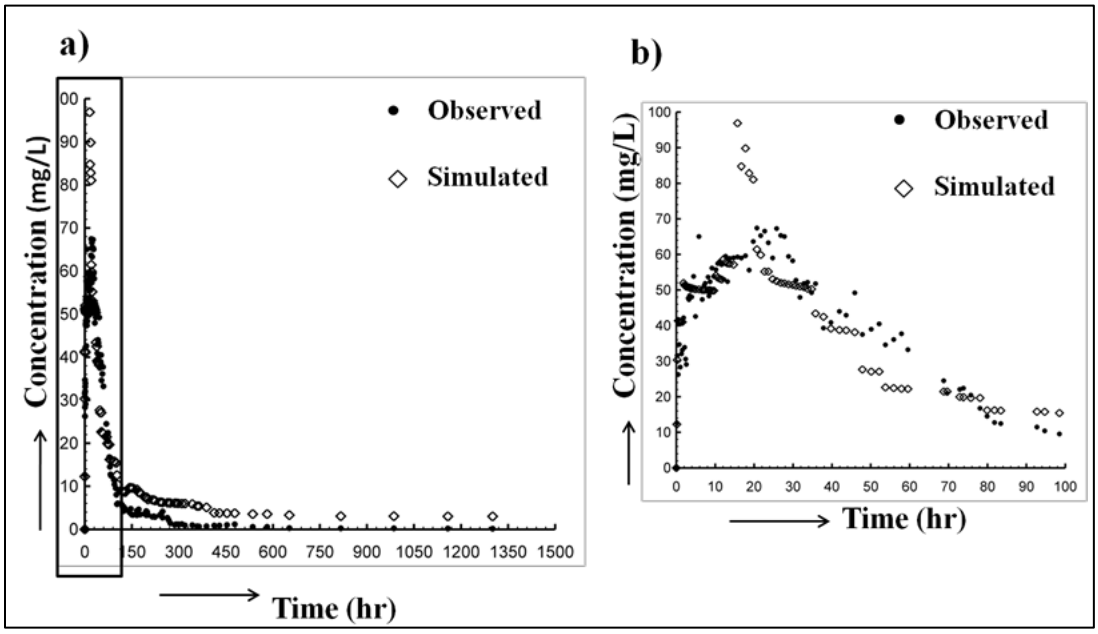

Figure 9.7: a) Observed and Simulated Breakthrough Curves in Case 2 (using the stochastic continuum modeling approach) and b) Observed and Simulated Breakthrough Curves at Early Time. The solid black circles represent the observed TCE concentration in the laboratory experiment while the diamonds represent the simulated concentration.

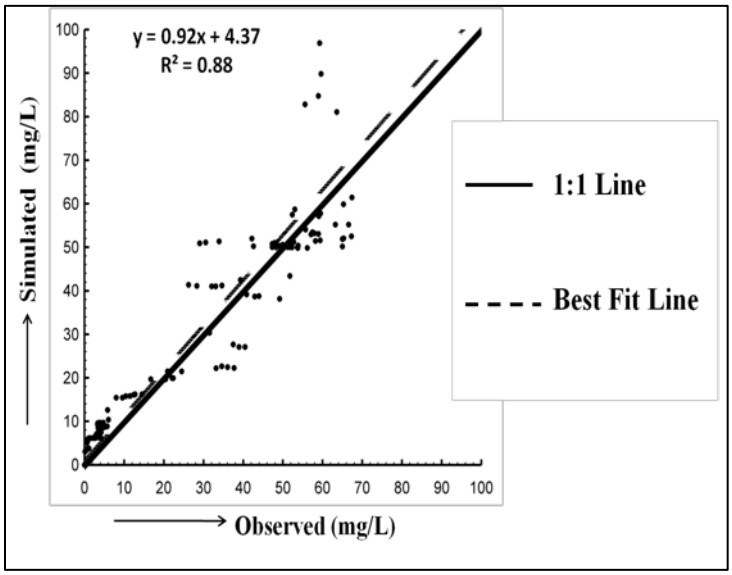

Figure 9.8: Scatter Plot of Observed and Simulated TCE Concentration in Case 2 (using the stochastic continuum modeling approach). The solid line is a 1:1 line indicating a perfect match. The dashed line is a best fit line, and the parameters describing this line are on the plot.

Figure 9.6 and Figure 9.8 are the scatter plots comparing simulated and observed TCE concentrations at the sampling port in cases 1 and 2 respectively. The solid line is a 1:1 line indicating a perfect match. The dashed line is a best fit line, and the parameters describing this line are included on each plot. From Figure 9.6 and Figure 9.8, it is seen that the data points cluster around the 1:1 line, indicating a fair match between the observed and simulated breakthrough curves, although some bias is evident due to the deviation of simulated concentrations from the observed values, which has been discussed above. The R^2 values were close to 1 in both cases (0.86 in case 1 and 0.88 in case 2) indicating a good correspondence between the simulated and observed TCE concentration in both cases.

The set of parameters used to produce the simulated breakthrough curves in case 1 (Figure 9.5) and case 2 (Figure 9.7) are listed in Table 9-2 and Table 9-3 respectively. As mentioned earlier, the simulation was conducted several times changing some of the transport parameters such as dispersivity and free solution diffusion coefficient until a good match between the observed and simulated break through curves was obtained. The simulated breakthrough curves represented here are the ones that best matched the observed. Note that, similar matches can be obtained using a different combination of transport parameters such as dispersivity and free solution diffusion coefficient, suggesting the non-uniqueness of the parameters.

9.3.3 Conclusion

The purpose of the transport modeling was to investigate whether it is possible to capture the pattern of the observed TCE breakthrough curve in a fractured rock block using:

1) the discrete fracture network modeling approach, in which the fracture geometry and the flow through the system were exact replica of the experimental block and
2) the stochastic continuum modeling approach, in which the model domain was treated as a porous medium.

The discrete fracture network modeling approach captured the pattern of the TCE breakthrough curve based on the experiments in this fractured rock block quite well. On the other hand, the stochastic continuum modeling approach also captured the overall pattern of TCE breakthrough curve despite some early time deviation.

These studies are still at the early stage and were conducted under laboratory conditions in a controlled environment. The experimental block and the flow through the system were well

characterized through the hydraulic and tracer experiments. Thus small scale field experiment is required to validate these approaches to predict DNAPL plume behavior in the field. However, it would be very expensive and time consuming to model TCE dissolution in the field using the discrete fracture approach, as it requires detailed deterministic and statistical information of the geometry of fractured zone and the spatial distribution of fracture apertures, which information are not available between boreholes. On the other hand, stochastic continuum approach could be comparatively less expensive and time consuming, as it does not require these detail information about the spatial distribution of fractures.

Chapter 10
Conclusions and Recommendations

10.1 Conclusions

The main conclusions of this thesis are presented in two groups; 1) conclusions from transient hydraulic tomography (THT) analysis in a fractured rock and 2) conclusions from the TCE dissolution experiment and dissolution modeling.

Conclusions from the transient hydraulic tomography (THT) analysis are –

- It is possible to delineate discrete fractures, their pattern and connectivity of a laboratory scale fractured rock by careful application of THT analysis of multiple pumping tests along with the inverse code SSLE developed by *Zhu and Yeh* [2005]. The high hydraulic conductivity (K) and low specific storage (S_s) zone clearly showed the fractures and their connectivity.
- Estimated K and S_s values for the fractures and the matrix may not exactly replicate the actual K and S_s values for the fractured rock but the model also provides uncertainty estimates associated with the resulting K and S_s tomograms.
- The estimated K and S_s tomograms were able to capture the observed drawdown behaviors at the monitoring ports, while conducted the independent pumping tests using the estimates from THT analysis, indicating the soundness of the estimates.
- Changing the location of the 2nd and 3rd pumping tests did not have significantly impact on the estimates. However, Initial pumping tests must be selected carefully based on their ability to stress the entire aquifer.
- THT appears to be a promising approach to delineate fracture pattern given that the study was conducted based on the laboratory experiment in a controlled environment. However, the study is still at the early stage and small scale field experiment needs to be conducted to validate THT as a tool to characterize the fractured rock.

Conclusions from TCE dissolution experiment and dissolution modeling studies are –

- Both the discrete fracture network approach and the stochastic continuum approach appear to be promising in capturing the pattern of the TCE breakthrough curve based on the laboratory experiments in the fractured rock. In stochastic continuum approach, some early time deviation was evident, but the simulated breakthrough curve captured the overall observed pattern of TCE breakthrough.
- Note that, the studies were conducted based on a laboratory experiment conducted in a controlled environment. The experimental block and the flow through the system were well characterized through the hydraulic and tracer experiments.

10.2 Recommendations

Some recommendations for future works are listed below-

- Application of THT to small scale field site to characterize a fractured rock aquifer.
- Inclusion of pumping test data for a longer period of time.
- Inclusion and assessment of different pumping strategies such as cross-hole and single-hole tests.
- Simulation of TCE dissolution using equivalent porous medium approach as well as for different spatial distributions of fractures using discrete fracture approach to investigate if the observed pattern of the break-through curve can be captured.
- Conducting a small scale TCE dissolution experiment in the field to observe the dissolution behavior and model the dissolution using different approaches to validate the laboratory scale studies in the field.

Appendix A

Pumping Test Data

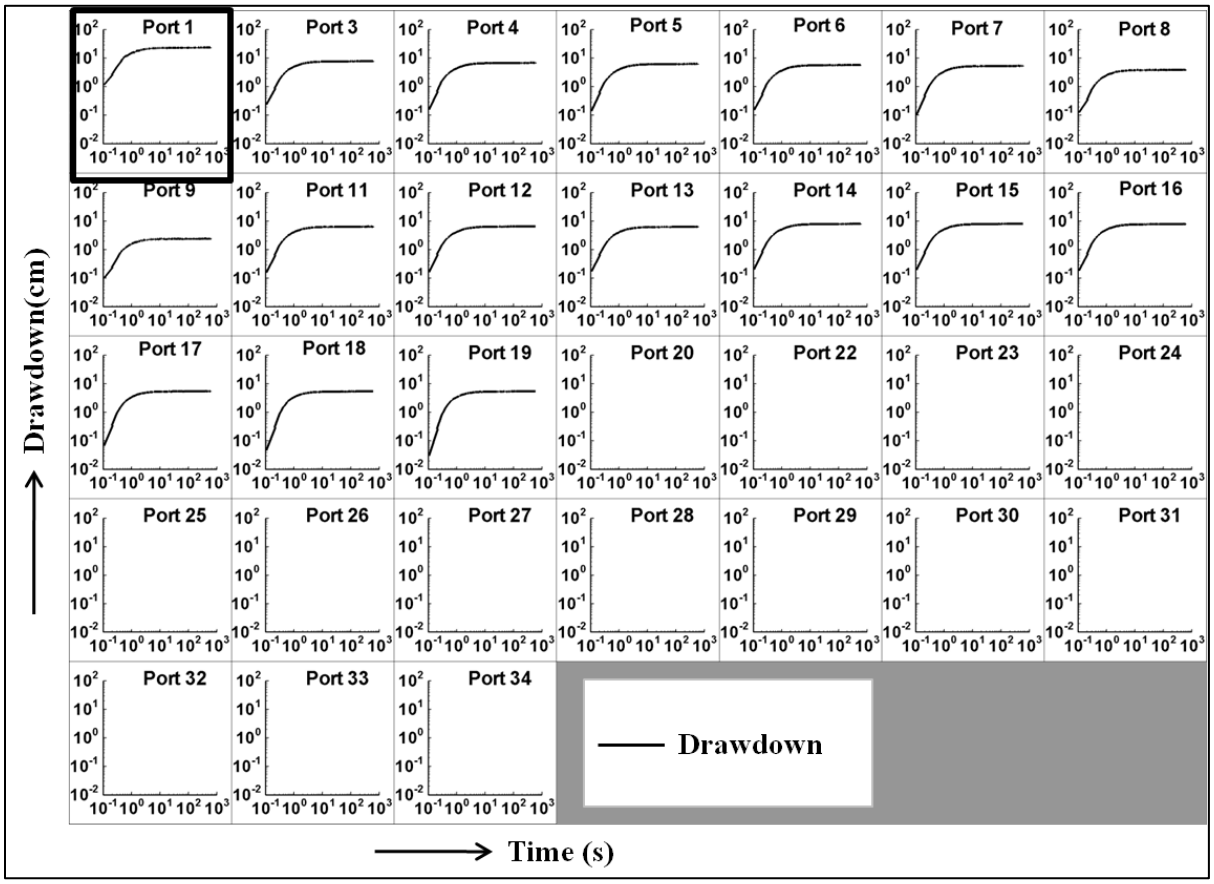

Figure A1: Observed drawdown at fracture and matrix ports during a pumping test at port 1. The pumped port is indicated by the black rectangular box.

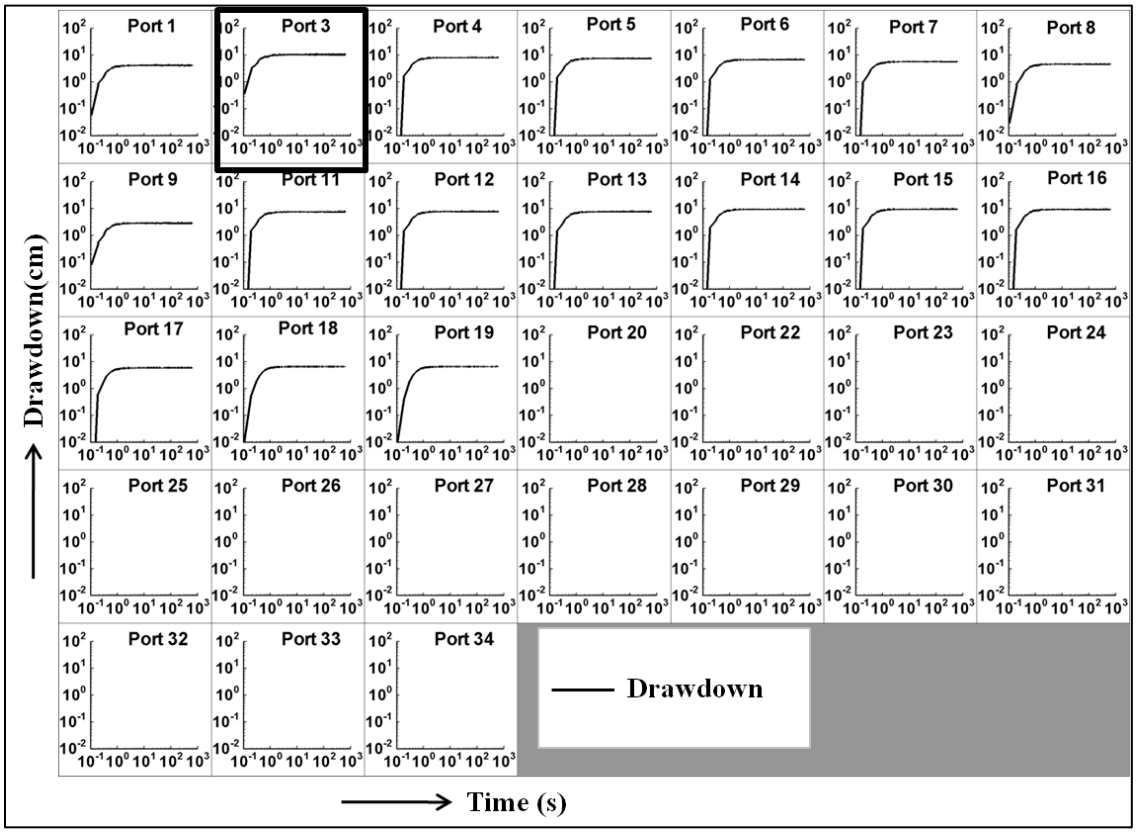

Figure A2: Observed drawdown at fracture and matrix ports during a pumping test at port 3. The pumped port is indicated by the black rectangular box.

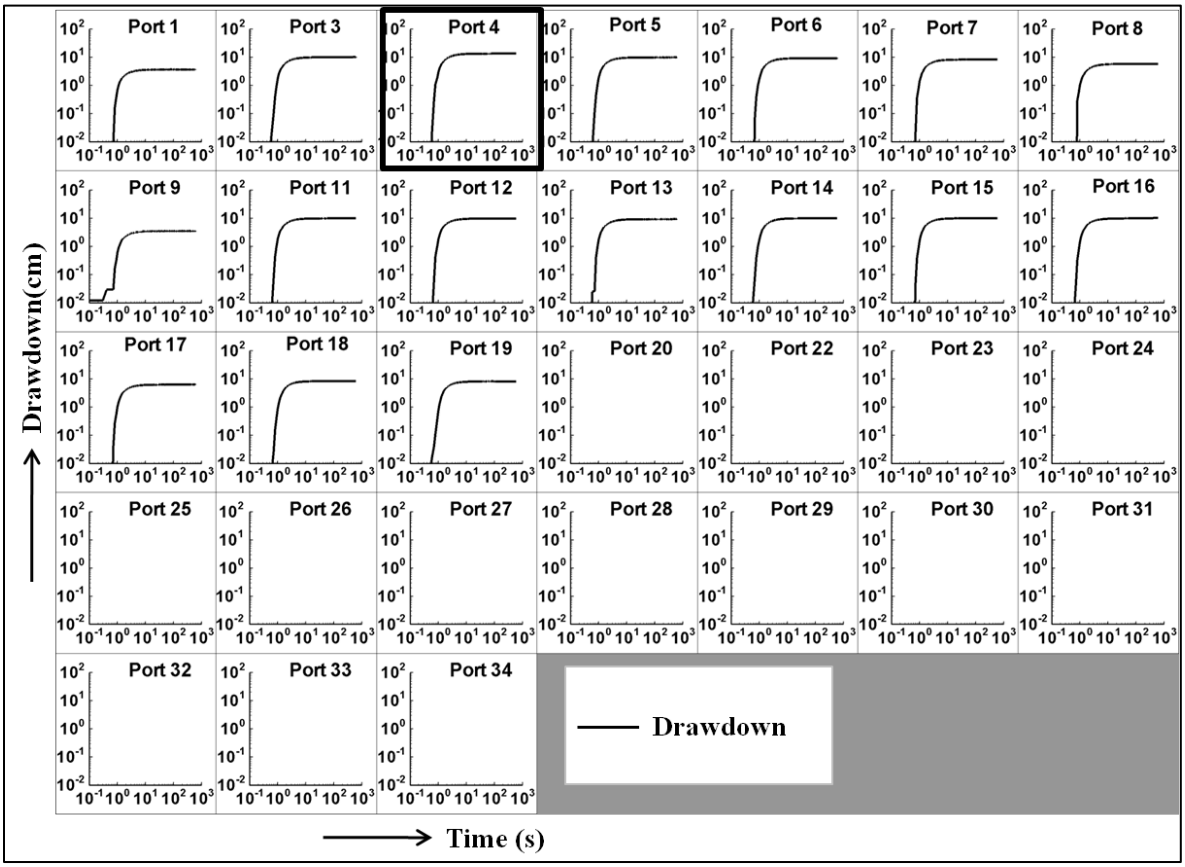

Figure A3: Observed drawdown at fracture and matrix ports during a pumping test at port 4. The pumped port is indicated by the black rectangular box.

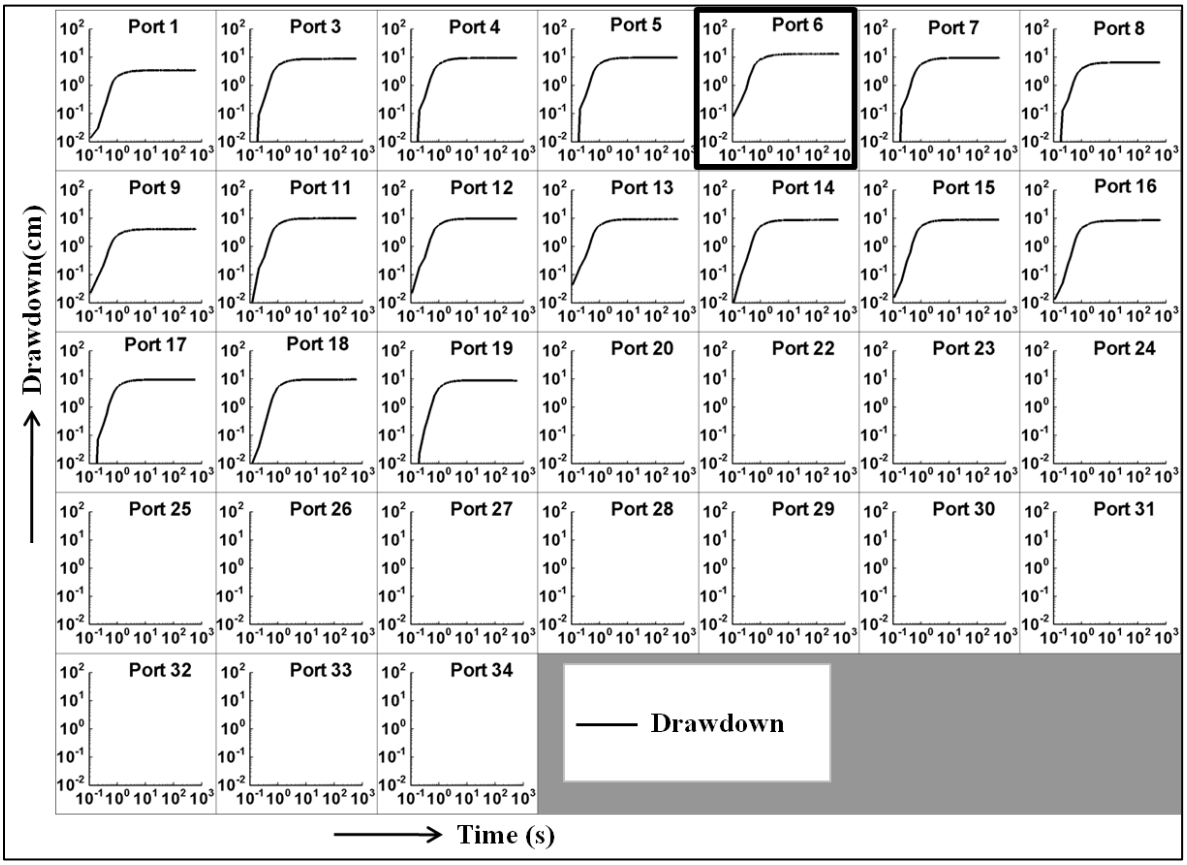

Figure A4: Observed drawdown at fracture and matrix ports during a pumping test at port 6. The pumped port is indicated by the black rectangular box.

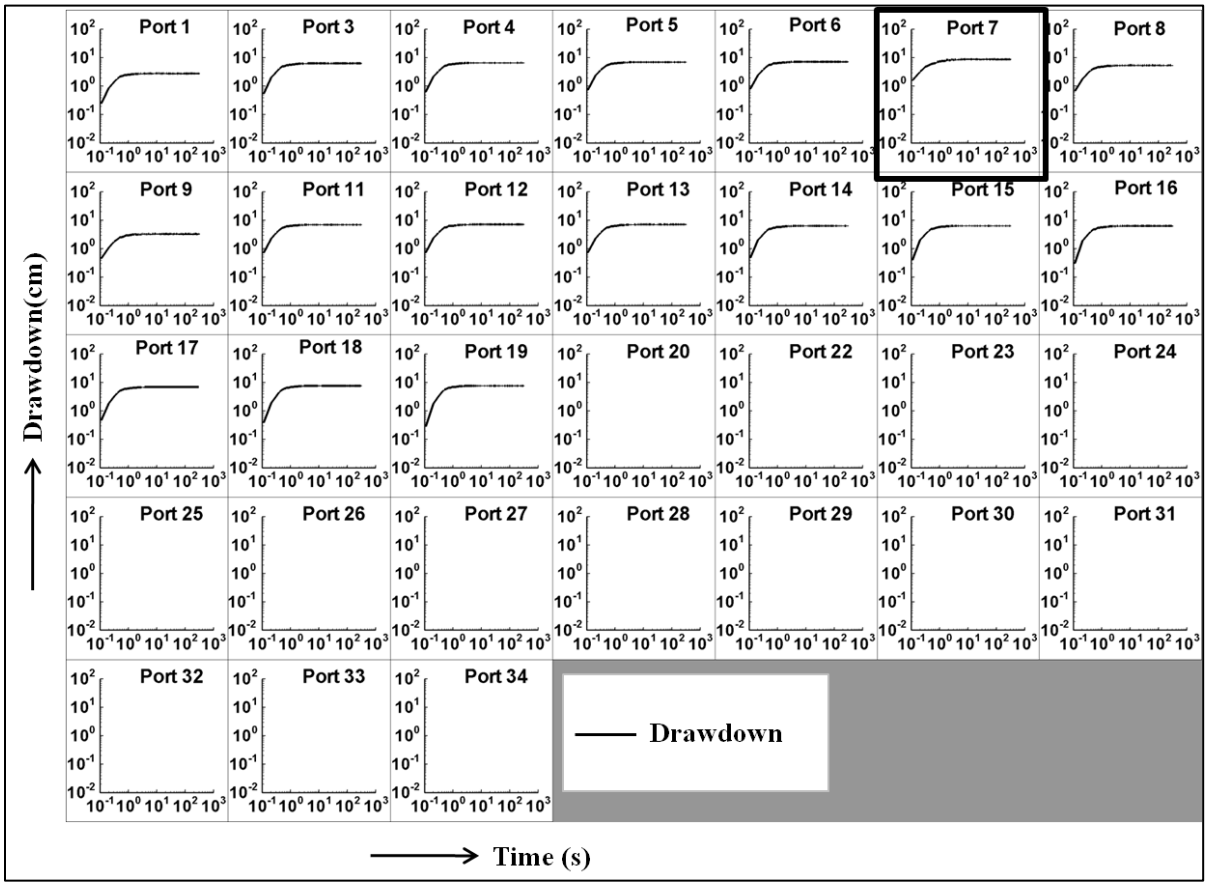

Figure A5: Observed drawdown at fracture and matrix ports during a pumping test at port 7. The pumped port is indicated by the black rectangular box.

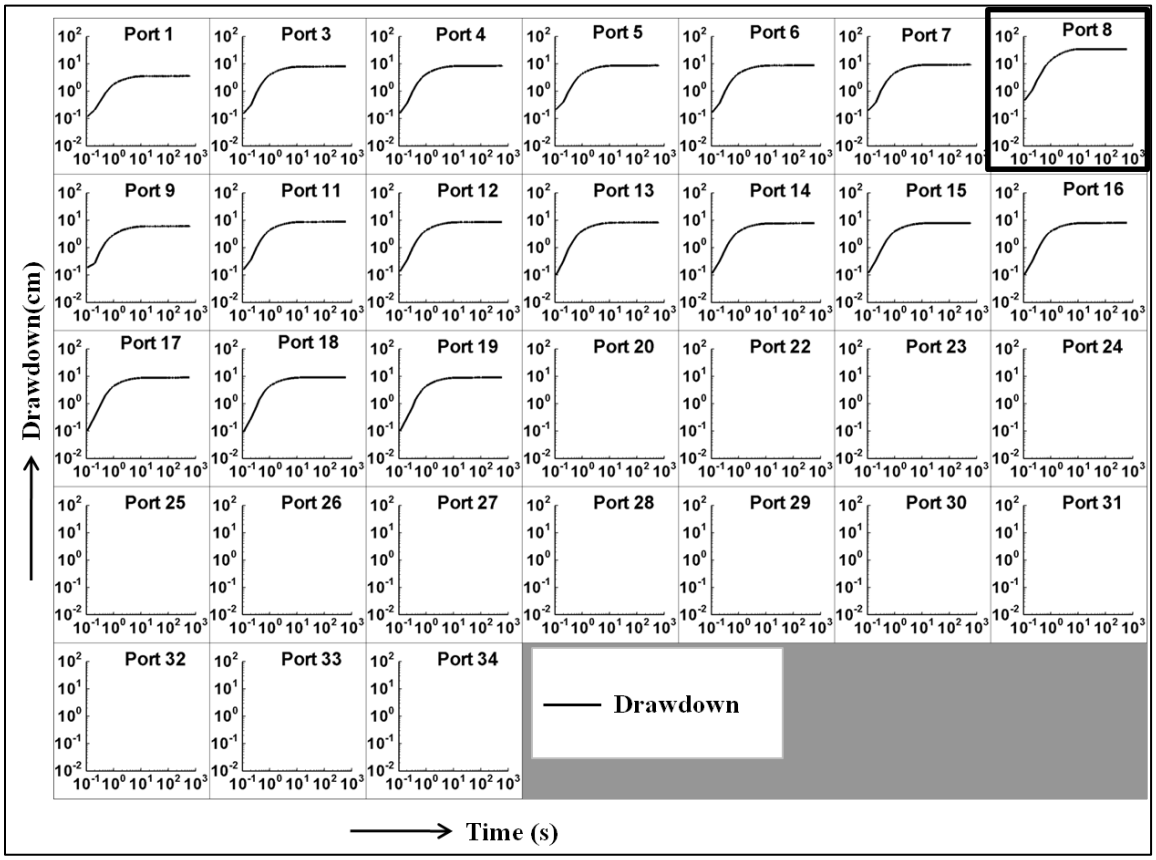

Figure A6: Observed drawdown at fracture and matrix ports during a pumping test at port 8. The pumped port is indicated by the black rectangular box.

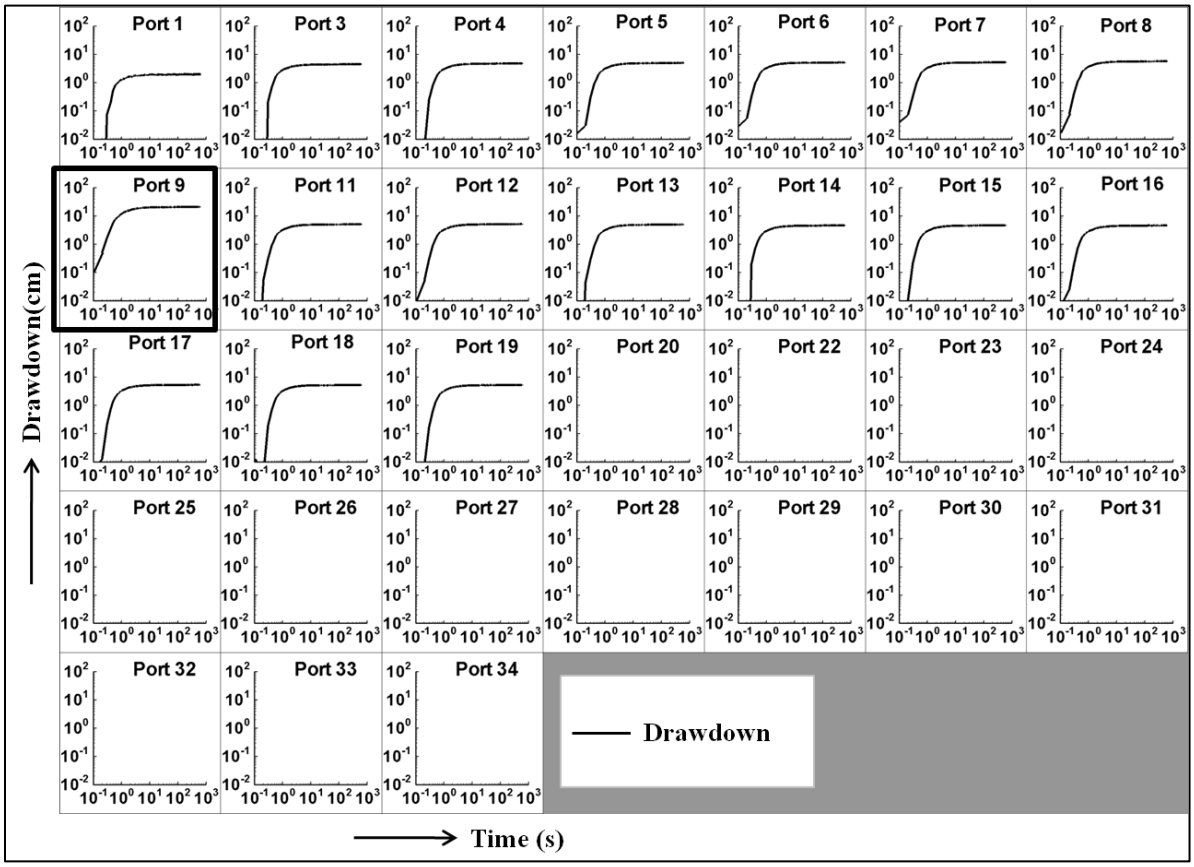

Figure A7: Observed drawdown at fracture and matrix ports during a pumping test at port 9. The pumped port is indicated by the black rectangular box.

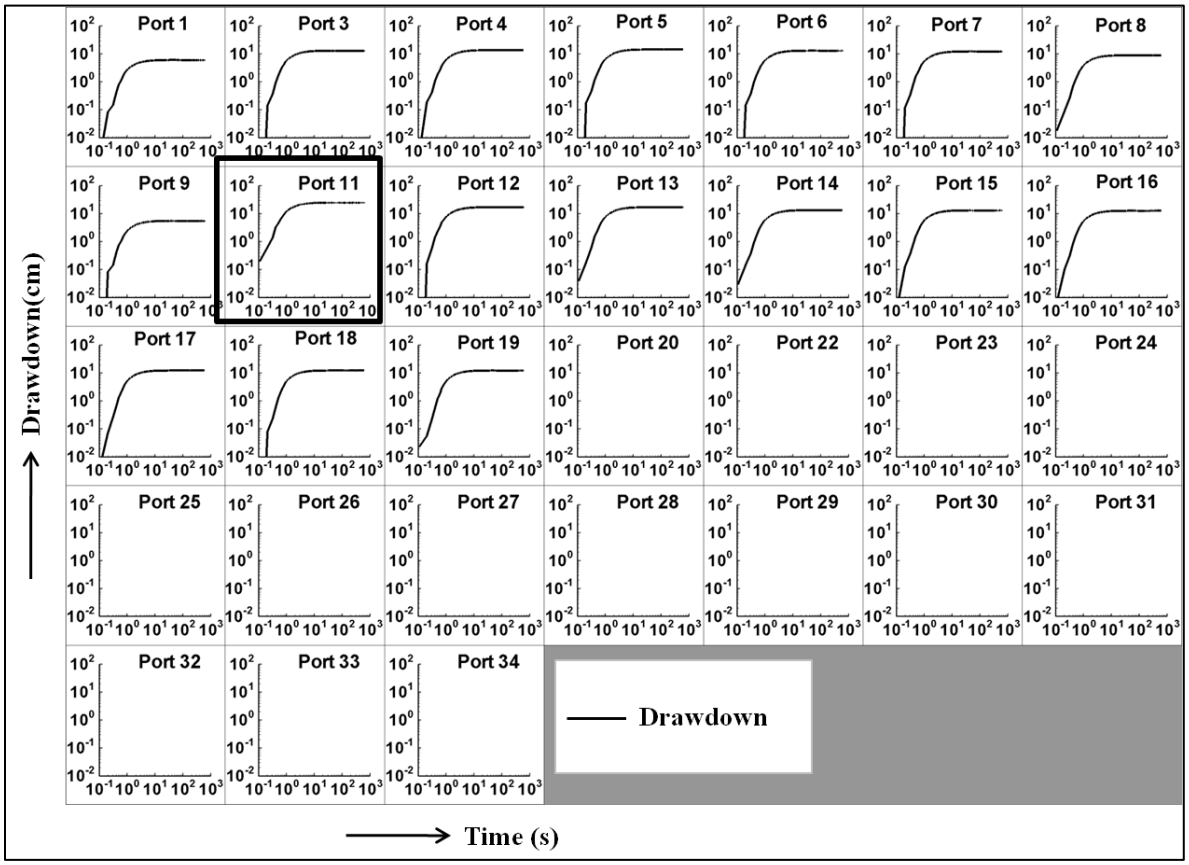

Figure A8: Observed drawdown at fracture and matrix ports during a pumping test at port 11. The pumped port is indicated by the black rectangular box.

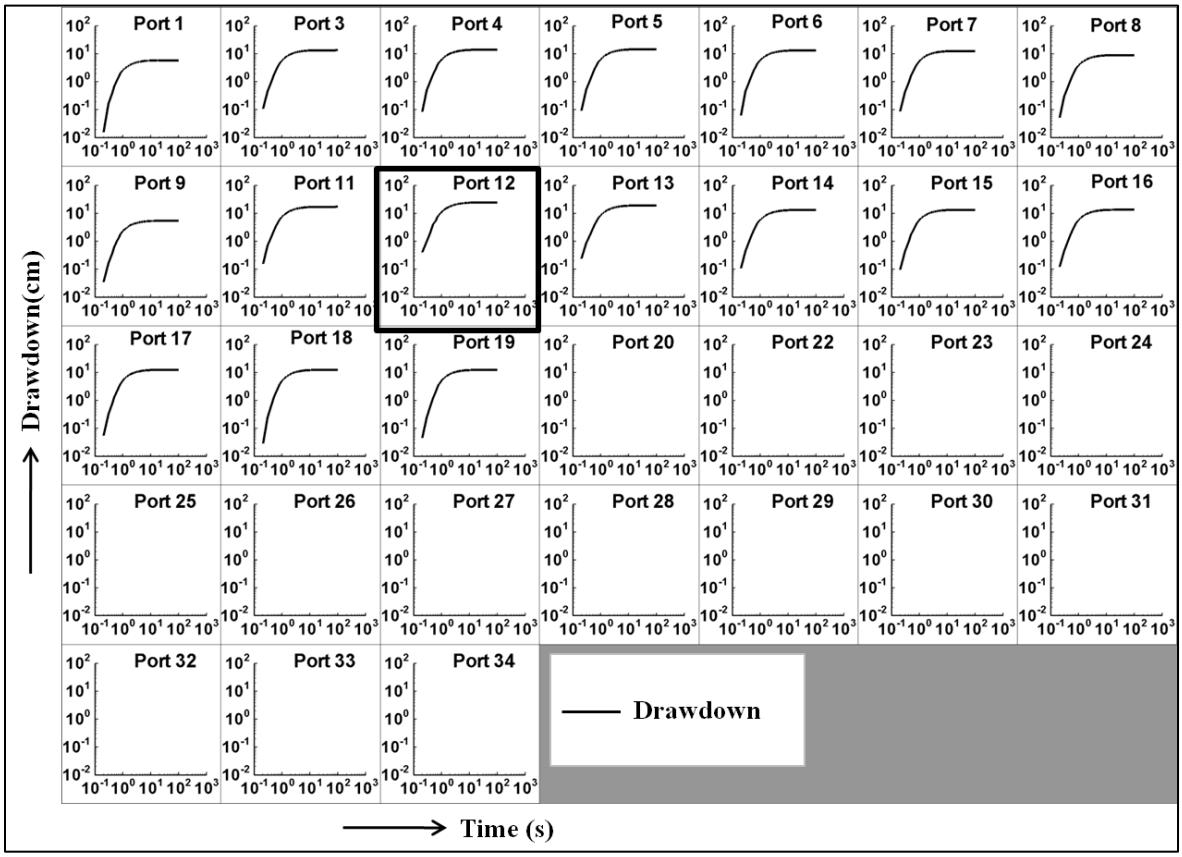

Figure A9: Observed drawdown at fracture and matrix ports during a pumping test at port 12. The pumped port is indicated by the black rectangular box.

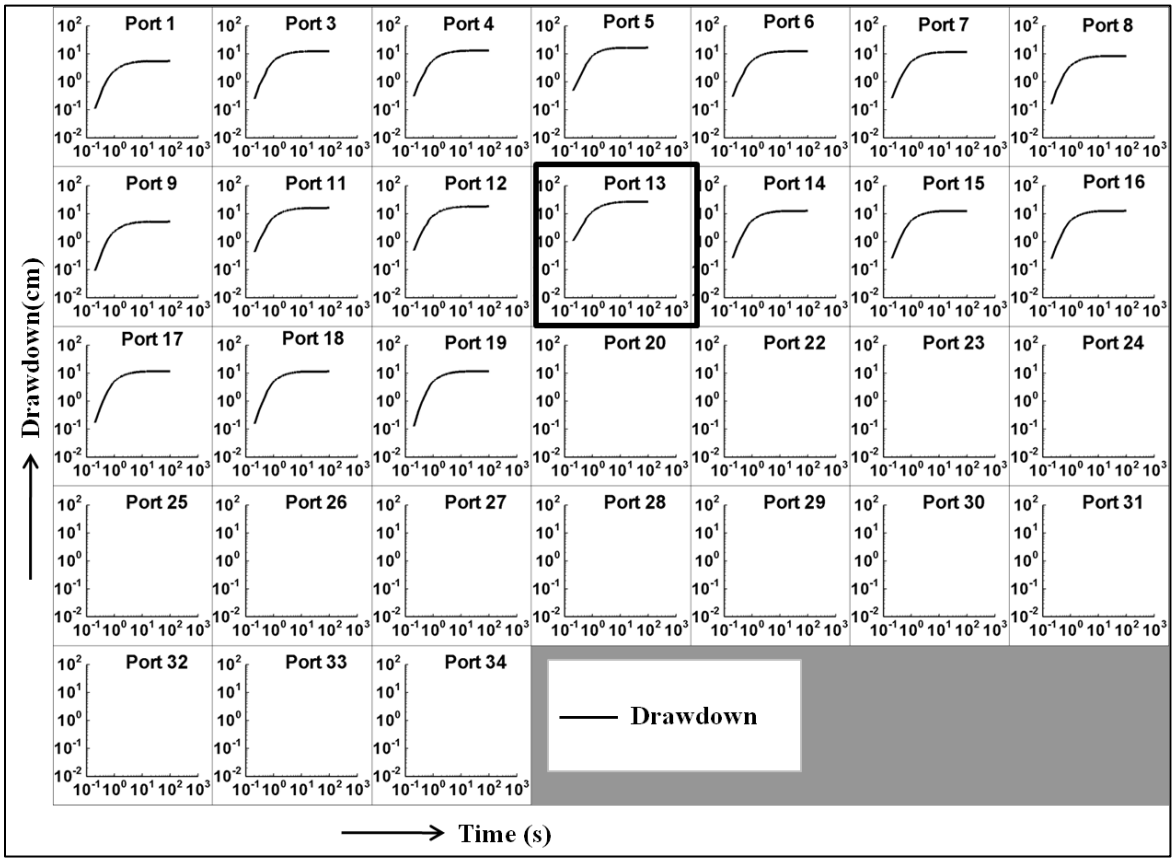

Figure A10: Observed drawdown at fracture and matrix ports during a pumping test at port 13. The pumped port is indicated by the black rectangular box.

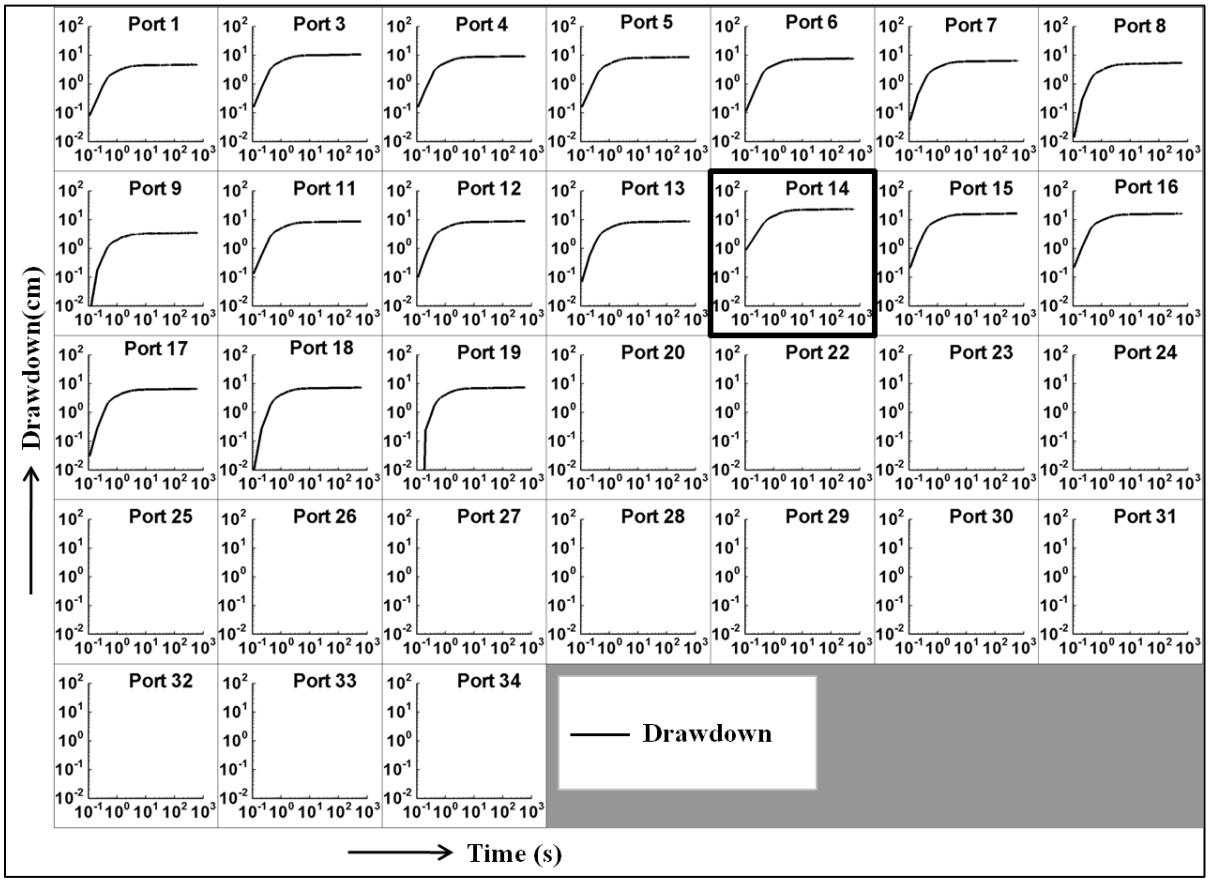

Figure A11: Observed drawdown at fracture and matrix ports during a pumping test at port 14. The pumped port is indicated by the black rectangular box.

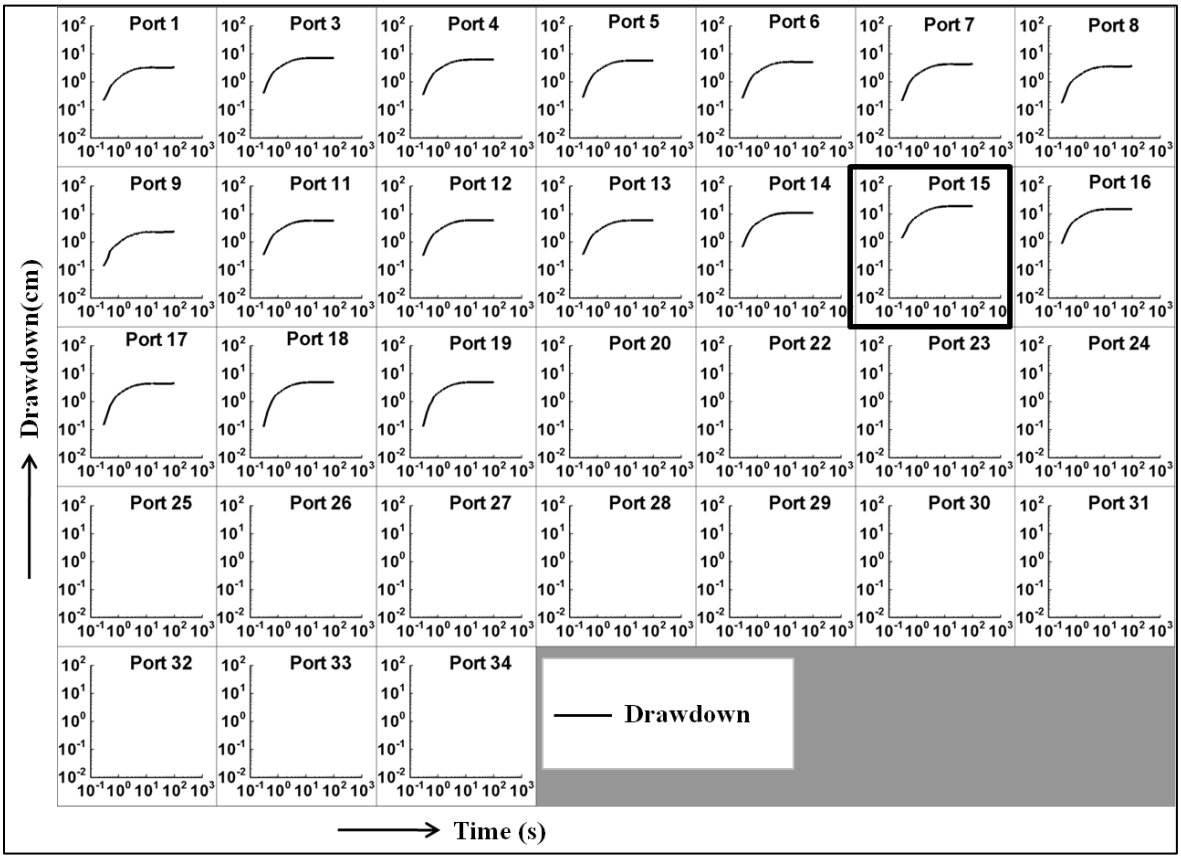

Figure A12: Observed drawdown at fracture and matrix ports during a pumping test at port 15. The pumped port is indicated by the black rectangular box.

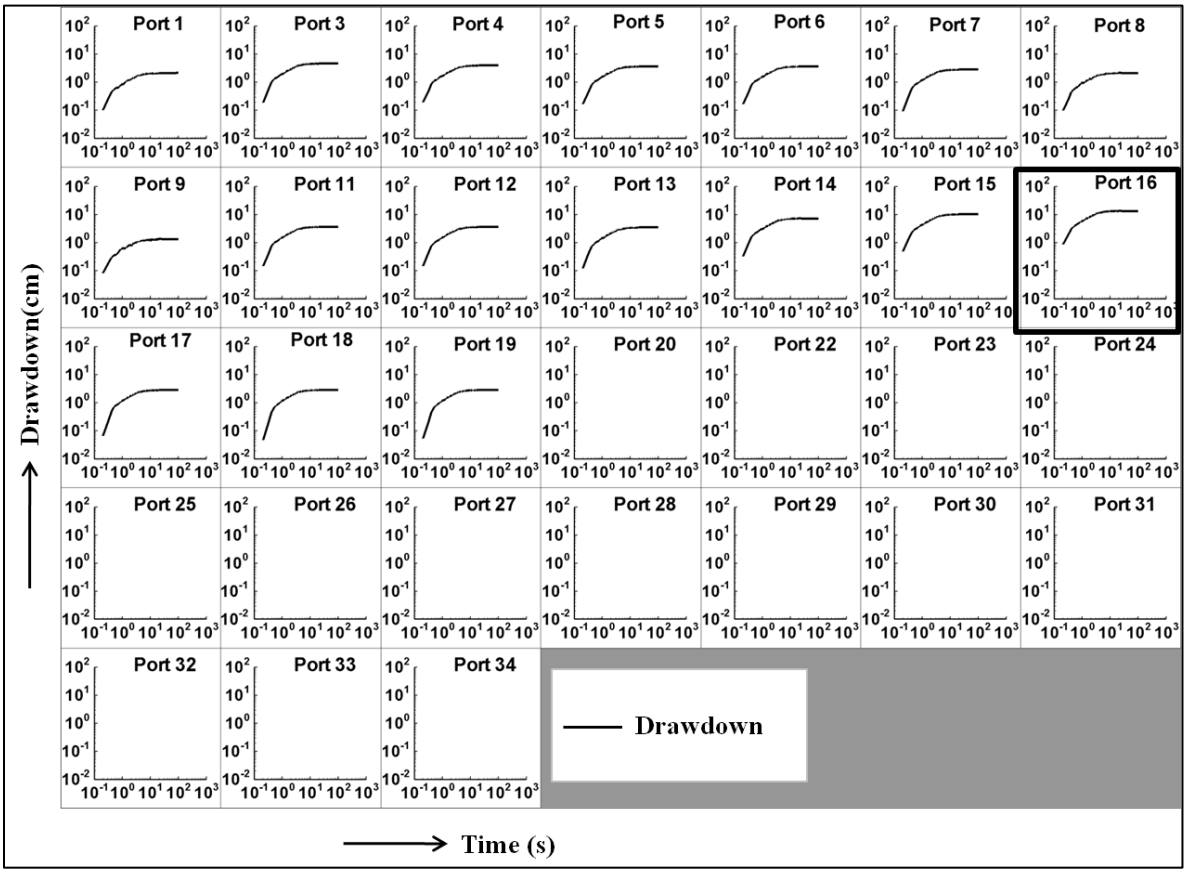

Figure A13: Observed drawdown at fracture and matrix ports during a pumping test at port 16. The pumped port is indicated by the black rectangular box.

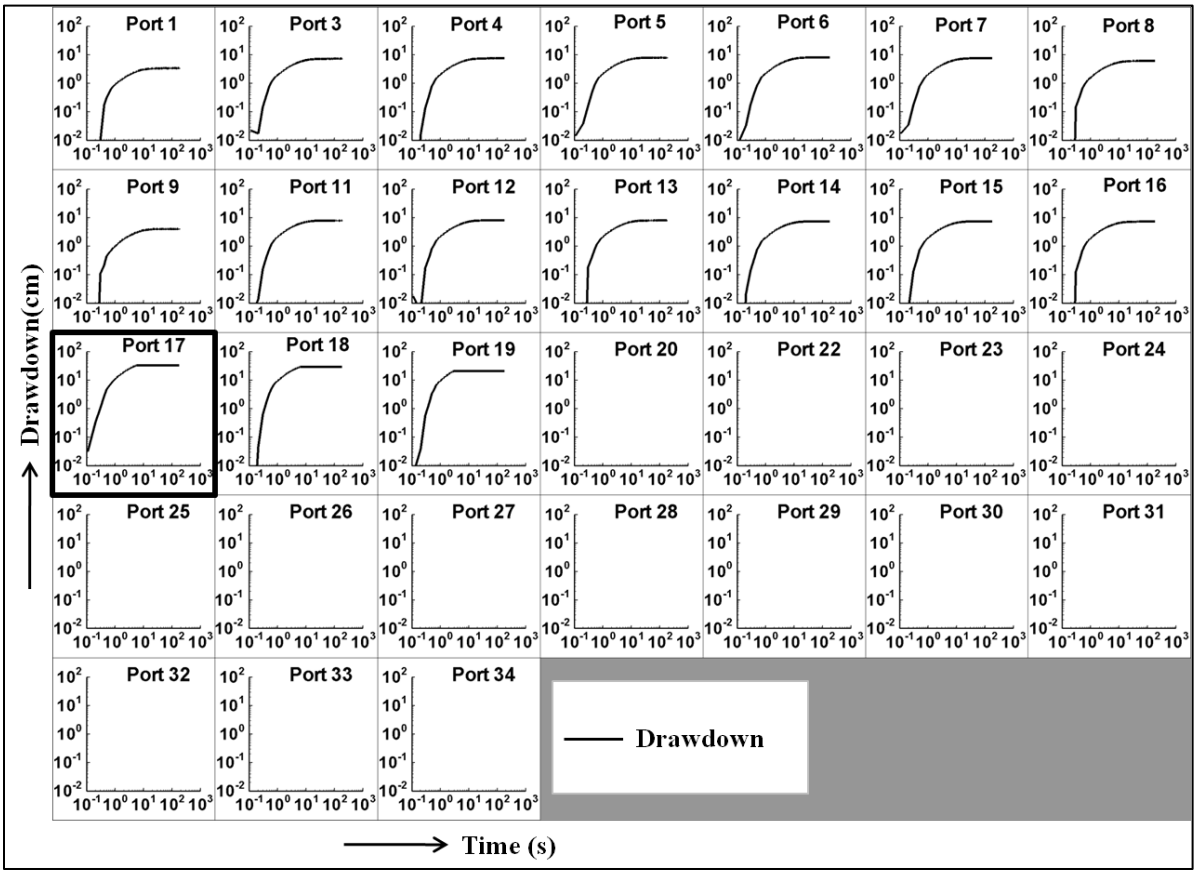

Figure A14: Observed drawdown at fracture and matrix ports during a pumping test at port 17. The pumped port is indicated by the black rectangular box.

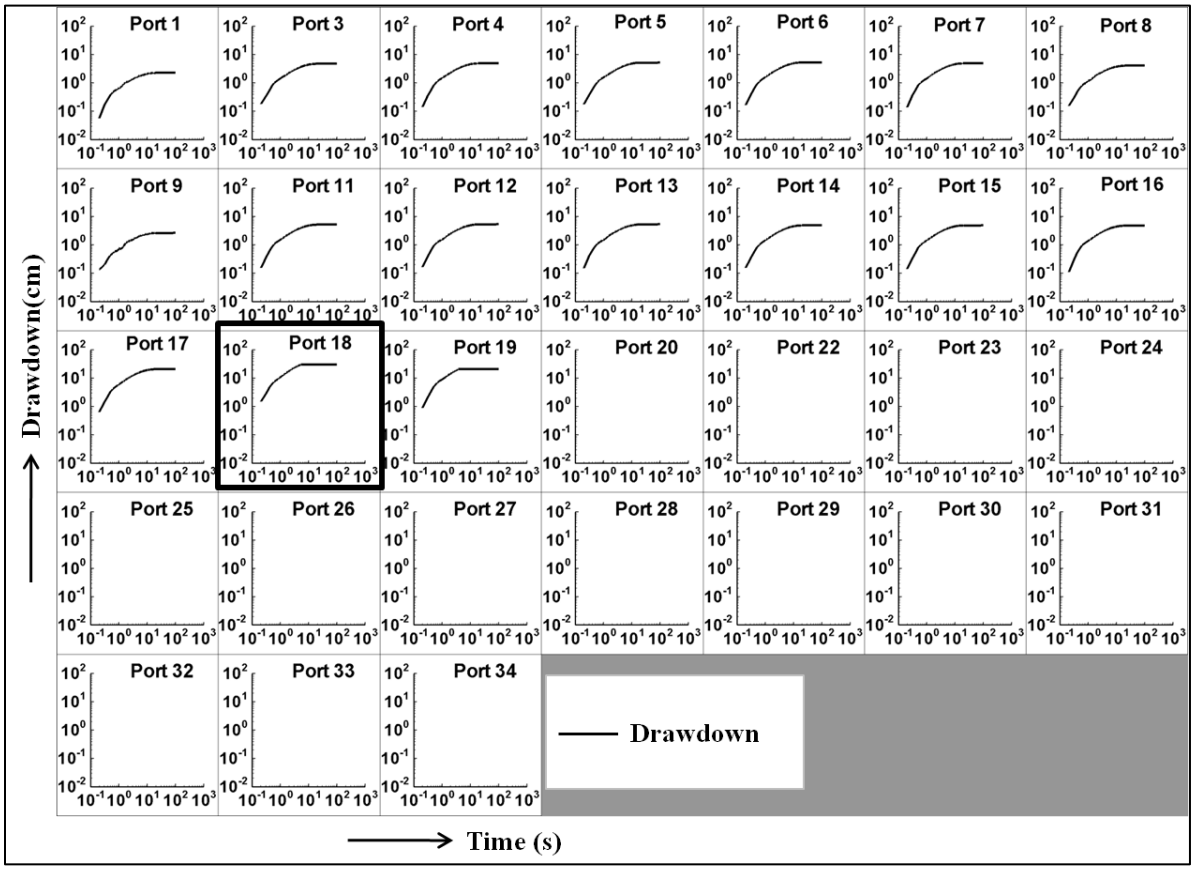

Figure A15: Observed drawdown at fracture and matrix ports during a pumping test at port 18. The pumped port is indicated by the black rectangular box.

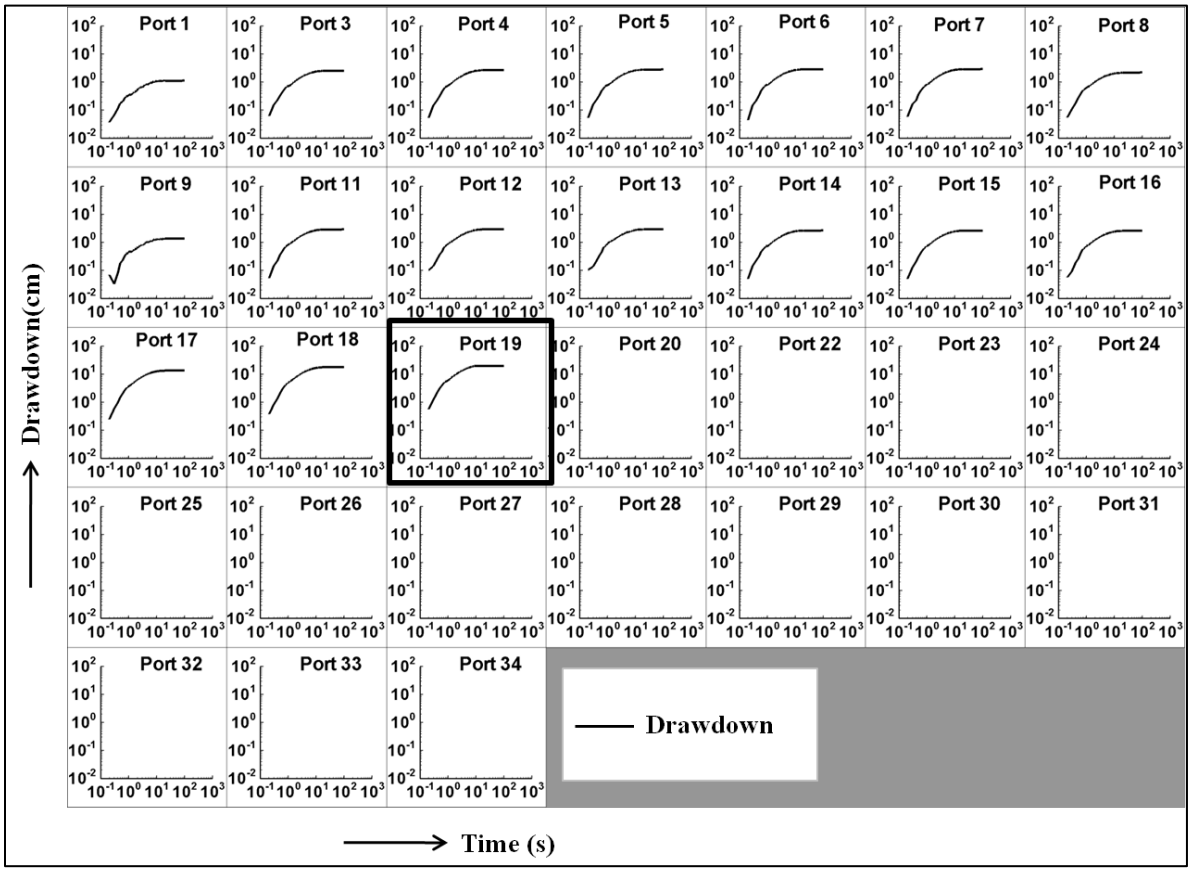

Figure A16: Observed drawdown at fracture and matrix ports during a pumping test at port 19. The pumped port is indicated by the black rectangular box.

Appendix B

Pumping Tests Conducted using HGS

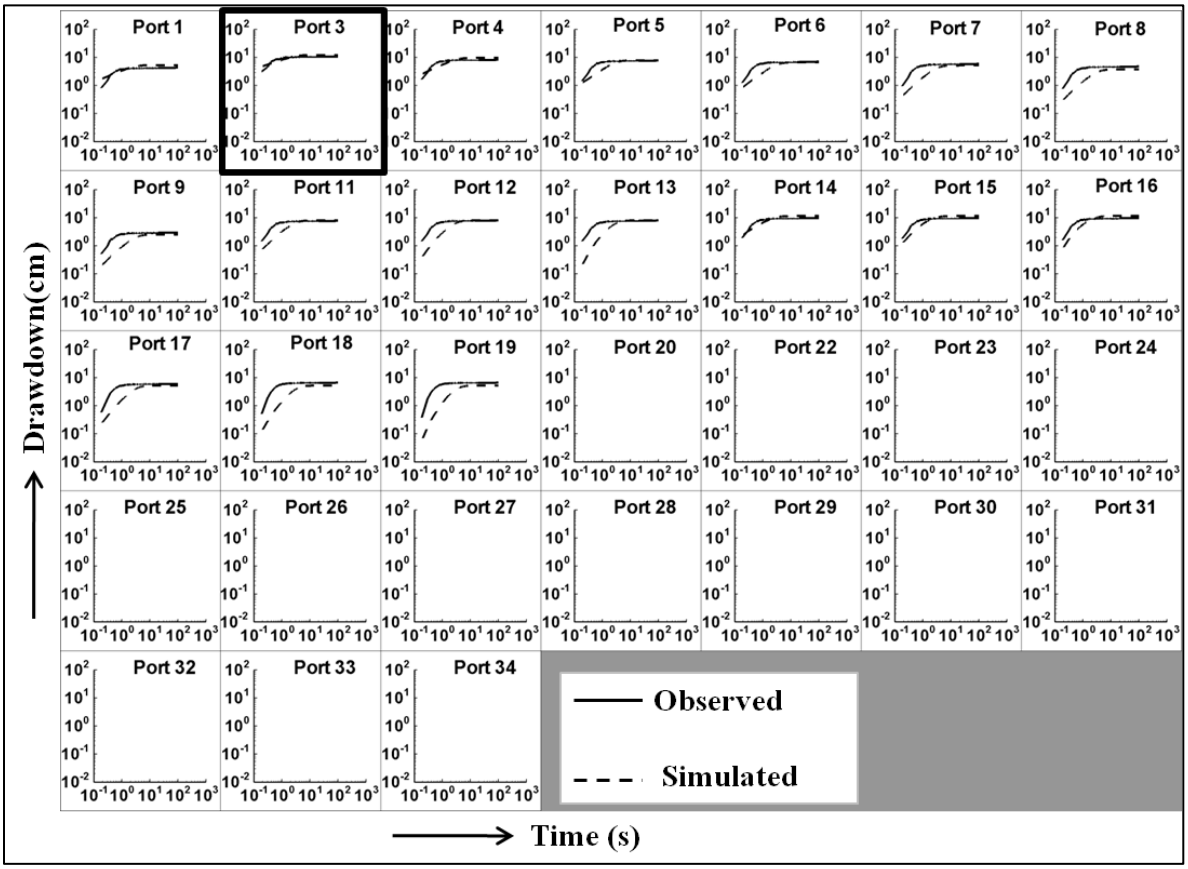

Figure B1: Observed and Simulated Drawdown during Pumping Test at Port 3. The solid line represents observed drawdown and the dashed line represents simulated drawdown. The pumped port is indicated by the black rectangular box.

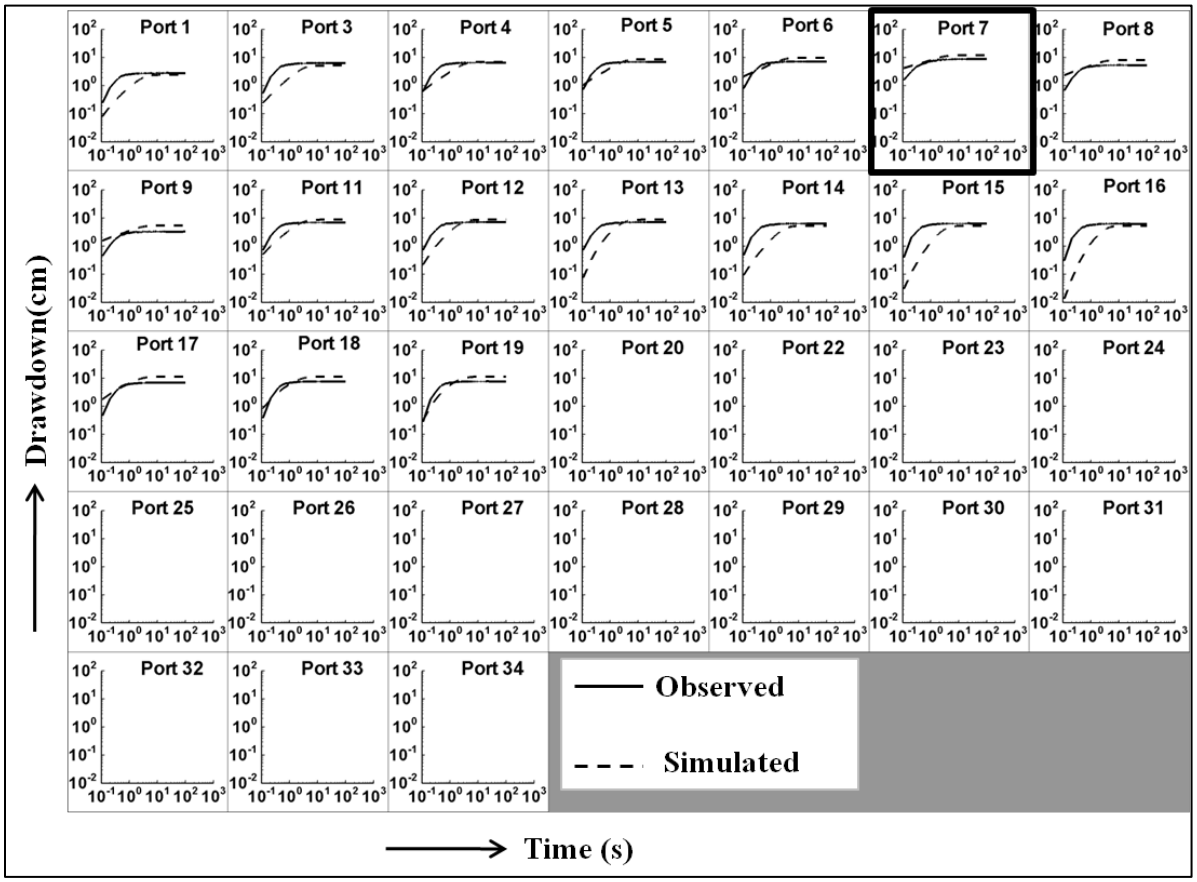

Figure B2: Observed and Simulated Drawdown during Pumping Test at Port 7. The solid line represents observed drawdown and the dashed line represents simulated drawdown. The pumped port is indicated by the black rectangular box.

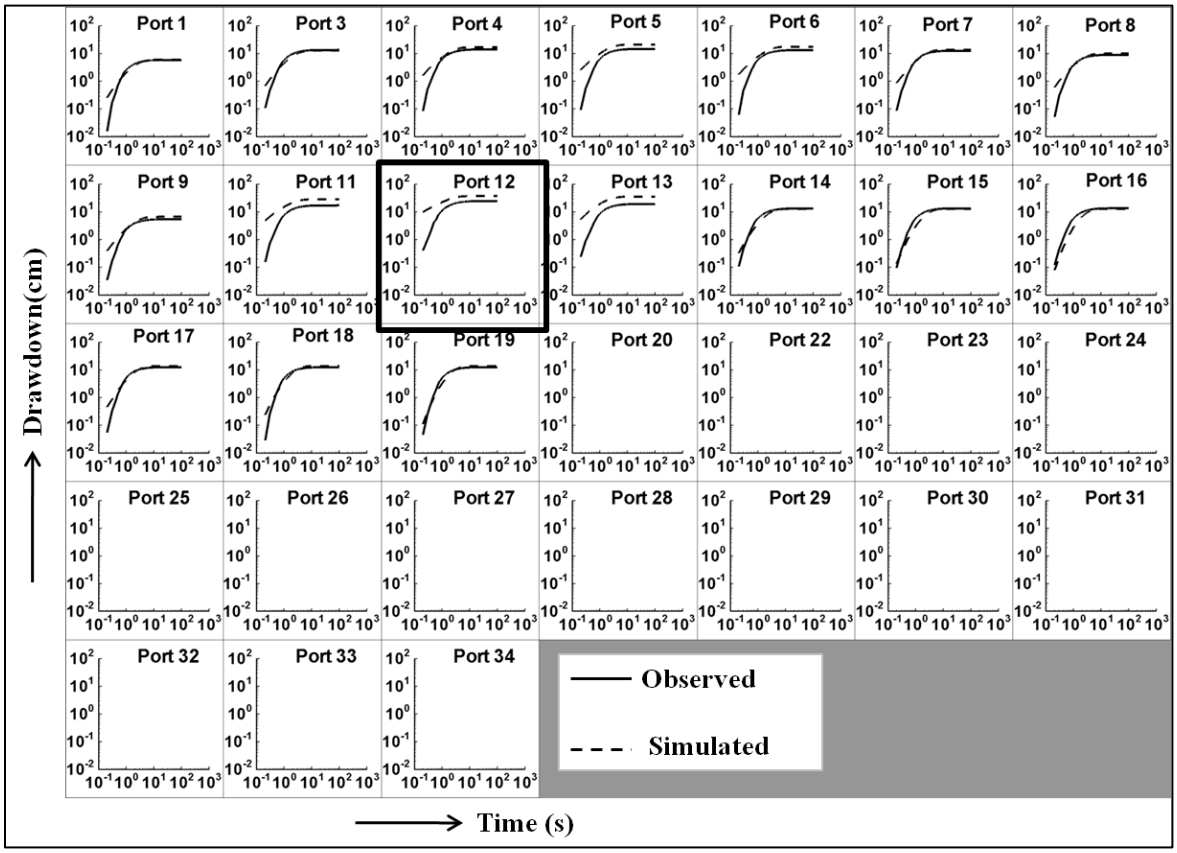

Figure B3: Observed and Simulated Drawdown during Pumping Test at Port 12. The solid line represents observed drawdown and the dashed line represents simulated drawdown. The pumped port is indicated by the black rectangular box.

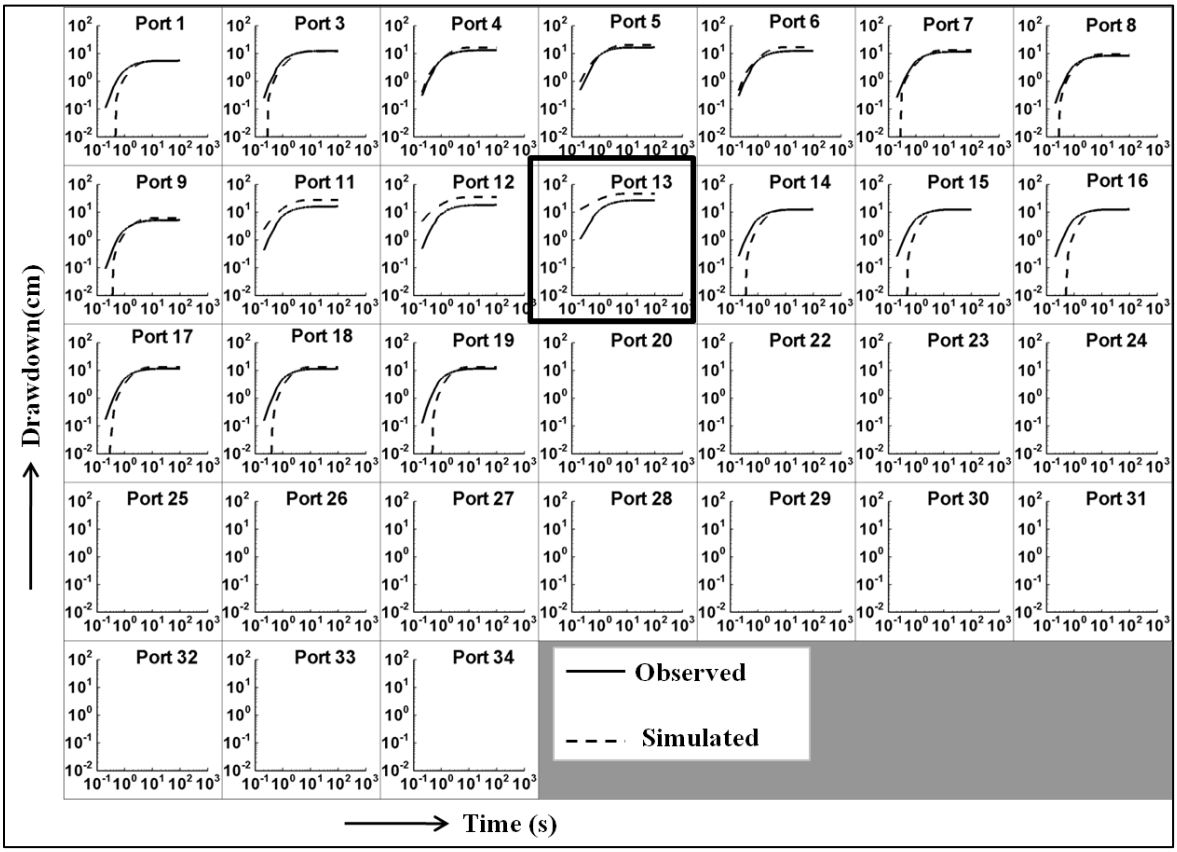

Figure B4: Observed and Simulated Drawdown during Pumping Test at Port 13. The solid line represents observed drawdown and the dashed line represents simulated drawdown. The pumped port is indicated by the black rectangular box.

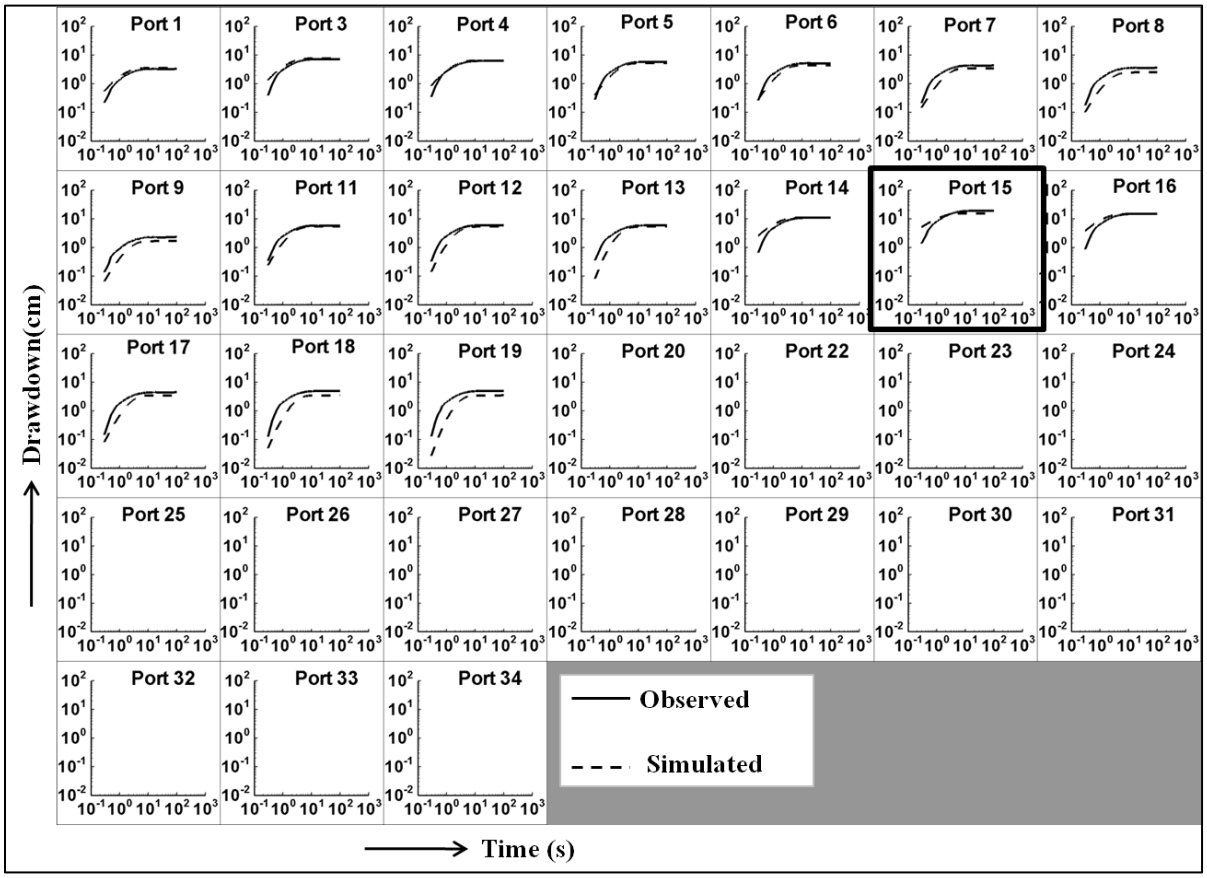

Figure B5: Observed and Simulated Drawdown during Pumping Test at Port 15. The solid line represents observed drawdown and the dashed line represents simulated drawdown. The pumped port is indicated by the black rectangular box.

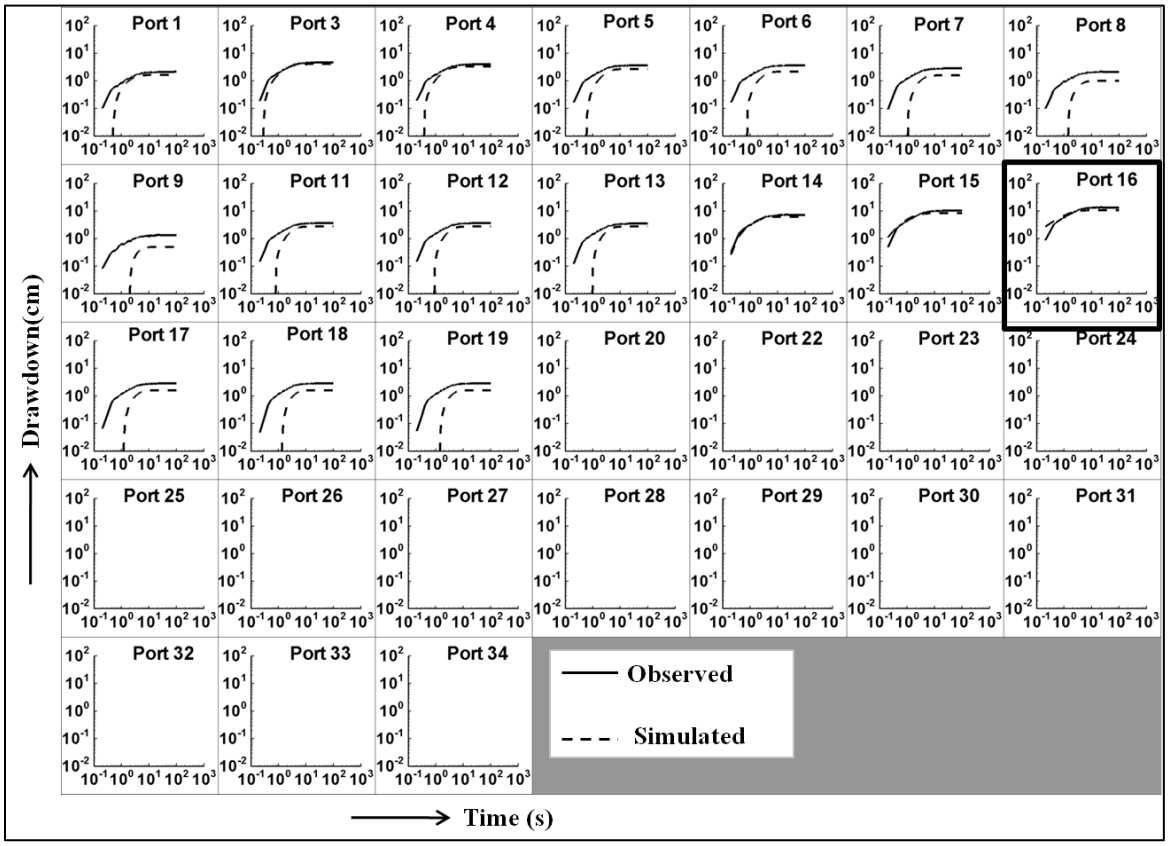

Figure B6: Observed and Simulated Drawdown during Pumping Test at Port 16. The solid line represents observed drawdown and the dashed line represents simulated drawdown. The pumped port is indicated by the black rectangular box.

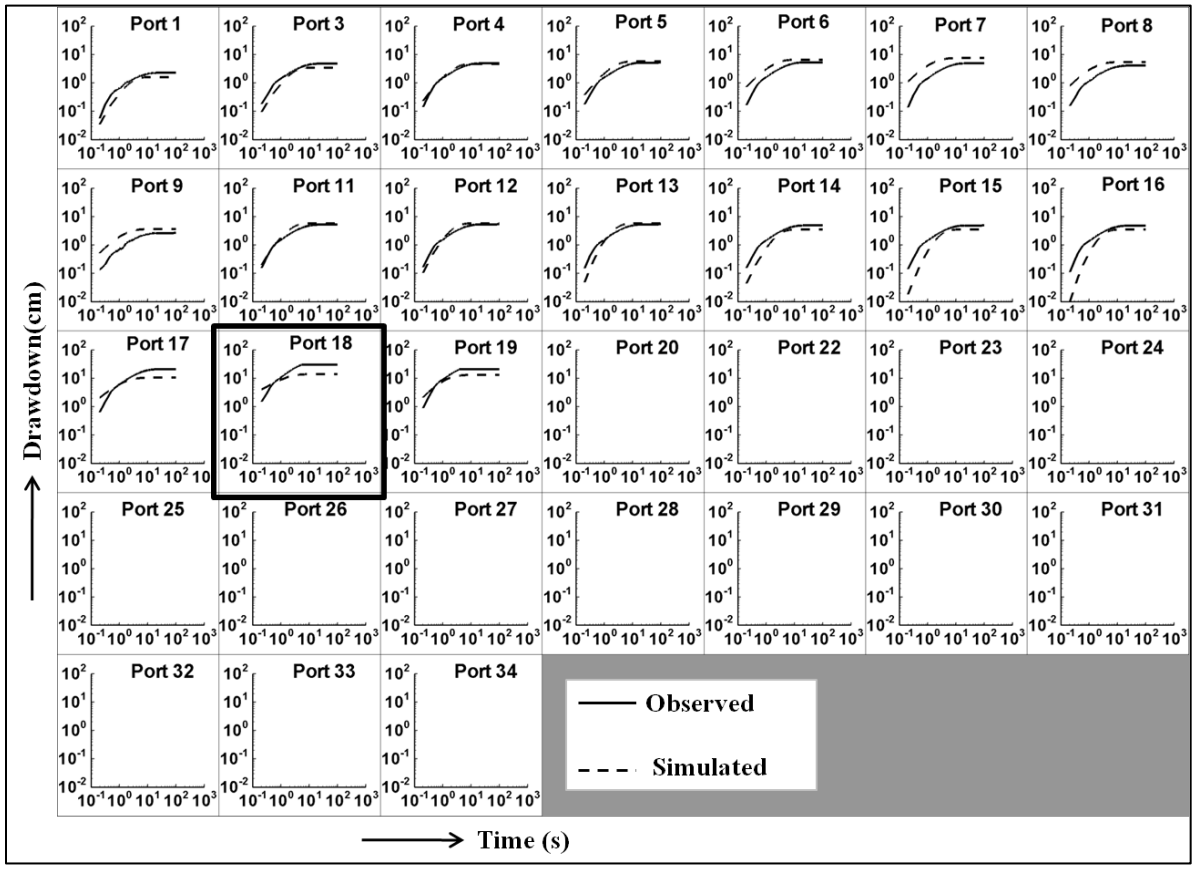

Figure B7: Observed and Simulated Drawdown during Pumping Test at Port 18. The solid line represents observed drawdown and the dashed line represents simulated drawdown. The pumped port is indicated by the black rectangular box.

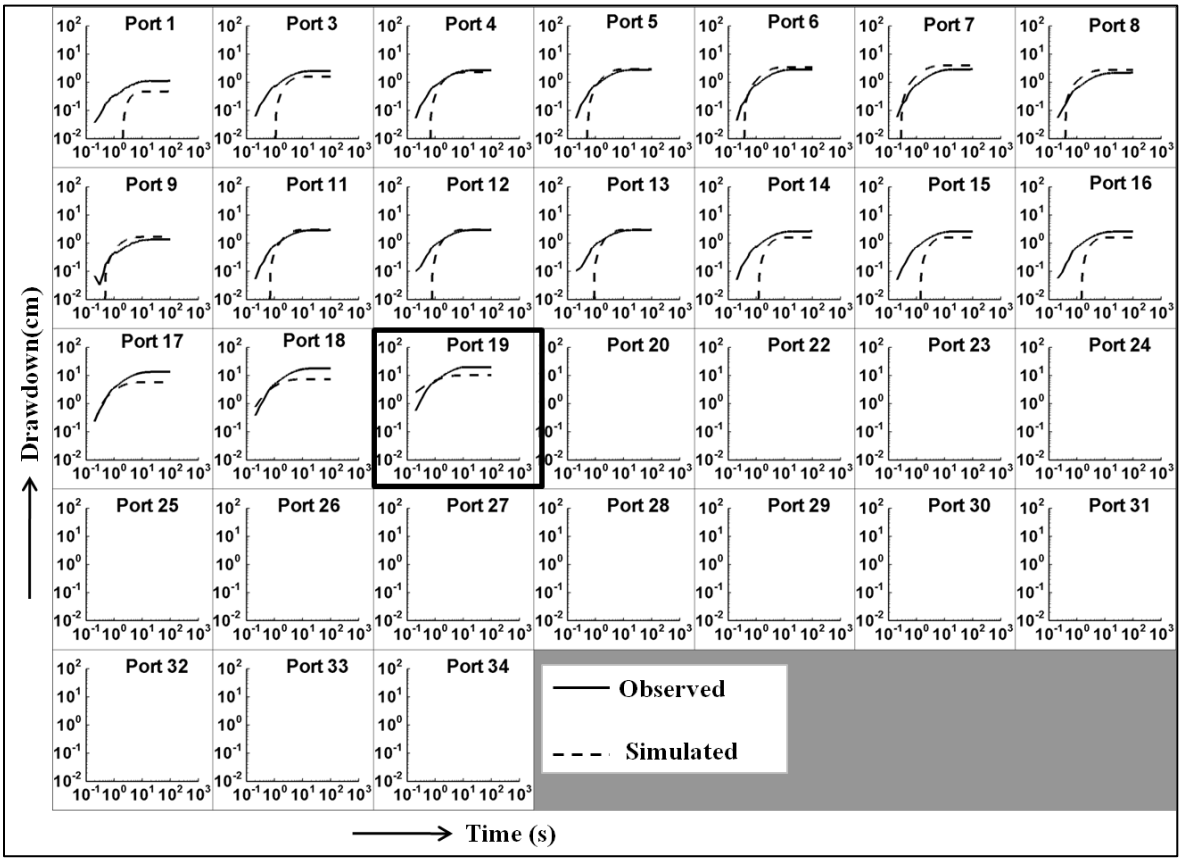

Figure B8: Observed and Simulated Drawdown during Pumping Test at Port 19. The solid line represents observed drawdown and the dashed line represents simulated drawdown. The pumped port is indicated by the black rectangular box.

Appendix C

Drawdown Data Included in the Inverse Model

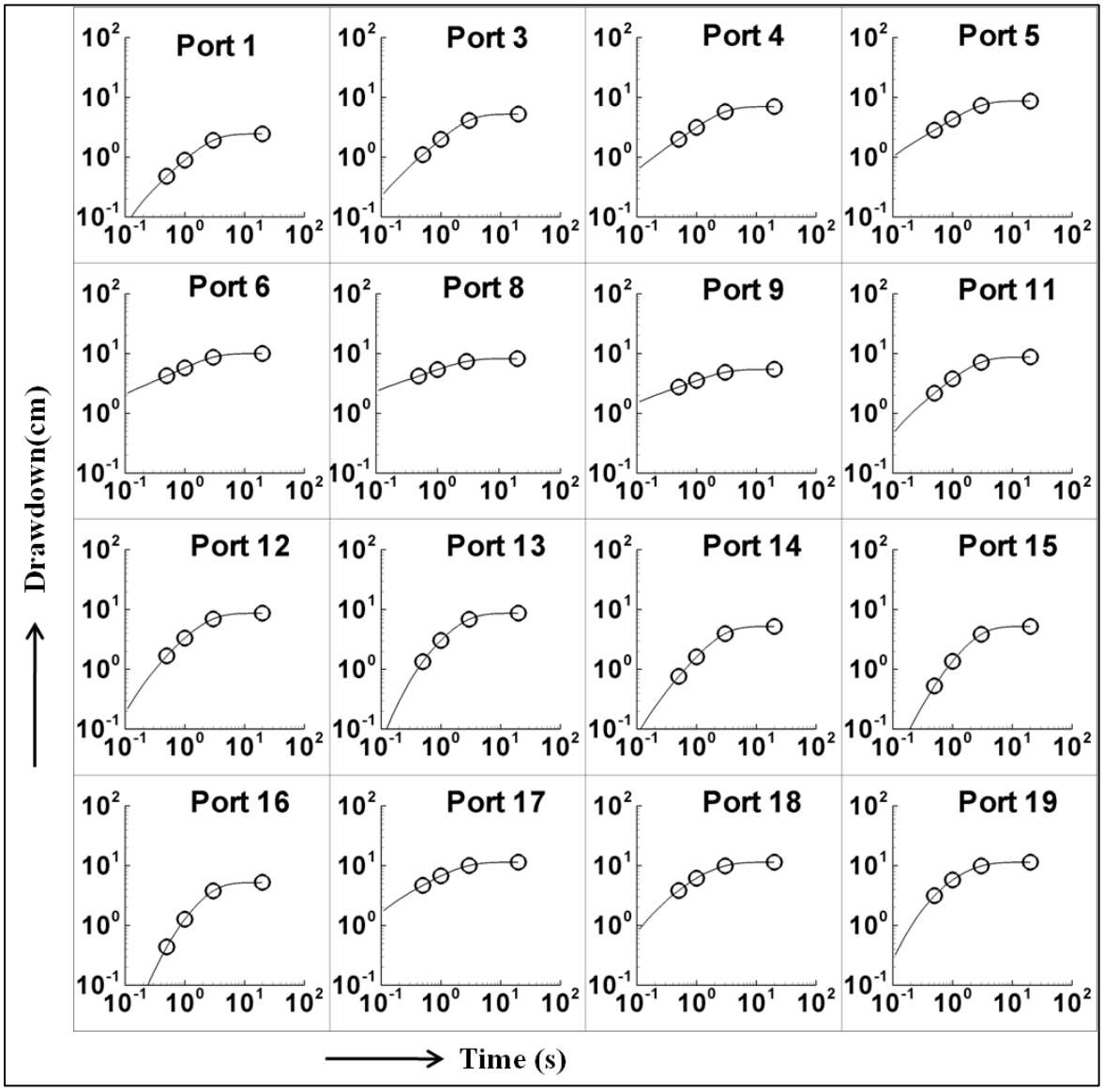

Figure C1: Selected Data Points at the Fracture Observation Ports from pumping test at port 7 for Synthetic THT analysis. The solid line represents the drawdown curve at each fracture port and the circles represent the data points used for inversion.

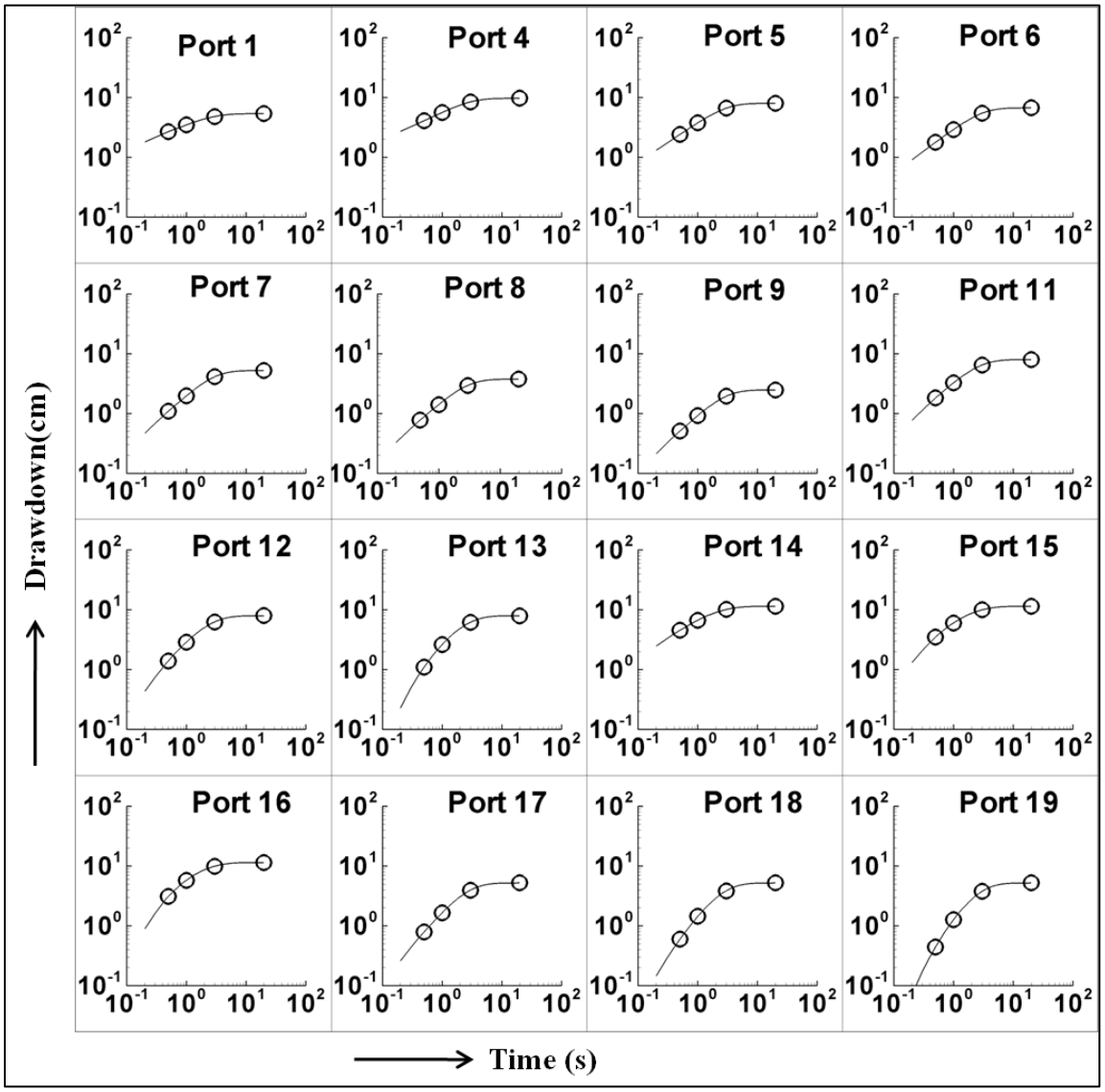

Figure C2: Selected Data Points at the Fracture Observation Ports from pumping test at port 3 for Synthetic THT analysis. The solid line represents the drawdown curve at each fracture port and the circles represent the data points used for inversion.

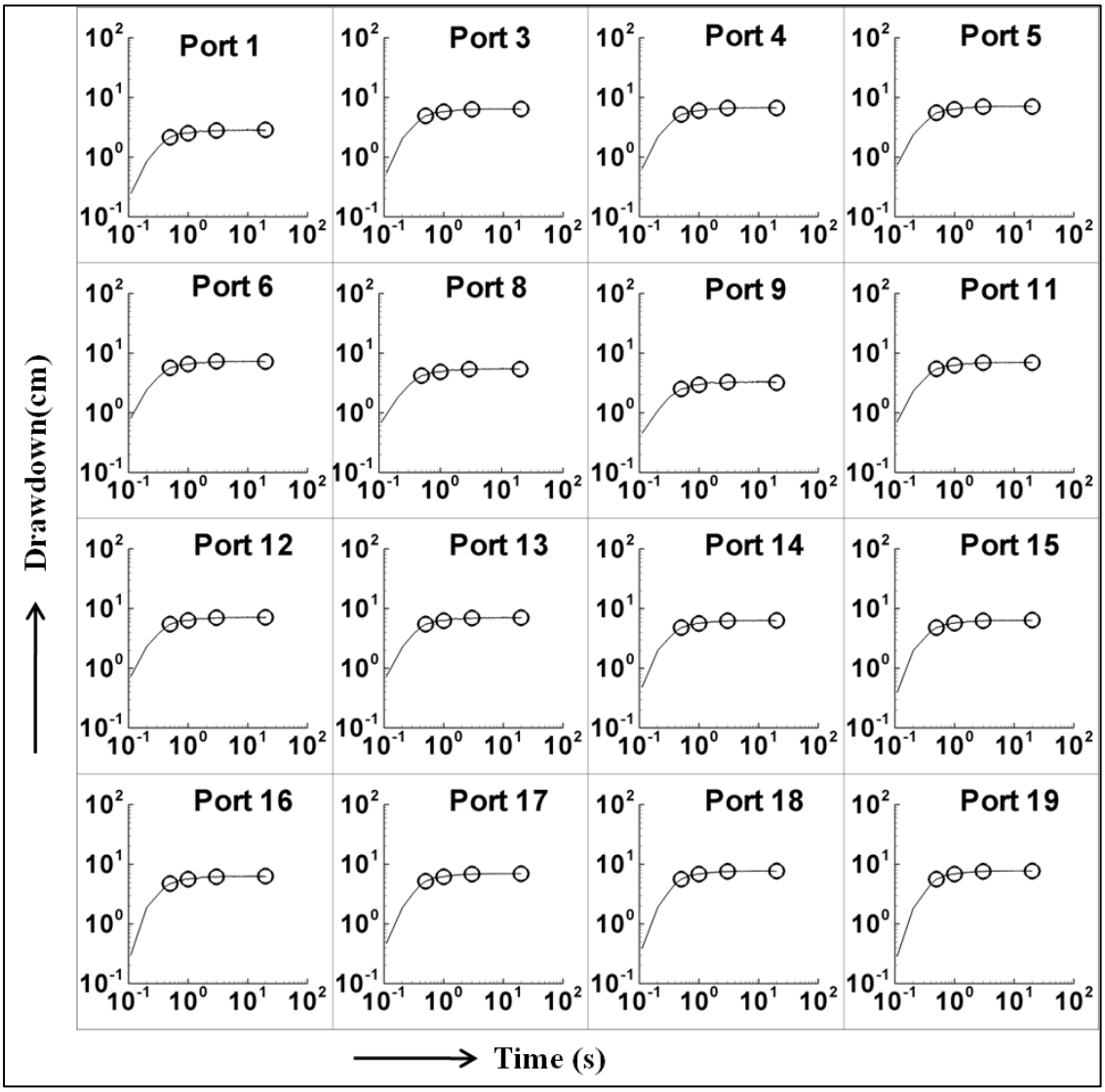

Figure C3: Selected Data Points at the Fracture Observation Ports from pumping test at port 7 for real THT case 1 (inversion of laboratory pumping tests). The solid line represents the drawdown curve at each fracture port and the circles represent the data points used for inversion.

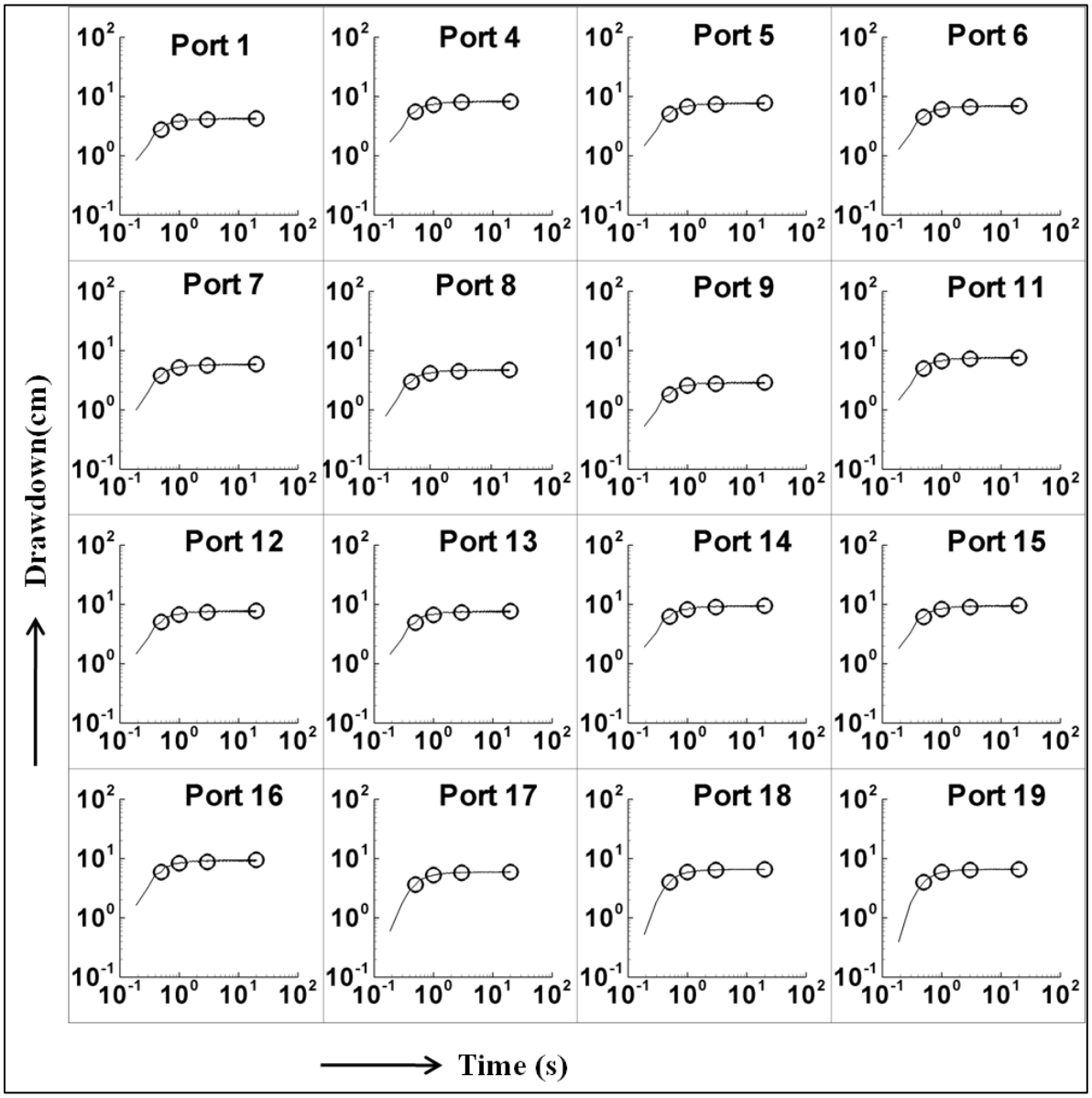

Figure C4: Selected Data Points at the Fracture Observation Ports from pumping test at port 3 for real THT case 1 (inversion of laboratory pumping tests). The solid line represents the drawdown curve at each fracture port and the circles represent the data points used for inversion.

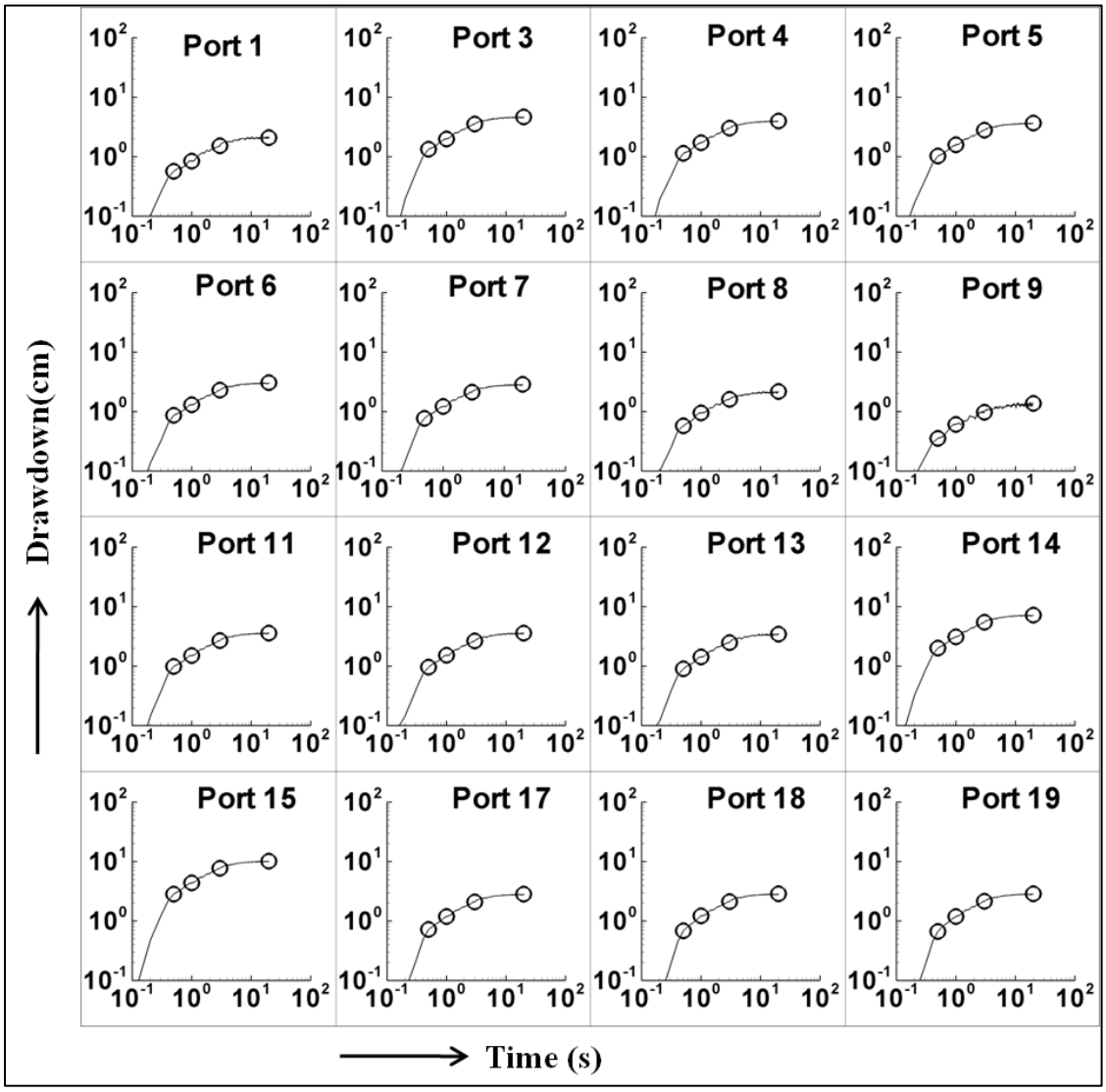

Figure C5: Selected Data Points at the Fracture Observation Ports from pumping test at port 16 for real THT case 2 (inversion of laboratory pumping tests). The solid line represents the drawdown curve at each fracture port and the circles represent the data points used for inversion.

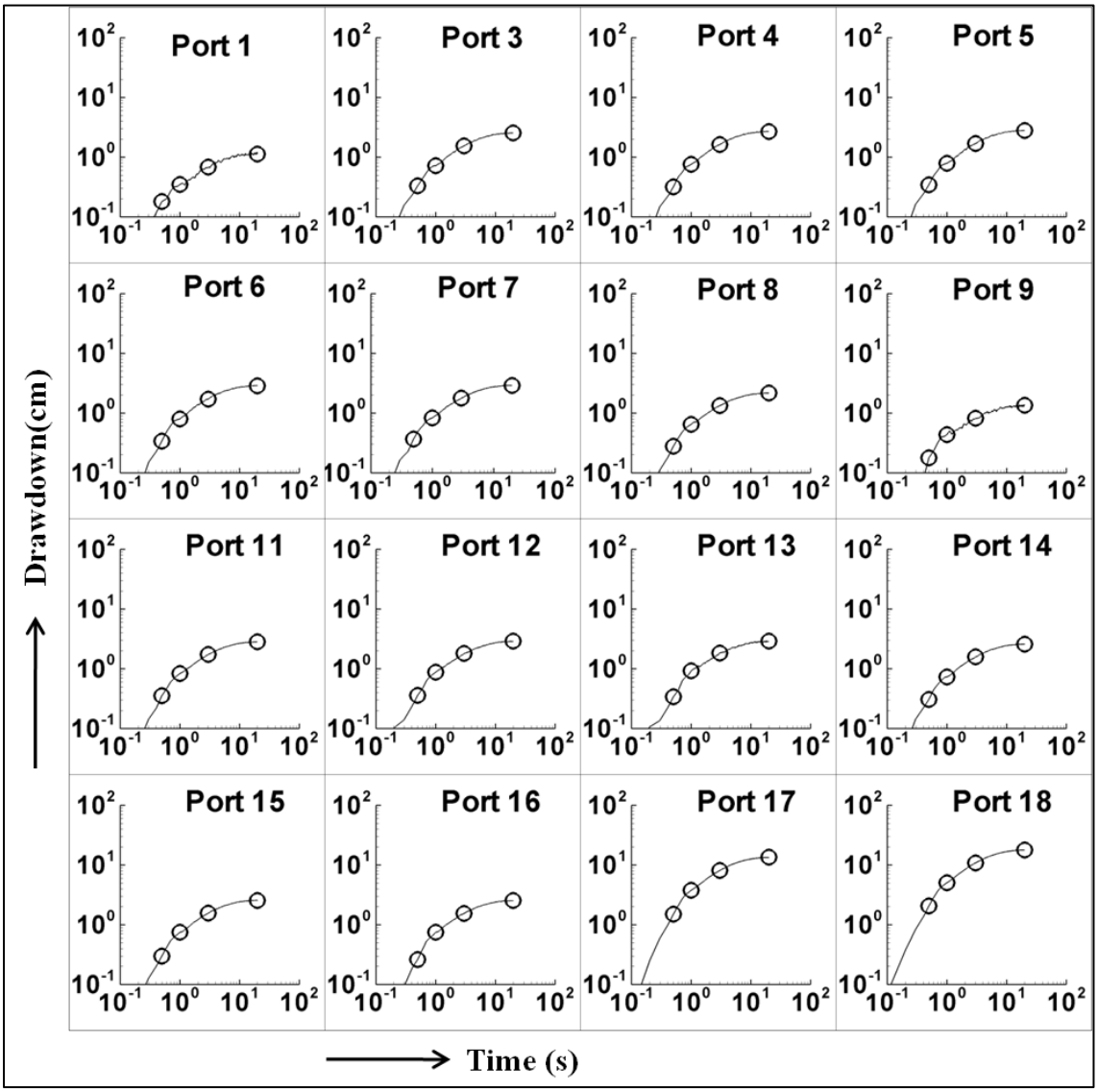

Figure C6: Selected Data Points at the Fracture Observation Ports from pumping test at port 19 for real THT case 2 (inversion of laboratory pumping tests). The solid line represents the drawdown curve at each fracture port and the circles represent the data points used for inversion.

Appendix D

THT Calibrations and Predictions – Case 2

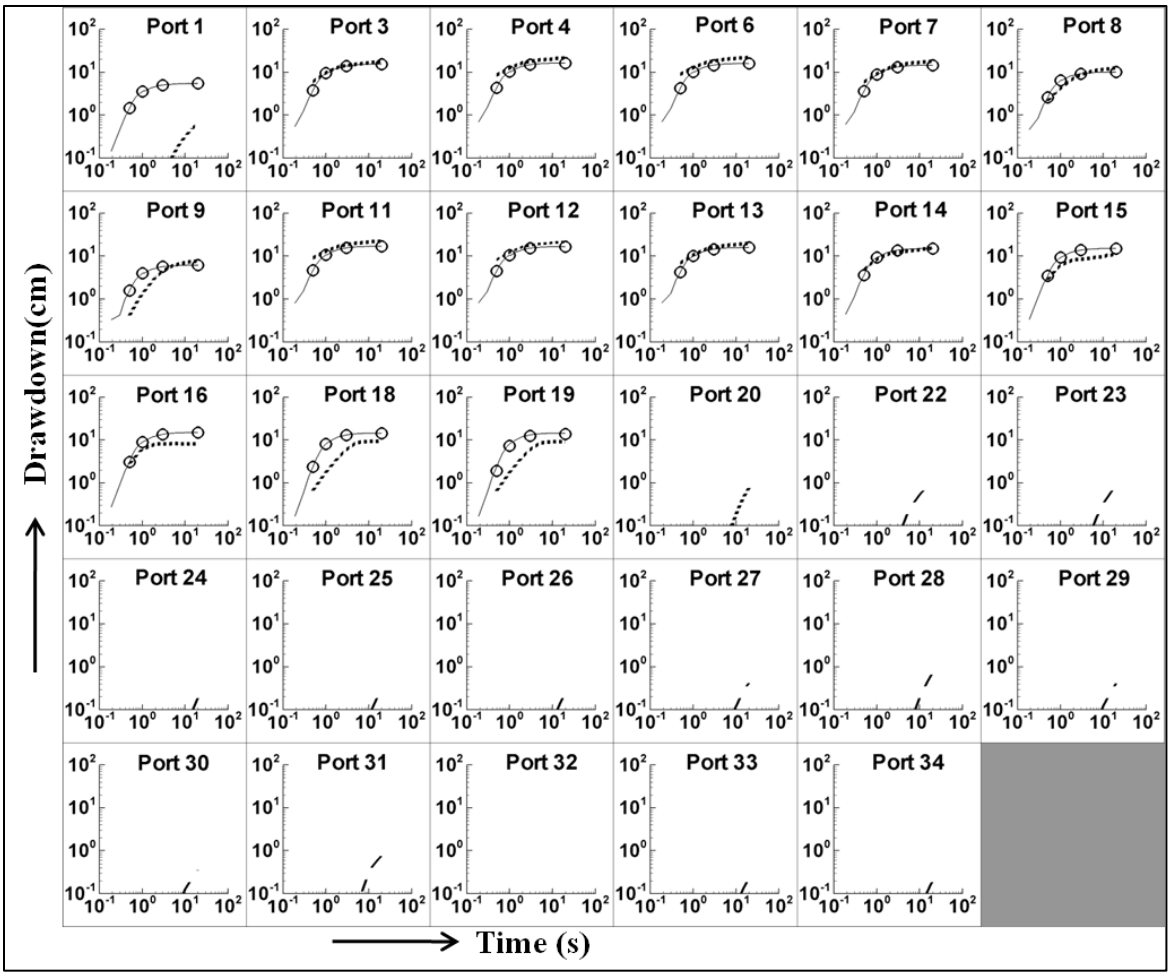

Figure D1: Observed and Calibrated Drawdown (cm) versus Time (s) at the monitoring ports during the Pumping Test at Port 5 in real THT Case 2. The solid line represents observed drawdown curve while the dashed line represents calibrated drawdown curve. The solid circles indicate the match points.

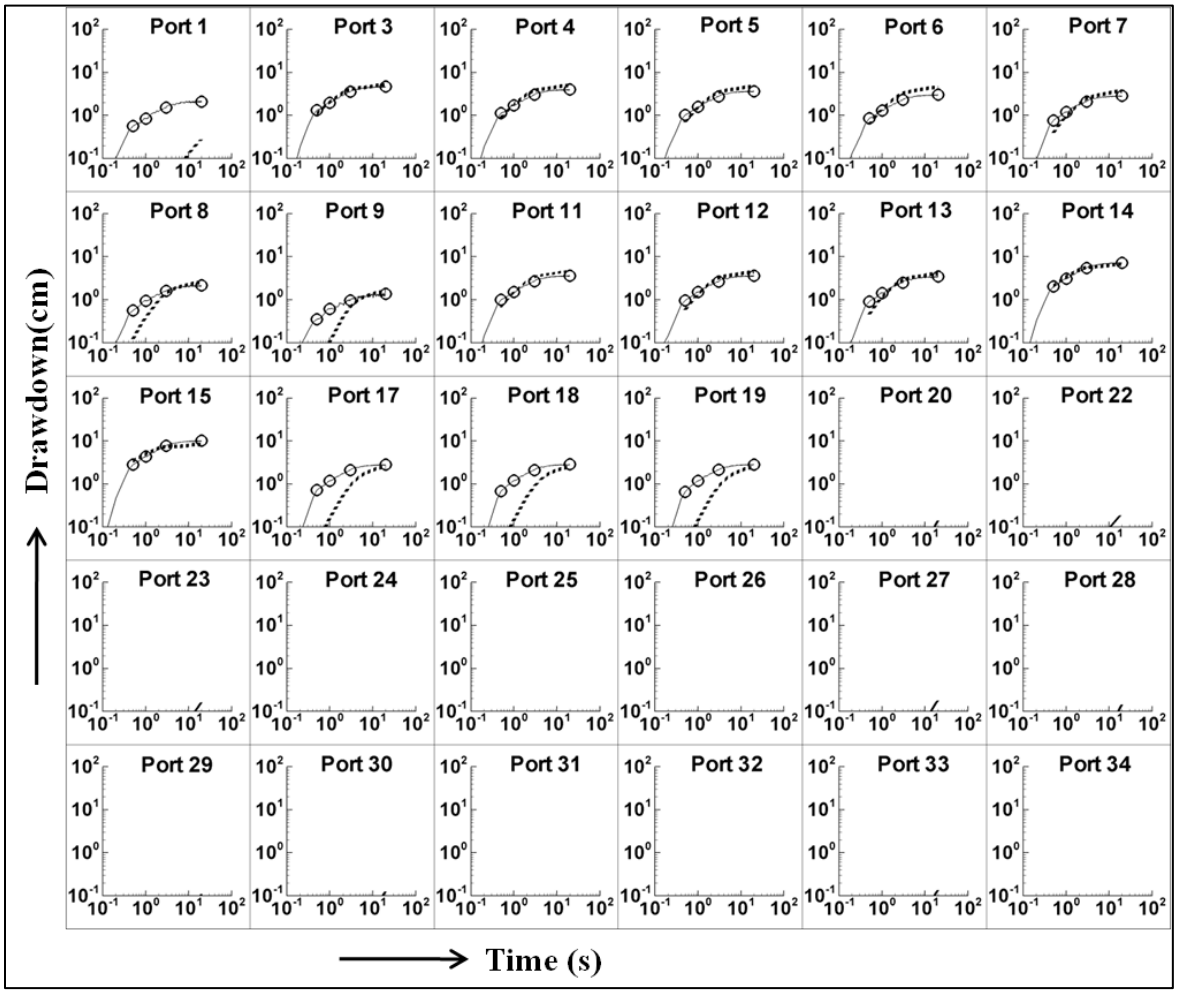

Figure D2: Observed and Calibrated Drawdown (cm) versus Time (s) at the monitoring ports during the Pumping Test at Port 16 in real THT Case 2. The solid line represents observed drawdown curve while the dashed line represents calibrated drawdown curve. The black circles indicate the match points.

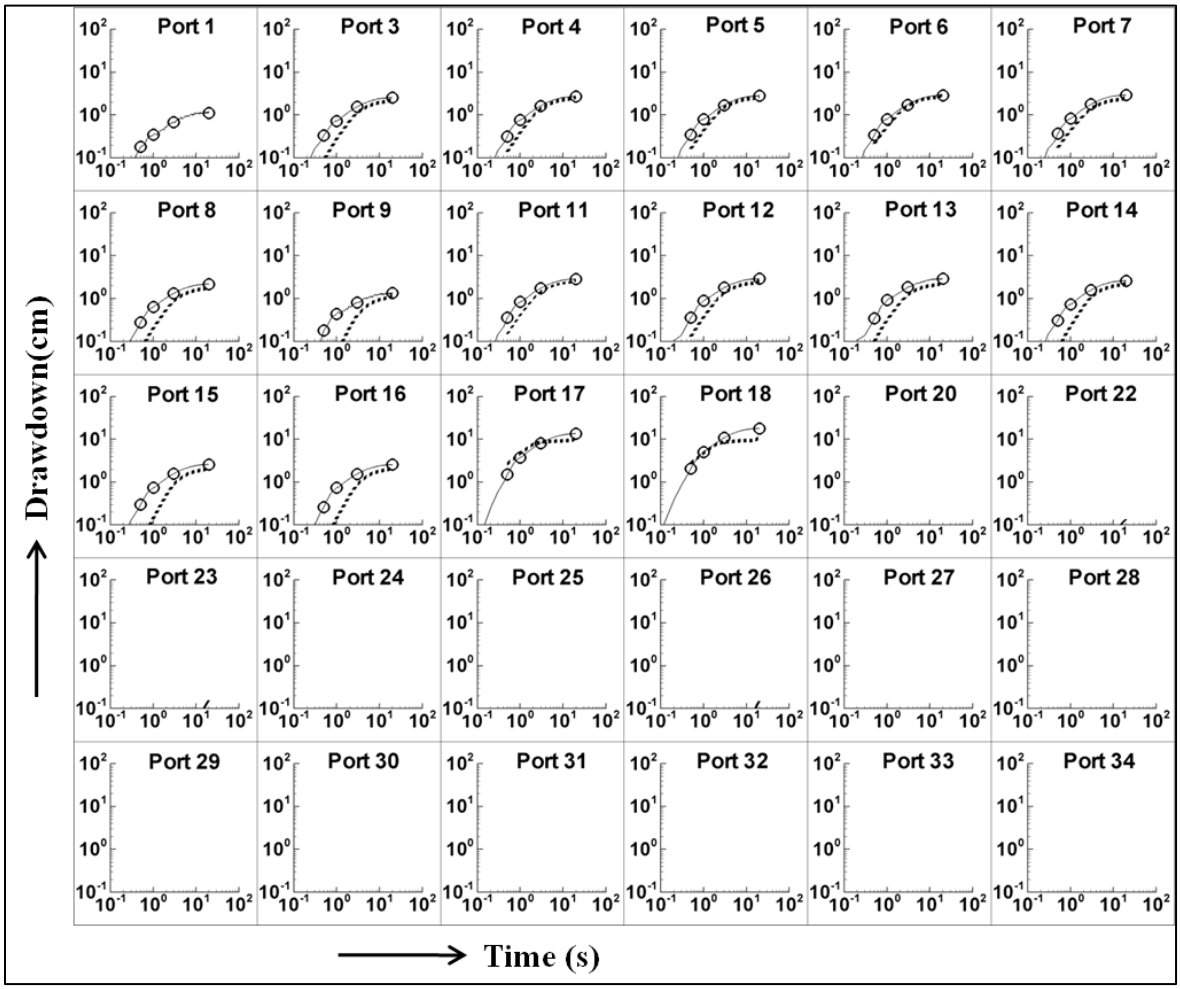

Figure D3: Observed and Calibrated Drawdown (cm) versus Time (s) at the monitoring ports during the Pumping Test at Port 19 in real THT Case 2. The solid line represents observed drawdown curve while the dashed line represents calibrated drawdown curve. The black circles indicate the match points.

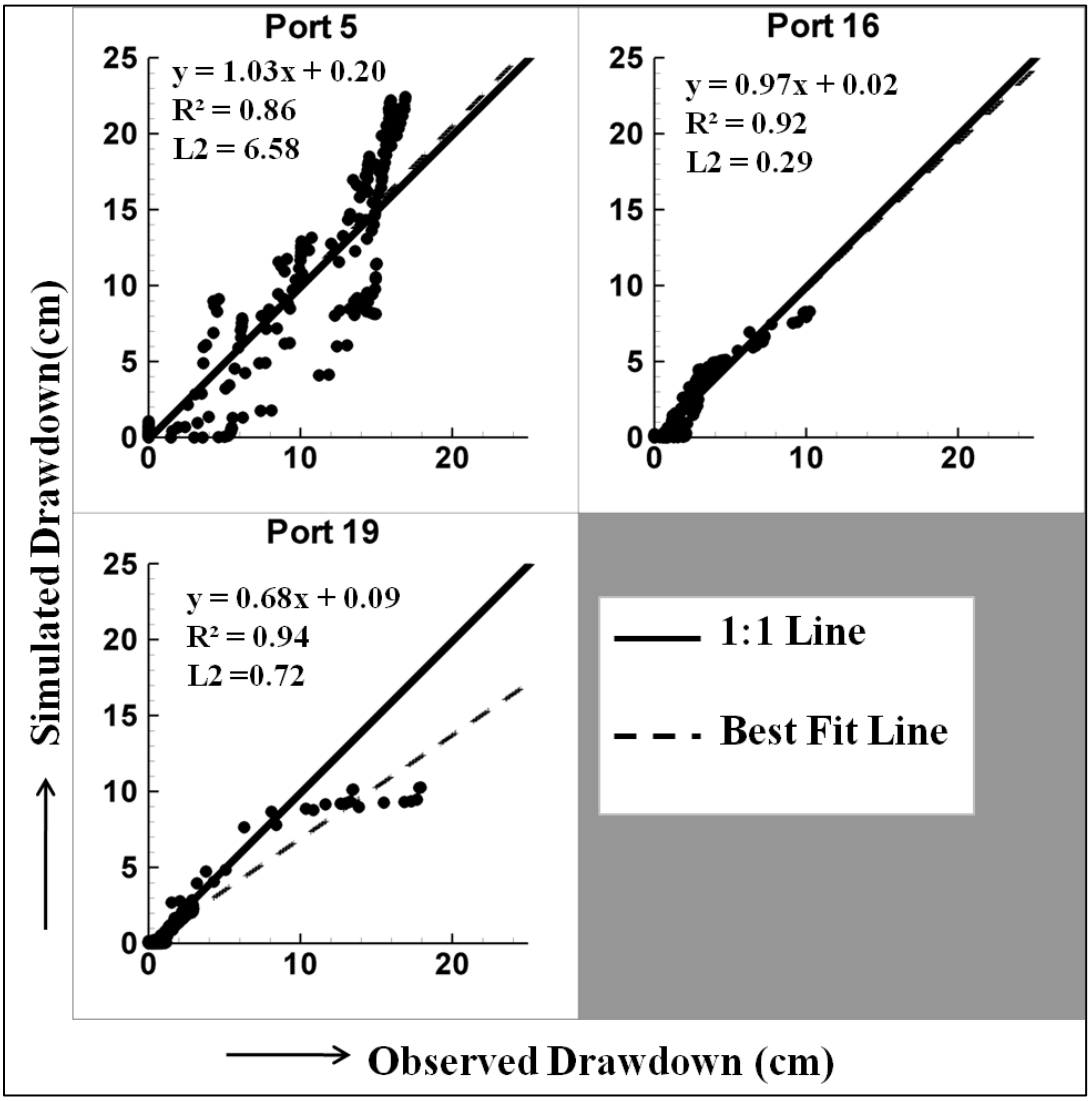

Figure D4: Calibration Scatter plots for real THT Cases 2. The pumped port is mentioned in bold letters on each plot. The solid line is a 1:1 line indicating a perfect match. The dashed line is a best fit line, and the parameters describing this line as well as *L2* norm for the corresponding tests are on each plot.

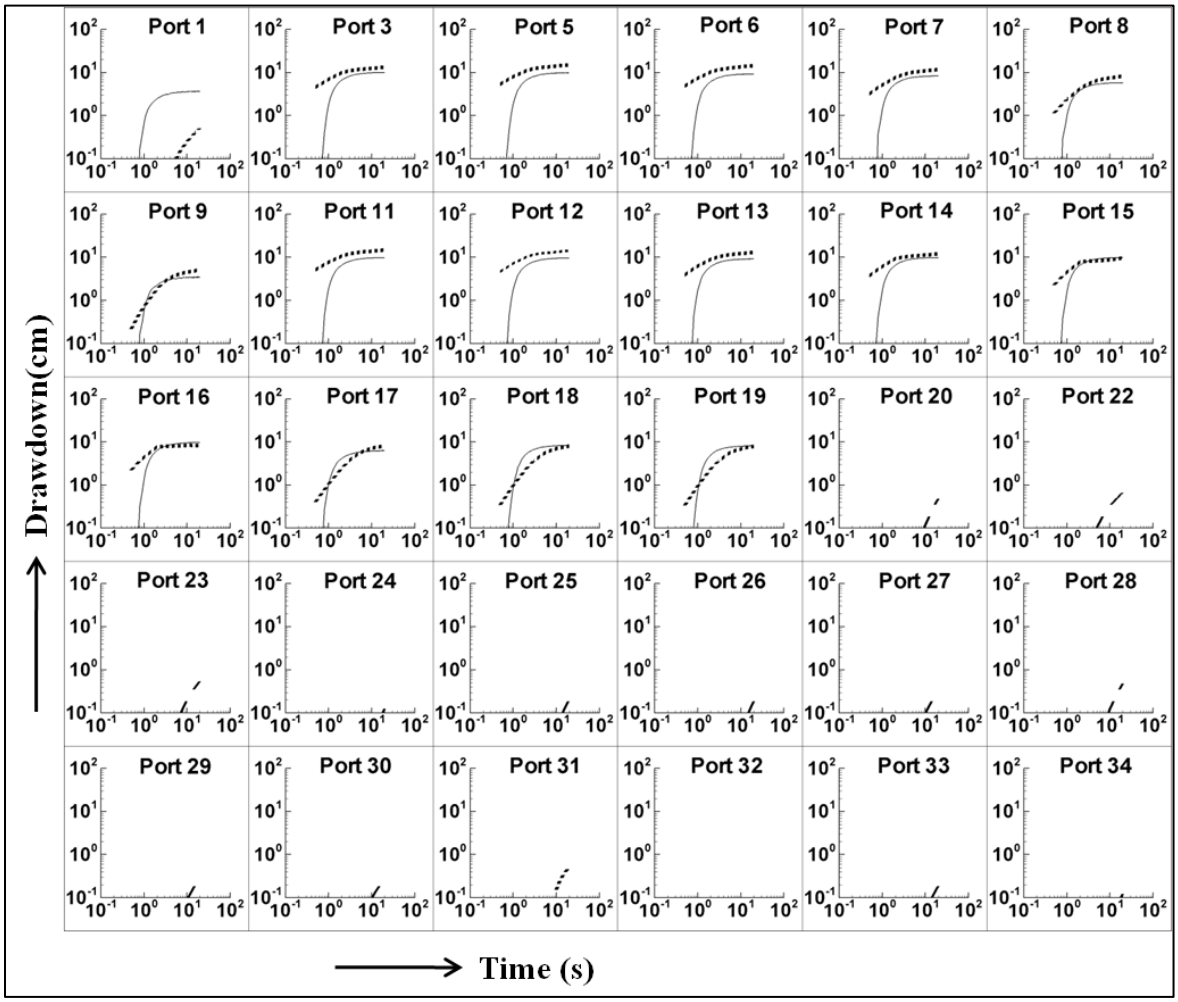

Figure D5: Observed and Predicted Drawdown (cm) versus Time (s) at the monitoring ports during the Pumping Test at Port 4 in real THT Case 2. The solid line represents observed drawdown curve while the dashed line represents predicted drawdown curve.

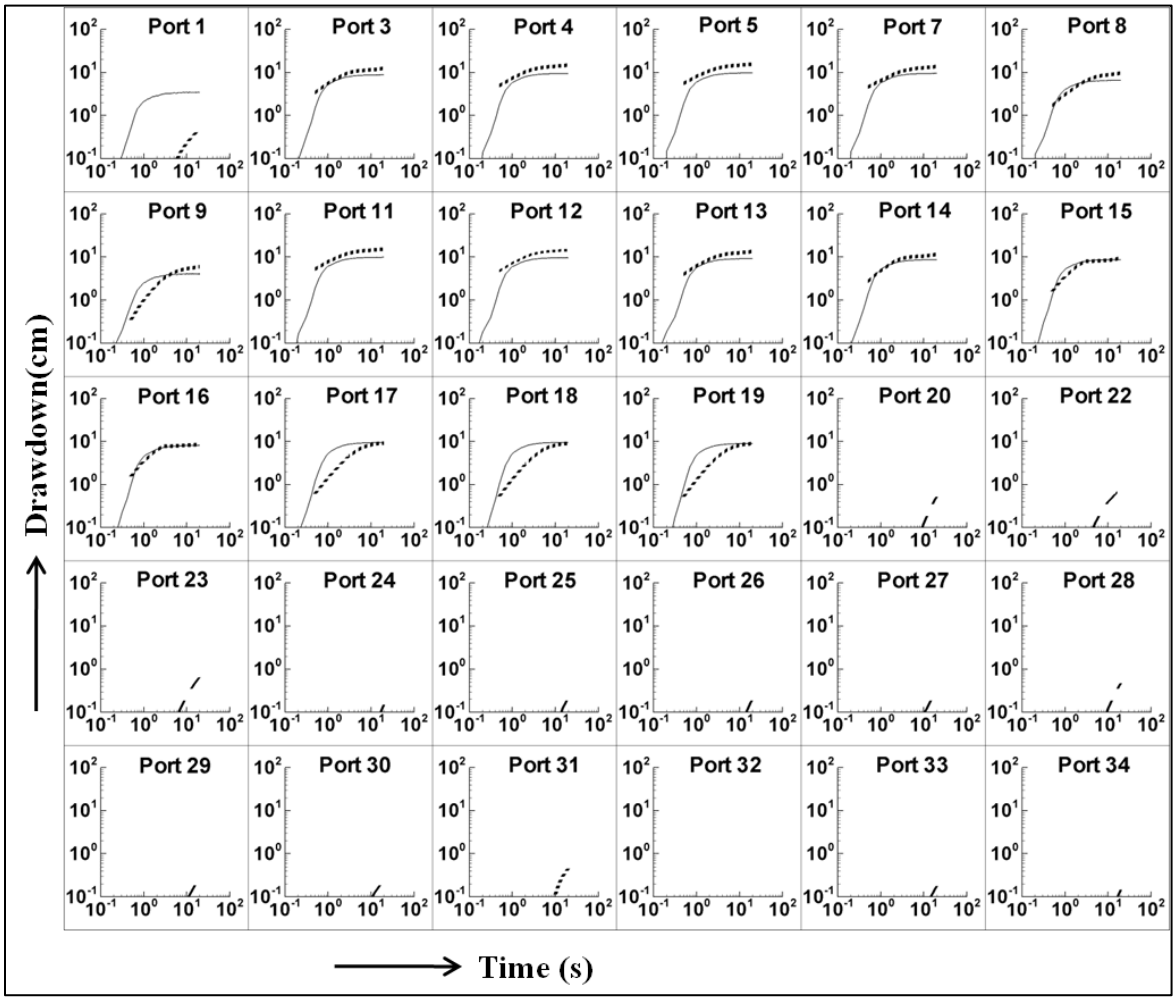

Figure D6: Observed and Predicted Drawdown (cm) versus Time (s) at the monitoring ports during the Pumping Test at Port 6 in real THT Case 2. The solid line represents observed drawdown curve while the dashed line represents predicted drawdown curve.

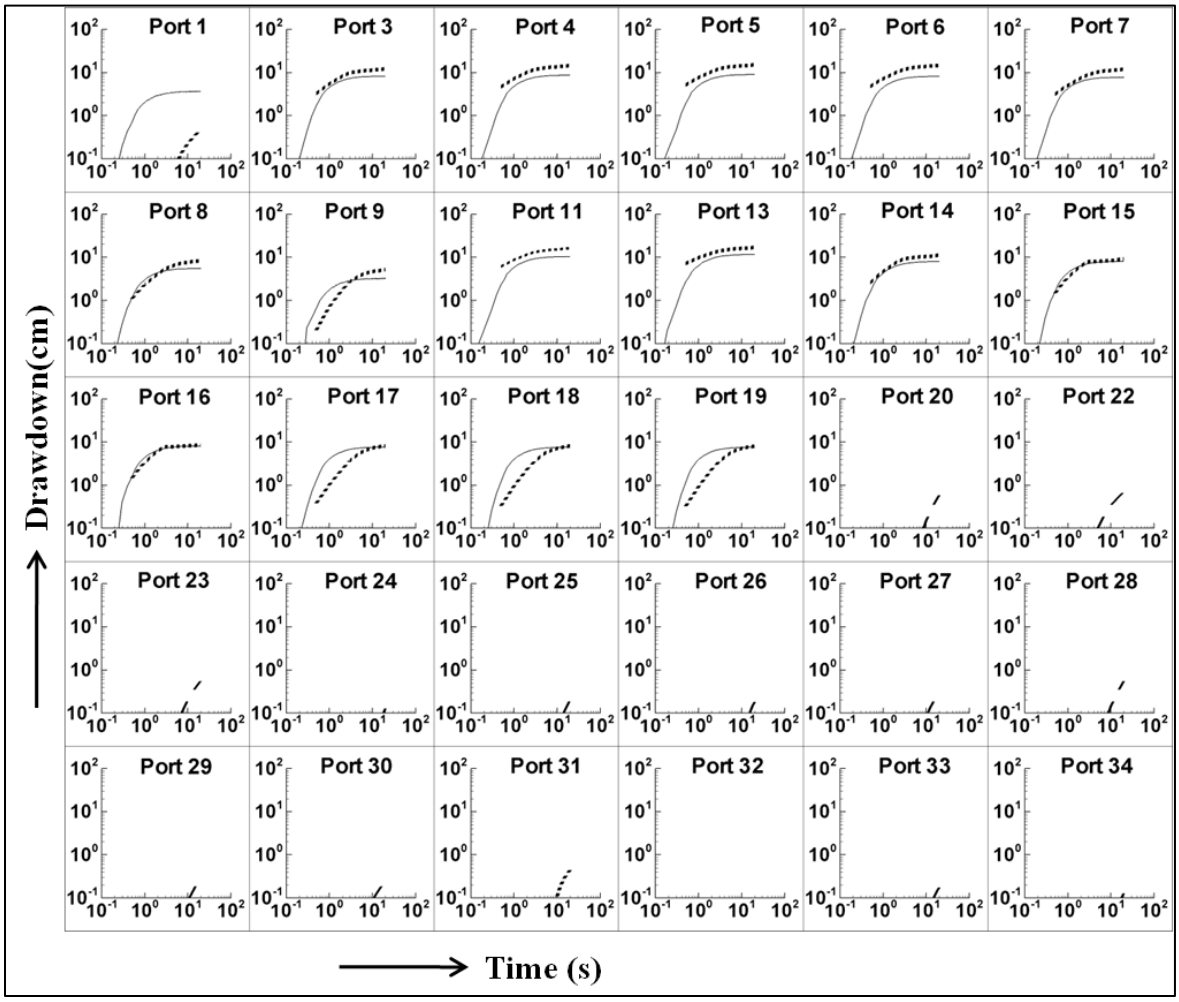

Figure D7: Observed and Predicted Drawdown (cm) versus Time (s) at the monitoring ports during the Pumping Test at Port 12 in real THT Case 2. The solid line represents observed drawdown curve while the dashed line represents predicted drawdown curve.

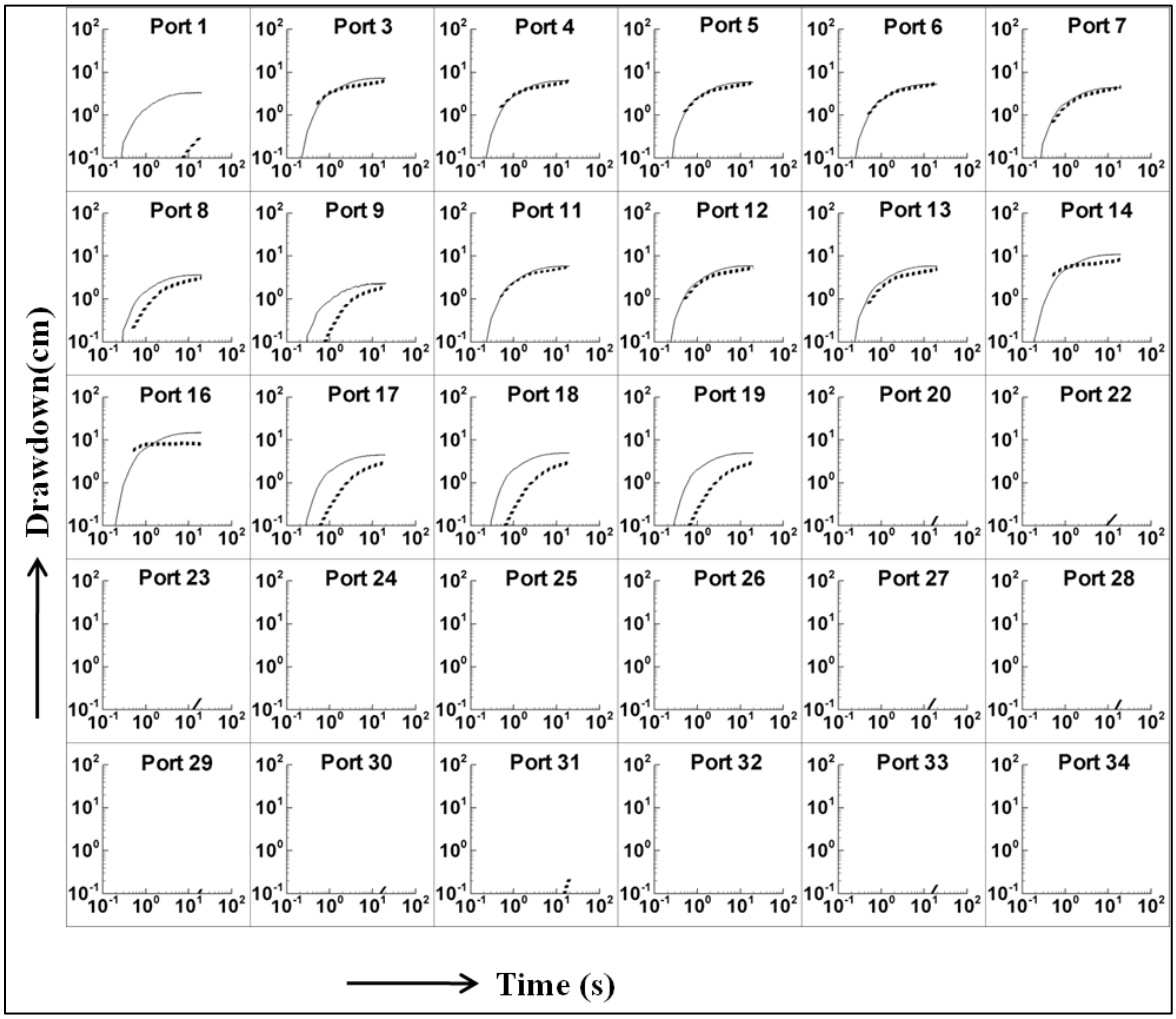

Figure D8: Observed and Predicted Drawdown (cm) versus Time (s) at the monitoring ports during the Pumping Test at Port 15 in real THT Case 2. The solid line represents observed drawdown curve while the dashed line represents predicted drawdown curve.

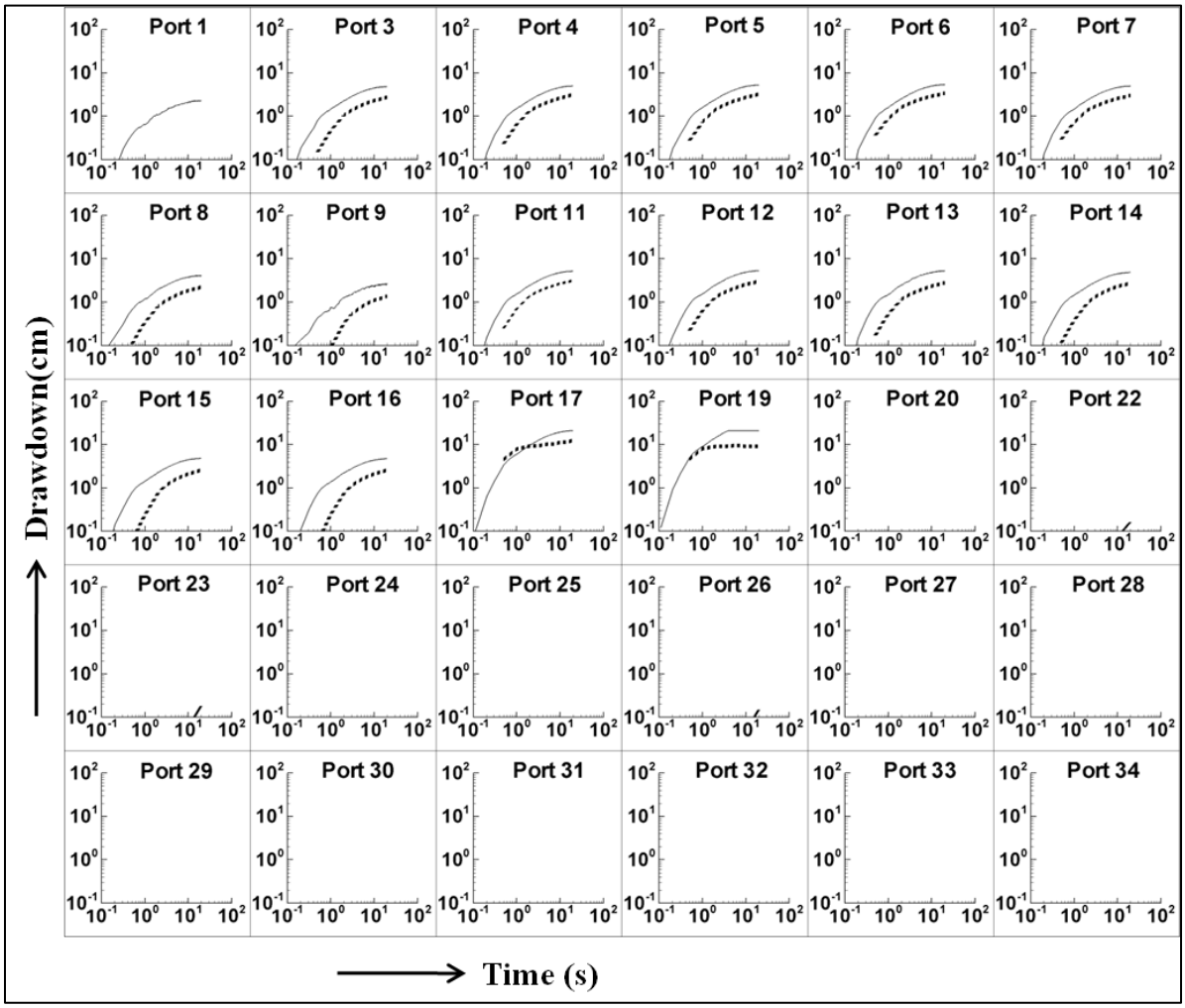

Figure D9: Observed and Predicted Drawdown (cm) versus Time (s) at the monitoring ports during the Pumping Test at Port 18 in real THT Case 2. The solid line represents observed drawdown curve while the dashed line represents predicted drawdown curve.

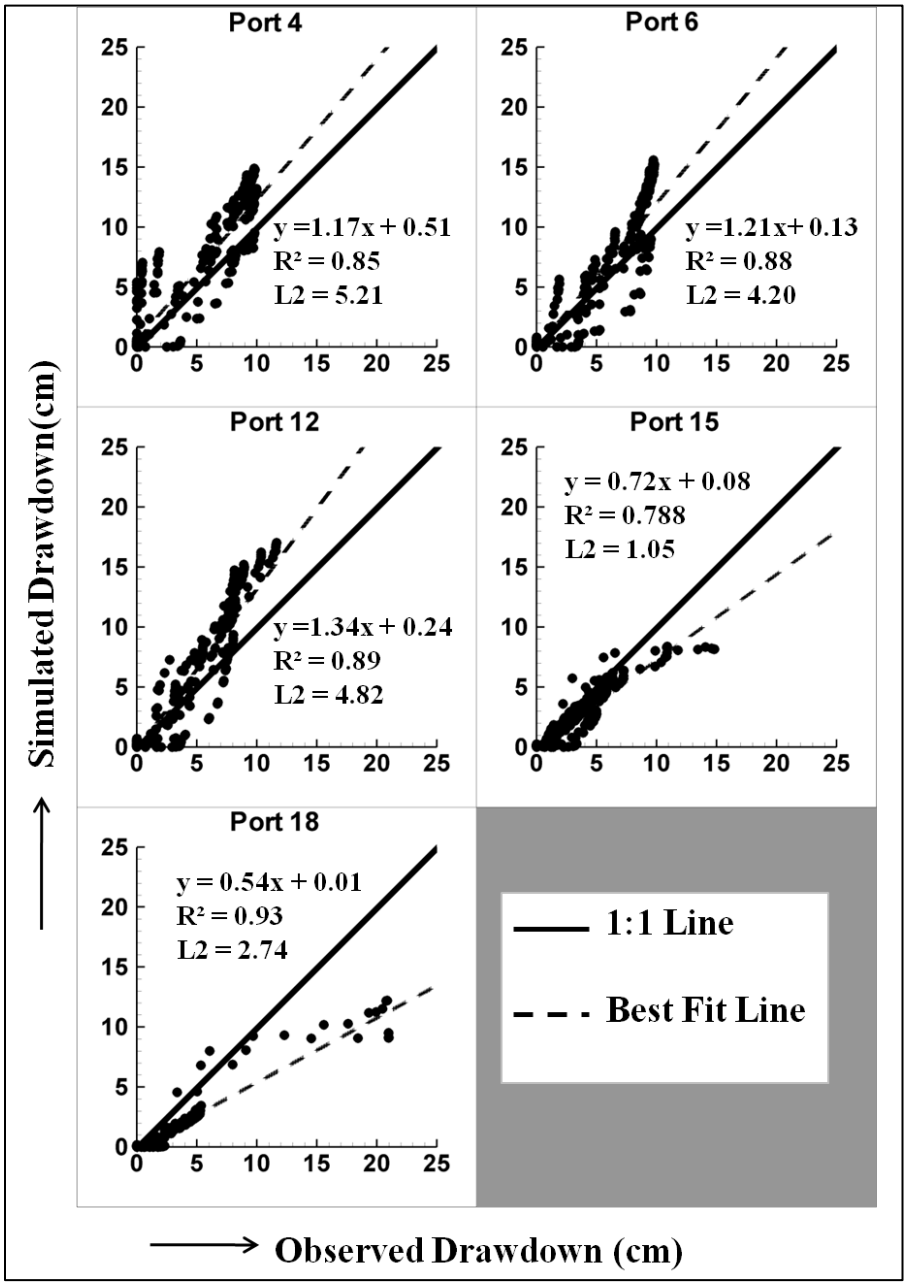

Figure D10: Validation Scatter plots for real THT Cases 2. The pumped port is mentioned in bold letters on each plot. The solid line is a 1:1 line indicating a perfect match. The dashed line is a best fit line, and the parameters describing this line as well as *L2* norm for the corresponding tests are on each plot.

Appendix E
IC and GC Analysis Methods

E1 IC Analytical Procedure

For the analysis a 2.0mL sample was removed and added to a plastic 5ml Dionex IC autosampler vial. The sample is then place on a Dionex AS-40 autosampler. A 25 µl sample was then injected onto a Dionex ICS-2000 Ion Chromatograph equipped with an Ion-Eluent Generator and conductivity detector. A Dionex IonPac AS18 column (4x250mm) was used. The mobile phase used was 30mM KOH at a flow rate of 1.0 ml/min. The chromatograph was obtained on a Dell p4-3GHz computer using Dionex Chromeleon 6.5 software.

Table E-1: Method Detection Limit (MDL)

Anion	MDL (mg/L)
Bromide (Br^-)	0.5

E2 GC Analytical Procedure

For the analysis a 2.0mL sample was removed and added to 2 ml of internal standard solution (500 µg/L of 1, 2-Dibromoethane in pentane) in a 5ml. glass screw cap vial with Teflon-faced septum. The sample was placed on an orbital shaker for 15 minutes at 300 RPM. The supernatant was then removed, placed in a 2 mL glass crimp-top GC vial and put on a Hewlett Packard 5890 Series II gas chromatograph equipped with a Ni^{63} ECD detector. Using a HP 7673 liquid auto sampler a 1uL sample was injected onto a DB-624 capillary column. The detector temperature was 300C, injection temperature was 200C and the column temperature ramp is 50C to 150C at a rate of 15C/min and then held for 1 min. The carrier gas is pre-purified helium with a total flow rate of 25 mL/min and the make-up gas is 5% methane, 95% argon.

Table E-2: Method Detection Limit (MDL)

Compound	MDL (µg/L)
Trichloroethylene (TCE)	1.0

E3 Quality Control and Quality Assurance Program

Quality control procedures are used to estimate and evaluate the information on the analytical data and to determine if operations are in order or if corrective action is necessary. To evaluate these procedures; precision, accuracy, detection limits and other quantifiable and qualitative indicators are monitored. These measures are used to monitor the program and to ensure that all data generated are suitable for their intended use.

Analytical quality control involved method blanks which are carried through the entire analytical procedures, as well as spiked blanks which are spiked with the analytes from an independent source in order to monitor the execution of the analytical method, with percent recoveries recorded (%R). The two blanks and approximately eight spiked blanks are analyzed every time sampling is undertaken. Calibrations are conducted in accordance with requirements, which were specific to the particular instrumentation and procedures.

Method detection limits were determined for each compound as the minimum concentration of a substance that can be identified, measures and reported with 99% confidence that the analyte concentration is greater than zero. The method detection limits were determined from the analysis of samples from a solution matrix containing the analyte of interest. Detection limits for all compounds studied, as given in Table E-1 and Table E-2, were determined using the EPA procedure for Method Detection Limit (MDL) (US EPA, 1982).

Bibliography

Abriola, L. M., and G. F. Pinder (1985a), A multiphase approach to the modeling of porous-media contamination by organic-compounds. 1. Equation development, *Water Resources Research*, *21*(1), 11-18.

Abriola, L. M., and G. F. Pinder (1985b), A multiphase approach to the modeling of porous-media contamination by organic-compounds. 2. Numerical-simulation, *Water Resources Research*, *21*(1), 19-26.

Anderson, M. R., R. L. Johnson, and J. F. Pankow (1992b), Dissolution of dense chlorinated solvents into groundwater. 1. Dissolution from well-defined source, *Ground Water*,, *30*(2), 250-256.

Anderson, M. R., R. L. Johnson, and J. F. Pankow (1992b), Dissolution of dense chlorinated solvents into groundwater. 3. Modeling contaminant plumes from fingers and pools of solvent, *Environmental Science & Technology*, *26*(5), 901-908.

Ando, K., A. Kostner, and S. P. Neuman (2003), Stochastic continuum modeling of flow and transport in a crystalline rock mass: Fanay-Auge`res, France, revisited, *Hydrogeol. J.*, *11*(5), 521 – 535, doi:10.1007/s10040-003-0286-0.

Basu, N. B., A. D. Fure, and J. W. Jawitz (2008a), Simplified contaminant source depletion models as analogs of multiphase simulators, *Journal of Contaminant Hydrology*, *97*(3-4), 87-99.

Basu, N. B., S. C. Rao, R. W. Falta, M. D. Annable, J. W. Jawitz, and K. Hatfield (2008b), Temporal evolution of DNAPL source and contaminant flux distribution: Impacts of source mass depletion, *Journal of Contaminant Hydrology*, *95*(3-4), 93-109.

Bear, J. (1972), *Dynamics of Fluids in Porous Media*, 764 pp., Dover, New York.

Berg, S. J. and W. A., Illman, (2011), Three-dimensional transient hydraulic tomography in a highly heterogeneous glaciofluvial aquifer–aquitard system, *Water Resources Research* doi: 10.1029/2011WR010616, in press.

Benke, R., and S. Painter (2003), Modeling conservative tracer transport in fracture networks with a hybrid approach based on the Boltzmann transport equation, *Water Resources Research*, *39*(11).

Bibby, R. (1981), Mass-transport of solutes in dual porosity media, *Water Resources Research*, *17*(4), 1075-1081.

Bohling, G. C., Zhan, X. Y. Butler, J. J. and Zheng, L. (2002), Steady shape analysis of tomographic pumping tests for characterization of aquifer heterogeneities, *Water Resources Research*, *38*(12).

Bohling, G. C., J. J. Butler, Jr., X. Zhan, and M. D. Knoll (2007), A field assessment of the value of steady shape hydraulic tomography for characterization of aquifer heterogeneities, *Water Resources Research*, *43*(5).

Borden, R. C., and M. D. Piwoni (1992), Hydrocarbon dissolution and transport - A comparison of equilibrium and kinetic-models, *Journal of Contaminant Hydrology*, *10*(4), 309-323.

Brauchler, R., R. Liedl, and P. Dietrich (2003), A travel time based hydraulic tomographic approach, *Water Resources Research*, *39*(12).

Brooks, M. C., M. D. Annable, P. S. C. Rao, K. Hatfield, J. W. Jawitz, W. R. Wise, A. L. Wood, and C. G. Enfield (2002), Controlled release, blind tests of DNAPL characterization using partitioning tracers, *Journal of Contaminant Hydrology*, *59*(3-4), 187-210.

Brooks, M. C., M. D. Annable, P. S. C. Rao, K. Hatfield, J. W. Jawitz, W. R. Wise, A. L. Wood, and C. G. Enfield (2004), Controlled release, blind test of DNAPL remediation by ethanol flushing, *Journal of Contaminant Hydrology*, *69*(3-4), 281-297.

Butler, J. J., C. D. McElwee, and G. C. Bohling (1999), Pumping tests in networks of multilevel sampling wells: Motivation and methodology, *Water Resources Research*, *35*(11), 3553-3560.

Cacas, M. C., E. Ledoux, G. De Marsily, B. Tillie, A. Barbreau, E. Durand, B. Feuga, and P. Peaudecerf (1990b), Modeling Fracture Flow With A Stochastic Discrete Fracture Flow With A Stochastic Discrete Fracture Network - Calibration and Validation. 1. The Flow Model, *Water Resources Research*, *26*(3), 479-489.

Cacas, M. C., E. Ledoux, G. De Marsily, A. Barbreau, P. Calmels, B. Gaillard, and R. Margritta (1990a), Modeling Fracture Flow With A Stochastic Discrete Fracture Flow With A Stochastic Discrete Fracture Network - Calibration and Validation. 2. The Transport Model, *Water Resources Research*, *26*(3), 491-500.

Castagna, M., M. Becker, and A. Bellin (2011), Joint estimation of transmissivity and storativity in a bedrock fracture, *Water Resour. Res.*, 47, W09504, doi:10.1029/2010WR009262.

Conrad, S. H., J. L. Wilson, W. R. Mason, and W. J. Peplinski (1992), Visualization of residual organic liquid trapped in aquifers, *Water Resources Research*, *28*(2), 467-478.

Corapcioglu, M. Y., and A. L. Baehr (1987), A compositional multiphase model for groundwater contamination by petroleum-products. 1. Theoretical considerations, *Water Resources Research*, *23*(1), 191-200.

Cvetkovic, V., S. Painter, N. Outters, and J. O. Selroos (2004), Stochastic simulation of radionuclide migration in discretely fractured rock near the Aspo Hard Rock Laboratory, *Water Resources Research*, *40*(2).

Darcel, C., O. Bour, P. Davy, and J. R. de Dreuzy (2003), Connectivity properties of two-dimensional fracture networks with stochastic fractal correlation, *Water Resources Research*, *39*(10).

Day-Lewis, F. D., P. A. Hsieh, and S. M. Gorelick (2000), Identifying fracture-zone geometry using simulated annealing and hydraulic-connection data, *Water Resources Research*, *36*(7), 1707-1721.

Day-Lewis, F. D., J. W. Lane, and S. M. Gorelick (2006), Combined interpretation of radar, hydraulic, and tracer data from a fractured-rock aquifer near Mirror Lake, New Hampshire, USA, *Hydrogeology Journal*, *14*(1-2), 1-14.

Day-Lewis, F. D., J. W. Lane, J. M. Harris, and S. M. Gorelick (2003), Time-lapse imaging of saline-tracer transport in fractured rock using difference-attenuation radar tomography, *Water Resources Research*, *39*(10).

Dekker, T. J., and L. M. Abriola (2000a), The influence of field-scale heterogeneity on the surfactant-enhanced remediation of entrapped nonaqueous phase liquids, *Journal of Contaminant Hydrology*, *42*(2-4), 219-251.

Dekker, T. J., and L. M. Abriola (2000b), The influence of field-scale heterogeneity on the infiltration and entrapment of dense nonaqueous phase liquids in saturated formations, *Journal of Contaminant Hydrology*, *42*(2-4), 187-218.

De Marsily, G. (1986), *Quantitative hydrogeology: groundwater hydrology for engineers*, 440pp, Academic Press.

Dershowitz, W. S., and H. H. Einstein (1988), Characterizing rock joint geometry without joint system models, *Rock Mechanics and Rock Engineering*, *21*(1), 21-51.

Di Federico, V., and S. P. Neuman (1998a), Flow in multiscale log conductivity fields with truncated power variograms, *Water Resources Research, 34*(5), 975-987.

Di Federico, V., and S. P. Neuman (1998b), Transport in multiscale log conductivity fields with truncated power variograms, *Water Resources Research, 34*(5), 963-973.

Di Federico, V., S. P. Neuman, and D. M. Tartakovsky (1999), Anisotropy, lacunarity, and upscaled conductivity and its autocovariance in multiscale random fields with truncated power variograms, *Water Resources Research, 35*(10), 2891-2908.

Dickson, S. E., and N. R. Thomson (2003), Dissolution of entrapped DNAPLs in variable aperture fractures: Experimental data and empirical model, *Environmental Science & Technology, 37*(18), 4128-4137.

Doherty, J. (2005), *PEST Model-independent parameter estimation user manual: 5th Edition.* Watermark Numerical Computing, Brisbane, Australia.

Domenico, P.A., and F.W. Schwartz (1997), *Physical and Chemical Hydrogeology*. New York: John Wiley and Sons, 506.

Duguid, J. O., and P. C. Y. Lee (1977), Flow in fractured porous-media, *Water Resources Research, 13*(3), 558-566.

Dverstorp, B., and J. Andersson (1989), Application Of the discrete fracture network concept with field data - Possibilities of model calibration and validation, *Water Resources Research, 25*(3), 540-550.

Dverstorp, B., J. Andersson, and W. Nordqvist (1992), Discrete fracture network interpretation of field tracer migration in sparsely fractured rock, *Water Resources Research, 28*(9), 2327-2343.

Folger, P. F., E. Poeter, R. B. Wanty, W. Day, and D. Frishman (1997), Rn-222 transport in a fractured crystalline rock aquifer: Results from numerical simulations, *Journal of Hydrology, 195*(1-4), 45-77.

Franssen, H., and J. J. Gomez-Hernandez (2002), 3D inverse modelling of groundwater flow at a fractured site using a stochastic continuum model with multiple statistical populations, *Stochastic Environmental Research and Risk Assessment, 16*(2), 155-174.

Fried, J. J., P. Muntzer, and L. Zilliox (1979), Groundwater pollution by transfer of oil hydrocarbons, *Ground Water, 17*(6), 586-594.

Frind, E. O., J. W. Molson, M. Schirmer, and N. Guiguer (1999), Dissolution and mass transfer of multiple organics under field conditions: The Borden emplaced source, *Water Resources Research*, *35*(3), 683-694.

Fure, A. D., J. W. Jawitz, and M. D. Annable (2006), DNAPL source depletion: Linking architecture and flux response, *Journal of Contaminant Hydrology*, *85*(3-4), 118-140.

Geller, J. T., and J. R. Hunt (1993), Mass-transfer from nonaqueous phase organic liquids in water-saturated porous-media, *Water Resources Research*, *29*(4), 833-845.

Gerke, H. H., and M. T. Vangenuchten (1993a), A dual-porosity model for simulating the preferential movement of water and solutes in structured porous-media, *Water Resources Research*, *29*(2), 305-319.

Gerke, H. H., and M. T. Vangenuchten (1993b), Evaluation of a 1st-order water transfer term for variability saturated dual-porosity flow models, *Water Resources Research*, *29*(4), 1225-1238.

Gottlieb, J., and P. Dietrich (1995), identification of the permeability distribution in soil by hydraulic tomography, *Inverse Problems*, *11*(2), 353-360.

Hao, Y., T.-C. J. Yeh, J. Xian, W. A. Illman, K. Ando, K.-C. Hsu, and C.-H. Lee (2008), Hydraulic tomography for detecting fracture zone connectivity, *Ground Water*, *46*(2), 183-192.

Hu, Q. H., T. J. Kneafsey, J. J. Roberts, L. Tomutsa, and J. S. Y. Wang (2004), Characterizing unsaturated diffusion in porous tuff gravel, *Vadose Zone Journal*, *3*(4), 1425-1438.

Hughson, D. L., and T. C. J. Yeh (2000), An inverse model for three-dimensional flow in variably saturated porous media, *Water Resources Research*, *36*(4), 829-839.

Hunt, J. R., N. Sitar, and K. S. Udell (1988a), Nonaqueous phase liquid transport and cleanup. 1. Analysis of mechanisms, *Water Resources Research*, *24*(8), 1247-1258.

Hunt, J. R., N. Sitar, and K. S. Udell (1988b), Nonaqueous phase liquid transport and cleanup. 2. Experimental studies, *Water Resources Research*, *24*(8), 1259-1269.

Hyun, Y., S. P. Neuman, V. V. Vesselinov, W. A. Illman, D. M. Tartakovsky, and V. Di Federico (2002), Theoretical interpretation of a pronounced permeability scale effect in unsaturated fractured tuff, *Water Resources Research*, *38*(6).

Illman, W. A. (2004), Analysis of permeability scaling within single boreholes, *Geophysical Research Letters, 31*(5).

Illman, W. A., and S. P. Neuman (2000), Type-curve interpretation of multirate single-hole pneumatic injection tests in unsaturated fractured rock, *Ground Water*, *38*(6), 899-911.

Illman, W. A., and S. P. Neuman (2001), Type curve interpretation of a cross-hole pneumatic injection test in unsaturated fractured tuff, *Water Resources Research*, *37*(3), 583-603.

Illman, W. A., and S. P. Neuman (2003), Steady-state analysis of cross-hole pneumatic injection tests in unsaturated fractured tuff, *Journal of Hydrology*, *281*(1-2), 36-54.

Illman, W. A., and D. L. Hughson (2005), Stochastic simulations of steady state unsaturated flow in a three-layer, heterogeneous, dual continuum model of fractured rock, *Journal of Hydrology*, *307*(1-4), 17-37.

Illman, W. A., and D. M. Tartakovsky (2005a), Asymptotic analysis of three-dimensional pressure interference tests: A point source solution, *Water Resources Research*, *41*(1).

Illman, W. A., and D. M. Tartakovsky (2005b), Asymptotic analysis of cross-hole pneumatic injection tests in unsaturated fractured tuff, *Advances in Water Resources*, *28*(11), 1217-1229.

Illman, W. A., and D. M. Tartakovsky (2006), Asymptotic analysis of cross-hole hydraulic tests in fractured granite, *Ground Water*, *44*(4), 555-563.

Illman, W. A., X. Liu, and A. Craig (2007), Steady-state hydraulic tomography in a laboratory aquifer with deterministic heterogeneity: Multi-method and multiscale validation of hydraulic conductivity tomograms, *Journal of Hydrology*, *341*(3-4), 222-234.

Illman, W. A., A. J. Craig, and X. Liu (2008), Practical issues in imaging hydraulic conductivity through hydraulic tomography, *Ground Water*, *46*(1), 120-132.

Illman, W. A., X. Liu, S. Takeuchi, T.-C. J. Yeh, K. Ando, and H. Saegusa (2009), Hydraulic tomography in fractured granite: Mizunami Underground Research site, Japan, *Water Resources Research*, *45*.

Illman, W. A., J. Zhu, A. J. Craig, and D. Yin (2010a), Comparison of aquifer characterization approaches through steady state groundwater model validation: A controlled laboratory sandbox study, *Water Resour. Res*., 46, W04502, doi:10.1029/2009WR007745

Illman, W. A., S. J. Berg and T.-C. J. Yeh (2011), Comparison of approaches for predicting solute transport: Sandbox experiments, *Ground Water*, doi: 10.1111/j.1745-6584.2011.00859.x

Imhoff, P. T., P. R. Jaffe, and G. F. Pinder (1994a), An experimental-study of complete dissolution of a nonaqueous phase liquid in saturated porous-media, *Water Resources Research*, *30*(2), 307-320.

Imhoff, P. T., P. R. Jaffe, and G. F. Pinder (1994b), Correction to "An experimental-study of complete dissolution of a nonaqueous phase liquid in saturated porous-media", *Water Resources Research*, *30*(2), 307-320.

Imhoff, P. T., and C. T. Miller (1996), Dissolution fingering during the solubilization of nonaqueous phase liquids in saturated porous media .1. Model predictions, *Water Resources Research*, *32*(7), 1919-1928.

Imhoff, P. T., G. P. Thyrum, and C. T. Miller (1996), Dissolution fingering during the solubilization of nonaqueous phase liquids in saturated porous media .2. Experimental observations, *Water Resources Research*, *32*(7), 1929-1942.

Imhoff, P. T., M. W. Farthing, S. N. Gleyzer, and C. T. Miller (2002), Evolving interface between clean and nonaqueous phase liquid (NAPL)-contaminated regions in two-dimensional porous media, *Water Resources Research*, *38*(6).

Jawitz, J. W., D. P. Dai, P. S. C. Rao, M. D. Annable, and R. D. Rhue (2003), Rate-limited solubilization of multicomponent nonaqueous-phase liquids by flushing with cosolvents and surfactants: Modeling data from laboratory and field experiments, *Environmental Science & Technology*, *37*(9), 1983-1991.

Jawitz, J. W., A. D. Fure, G. G. Demmy, S. Berglund, and P. S. C. Rao (2005), Groundwater contaminant flux reduction resulting from nonaqueous phase liquid mass reduction, *Water Resources Research*, *41*(10).

Johnson, R. L., and J. F. Pankow (1992), Dissolution of dense chlorinated solvents into groundwater. 2. Source functions for pools of solvent, *Environmental Science & Technology*, *26*(5), 896-901.

Keller, C. K., G. Vanderkamp, and J. A. Cherry (1986), Fracture permeability and groundwater-flow in clayey till near Saskatoon, Saskatchewan, *Canadian Geotechnical Journal*, *23*(2), 229-240

Kim, T. J., and C. V. Chrysikopoulos (1999), Mass transfer correlations for nonaqueous phase liquid pool dissolution in saturated porous media, *Water Resources Research*, *35*(2), 449-459.

Knudby, C., and J. Carrera (2005), On the relationship between indicators of geostatistical, flow and transport connectivity, *Advances in Water Resources*, *28*(4), 405-421.

Knudby, C., and J. Carrera (2006), On the use of apparent hydraulic diffusivity as an indicator of connectivity, *Journal of Hydrology*, *329*(3-4), 377-389.

Lamarche, P., Dissolution of immiscible organics in porous media, Ph.D. thesis, Dep. of Civ. Eng., Univ. of Waterloo, Waterloo, Ontario, Canada, 1991.

Le Borgne, T., O. Bour, F. L. Paillet, and J. P. Caudal (2006), Assessment of preferential flow path connectivity, and hydraulic properties at single-borehole and cross-borehole scales in a fractured aquifer, *Journal of Hydrology*, *328*(1-2), 347-359.

Lemke, L. D., L. M. Abriola, and J. R. Lang (2004b), Influence of hydraulic property correlation on predicted dense nonaqueous phase liquid source zone architecture, mass recovery and contaminant flux, *Water Resources Research*, *40*(12).

Li, W., A. Englert, O. A. Cirpka, and H. Vereecken (2008), Three-dimensional geostatistical inversion of flowmeter and pumping test data, *Ground Water*, *46*(2), 193-201.

Li, W., A. Englert, O. A. Cirpka, J. Vanderborght, and H. Vereecken (2007), Two-dimensional characterization of hydraulic heterogeneity by multiple pumping tests, *Water Resources Research*, *43*(4).

Liu, H. H., C. B. Haukwa, C. F. Ahlers, G. S. Bodvarsson, A. L. Flint, and W. B. Guertal (2003), Modeling flow and transport in unsaturated fractured rock: an evaluation of the continuum approach, *Journal of Contaminant Hydrology*, *62-3*, 173-188.

Liu, H. H., R. Salve, J. S. Wang, G. S. Bodvarsson, and D. Hudson (2004a), Field investigation into unsaturated flow and transport in a fault: model analyses, *Journal of Contaminant Hydrology*, *74*(1-4), 39-59.

Liu, S. Y., T. C. J. Yeh, and R. Gardiner (2002), Effectiveness of hydraulic tomography: Sandbox experiments, *Water Resources Research*, *38*(4).

Liu, X., W. A. Illman, A. J. Craig, J. Zhu, and T. C. J. Yeh (2007), Laboratory sandbox validation of transient hydraulic tomography, *Water Resources Research*, *43*(5).

Liu, X and P. K. Kitanidis (2011), Large-scale inverse modeling with an application in hydraulic tomography, *Water Resour. Res.*, 47, W02501, doi:10.1029/2010WR009144.

Long, J. C. S., J. S. Remer, C. R. Wilson, and P. A. Witherspoon (1982), Porous-media equivalents for networks of discontinuous fractures, *Water Resources Research*, *18*(3), 645-658.

Mackay, D. M., and J. A. Cherry, Groundwater contamination: Pump and treat remediation, *Environ. Sci. Technol*., *23*(6), 630–636, 1989.

Maji, R., and E. A. Sudicky (2008), Influence of mass transfer characteristics for DNAPL source depletion and contaminant flux in a highly characterized glaciofluvial aquifer, *Journal of Contaminant Hydrology*, *102*(1-2), 105-119.

Malone, D. R., C. M. Kao, and R. C. Borden (1993), Dissolution and biorestoration of nonaqueous phase hydrocarbons - model development and laboratory evaluation, *Water Resources Research*, *29*(7), 2203-2213.

Maloszewski, P., and A. Zuber (1993), Tracer experiments in fractured rocks - matrix diffusion and the validity of models, *Water Resources Research*, *29*(8), 2723-2735.

Mayer, A. S., and C. T. Miller (1996), The influence of mass transfer characteristics and porous media heterogeneity on nonaqueous phase dissolution, *Water Resources Research*, *32*(6), 1551-1567.

McDermott, C. I., M. Sauter, and R. Liedl (2003), New experimental techniques for pneumatic tomographical determination of the flow and transport parameters of highly fractured porous rock samples, *Journal of Hydrology*, *278*(1-4), 51-63.

McGuire, T. M., J. M. McDade, and C. J. Newell (2006), Performance of DNAPL source depletion technologies at 59 chlorinated solvent-impacted sites, *Ground Water Monitoring and Remediation*, *26*(1), 73-84.

McKenna, S. A., L. C. Meigs, and R. Haggerty (2001), Tracer tests in a fractured dolomite 3. Double-porosity, multiple-rate mass transfer processes in convergent flow tracer tests, *Water Resources Research*, *37*(5), 1143-1154.Moench, A. F. (1984), Double-Porosity Models For A Fissured Groundwater Reservoir With Fracture Skin, *Water Resources Research*, *20*(7), 831-846.

Miller, C. T., M. M. Poiriermcneill, and A. S. Mayer (1990), Dissolution of trapped non-aqueous phase liquids - mass- transfer characteristics, *Water Resources Research*, *26*(11), 2783-2796.

Moench, A. F. (1984), Double-porosity models for a fissured groundwater reservoir with fractured skin, *Water Resources Research*, *20*(7), 831-846.

Nambi, I. M., and S. E. Powers (2000), NAPL dissolution in heterogeneous systems: an experimental investigation in a simple heterogeneous system, *Journal of Contaminant Hydrology*, *44*(2), 161-184.

Nambi, I. M., and S. E. Powers (2003), Mass transfer correlations for nonaqueous phase liquid dissolution from regions with high initial saturations, *Water Resources Research*, *39*(2).

Neretnieks, I. (1980), Diffusion in the rock matrix - an important factor in radionuclide retardation, *Journal of Geophysical Research*, *85*(NB8), 4379-4397.

Neretnieks, I., T. Eriksen, and P. Tahtinen (1982), Tracer movement in a single fissure in granitic rock - some experimental results and their interpretation, *Water Resources Research*, *18*(4), 849-858.

Neuman, S.P. 1987. Stochastic continuum representation of fractured rock permeability as an alternative to the REV and fracture network concepts. In *Rock Mechanics: Proceedings of the 28th US Symposium, Tucson, AZ,* ed. I.W. Farmer, J.J.K. Daemen, C.S. Desai, C.E. Glass, and S.P. Neuman, 533–561. Rotterdam, The Netherlands: A.A. Balkema, 1240. (Also *in Groundwater Flow and Quality Modelling*, ed. E. Custodio, A. Gurgui, and J.B. Lobo Ferreira, 331–362. NATO ASI Series C, 224. Dordrecht, Holland: D. Reidel, 843, 1988).

Neuman S.P and Depner JS (1988), Use of variable-scale pressure test data to estimate the log hydraulic conductivity covariance and dispersivity of fractured granites near Oracle, Arizona. *Journal of Hydrology 102(1–4)*, 475–501.

Neuman, S. P. (2005), Trends, prospects and challenges in quantifying flow and transport through fractured rocks, *Hydrogeology Journal*, *13*(1), 124-147.

Page, J. W. E., K. Soga, and T. Illangasekare (2007), The significance of heterogeneity on mass flux from DNAPL source zones: An experimental investigation, *Journal of Contaminant Hydrology*, *94*(3-4), 215-234.

Painter, S., and V. Cvetkovic (2005), Upscaling discrete fracture network simulations: An alternative to continuum transport models, *Water Resources Research*, *41*(2).

Pankow, J. F., and J. A. Cherry, *Dense Chlorinated Solvents and other DNAPLs in Groundwater*, Waterloo Press, Portland, Oreg., 1996.

Park, E., and J. C. Parker (2005), Evaluation of an upscaled model for DNAPL dissolution kinetics in heterogeneous aquifers, *Advances in Water Resources*, *28*(12), 1280-1291.

Park, Y. J., K. K. Lee, and B. Berkowitz (2001a), Effects of junction transfer characteristics on transport in fracture networks, *Water Resources Research*, *37*(4), 909-923.

Park, Y. J., J. R. de Dreuzy, K. K. Lee, and B. Berkowitz (2001b), Transport and intersection mixing in random fracture networks with power law length distributions, *Water Resources Research*, *37*(10), 2493-2501.

Park, Y. J., K. K. Lee, G. Kosakowski, and B. Berkowitz (2003), Transport behavior in three-dimensional fracture intersections, *Water Resources Research*, *39*(8).

Parker, J. C., A. K. Katyal, J. J. Kaluarachch, R. J. Lenhard, T. J. Johnson, K. Jayaraman, K. Unlu and J. L. Zhu (1991), Modeling multiphase organic chemical transport in soils and ground water, *Rep. EPA/600/2-91/042*, U. S. Environ. Protect. Agency, Washington, D.C.

Parker, J. C., and J. J. Kaluarachchi (1992), Modeling multi-component organic-chemical transport, *Subsurface Contamination by Immiscible Fluids*, 159-165.

Perry, R. H., D. W. Green, and J. O. Maloney (1984), *Perry's Chemical engineers' handbook*, 2336pp, McGraw-Hill.

Phelan, T. J., L. D. Lemke, S. A. Bradford, D. M. O'Carroll, and L. M. Abriola (2004), Influence of textural and wettability variations on predictions of DNAPL persistence and plume development in saturated porous media, *Advances in Water Resources*, *27*(4), 411-427.

Pinder, G. F., and L. M. Abriola (1986), On the simulation of nonaqueous phase organic-compounds in the subsurface, *Water Resources Research*, *22*(9), S109-S119.

Powers, S. E., C. O. Loureiro, L. M. Abriola, and W. J. Weber (1991), Theoretical-study of the significance of nonequilibrium dissolution of nonaqueous phase liquid in subsurface systems, *Water Resources Research*, *27*(4), 463-477.

Powers, S. E., L. M. Abriola, and W. J. Weber (1992), An experimental investigation of nonaqueous phase liquid dissolution in saturated subsurface systems - steady-state mass-transfer rates, *Water Resources Research*, *28*(10), 2691-2705.

Powers, S. E., L. M. Abriola, and W. J. Weber (1994a), An experimental investigation of nonaqueous phase liquid dissolution in saturated subsurface systems - transient mass-transfer rates, *Water Resources Research*, *30*(2), 321-332.

Powers, S. E., L. M. Abriola, J. S. Dunkin, and W. J. Weber (1994b), Phenomenological models for transient napl-water mass-transfer processes, *Journal of Contaminant Hydrology*, *16*(1), 1-33.

Powers, S. E., I. M. Nambi, and G. W. Curry (1998), Non-aqueous phase liquid dissolution in heterogeneous systems: Mechanisms and a local equilibrium modeling approach, *Water Resources Research*, *34*(12), 3293-3302.

Rao, P. S. C., M. D. Annable, R. K. Sillan, D. P. Dai, K. Hatfield, W. D. Graham, A. L. Wood, and C. G. Enfield (1997), Field-scale evaluation of in situ cosolvent flushing for enhanced aquifer remediation, *Water Resources Research*, 33(12), 2673-2686.

Rasmuson, A., T. N. Narasimhan, and I. Neretnieks (1982), Chemical transport in a fissured rock - verification of a numerical-model, *Water Resources Research*, 18(5), 1479-1492.

Rathfelder, K. M., L. M. Abriola, T. P. Taylor, and K. D. Pennell (2001), Surfactant enhanced recovery of tetrachloroethylene from a porous medium containing low permeability lenses - 2. Numerical simulation, *Journal of Contaminant Hydrology*, 48(3-4), 351-374.

Reimus, P. W., and T. J. Callahan (2007), Matrix diffusion rates in fractured volcanic rocks at the Nevada Test Site: Evidence for a dominant influence of effective fracture apertures, *Water Resources Research*, 43(7).

Romm, E. S. (1966), *Flow characteristics of fractured rocks* (in Russian), Nedra, Moscow.

Russel, H.H., J.E., Matthews, and G. W. Sewell (1992), TCE removal from contaminated soil and ground Water, *EPA Ground Water Issue*, 1-10.

Saba, T., and T. H. Illangasekare (2000), Effect of groundwater flow dimensionality on mass transfer from entrapped nonaqueous phase liquid contaminants, *Water Resources Research*, *36*(4), 971-979.

Saenton, S., T. H. Illangasekare, K. Soga, and T. A. Saba (2002), Effects of source zone heterogeneity on surfactant-enhanced NAPL dissolution and resulting remediation end-points, *Journal of Contaminant Hydrology*, *59*(1-2), 27-44.

Schaefer, C. E., A. V. Callaghan, J. D. King, and J. E. McCray (2009), Dense nonaqueous phase liquid architecture and dissolution in discretely fractured sandstone blocks (vol 43, pg 1877, 2009), *Environmental Science & Technology*, *43*(9), 3402-3402.

Schwartz, F. W., L. Smith, and A. S. Crowe (1983), A stochastic-analysis of macroscopic dispersion in fractured media, *Water Resources Research*, *19*(5), 1253-1265.

Schwartz, F.W., H. Zhang (2003), *Fundamentals of Ground Water*, 764 pp. John Wiley & Sons.

Schwille, F., *Dense Chlorinated Solvents in Porous and Fractured Media: Model Experiments*, translated from German by J. F. Pankow, Lewis, Chelsea, Mich., 1988.

Selroos, J. O., D. D. Walker, A. Strom, B. Gylling, and S. Follin (2002), Comparison of alternative modelling approaches for groundwater flow in fractured rock, *Journal of Hydrology*, *257*(1-4), 174-188.

Singhal, B. B., and R. P. Gupta (2010), *Applied Hydrogeology of Fractured Rocks*, 408pp, Springer.

Slough, K. J., E. A. Sudicky, and P. A. Forsyth (1999), Numerical simulation of multiphase flow and phase partitioning in discretely fractured geologic media, *Journal of Contaminant Hydrology*, *40*(2), 107-136.

Smith, L., and F. W. Schwartz (1984), An analysis of the influence of fracture geometry on mass-transport in fractured media, *Water Resources Research*, *20*(9), 1241-1252.

Soga, K., J. W. E. Page, and T. H. Illangasekare (2004), A review of NAPL source zone remediation efficiency and the mass flux approach, *Journal of Hazardous Materials*, *110*(1-3), 13-27.

Straface, S., T. C. J. Yeh, J. Zhu, S. Troisi, and C. H. Lee (2007), Sequential aquifer tests at a well field, Montalto Uffugo Scalo, Italy, *Water Resources Research*, *43*(7).

Sudicky, E. A., and E. O. Frind (1982), Contaminant transport in fractured porous-media - analytical solutions for a system of parallel fractures, *Water Resources Research*, *18*(6), 1634-1642.

Therrien, R., and E. A. Sudicky (1996), Three-dimensional analysis of variably-saturated flow and solute transport in discretely-fractured porous media, *Journal of Contaminant Hydrology*, *23*(1-2), 1-44.

Therrien, R., R. G. McLaren, E. A. Sudicky, and S. M. Panday (2009), Hydrogeosphere: A three-dimensional numerical model describing fully-integrated subsurface and surface flow and solute transport, edited, Groundwater Simulations Group, Waterloo, Ontario, Canada.

Tsang, Y. W., C. F. Tsang, F. V. Hale, and B. Dverstorp (1996), Tracer transport in a stochastic continuum model of fractured media, *Water Resources Research, 32*(10), 3077-3092.

Unger, A. J. A., E. A. Sudicky, and P. A. Forsyth (1995), Mechanisms controlling vacuum extraction coupled with air sparging for remediation of heterogeneous formations contaminated by dense nonaqueous phase liquids, *Water Resources Research*, *31*(8), 1913-1925

Unger, A. J. A., P. A. Forsyth, and E. A. Sudicky (1996), Variable spatial and temporal weighting schemes for use in multi phase compositional problems, *Advances in Water Resources*, *19*(1), 1-27.

Unger, A. J. A., P. A. Forsyth, and E. A. Sudicky (1998), Influence of alternative dissolution models and subsurface heterogeneity on DNAPL disappearance times, *Journal of Contaminant Hydrology*, *30*(3-4), 217-242.

Vasco, D. W., H. Keers, and K. Karasaki (2000), Estimation of reservoir properties using transient pressure data: An asymptotic approach, *Water Resources Research*, *36*(12), 3447-3465.

VanderKwaak, J. E., and E. A. Sudicky (1996), Dissolution of non-aqueous-phase liquids and aqueous-phase contaminant transport in discretely-fractured porous media, *Journal of Contaminant Hydrology*, *23*(1-2), 45-68.

Vesselinov, V. V., and S. P. Neuman (2001), Numerical inverse interpretation of single-hole pneumatic tests in unsaturated fractured tuff, *Ground Water*, *39*(5), 685-695.

Vesselinov, V. V., S. P. Neuman, and W. A. Illman (2001a), Three-dimensional numerical inversion of pneumatic cross-hole tests in unsaturated fractured tuff 2. Equivalent parameters, high-resolution stochastic imaging and scale effects, *Water Resources Research*, *37*(12), 3019-3041.

Vesselinov, V. V., S. P. Neuman, and W. A. Illman (2001b), Three-dimensional numerical inversion of pneumatic cross-hole tests in unsaturated fractured tuff 1. Methodology and borehole effects, *Water Resources Research*, *37*(12), 3001-3017.

Wellman, T. P., and E. P. Poeter (2005), Estimating spatially variable representative elementary scales in fractured architecture using hydraulic head observations, *Water Resources Research*, *41*(3).

Wilkins, M. D., L. M. Abriola, and K. D. Pennell (1995), An experimental investigation of rate-limited nonaqueous phase liquid volatilization in unsaturated porous-media - steady-state mass-transfer, *Water Resources Research*, *31*(9), 2159-2172.

Williams, J. H., and F. L. Paillet (2002), Using flowmeter pulse tests to define hydraulic connections in the subsurface: a fractured shale example, *Journal of Hydrology*, *265*(1-4), 100-117.

Wu, Y.-S., M. Ye, and E. A. Sudicky (2010), Fracture-flow-enhanced matrix diffusion in solute transport through fractured porous media, *Transport in Porous Media*, *81*(1), 21-34.

Yeh, W. W. G. (1986), Review of parameter-identification procedures in groundwater hydrology - the inverse problem, *Water Resources Research*, *22*(2), 95-108.

Yeh, T. C. J., A. L. Gutjahr, and M. G. Jin (1995a), An iterative cokriging-like technique for groundwater-flow modeling, *Ground Water*, *33*(1), 33-41.

Yeh, T. C. J., M. H. Jin, and S. Hanna (1996), An iterative stochastic inverse method: Conditional effective transmissivity and hydraulic head fields, *Water Resources Research*, *32*(1), 85-92.

Yeh, T. C. J., and J. Q. Zhang (1996), A geostatistical inverse method for variably saturated flow in the vadose zone, *Water Resources Research*, *32*(9), 2757-2766.

Yeh, T. C. J., and S. Y. Liu (2000), Hydraulic tomography: Development of a new aquifer test method, *Water Resources Research*, *36*(8), 2095-2105.

Yeh, T.-C.J., Simunek, J., 2002. Stochastic fusion of information for characterizing and monitoring the vadose zone. *Vadose Zone Journal* 1, 207–221.

Yeh, T.-C. J., D. Mao, L. Wan, K.-C. Hsu, J.-C. Wen, and C.-H. Lee (2011), Uniqueness, scale, and resolution issues in groundwater model parameter identification, technical report, Dep. of Hydrol. and Water Resour., Univ. of Ariz., Tucson, Ariz.

Zhang, J. Q., and T. C. J. Yeh (1997), An iterative geostatistical inverse method for steady flow in the vadose zone, *Water Resources Research*, *33*(1), 63-71.

Zheng, Q. and Coniglio, M. (1998), Subsurface dedolomitization in the pinnacle reefs of the Guelph Formation (Middle Silurian), southwestern Ontario, Canada. Conference: *American Association of Petroleum Geologists,1998 Annual Meeting.*

Zhu, J. F., and T. C. J. Yeh (2005), Characterization of aquifer heterogeneity using transient hydraulic tomography, *Water Resources Research*, *41*(7).

Zhu, J. F., and T. C. J. Yeh (2006), Analysis of hydraulic tomography using temporal moments of drawdown recovery data, *Water Resources Research*, *42*(2).

Zimmerman, R. W., G. Chen, T. Hadgu, and G. S. Bodvarsson (1993), A Numerical Dual-Porosity Model With Semi-Analytical Treatment Of Fracture Matrix Flow, *Water Resources Research*, *29*(7), 2127-2137.